Robustness and Thermophysical Properties of MOF-5: A Prototypical Hydrogen Storage Material

by

Yang Ming

A dissertation submitted in partial fulfillment
of the requirements for the degree of
Doctor of Philosophy
(Physics)
in the University of Michigan
2015

Doctoral Committee:

Associate Professor Donald J. Siegel, Co-Chair
Professor Finn Larsen, Co-Chair
Professor David W. Gidley
Professor Adam J. Matzger
Professor Ctirad Uher

Acknowledgments

First of all, I would like to thank my advisor, Professor Siegel, for giving me so much help during my Ph.D studies. He provided much useful advice on my research, and demonstrated unlimited patience with my grammar when editing my papers and thesis. Outside the study, I also learned how to communicate politely, which has helped me build strong connections here in the US.

For serving on my Ph.D. committee, I thank Professors Finn Larson, David Gidley, Adam Matzger, and Ctirad Uher.

Special thanks are due to my collaborators and mentors at Ford motor company: Mike Veenstra, Jun Yang, Chunchuan Xu and Justin Purewal. I received substantial instruction and assistance from the Ford team on designing and conducting experiments during the past 3 years.

I also want to thank the members of Professor Siegel's group at UM for helping me with my simulation research, especially Malay, Hyun, Max and Sheng. I bothered them repeatedly with many questions, but they were always ready and willing to help.

Five years as a PhD student is not always easy in a foreign country. Support from my parents and my girlfriend helped immensely during these times. They believed in me and were a constant source of strength, no matter what difficulties I faced along the way.

Last but not the least, I want to acknowledge the advice I gleaned from reading ancient Chinese culture and history books. Great ancestors such as Confucius taught me how to be a person with honesty, kindness, inner peace and self-discipline. Exercises and tips from ancient Chinese medicine helped me develop an energetic body while maintaining a peaceful mind.

Table of Contents

Acknowledgments .... **ii**

List of Figures .... **ix**

List of Tables .... **xxi**

List of Appendices .... **xxiii**

Abstract .... **xxiv**

Chapter 1 Introduction **1**

- 1.1 Motivation 1
  - 1.1.1 Greenhouse effect 1
  - 1.1.2 Air pollution 3
  - 1.1.3 Resource exhaustion 5
- 1.2 Hydrogen energy and hydrogen storage 6
- 1.3 Metal organic frameworks 7
- 1.4 Goals of this Research and Overview of this Dissertation 9

Chapter 2 Methodology 16

2.1 Volumetric PCT measurements 16

2.2 X-ray diffraction 19

2.3 Surface area 20

2.3.1 Langmuir Theory 20

2.3.2 BET theory 21

2.4 FTIR 21

2.5 Thermal conductivity measurements 23

2.5.1 Direct steady state heat flow method 23

2.5.2 Laser flash thermal diffusivity measurement 25

2.5.3 Thermal capacity measurement (DSC) 26

2.6 Density Functional Theory 28

2.6.1 Conventional Density Functional Theory 28

Chapter 3 Thermophysical Properties of MOF-5 Powders 33

3.1 Introduction 33

3.2 Experimental Procedure 35

3.2.1 Materials Preparation 35

3.2.2 Materials Characterization 37

3.3 Results and Discussion 44

3.3.1 Structural Properties 46

3.3.2 Thermal Properties 52

3.3.3 Hydrogen Adsorption Isotherms 57

3.3.4 Robustness to Air Exposure 66

3.4 Conclustion 69

Chapter 4 Anisotropic Thermal Transport in MOF-5 Composites 71

4.1 Introduction 71

4.2 Experimental Procedure 75

4.2.1 Materials Preparation 75

4.2.2 Materials Characterization 78

4.3 Results and Discussion 83

4.3.1 Pellets with Homogeneous ENG Distribution 83

4.3.2 Pellets with Layered ENG Distribution 92

4.4 Conclusion 94

Chapter 5 Kinetic Stability of MOF-5 in Humid Environments: Impact of Powder Densification, Humidity Level, and Exposure Time 96

5.1 Introduction 96

5.2 Experimental Details 98

5.2.1 Materials Preparation 98

5.2.2 Characterization 100

5.3 Results and Discussion 102

5.3.1 MOF-5 powder 102

5.3.2 MOF-5 Pellets 112

5.4 Conclusion 116

Chapter 6 Water Adsorption and Insertion in MOF-5 118

6.1 Introduction 118

6.2 Computational Method 121

6.3 Results and discussion 122

6.3.1 Adsorption of Isolated Water Molecules 122

6.3.2 Adsorption of Multiple Water Molecules 126

6.3.3 Water insertion 129

6.4 Conclusion 134

Chapter 7 Stability of MOF-5 in a Hydrogen Gas Environment with Expected Fueling Station Impurities 137

7.1 Introduction 137

7.2 Experiment detail 141

7.2.1 Materials preparation 141

7.2.2 Impurity test gases 141

7.2.3 Cycle test procedures 144

7.2.4 Storage test procedure 146

7.2.5 Capacity Test Procedure 146

7.2.6 XRD and FTIR Characterization 148

7.3 Result and discussion 149

7.3.1 Maximum Impurity Accumulation 149

7.3.2 Impurity cycle test 151

7.3.3 Static exposure tests 156

7.4 Conclusion 159

Chapter 8 Imaging the Microstructure and Hydrogen Permeation in MOF-5 Pellets 160

8.1 Introduction 160

8.2 Method 162

8.2.1 Material preparation 162

8.2.2 Neutron imaging 163

8.2.3 MicroCT 168

8.3 Results and discussion 168

8.3.1 Transient hydrogen distribution 168

8.3.2 Neutron imaging tomography 172

8.3.3 Density variation 173

8.4 Conclusion 176

Chapter 9 Conclusion 177

9.1 Heat transport in MOF-5 177

9.2 Mass transport in MOF-5 178

9.3 Outlook and Future work 181

Appendices 183

Bibliography 196

List of Figures

Figure 1.1 CO_2 concentration (ppm) in atmosphere from 1960s to 2014. 2

Figure 1.2. Human sources of carbon dioxide 3

Figure 2.1. Calculation of excess adsorption by the volumetric method. 17

Figure 2.2. X-rays reflected off adjacent planes. 20

Figure 2.3. Thermal couple positions for the steady state heat flow method 24

Figure 2.4. Schematic of the laser flash method. 26

Figure 3.1. Comparison of space-time-yields (STY) for synthesis of various framework materials in both laboratory and commercial settings. 49

Figure 3.2. Crystal size histogram and statistics for MOF-5 powder. The distribution has a mean diameter of 0.36 μm and standard deviation of 0.144 μm. 50

Figure 3.3. Particle size distribution and cumulative volume percentage for a representative MOF-5 powder. The distribution has a mean diameter of 215 μm; 99% of the particles have a diameter less than 857 μm. 51

Figure 3.4. Tap density of MOF-5 as a function of the number of taps. 52

Figure 3.5. Specific heat capacity (c_p) ($Jg^{-1}K^{-1}$) for powder MOF-5 as a function of temperature (K). 54

Figure 3.6. Thermal conductivity data for MOF-5 powders as a function of temperature and bulk density: 0.35 g cm^{-3} (diamonds), 0.52 g cm^{-3} (triangles) and 0.69 g

cm^{-3} (circles). The thermal conductivity for a single crystal of MOF-5 at 300 K (square) is provided for reference[157]. 56

Figure 3.7. Excess hydrogen adsorption isotherms for powder MOF-5 at five temperatures (77, 103, 118, 138, 200 and 295 K). Measured data corresponds to symbol points, and solid lines are fits using the modified D-A equation (2). (Left axis) Gravimetric excess capacity in mol/kg. **(**Right axes**)** Volumetric excess adsorption (g/L), where the near-right ordinate is based on the MOF-5 loose-packed powder density (ρ_{bulk}=0.13 gcm^{-3}) and the rightmost ordinate assumes a density equal to the MOF-5 crystal density (ρ_{sx}=0.605 gcm^{-3}). 62

Figure 3.8. Absolute hydrogen adsorption isotherms for powder MOF-5 at six temperatures (77, 103, 118, 138, 200, and 295 K) based on D-A parameters in Section 3.3.2. On the left ordinate, absolute adsorption is listed in gravimetric units of mol/kg. The right ordinate lists absolute adsorption in volumetric units of g/L, assuming the bulk density of loosely-packed MOF-5 powder (ρ_{bulk}=0.13 gcm^{-3}). 63

Figure 3.9. Total hydrogen storage within the gross volume occupied by the powder MOF-5, assuming a bulk powder density of ρ_{bulk} = 0.13 g/cm^3. The dashed red line indicates the density of bulk H_2 gas at 77 K. 64

Figure 3.10. Differential H_2 adsorption enthalpy ($-\Delta H_{\mathrm{ads}}$) of powder MOF-5. Experimental estimates of $-\Delta H_{\mathrm{ads}}$ are plotted on the top axis versus the

fractional excess adsorption. The modeled -ΔH_{ads} [eq (3.3)] is plotted on the bottom axis versus fractional absolute adsorption. 66

Figure 3.11. MOF-5 hydrogen uptake isotherms following exposure to humid air (45% relative humidity at 22^{0}C) for various times. “Activated” samples were heated to 130ºC and evacuated for at least 6 hours; “non-activated” samples were evacuated without heating for only 15 minutes. The inset shows a magnification of the maximum uptake region of the isotherms. 67

Figure 3.12. *In situ* X-ray diffraction pattern for MOF-5 powder as a function of exposure time to laboratory air (relative humidity around 45% at 22^{0}C). Vertical lines show the peak positions and relative intensities for the reference desolvated MOF-5 structure[125]. 69

Figure 4.1. Images of MOF-5 (upper panel) and ENG powders (lower panel). 76

Figure 4.2. Cylindrical and rectangular MOF-5/ENG composite pellets. (a, b) Cylindrical pellet used for room temperature measurements and microstructure characterization. Pellet diameter = 1.28 cm, thickness = 3 mm, density = 0.4g/cm^3. The pellet in (a) has a homogeneous ENG distribution, while the pellet in (b) has a layered ENG distribution. (c) Rectangular sample used for low-temperature measurements (80 – 300 K). The sample dimensions are 10 × 5 × 5 mm. Sample density = 0.35 g/cm^3. 78

Figure 4.3. (a) Optical microscopy image of MOF-5 particles (white) coated with

ENG (black) after milling. (b) SEM of the interface between MOF-5 and ENG within a densified pellet containing 5 wt.% ENG and with a pellet density = 0.50 g/cm^3. 84

Figure 4.4. Cross sections of MOF-5 pellets containing 5 wt.% ENG and with density of 0.38 g/cc imaged using optical microscopy. The images depict boundary lines consisting of ENG deposits at (a) magnifications of x50 and x200 as well as at (b) x50 and x400. 85

Figure 4.5. Cross section of a MOF-5/ENG pellet from optical microscopy. Arrows indicate the pressing direction. The sketch below each image shows the relationship of the cross-section plane to the pressing direction. (a) MOF-5 mixed with 5% ENG, pressed axially; (b) MOF-5 mixed with 10% ENG, pressed axially; and (c) MOF-5 mixed with 5% ENG, pressed radially.... 86

Figure 4.6. Near-ambient temperature thermal conductivity for MOF-5/ENG pellets (0.4g/cm^3) as a function of temperature, ENG content, and pressing direction. Error bars correspond to the range of measured values............ 89

Figure 4.7. Thermal conductivity of 0.35 g/cm^3 pellets containing 5% ENG formed using two orthogonal pressing directions over the temperature range of 80 - 300K.. 90

Figure 4.8. (Left) Optical microscopy image of a cross-section of a MOF-5 pellet containing ~5 wt.% ENG in a layered distribution. The graph shows the cross section of pellet after being cut perpendicular to the ENG layers; the

top and bottom surfaces of pellet are labeled. MOF-5 layers are white, while the ENG layers are black. (Right) Schematics showing the orientation of the ENG layers. The dashed rectangle shows the cross-sectional plane..........92

Figure 4.9. Thermal conductivity of pellets with two different ENG distributions (layered and homogeneous) at near-ambient temperatures. Both pellets contain approximately 5 wt. % ENG. Layered pellets contain ENG layers which are parallel to the heat flow direction. Data for the homogeneous pellets are reproduced from figure 4.5, and refer to the samples identified as "5% ENG parallel to heat flow."..94

Figure 5.1. MOF-5 morphologies examined. Left: powder; right: pellets..................99

Figure 5.2. Excess gravimetric hydrogen uptake in MOF-5 powders as a function of relative humidity and exposure time. Top: relative humidity = 45%, T = 22°C; Bottom: relative humidity = 61%, T = 22°C. Isotherms are plotted before exposure to humid air (0 h), and after 5 increasingly longer exposure times: 0.5 h, 1.5 h, 24 h, 48 h and 66 h. Solid symbols represent experimental data; these data are fit using the Unilan isotherm model (solid lines)...103

Figure 5.3. BET surface area of MOF-5 powders (filled data points) and pellets (open symbols) as a function of exposure time to humid air with relative humidities (RH) of 45% (square symbols) and 61% (circular symbols). T = 22°C in all cases. Data points at t = 0 correspond to samples which were not

exposed to humidity. 105

Figure 5.4. XRD spectra for MOF-5 powders as a function of exposure time to humid air with relative humidities of 45% (top) and 61% (bottom). In both cases T = 22°C. 106

Figure 5.5. Water adsorption in MOF-5 powder at 25°C vs. relative humidity for three adsorption/desorption cycles. 108

Figure 5.6. FTIR spectra for MOF-5 powders exposed to air with RH = 61% for 0 h, 24 h, and 66 h at 22 °C. 109

Figure 5.7. (a) Magnification of a portion of the MOF-5 crystal structure. Red represents O, blue: Zn, black: C, pink, H. The trapezoid represents the region of interest for water interactions with MOF-5, as shown in the lower four panels. (b) Physisorption of water near the Zn cluster. (c) Insertion of molecular water into the MOF-5 framework via bonding to Zn and displacement of the BDC linker. (d) Water insertion and dissociation, resulting in a hydroxyl group bonding to Zn and carboxylic acid at the terminus of the linker. (e) An example of a carboxylic acid dimer that may contribute to peak 4 in the FTIR spectra. Numbers 1 – 4 refer to bonds associated with peaks in the FTIR spectrum in Figure 5.6. 111

Figure 5.8. Excess gravimetric H_2 adsorption amount for MOF-5 pellets (density ~0.37 g/cm^3) exposed to a humid environment for 0.5h, 2h, 24h and 66h, respectively. (a) Pure MOF-5 pellet, RH=45%; (b) Pure MOF-5 pellet,

RH=61%; (c) MOF-5/5%ENG pellet, RH=45%; (d) MOF-5/5%ENG pellet, RH=61%. Symbols represent experimental data, lines are fits to the data using the Unilan isotherm model. 113

Figure 6.1. (a) Conventional unit cell of MOF-5. Red spheres represent Oxygen, blue: Zn, grey: C, white: H. (b) Magnification of the metal cluster and organic linker from panel (a). The purple spheres represent 5 distinct sites for water adsorption, and are labeled with Greek symbols. 124

Figure 6.2. (a) Calculated adsorption energies for water as a function of exchange-correlation functional and adsorption site in MOF-5. (b-d) Calculated distance from proximal O in an adsorbed water molecule to various atoms in MOF-5 for adsorption sites located on the metal cluster (sites α, β, and γ). 126

Figure 6.3. Calculated total adsorption energy for water molecules as a function of water coverage and adsorption configuration. For each coverage the yellow bar on the left represents the adsorption energy in the case where only α sites are filled. Blue bars on the right represent the adsorption energy for the most energetically favorable water distribution. Adsorption geometries are labeled inside each bar. 128

Figure 6.4. Water insertion energy in MOF-5 as a function of coverage on a Zn-O cluster. The labels within in each bar indicate the configuration of adsorbed H_2O before insertion. 130

Figure 6.5. Water insertion process in MOF-5. (a) Magnification of MOF-5 structure with 4 water molecules physically adsorbed near the Zn-O cluster. (b) Transition state. (c) Final MOF-5 structure containing a Zn-O bond broken via the insertion of a single water molecule. The color scheme for MOF atoms is the same as in figure 6.1(b); O atoms in the water molecules are purple to distinguish them from oxygen in the MOF (blue). Black dashed lines/text indicate hydrogen bond lengths between H and O in adjacent water molecules. Red lines/text illustrate Zn-O bond distances. 131

Figure 6.6. Calculated energy barrier for the insertion of a water molecule into MOF-5. The insertion process breaks a Zn-O bond, and occurs in the presence of 3 additional adsorbed water molecules adsorbed on the metal cluster. 132

Figure 7.1. An example of the pressure cycling procedure shown as excess adsorption and pressure versus test time. The lower graph displays the reservoir pressure, plotted on a square root scale. The upper axis displays the calculated adsorption amount of the MOF-5 sample. Both are plotted versus total elapsed time. For cycle number two. the adsorption phase (labelled **A**), desorption phase (labelled **D**) and vacuum phase (**V**) are annotated in the graph. The split *x*-axis shows the first 5 and last 5 cycles from this experiment.. 151

Figure 7.2. (a) Adsorption isotherm of MOF-5 powders with test gas mixture 1 including NH_3 as the impurity. Capacity measurement are taken every 60

cycles (b) XRD spectra for MOF-5 powders before and after cycle test (c) FTIR spectra for MOF-5 powders before and after cycle test. 152

Figure 7.3. (a) Adsorption isotherm of MOF-5 powders with test gas mixture 3 including HCl as the impurity. Capacity measurement are taken every 60 cycles (b) XRD spectra for MOF-5 powders before and after cycle test (c) FTIR spectra for MOF-5 powders before and after cycle test. 154

Figure 7.4. Summary of MOF-5 hydrogen storage capacity at 77 K during pressure cycling with impurity gas mixtures. The y-axis indicates the maximum excess adsorption amount measured during the capacity test each point during the pressure cycling test, expressed as a percentage of the maximum excess adsorption measured before the start of the cycle test. 156

Figure 7.5. (a) Adsorption isotherm of MOF-5 powders with test gas mixture 4 including H_2O as the impurity. Capacity measurement are taken before and after 1 week static exposure (b) XRD spectra for MOF-5 powders before and after static exposure (c) FTIR spectra for MOF-5 powders before and after static exposure. 157

Figure 7.6. (a) Adsorption isotherm of MOF-5 powders with test gas mixture 2 including H_2S as the impurity. Capacity measurement are taken before and after 1 week static exposure (b) XRD spectra for MOF-5 powders before and after static exposure (c) FTIR spectra for MOF-5 powders before and after static exposure. 158

Figure 8.1. Plan view of the neutron imaging facility at the NIST Center for Neutron Research[247]. 163

Figure 8.2. Picture of vessel used in NIST neutron imaging experiment. Dimensions are shown in the graph. 165

Figure 8.3. Schematic representation of neutron imaging radiography[247]. 166

Figure 8.4. Cartoon illustrating the technique of tomography. The sample is colored green. The sample is rotated from its previous orientation by a degree of θ. The parallel arrays represent the neutron beam[249]. 168

Figure 8.5. (a) Temproal evolution of the hydrogen density distribution in a vessel containing MOF-5 pellets during adsorption. (b) Hydrogen density distribution during desorption. Red represents high hydrogen density, while black represents low hydrogen density. 170

Figure 8.6. Transient hydrogen density distribution of a MOF-5 puck. Red stands for higher density, and black stands for lower density. 171

Figure 8.7. Average adsorbed hydrogen density as a function of hydrogen gas pressure and radial distance from pellet center. 172

Figure 8.8. Tomography of MOF-5/ENG pellet using neutron imaging technique. The color bar shows the attenuation coefficient. 173

Figure 8.9. MicroCT tomography images for a MOF-5/ENG pellet, and for several pure MOF-5 pellets fabricated using powders filtered with different mesh sizes. Blue represents regions of low density, while red represents high density.

....174

Figure 8.10, Density fluctuation percentage across the cross sections of MOF-5 pellets using different pre-meshing treatments. 175

Figure A.1. Pilot-plant pellets 6x6 mm, 5% ENG, density of.391 g/cc with standard deviation of 0.013 g/cm^3. Both top view (left) and side view (right) are shown here. 184

Figure A.2. MOF-5 conglomerates surrounded by ENG particles prior to the compaction of pellets. 184

Figure A.3. Quanta SEM used to obtain images with red = Carbon, green = Zinc, blue = Oxygen (a) Elemental map of lab made MOF-5 + 5wt.% ENG pellet with density of 0.5019 g/cc (b) SEM image of area mapped for lab pellet. 186

Figure A.4. (a) a lab prepared pellet containing MOF-5 with 5wt% ENG and a density of 0.378g/cc embedded in resin and (b) a pilot plant pellet containing MOF-5 with 5wt% ENG and a density of 0.378g/cm^3 embedded in resin. 186

Figure A.5. (Left) Pressing cylindrical pellet along the axial direction. (Right) Pressing cylindrical pellet along the radial direction 187

Figure A.6. Thermal couple positions for the steady state heat flow method............187

Figure B.1. Geometry of humidity chamber for sample exposure. 188

Figure B.2. Humidity chamber configuration..188

Figure C.1. Crystal structure for the hypothetical MOF, IRMOF-0h, which was used to approximate MOF-5 in Ref. [210]. This structure is a simplification of the MOF-5 structure, wherein the benzene ring present in the MOF-5 linker is replaced with two C atoms. Carbon atoms are grey, oxygen is red, and Zn atoms are shown in blue. 189

Figure C.2. Calculated distance between certain atom in water and that in MOF-5 metal cluster. Results from GGA and vdW functionals are compared. Panel (a) (b) (c) correspond to site α, β and γ. 190

Figure D.1. (a) Adsorption isotherm of MOF-5 powders with test gas mixture 2 including H_2S as the impurity. Capacity measurement are taken every 60 cycles (b) XRD spectra for MOF-5 powders before and after cycle test (c) FTIR spectra for MOF-5 powders before and after cycle test. 193

Figure D.2. (a) Adsorption isotherm of MOF-5 powders on with testing gas mixture 4 including H2O as the impurity. Capacity measurement are taken every 60 cycles (b) XRD spectra for MOF-5 powders before and after cycle test (c) FTIR spectra for MOF-5 powders before and after cycle test. 194

Figure D.3. (a) Adsorption isotherm of MOF-5 powders on with testing gas mixture 5 including CO, CO2, CH4, O2, N2, and He as the impuritiesy. Capacity measurement are taken every 60 cycles (b) XRD spectra for MOF-5 powders before and after cycle test (c) FTIR spectra for MOF-5 powders before and after cycle test. 195

List of Tables

Table 3.1. Comparison of space-time-yields (STY) for synthesis of various framework materials in both laboratory and commercial settings. MeIM=2-Methylimidazolate, BTC=benzene-1,3,5-tricarboxylate , BDC=1,4-benzene dicarboxylate 37

Table 3.2. Summary of structural, thermal, and hydrogen isotherm materials properties for MOF-5. Unless otherwise indicated, all measurements performed on loose powder form of MOF-5 45

Table 4.1. Average orientation and standard deviation of ENG particles in MOF-5/ENG composites with respect to the pressing direction for the three pellets described in Fig. 5: (a) MOF-5 mixed with 5 wt.% ENG, pressed axially; (b) MOF-5 mixed with 10 wt.% ENG, pressed axially; and (c) MOF-5 mixed with 5 wt.% ENG, pressed radially. The solid black segment represents the average orientation of ENG in the pellet. Black arrows and the dashed line represent the pressing direction. The standard deviation refers to the distribution of ENG orientations observed in cross-sectioned pellets. 88

Table 6.1. Number and location of each type of adsorption site depicted in Figure 6.1. 123

Table 7.1. Impurity test gas mixtures used in this MOF-5 study. 138

Table 7.2. Estimated maximum impurity accumulation by MOF-5 based on SAE J2719 PPM levels 142

Table 8.1. Sizes and compositions of pellets used in neutron imaging and microCT experiments. 162

Table 8.2. Standard deviation in the density of pellets with different filtering pre-treatment. The sizes listed in the left column refer to the aperature size of the mesh used to filter MOF-5 powders before pressing into pellets. 175

List of Appendices

A.Supporting information for Anisotropic Thermal Transport in MOF-5 Composites…… ……………………………………………………………...183

B.Supporting information for Kinetic Stability of MOF-5 in Humid Environments: Impact of Powder Densification, Humidity Level, and Exposure Time...188

C.Supporting information for Water adsorption on, and Insertion into MOF-5 189

D.Stability of MOF-5 in a hydrogen gas environment with expected fueling station impurities 193

Abstract

Metal-organic frameworks (MOFs) are an emerging class of microporous, crystalline materials with potential applications in the capture, storage, and separation of gasses. Of the many known MOFs, the compound known as MOF-5 has attracted considerable attention due to its ability to store gaseous fuels at low pressure with high densities. However, low thermal conductivity and limited robustness upon exposure to water and other reactive species are two challenges which limit the application of MOF-5; similar issues plague several other MOFs. The focus of this dissertation is to understand and overcome these shortcomings through detailed experimental and computational characterization of the prototype compound, MOF-5. The insight provided by this study regarding the properties of MOFs will aid in the transition of these materials from lab bench to applications.

Improvements to the thermal conductivity of MOF-5 are demonstrated using densified pellets consisting of a physical mixture of MOF-5 and expanded natural graphite (ENG). The high-aspect ratio of ENG particles, combined with uni-axial compression, results in anisotropic microstructural and thermal transport properties in the pellets. Perpendicular to the pressing direction the thermal conductivity was observed to be two to four times higher than in the orthogonal direction. We further demonstrate that this anisotropy can be exploited to enhance conductivity along a preferred direction in the pellets by altering the pellet processing conditions. We

conclude that the low thermal conductivity typical of MOFs can be improved using a judicious combination of second phase additions and processing techniques.

Regarding robustness, we first quantify experimentally the impact of humid air exposure on the properties of MOF-5 as a function of exposure time, humidity level, and morphology (i.e., powders *vs.* pellets). For humidity levels below 50% only minor degradation is observed for exposure times up to several hours. In contrast, irreversible degradation occurs in a matter of minutes for exposures above the 50% threshold. This transition in performance can be linked to the shape of the water isotherm, which shows a large increase in uptake at ~50% relative humidity. Densification into pellets can slow the degradation of MOF-5 significantly, and may present a pathway to enhance the stability of some MOFs.

We subsequently examined the thermodynamics and kinetics of water adsorption/insertion into MOF-5 using van der Waals-augmented Density Functional Theory calculations and transition state finding techniques. Adsorption and insertion energetics were evaluated as a function of water coverage while accounting for the full periodicity of the MOF-5 crystal structure, i.e., without resorting to cluster approximations or structure simplification. We find that incoming water molecules preferentially adsorb at adjacent sites on Zn-O clusters rather than filling widely separated low energy sites. Our calculations also suggest that the thermodynamics of MOF hydrolysis are coverage dependent: water insertion into the framework becomes exothermic (with a low, 0.17eV activation barrier) only after a sufficient number of

H_2O molecules are adsorbed on a Zn-O cluster. This observation is in good agreement with experimental measurements, which show that hydrolysis is slow at low water coverages and is preceded by an incubation period.

The third component in our study of MOF-5 robustness involved cyclic and static exposure to impure hydrogen gas. Five impurity gas mixtures were prepared by introducing low levels of selected contaminants (NH_3, H_2S, HCl, H_2O, CO, CO_2, CH_4, O_2, N_2, and He) to high-purity hydrogen gas. MOF-5 was exposed to these mixtures over hundreds of adsorption/desorption pressure cycles and for extended periods of static exposure lasting up to 1 week. Hydrogen chloride was the only impurity that yielded a measurable decrease in hydrogen storage capacity. Post-cycling and post-storage samples were analyzed using FTIR spectroscopy and x-ray diffraction. These analyses reveal slight changes in the spectra (compared to the pristine samples) only for those samples exposed to HCl and NH_3 impurities.

In closing, we briefly examine hydrogen permeation into- and the internal structure of- MOF-5 pellets using neutron and x-ray imaging techniques (tomography and radiography). Neutron tomography reveals the 3-dimensional distribution of the ENG network inside MOF-5/ENG composite pellets. MicroCT allows for the characterization of density variations within MOF-5 pucks. *In situ* neutron radiography shows that hydrogen permeation is rapid in densified MOF-5 bodies.

Chapter 1

Introduction

1.1 Motivation

Fossil fuels—coal, petroleum (oil), and natural gas — have been an essential part of human beings' lives for hundreds of years. These fuels are the major source for electricity generation, public transportation and tens of thousands of commercial goods such as ink, plastic and tires. According to the US Energy Information Administration (EIA), fossil fuels comprise 95% of the fuels used in transportation, and 67.2% of those used in electric power generation in the US[1]. Due to the long history associated with their use, the EIA credits fossil fuels for bringing about "one of the most profound social transformations in history."

However, like a double-edged sword, fossil fuels leave us many issues to address. The most urgent of these are: the greenhouse effect, atmospheric pollution, and resource exhaustion.

1.1.1 Greenhouse effect

The greenhouse effect is the process by which thermal radiation from a planetary surface is absorbed by atmospheric greenhouse gases, and is re-radiated in all directions.

Since part of this re-radiation is back towards the surface and the lower atmosphere, it results in an elevation of the average surface temperature above what it would be in the absence of the gases [2]. Human activities can strengthen the greenhouse effect, which is known as the enhanced (or anthropogenic) greenhouse effect[3]. This increase in radiative forcing from human activity is mainly due to increased atmospheric carbon dioxide levels[4]. According to the report from the National Oceanic & Atmospheric Administration (NOAA), the concentration of atmospheric CO_2 has been continuously increasing from a baseline of 320 ppm since it was observed in the 1960s[5]. Figure 1.1 shows the linear uptrend in CO_2 concentration in the atmosphere from the 1960s to June 2014, when the concentration hit 397 ppm. In May 2015 the NOAA's Mauna Loa Observatory announced that the concentration of CO_2 had reached 403.26 ppm, which is the highest level ever recorded[6].

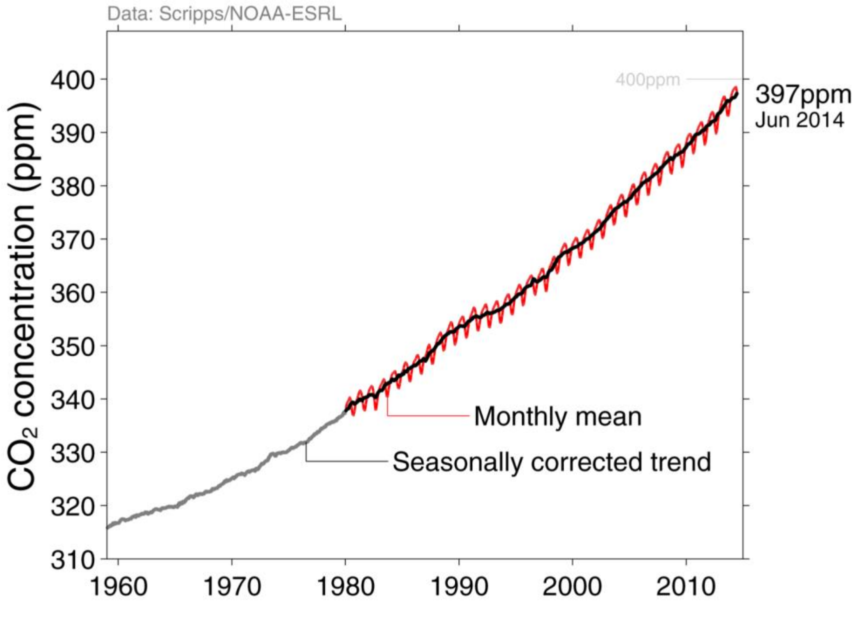

Figure 1.1 CO_2 concentration (ppm) in atmosphere from 1960s to 2014.

Human sources of carbon dioxide emissions have been growing since the Industrial Revolution. Human activities such as the burning of oil, coal and gas, as well as deforestation are the primary cause of the increased carbon dioxide concentrations in the atmosphere. Figure 1.2 shows the sources of CO_2 created by human beings. These data reveal that 87 percent of all human-produced carbon dioxide emissions come from the burning of fossil fuels like coal, natural gas and oil. The remainder results from the clearing of forests and other land use changes (9%), as well as some industrial processes such as cement manufacturing (4%)[7]. This leaves us the first question: Is it possible to find an alternative energy resource or ‘fuel’ that does not produce CO_2 so as to minimize human contributions to the greenhouse effect?

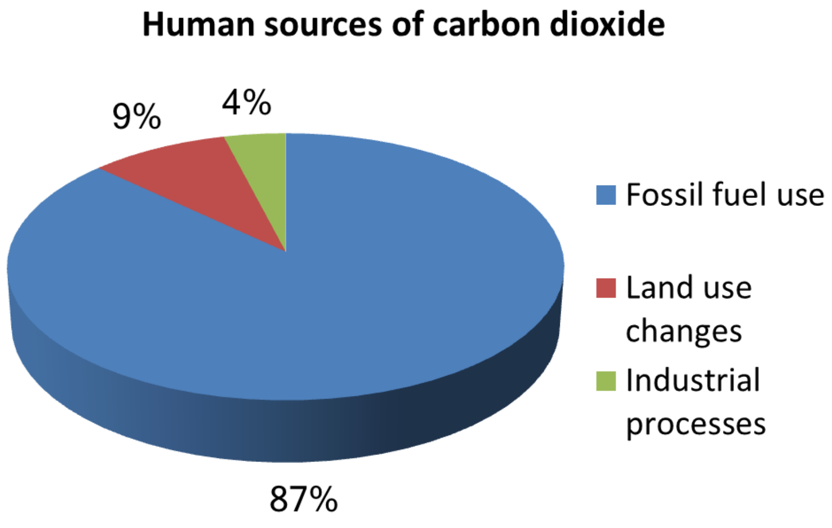

Figure 1.2. Human sources of carbon dioxide

1.1.2 Air pollution

Besides the greenhouse effect, another major issue facing humanity is air pollution. Air pollution is the introduction of particulates, biological molecules, or other harmful gases into Earth's atmosphere, causing disease, death to humans, damage to other living organisms such as food crops, or the natural or built environment[8]. Air pollution may come from anthropogenic or natural sources. Several important pollutants are produced by fossil fuel combustion: carbon monoxide, nitrogen oxides, sulfur oxides, and hydrocarbons.

Carbon monoxide (CO) is a by-product from the incomplete combustion of fossil fuels. Cars and trucks are the primary source of carbon monoxide emissions. This odorless, colorless, and poisonous gas can block oxygen from the brain, heart, and other vital organs after being inhaled. It has a severe effect on fetuses, newborn children, and people with chronic illnesses such as heart disease.

Nitrogen dioxide (NO_2) is formed in high temperature combustion. It can be observed as yellowish-brown haze over many cities. NO2 is a toxic gas that can cause lung irritation, bronchitis and pneumonia, and weaken the body’s resistance to respiratory infections. The transportation sector is responsible for close to half (47.8%) of the emissions of nitrogen oxides; power plants produce most of the rest (35.1%)[9].

Sulfur oxides, especially sulfur dioxide (SO_2), are produced by power plants and motor vehicles from the burning the sulfur-containing fuels, especially diesel. According to the U.S. environmental protection agency, fuel combustion produces 84% of the nation's sulfur dioxide emissions[10]. Nitrogen oxides and sulfur oxides can form sulfuric and nitric acids and become part of rain and snow when they combine with water vapor in clouds. As these acids accumulate in lakes and rivers afterwards, plants and animals can no longer live nearby. Acid rain also adversely impacts crops and buildings.

Hydrocarbons are emitted from human-made sources such as auto and truck exhaust, the evaporation of gasoline and solvents, and petroleum refining. They react with nitrogen oxides in the presence of sunlight to form ground level ozone, a primary ingredient in smog. Although it is beneficial in the upper atmosphere, near the ground this gas may irritate the respiratory system, causing coughing, choking, and reduced lung capacity.

These observations bring us to a second question: Is there any clean energy source or fuel that will not harm the environment?

1.1.3 Resource exhaustion

Fossil fuels are formed by natural processes such as anaerobic decomposition of buried organisms. Most fossil fuels are typically millions of years old, on some occasions the age exceeds 650 million years[11]. Even though fossil fuels are still continually being formed via natural processes, they are generally non-renewable resources due to the millions of years' formation time, as well as because the known viable reserves are being used at a much faster rate than new ones are being made.

The so-called "reserves-to-production ratio" (RP ratio) is often used in forecasting the future availability of a resource. The reserve portion (numerator) of the ratio is the amount of a resource known to exist in an area and to be economically recoverable (proved reserves). The production portion (denominator) of the ratio is the amount of resource used in one year at the current rate[12]. Although the reserve and production of a resource may change year by year, the RP ratio can give us a general sense about when the resource will run out. According to the BP (British Petroleum) Statistical Review of World Energy 2014, the RP ratio for oil, natural gas and coal are 53.3, 55.1 and 113 years respectively[13], which suggests that humanity will face resource depletion in this century. This brungs us a third question: Is there an abundant alternative resource that can avoid fossil fuel depletion?

1.2 Hydrogen energy and hydrogen storage

Hydrogen fuel is one promising energy candidate that can potentially address the three questions asked above. First, when generated using renewable sources such as wind or solar, it will not generate greenhouse gases. Obviously, hydrogen is carbon-free and will not generate CO_2. Second, the combustion or use of hydrogen, such as in a combustion engine or fuel cell, will not contribute to air pollution. For hydrogen gas burning in an oxygen environment, the reaction is $2H_2(g) + O_2(g) \rightarrow 2H_2O(g)$. Although hydrogen combustion in the atmosphere may yield a small amount of nitrogen oxide, the majority emission is water vapor, which is friendly to environment[14]. Third, hydrogen is abundant, as more than 71% of the area of the Earth is covered with water. Hydrogen can be produced via electrolysis, in which electricity is used to separate the hydrogen and oxygen atoms. Electrolysis can use wind, solar, geothermal, hydro, fossil fuels, biomass, nuclear, and many other energy sources[15].

However, since hydrogen has a very small density (0.08988 g/L at STP), it is very challenging to store and transfer. Although hydrogen has a gravimetric energy density of 141.86 MJ/kg, which is more than 3 times larger than that of gasoline (46.4 MJ/kg), it has a very small volumetric energy density, ~ 0.01005 MJ/L at standard temperature and pressure. This density pales in comparison to liquid fuels such as gasoline, which has a energy density of 34.2 MJ/L [16, 17]. To improve the volumetric energy density, hydrogen gas is often stored in compressed form in high-pressure tanks at 350 bar (5,000 psi) and 700 bar (10,000 psi), for mobile storage in hydrogen vehicles[18]. However, this compression process requires compromises in cost and efficiency. The compression energy requirements for a final pressure of 800 bar would amount to about 13% of the energy content of hydrogen, omitting electrical losses in the power supply system[19]. To achieve weights consistent with practical vehicular use, the vessels used to store hydrogen at high pressures are constructed of costly and lightweight carbon fiber. These systems are roughly an order of magnitude more expensive than an equivalent (plastic) gasoline tank[20]. Some observers have argued that public education programs are likely necessary before hydrogen vehicles will be widely adopted [21]. An alternative method for increasing the density of hydrogen is to liquefy hydrogen gas by cooling to ~20 K. However, the liquefaction process requires more than 1/3 of the hydrogen's energy content, making this approach unattractive from an energy efficiency point of view [22].

1.3 Metal organic frameworks

Materials-based hydrogen storage techniques represent another strategy to increase the hydrogen storage density. Such an approach takes advantage of adsorptive or absorptive interactions between hydrogen and host material. Candidate hydrogen storage materials include conventional metal hydrides[23-26], complex hydrides[27-30], sorbents[31-37] and chemical hydrides[38-41]. These materials take advantage of either weak van der Waals interactions typical of the physisorptive binding of molecular H_2 (common for adsorbents) or the strong chemisorptive binding of atomic hydrogen (typical of the other storage materials) [42].

Within the adsorbent class of materials, metal organic frameworks (MOFs)[43-47] are very promising compounds. MOFs are nano-porous crystalline materials constructed from metal clusters called secondary building units (SBU) and organic linkers. First, they have extremely high surface areas [48-50]. Indeed, MOFs hold the record for surface area with some compounds exhibiting surface areas greater than 7000 m^2/g[48]. For example, NU-109E has a Brunauer-Emmett-Teller (BET) surface area of 7010 m^2/g, and NU-110E has BET surface area of 7140 m^2/g[48]. Moreover, these high surface areas directly contribute to the large gravimetric adsorption capacity of hydrogen gas[51-53], since increasing the surface area enhances the contact between hydrogen and the adsorbent [54]. MOFs also have highly tunable properties and ordered (crystalline) structure. A tunable, “building-block” approach to the MOFs synthesis can be applied due to the large number of possible clusters and linkers, resulting in a wide variety of MOF structures and compositions[55-58]. Tranchemontagne *et al.*[55] discussed 131 possible geometries of the SBUs, and demonstrated that metal ions in each topology could be substituted with other metals. In addition, Wilmer *et al.*[56] constructed 137,953 hypothetical MOFs by variously combining 102 organic ligands and 5 SBUs. Also, differences in synthesis, filtration, drying, activation, and shaping can result in a wide variation in MOF properties such as pore volume, surface area, and crystallite size[59-62].

1.4 Goals of this Research and Overview of this Dissertation

Of the many known MOFs, the compound known as MOF-5 has attracted considerable attention due to its ability to store gaseous fuels at low pressure with high densities. However, low thermal conductivity and limited robustness upon exposure to water and other reactive species are two challenges which limit the application of MOF-5; similar issues plague several other MOFs. The focus of this dissertation is to understand and overcome these shortcomings through detailed experimental and computational characterization of the prototype compound, MOF-5. MOF-5 consists of ZnO_4 clusters connected by 1,4-benzenedicarboxylate (BDC) linkers. While many of MOFs have been reported, we focus on MOF-5 as it represents the most widely studied MOF [36], and therefore serves as a *de facto* MOF “standard.” The MOF-5 samples examined have been produced by quasi-commercial-scale (i.e., pilot scale) production techniques[63, 64], and therefore serve as a reasonable approximation to the properties of a commercialized hydrogen adsorbent.

Properties examined include base-line material properties such as: density, surface area, pore volume, particle size distribution, and differential hydrogen adsorption enthalpy. Thermal properties assessed include the conductivity and heat capacity. Techniques for improving thermal transport via 2nd phase additions and alternative processing methods such as tailored compression into pellets, are also explored.

Additional experiments examined the kinetic and thermodynamic stability of MOF-5 under humid conditions, and robustness to ppm-level impurities present in ‘dirty’ hydrogen fuel streams. Imaging analysis using x-ray and neutron-based techniques were used to assess hydrogen adsorption kinetics *in situ* and to characterize variations in pellet density and the distribution of 2nd phase additions such as expanded natural graphite. Finally, first-principles simulations were used to reveal the water insertion (i.e., hydrolysis) process in MOF-5, which results in structure decomposition. The insight provided by this study regarding the properties of MOFs will aid in the transition of these materials from lab bench to applications.

Before proceeding further, we provide a brief outline of this thesis:

In **Chapter 2** we discuss the experimental and computational methodology. We start by introducing the principles and experimental details associated with pressure–composition–temperature (PCT) measurement, , X-ray diffraction (XRD) and Fourier transform infrared spectroscopy (FTIR) measurements. Next, we introduce the fundamentals of Density Functional Theory and its extension to include van der Waals interactions (vdW-DFT).

Chapter 3 presents a comprehensive assessment of the baseline thermophysical properties of MOF-5 =. Characterized properties include: packing density, surface area, pore volume, particle size distribution, thermal conductivity, heat capacity, stability against hydrolysis, differential enthalpy of H_2 adsorption, and Dubinin–Astakhov isotherm parameters. Hydrogen adsorption/desorption isotherms were measured at six temperatures spanning the range 77–295 K, and at pressures of 0–100 bar.

Chapter 4 discusses the thermal properties of densified composites consisting of a physical mixture of MOF-5 and expanded natural graphite (ENG). ENG is used to enhance the intrinsically low thermal conductivity of these materials. Here we demonstrate that the high-aspect ratio of ENG particles, combined with uni-axial compression, results in anisotropic microstructural and thermal transport properties in composite MOF-5/ENG pellets. Microscopy of pellet cross-sections revealed a textured microstructure with MOF particle boundaries and ENG orientations aligned perpendicular to the pressing direction. This anisotropy is manifested in the thermal conductivity, which is two to four times higher in directions perpendicular to the pressing direction. We further demonstrate that this anisotropy can be exploited using two processing techniques. First, a custom die and densification process allows for reorientation of the preferred heat flow pathway. Second, a layered MOF-5/ENG microstructure increases the thermal conductivity by an order of magnitude, with only minor ENG additions (5 wt.%). These results reveal that anisotropic thermal transport in MOF composites can be tailored using a judicious combination of second phase additions and processing techniques.

Chapter 5 quantifies the impact of humid air exposure on the properties of MOF-5 as a function of exposure time, humidity level, and morphology (i.e., powders vs pellets). Properties examined include hydrogen storage capacity, surface area, and crystallinity. Water adsorption/desorption isotherms are measured using a gravimetric technique; the first uptake exhibits a type V isotherm with a sudden increase in uptake at ~50% relative humidity. For humidity levels below this threshold only minor degradation is observed for exposure times up to several hours, suggesting that MOF-5 is more stable than generally assumed under moderately humid conditions. In contrast, irreversible degradation occurs in a matter of minutes for exposures above the 50% threshold. Fourier transform infrared spectroscopy indicates that molecular and/or dissociated water is inserted into the skeletal framework after long exposure times. Densification into pellets can slow the degradation of MOF-5 significantly, and may present a pathway to enhance the stability of some MOFs.

In **Chapter 6** we characterize the atomic-scale mechanisms associated with the hydrolysis of MOF-5 using first-principles calculations. Understanding this process will aid in the design of new compounds that are stable against water and other reactive species. van der Waals-augmented Density Functional Theory and transition state finding techniques to predict the thermodynamics and kinetics of water adsorption/insertion into MOF-5. Adsorption and insertion energetics were evaluated as a function of water coverage, while accounting for the full periodicity of the MOF-5 crystal structure, i.e., without resorting to cluster approximations or structure simplification. The calculations suggest that the thermodynamics of MOF hydrolysis are coverage dependent: water insertion into the framework becomes exothermic only after a sufficient number of H2O molecules are co-adsorbed in close proximity on a Zn-O cluster. Above this coverage threshold these formation of adsorbed clusters facilitates facile insertion via breaking of Zn-O bonds. Under these conditions the barrier for water insertion is low (0.17 eV), indicating the likelihood for rapid hydrolysis at the higher humidity levels where water clustering is expected.

In **Chapter 7** we studied the impact of contaminants in hydrogen gas used in fuel cell vehicles according to the purity standards outlined in SAE J2719. Five “impure” gas mixtures were prepared by introducing low levels of selected contaminants (NH3, H2S, HCl, H2O, CO, CO2, CH4, O2, N2, and He) to pure hydrogen gas. Subsequently, MOF-5 was exposed to these mixtures over hundreds of adsorption/desorption pressure cycles and for extended periods of static exposure lasting up to 1 week. Hydrogen chloride was the only impurity that yielded a measurable, albeit small, decrease in hydrogen storage capacity (from 6 to 5.8 wt.%, excess) during pressure cycling. For the remaining impurities, there was no change in hydrogen uptake in response to either the cyclic or static exposure. Post-cycling and post-storage MOF-5 samples were also analyzed using FTIR spectroscopy and x-ray diffraction. These analyses reveal slight changes in the spectra (compared to the pristine samples) for those samples exposed to HCl and NH3 impurities.

In Chapter 8 we introduce several imaging analysis method to characterize large scale of MOF-5 material. Neutron imaging radiography is used to get transient hydrogen distribution during adsorption and desorption. The steady state image obtained by neutron tomography helps to show the ENG(expanded natural graphite) network in the MOF-5/ENG pellet. What’s more, the density uniformity of MOF-5 pellet is analyzed based on the image from microCT. The successful application of those imaging analysis method points out potential ways to get information of large scale MOFs in future hydrogen storage system.

Finally, **Chapter 9** concludes this thesis with summary of our findings and a brief discussion of possible extensions.

The main chapters of this dissertation (Chapter 3-8) include the results presented in the following publications:

Paper 1: ***Thermophysical Properties of MOF-5 Powders***, Y. Ming, J. Purewal, D. Liu, A. Sudik, C. Xu, J. Yang, M. Veenstra, K. Rodes, R. Soltis, J. Warner, M. Gaab, U. Muller, and D. J. Siegel, Microporous and Mesoporous Materials, 185, 235 (2014). DOI: 10.1016/j.micromeso.2013.11.015.

Paper 2: ***Anisotropic Thermal Transport in MOF-5 Composites****,* Y. Ming, H. Chi, R. Blaser, C. Xu, J. Yang, M. Veenstra, M. Gaab, U. Muller, C. Uher, D.J. Siegel, *International Journal of Heat and Mass Transfer*, 82, 250 (2015). DOI: 10.1016/j.ijheatmasstransfer.2014.11.053.

Paper 3: ***Kinetic Stability of MOF-5 in Humid Environments: Impact of Powder Densification, Humidity Level, and Exposure Time***, Y. Ming, J. Purewal, J. Yang, C. Xu, R. Soltis, J. Warner, M. Veenstra, M. Gaab, U. Mueller, and D. J. Siegel, Langmuir, 31, 4988 (2015). DOI:10.1021/acs.langmuir.5b00833

Paper 4: ***Water Adsorption and Insertion in MOF-5***, Y. Ming, D. J. Siegel, Submitted to Langmuir.

Paper 5: ***Stability of MOF-5 in a hydrogen gas environment with expected fueling station impurities,*** Y. Ming, J. Purewal, J. Yang, C. Xu, A. Drews, M. Veenstra, M. Gaab, U. Müller, and D. J. Siegel, , submitted to International Journal of Hydrogen Energy.

Paper 6: ***In situ and real-time imaging analysis for large scale MOFs: hydrogen , ENG and density distribution,*** Y.Ming, J. Purewal, J. Yang, C. Xu, M. Veenstra, D.L.Jacobson, D.S. Hussey, D.J. Siegel**.** Draft.

Chapter 2

Methodology

2.1 Volumetric PCT measurements

Pressure-composition-temperature measurements (PCTs) are the most reported hydrogen storage measurement type in the literature. ‘Composition’ in this context is synonymous with the concentration of hydrogen in a sample. A PCT measurement is a collection of data points that records the pressure, concentration and temperature of a sample in equilibrium and relates the influence of external (or imposed) conditions on hydrogen concentration. PCTs are also commonly referred to as PCI (Pressure-Composition Isotherms) because they are taken at isothermal conditions. This minimizes the number of free variables and allows the relationship between concentration and pressure to be presented via two-dimensional graphics. The effect of temperature on hydrogen storage properties can be determined by comparing PCT isotherms measured at various temperatures. Because PCTs represent a sample in equilibrium, they can also be used to determine the thermodynamic properties of a hydrogen storage material.

The operating principles of a PCT instrument are shown in Figure 2.1. The reservoir pressure (V_r) refers to the total volume before Valve 1. The sample volume

(V_s) is the total volume after Valve 1. For measurements using a LN_2 bath, V_s is divided into two sub-volumes:

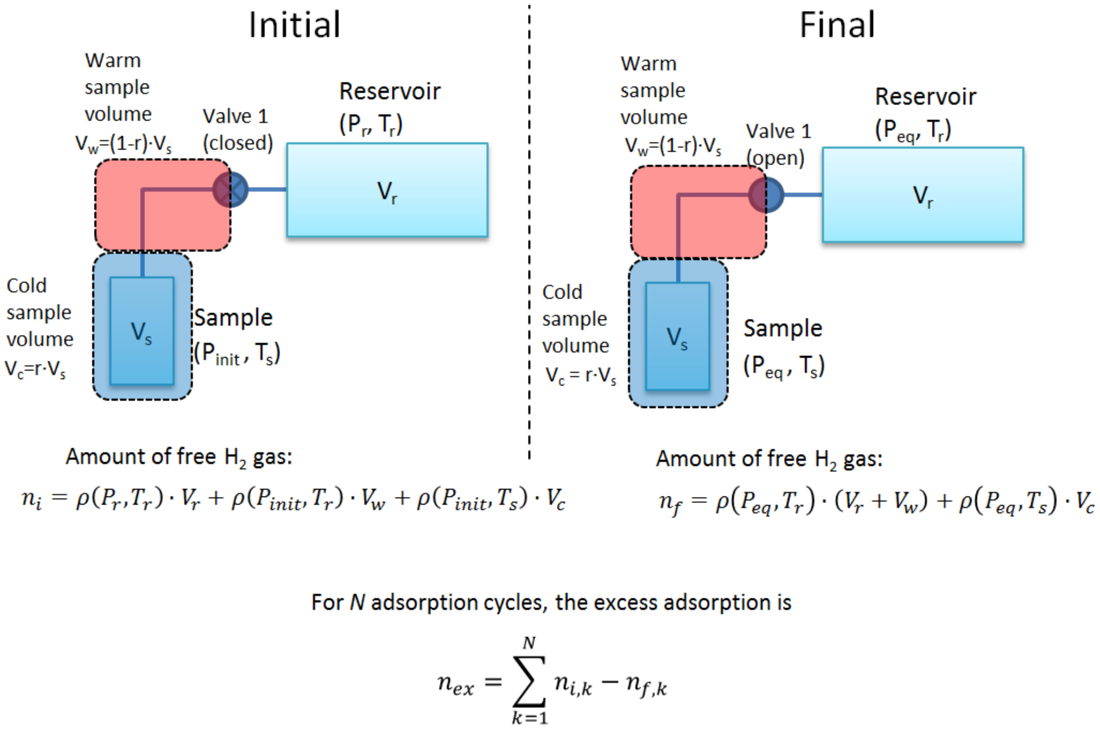

Figure 2.1. Calculation of excess adsorption by the volumetric method.

the cold volume ($V_c=r\cdot V_s$, where $0<r<1$) at sample temperature (T_s), and the warm volume ($V_w=V_s-V_c$) at the reservoir temperature (T_r). The value of r gives the fraction of V_s which is at the cold temperature (77K for liquid nitrogen), and can be determined empirically.

Figure 2.1 illustrates the two steps in an adsorption cycle. First: Valve 1 is closed; the sample holder pressure is approximately unchanged from the end of the previous cycle (P_{init}), while the reservoir pressure is set to the target pressure for the current cycle (P_r). Second: Valve 1 is opened, after several minutes an equilibrium pressure (P_{eq}) is reached for the combined sample and reservoir volumes. The reservoir volume (V_r) is known, and the sample holder volume (V_s) is measured for each sample using the Volume Calibration procedure[65]. We can also estimate V_s if the volume of the empty sample holder is known and the skeletal density [The ratio of the mass of discrete pieces of solid material to the sum of the volumes of: the solid material in the pieces and closed (or blind) pores within the pieces, represented as ρ_{sk}] of the sample is known (i.e., $V_s = V_{s,empty} - mass/\rho_{sk}$). The density of hydrogen gas for each pressure-temperature pair, $\rho[P,T]$, is estimated using the 14-term Helmholtz equation of state used in the NIST REFPROP 23 database. The excess adsorption for the current cycle is equal to n_i-n_f (n_i and n_f represent the amount of free H_2 gas in the reservoir and sample holder before and after the valve opening, their expressions are shown in Figure 2.1). The cumulative excess adsorption for all adsorption cycles is then equal to the sum of the adsorption amounts for each cycle.

2.2 X-ray diffraction

Materials having a (periodic) crystal structure can diffract radiation that has a wavelength similar to interatomic distances. X-ray wavelengths are on the order of a few angstroms, and are comparable to typical interatomic distances. During a diffraction measurement, X-rays impinging on the crystal will be scattered, and the scattered/diffracted beams can interfere constructively or destructively. As shown in Figure 2.2, if 1) the angle of incidence is equal to the angle of scattering; 2) the path length difference from two neighbor atoms is equal to an integer number of wave length, we will observe constructive interference following the equation

$$2dsin\theta = n\lambda \tag{2.1}$$

Where *d* is the separation of sample atoms, θ is the incident angle, λ is the wavelength of the X-ray beam. Since the structure of the crystal lattice varies from material to material, the X-ray diffraction pattern can be used to uniquely distinguish different materials. Additionally, a change in the pattern of a material corresponds to a change in its crystal structure.

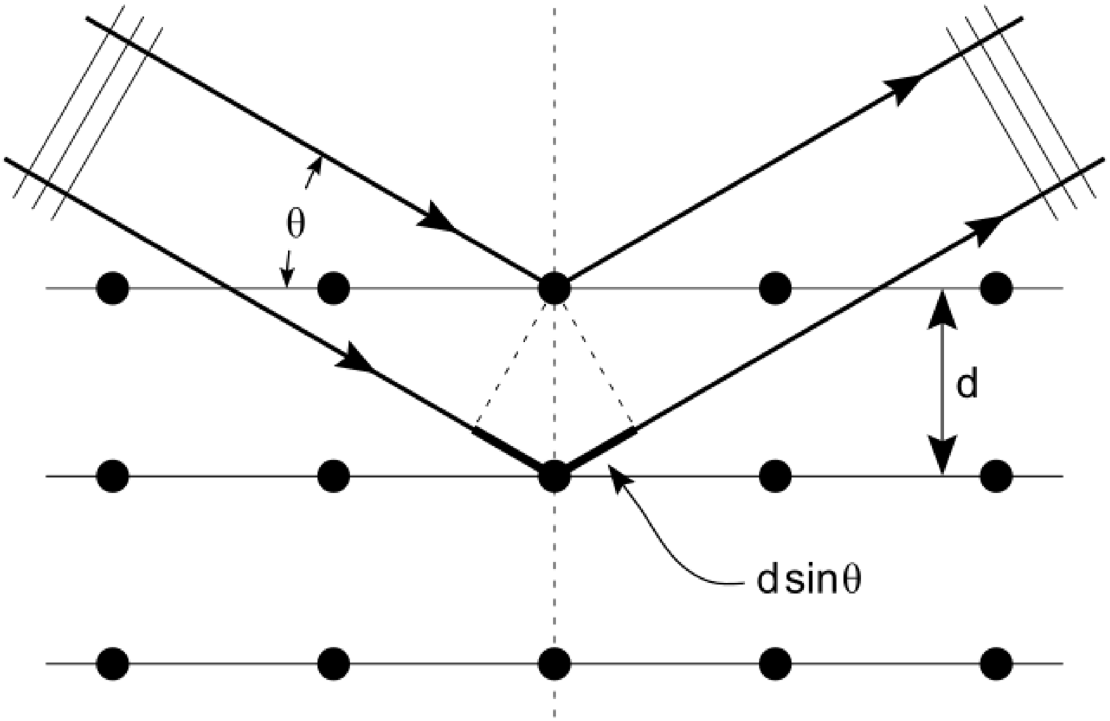

Figure 2.2. X-rays reflected off adjacent planes.

2.3 Surface area

2.3.1 Langmuir Theory

During gas adsorption, equilibrium will be established between the gaseous phase and the adsorbed gases on the adsorbent surface. The Langmuir theory describes the relationship between the number of active sites for adsorption on the surface as a function of pressure, by assuming an adsorbate behaves as an ideal gas at isothermal conditions and assuming the adsorbent to have an ideal solid surface composed of a monolayer of distinct sites capable of binding the adsorbate[65, 66]. The surface coverage θ follows the Langmuir equation:

$$\theta = \frac{W}{W_m} = \frac{KP}{1+KP} \quad , \tag{2.2}$$

where K is the equilibrium constant, W and Wm are the adsorbed weight and monolayer weights, respectively. A convenient form of equation (2.2) is

$$\frac{P}{W} = \frac{1}{KW_m} + \frac{P}{W_m} \quad , \qquad (2.3)$$

where $1/W_m$ is the slope when plotting P/W vs. P, and can be determined by fitting the adsorption data. The sample surface area S can be extracted from equation (2.3)

$$S = \frac{W_m N_A A}{M} \quad . \qquad (2.4)$$

In this equation, NA is Avogadro's number, M is the molecular mass of the adsorbate, and A is the cross-sectional adsorbate area.

2.3.2 BET theory

BET theory, proposed by Brunauer, Emmett and Teller, is an extension of the Langmuir theory [66, 67]. Instead of assuming monolayer adsorption, it incorporates the concept of multimolecular layer adsorption. The BET equation is given by:

$$\frac{1}{W(\frac{P}{P_0}-1)} = \frac{1}{W_m C} + \frac{C-1}{W_m C}\left(\frac{P}{P_0}\right) \ , \qquad (2.5)$$

where P_0 is the saturated pressure. The value of W_m can be extracted from the slope and intercept of a plot of $l/W[(P_0/P) - 1]$ versus P/P_0:

$$W_m = \frac{1}{slope+intercept} \quad . \qquad (2.6)$$

The BET surface area can then be calculated using equation (2.4)

2.4 FTIR

Fourier transform infrared spectroscopy (FTIR) is a technique applied to obtain an infrared spectrum of absorption, emission, and photoconductivity of a solid, liquid or gas[68]. Compared to a dispersive spectrometer which measures intensity over a narrow range of wavelengths at a time, the FTIR spectrometer collects data at high spectral resolution over a wide spectral range. The term Fourier transform infrared spectroscopy is used because a Fourier transform is required to convert the raw data into the actual spectrum.

In the FTIR measurement, infrared radiation is passed through the sample and a detector examines the transmitted light to measure how much energy has been absorbed at each wavelength. The concept of FTIR is based on the correspondence between adsorption energy and bond vibration energy. In covalent bonds, two atoms are held together because both nuclei are attracted to the same pair of electrons. The movements of the nuclei are known as molecular vibrations, which can lead to bond symmetric and asymmetric stretches, as well as bond bending. The stretching frequency of a bond is related to the masses of the two atoms connected by the bond and to the bond strength, which is then related to the force constant of the bond. For a bond in a diatomic molecule, the stretching frequency can be calculated according to the following equation:

$$\nu = \frac{1}{2\pi c}\left[\frac{f(m_1+m_2)}{m_1 m_2}\right]^{1/2} \quad , \qquad (2.7)$$

where ν is frequency, c is the velocity of light, f is the force constant and m_1 and m_2 are the masses of the two atoms. Since the parameters above are different for different types of bonds, and different functional groups absorb at known characteristic frequencies, the particular wavelength adsorbed by the sample in the FTIR spectrum can reveal details regarding the molecular structure of the material.

2.5 Thermal conductivity measurements

2.5.1 Direct steady state heat flow method

Low-temperature thermal conductivity was measured in the temperature range of 80 to 300 K using a comparative method that is well-suited for materials having low thermal conductivity [69]. A rectangular-shaped sample with a cross section of 5 mm × 5 mm and length of 3 mm was sandwiched between two stainless-steel contacts (SS304) with the same cross section and thickness of 10 mm (initial attempts employed a longer sample with typical length of 10 mm. However, the radiation losses associated with a sample of this size led to poor estimates of the thermal conductivity). The temperature-dependent thermal conductivity of the stainless-steel contacts have been previously measured [70]. Stycast epoxy was used to reduce the contact resistance between the sample and the steel contacts, and did not permeate the samples. A strain gauge heater was mounted on top of one steel contact, while the other contact (placed under the sample) was connected to the heat sink, thereby generating a heat flux from the top of the pellet to the bottom [71, 72].

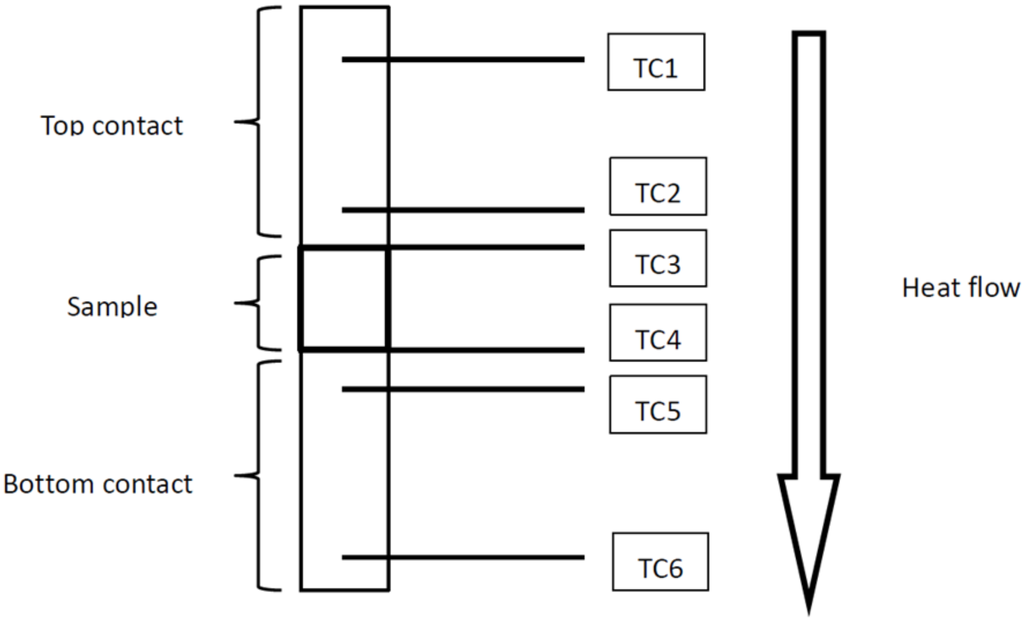

Figure 2.3. Thermal couple positions for the steady state heat flow method

Measurements were conducted in vacuum to prevent parasitic convection and adsorption within the MOF pores. Two copper cylinders were mounted outside the cold finger as radiation shields. The temperature of the sample holder was controlled by a Lakeshore 340 temperature controller. Six thermocouples (TC1–TC6) were inserted into small-bore holes in the top (TC1, TC2) and bottom (TC5, TC6) steel plates and affixed to the top and bottom of the sample (TC3, TC4) [see Figure 2.3]. These probes were used to determine the heat fluxes through the steel contacts (TC5, TC6, TC1, and TC2) and the temperature drop across the sample (TC3, TC4) upon heating, from which the sample's thermal conductivity was derived. The sample's thermal conductivity κ was determined using the 1D Fourier law:

$$K = \frac{Q \cdot t_s}{A_s(T_3 - T_4)} \quad , \tag{2.8}$$

where t_s and A_s are the sample thickness and cross-sectional area, and Q is the power through the sample. Q was estimated using the power $A_b\ k_b\ (T_5\text{-}T_6)/t_b$ transferred through the bottom steel plate, where k_b is the thermal conductivity of the steel contact and t_b is the distance between TC5 and TC6. T_3, T_4, T_5, T_6 are the temperatures measured using the thermocouples TC3, TC4, TC5 and TC6, respectively. Three major sources of error are associated with Q: uncertainty due to parasitic black-body radiation losses from the sample, uncertainty due to parasitic conduction losses through the thermocouples, and uncertainty in t_b due to the nonzero thermocouple diameter. Uncertainty in t_s due to surface roughness, uncertainties in temperature and voltage measurements, and the interfacial temperature drops at each end of the sample also contribute to the error. Accounting for the above sources of uncertainty, we estimate the maximum error in the thermal conductivity to be 18%.

2.5.2 Laser flash thermal diffusivity measurement

The laser flash method was developed by Parker *et al.* in 1961[73], and is widely used to measure thermal diffusivity of different materials. This method has the advantage of being fast while providing values with excellent accuracy and reproducibility. As shown in Figure 2.4, in a vertical setup a nearly instantaneous pulse of energy heats the plane-parallel sample from the front face (bottom side), and the time-dependent temperature rise of the rear face of the sample is recorded by a detector on top. The higher the thermal diffusivity of the sample, the faster the energy reaches the backside. Assuming the sample is isotropic and thermal transport is adiabatic (no heat loss), the thermal diffusivity α then can be determined from the sample thickness (d) and the time ($t_{1/2}$) needed for the sample rear face to reach half of the maximal temperature increase:

$$\alpha = 0.1388 \cdot \frac{d^2}{t_{1/2}} \quad . \qquad (2.9)$$

Several improvements have been made by considering radiation and convection on the surface, transient heat transfer, finite pulse effects and also heat losses[74-76].

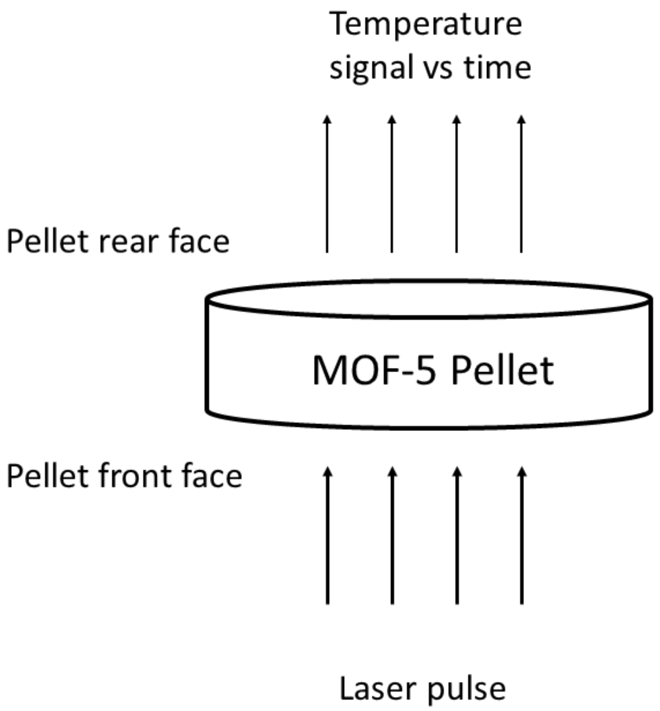

Figure 2.4. Schematic of the laser flash method.

2.5.3 Thermal capacity measurement (DSC)

Differential scanning calorimetry or DSC is a thermoanalytical technique developed by E.S. Watson and M.J. O'Neill in 1962[77]. In the DSC technique heat effects associated with phase transitions and chemical reactions are monitored as a function of temperature. In a DSC the difference in the amount of heat flowing into a sample and a known reference in a certain time is recorded as a function of temperature. The reference could be an inert material such as alumina, or just an empty aluminum pan. During the measurement, both sample and reference temperatures are increased at a constant rate, and the whole process is conducted under a constant pressure. Since the heat flow is equivalent to an enthalpy change, we have

$$(\frac{dq}{dt})_p = \frac{dH}{dt} \quad . \tag{2.10}$$

The heat flow difference between the sample and the reference can be expressed as:

$$\Delta\frac{dH}{dt} = (\frac{dH}{dt})_{sample} - (\frac{dH}{dt})_{reference} \quad . \tag{2.11}$$

According to the definition of heat capacity

$$C_p = (\frac{dq}{dT})_p = (\frac{dH}{dT})_p \quad , \tag{2.12}$$

and knowing the temperature scan rate,

$$r = \frac{dT}{dt} \quad , \tag{2.13}$$

we can then rewrite equation (2.12) as

$$C_p = (\frac{dH}{dT})_p = \frac{dH}{dt}\cdot\frac{dt}{dT} = \frac{dH}{dt}\cdot\frac{1}{r} \quad . \tag{2.14}$$

The difference of heat capacity between sample and reference can be expressed by combining equations (2.11) and (2.14):

$$\Delta C_p = C_{p_{sample}} - C_{p_{reference}} = \Delta\frac{dH}{dT} = \Delta\frac{dH}{dt}\cdot\frac{1}{r} \quad . \tag{2.15}$$

Once we know the heat capacity of the reference, we can determine the sample heat capacity.

2.6 Density Functional Theory

2.6.1 Conventional Density Functional Theory

Density Functional Theory (DFT)[78, 79] is a widely-used approach to solve the Schrödinger equation in a many-body system. For a many-body system consisting of N electrons and M ions, the Schrodinger equation can be written as:

$$\mathcal{H}\Psi(r_1, r_2, \cdots, r_N; R_1, R_2, \cdots, R_M) = E\Psi(r_1, \cdots, r_N; R_1, \cdots R_N) \qquad (2.16)$$

In equation (2.16) H, Ψ, and E are the Hamiltonian operator, the many-body wavefunction, and the total energy of system, respectively. All interactions between electrons and nuclei are included in H:

$$\mathcal{H} = T_i + T_I - \frac{1}{2}\sum_{i,I}\frac{Z_I e^2}{|r_i - R_I|} + \frac{1}{2}\sum_{i \neq j}\frac{e^2}{|r_i - r_j|} + \frac{1}{2}\sum_{I \neq J}\frac{Z_I Z_J e^2}{|R_I - R_J|} \qquad (2.17)$$

Here T_i and T_I represent the kinetic energy of electrons and nuclei; and the remaining three terms are expressions for ion-electron, electron-electron and ion-ion electrostatic interactions, respectively. However, the wavefunction Ψ has 3N+3M degrees of freedom, making it impractical to solve this equation analytically in all but the smallest of systems.

The Born-Oppenheimer approximation[80], which assumes the nuclear positions as frozen due to the large nuclear mass compared to that of electrons, can reduce the 3N+3M degrees of freedom to 3N. Under this approximation, the many-body Hamiltonian [equation (2.17)] can be decoupled into an electronic part and a nuclear part. For the purposes of understanding bonding interactions and the thermodynamics of adsorption it is sufficient to only solve the electronic part explicitly.

Density Functional Theory (DFT) further reduces the complexity of this problem by introducing the concept of charge density. Hohenberg and Kohn[78] demonstrated that the ground state charge density, $n_o(r)$, for a system of electrons in an external potential, $V_{ion}(r)$, uniquely determines that potential up to an arbitrary constant. Also, Kohn and Sham[79] proved that the total energy of the system is a universal functional of the charge density, E[n(r)], which will reside in a global minimum (i.e., the ground state energy) when the charge density is in its ground state, $n_o(r)$.

DFT makes it possible for the many-body problem to be expressed using the charge density rather than the 3N-dimensional wavefunction [79] :

$$E[n(r)] = T_0[n(r)] + \int V_{ion}(r)n(r)dr + E_h[n(r)] + E_{XC}[n(r)]. \qquad (2.18)$$

In equation (2.18), $T_0[n(r)]$, $V_{ion}(r)$, $E_h[n(r)]$, and $E_{XC}[n(r)]$ represent the many-body kinetic energy, ionic potential, the classical Coulomb interaction, and the exchange correlation energy, respectively. Some of these interactions can be expressed as:

$$T_0[n(r)] = \frac{-\hbar^2}{2m_e}\sum_{i=1}^{N}\langle\psi_i|\nabla^2|\psi_i\rangle \ (2.19)$$

$$E_h[n(r)] = \frac{1}{2}\int \frac{n(r)n(r')}{|r-r'|}drdr' \ (2.20)$$

$$n(r) = \sum_{i=1}^{N}|\psi_i(r)|^2 \ (2.21) \quad .$$

Equation (2.21) expresses the charge density in terms of non-interacting single-particle wavefunctions, ψ_i . The exchange-correlation energy E_{XC} contains all quantum-mechanical effects not included by the other terms in the energy functional, such as electron exchange and correlation.

Equation (2.18) can be solved via direct minimization or through a self-consistent approach using a set of single-particle Schrödinger-like equations, shown as equation (2.22), called the Kohn-Sham equations for non-interacting wavefunctions [79].

$$\hat{h}\psi_i(r) = \left[\frac{-\hbar^2}{2m}\nabla^2 + V_{eff}[n(r)]\right]\psi_i(r) = \epsilon_i\psi_i(r) \quad (2.22)$$

$$V_{eff}[n(r)] = V_{ion}[n(r)] + V_h[n(r)] + V_{XC}[n(r)] \quad (2.23)$$

$$V_h[n(r)] = \frac{\delta E_h[n(r)]}{\delta n(r)} \quad (2.24)$$

$$V_{XC}[n(r)] = \frac{\delta E_{XC}[n(r)]}{\delta n(r)} \quad (2.25)$$

The expression of the exchange and correlation energy is required to solve the Kohn-Sham equations. Unfortunately, the exact form of this functional is unknown. In this case, an approximation for E_{XC} is needed, and the quality of this approximation largely determines the accuracy of the DFT method. The most common approach is to adopt a local approximation [79]. In general, E_{XC} can be expressed using the exchange-correlation energy density, ϵ_{XC}:

$$E_{XC}[n(r)] = \int \epsilon_{XC}[n(r)]n(r)dr. \quad (2.26)$$

The local approximation assumes that ϵ_{XC} at some point r within the system is equal to the exchange-correlation energy in a homogenous electron gas of the same density, n[r]:

$$\epsilon_{XC}[n(r)] = \epsilon_{XC}^{hom}[n(r)] \ . \quad (2.27)$$

The E_{XC} of a homogenous gas can be accurately solved using Quantum Monte Carlo (QMC). [81]

The Generalized Gradient Approximation (GGA)[82] is another widely used approximation in modern DFT calculations. This functional further improves the accuracy of the calculation by incorporating gradients in the density. The DFT/GGA approach has proven successful in predicting the properties of many classes of materials. However, it yields poor predictions when treating systems exhibiting non-local, long-range dispersion energies such as during the physisorption [78, 83, 84]) of molecules on surfaces.

Recently, van der Waals interactions have been included in several density functionals [84-92]. Two notable methods are the semi-empirical approach of Grimme, variously referred to as DFT-D1[93], DFT-D2[94], and DFT-D3[95], and the non-empirical vdW-DF method of Dion *et al.* [96] These methods have demonstrated improved accuracy at moderate computational cost across a range of chemical environments [85, 97-101].

More details regarding the vdW-DF method will be discussed here since it is the primary approach used in Chapter 6. The starting point of vdW-DF methods are the adiabatic-connection fluctuation−dissipation (ACFD) theorem [102] and the plasmon-pole approximation for the response of electron density. In this method [96] the correlation energy is divided into local (E_c^0) and non-local (E_c^{nl}) parts,

$$E_c = E_c^0 + \quad {}_c^{nl} \tag{2.28}$$

With the total exchange-correlation energy given by:

$$E_{XC} = E_X^{GGA} + E_c^0 + E_C^{nl} \qquad (2.29)\ .$$

In equation (2.29), E_X^{GGA} is GGA exchange energy, and E_c^0 is the local part of the correlation energy, which is treated within the LDA. The nonlocal component E_c^{nl} accounts for long-ranged electron correlation effects responsible for van der Waals interactions, and is evaluated using a double integral over electron densities n(r) at two different locations, r and r':

$$E_c^{nl} = \frac{1}{2}\iint n(r)\Phi(r,r')n(r)drdr'. \qquad (2.30)$$

$\Phi(r,r')$ is a non-local kernel, which is a operator of the charge density, its gradient at *r* and *r'*, and $|r - r'|$. Since E^{nl} is only a function of distance, evaluation of equation(2.30) can be expedited by tabulating it in terms of *r* and *r'* in advance. Additional information can be found in Ref. [94].

Chapter 3

Thermophysical Properties of MOF-5 Powders

3.1 Introduction

Metal-organic frameworks, a relatively new class of crystalline, high-surface area materials [103, 104], are in the process of transitioning from the laboratory to commercial applications [105-111]. To facilitate this transition, knowledge of the physical and thermal properties of MOFs, typically in powder form, is essential. This data is needed for applications including gas capture and storage, catalysis, and gas separations. In the case of hydrogen storage, we note that an abundance of H_2 uptake measurements exist for MOFs [104, 112, 113]. Nevertheless, several other material properties needed for the design and modeling of a complete hydrogen storage system have received much less attention. For example, models originally developed for packed bed adsorbents used in pressure swing adsorption (PSA) processes have been adapted for sorption-based hydrogen storage at cryogenic[114] and ambient conditions[115]. These models aim to describe thermal and mass-transfer effects during charge and discharge. However, when parameters in the governing equations are not known from measurements, they must be estimated from existing, and potentially incompatible data. The availability of accurate thermophysical properties such as packing density, thermal conductivity, particle size distribution, along with an accurate equilibrium pressure-temperature-composition (PCT) equation of state for the adsorbed hydrogen, will greatly benefit the accuracy of these models and allow their use in making performance projections and for design optimization.

It is well known that differences in synthesis, filtration, drying, activation, and shaping can result in a wide variation in MOF properties such as pore volume, surface area, and crystallite size [60, 116-118]. However, with the advent of reproducible, commercial-scale production techniques [119, 120], it is now possible to establish a "standard" set of properties for many MOFs. Here we present measurements of structural, thermal, and hydrogen storage properties of the benchmark cryo-adsorption material MOF-5. While many of MOFs have been reported, in this chapter we focus on MOF-5 as it represents the most widely studied MOF [121]. MOF-5 consists of ZnO_4 clusters connected by 1,4-benzenedicarboxylate (BDC) linkers. We report an extensive set of MOF-5 material properties, including: density (and its dependence on tapping conditions), surface area, pore volume, particle size distribution, thermal conductivity, heat capacity, robustness with respect to humid air, and differential adsorption enthalpy. We also determine parameters for a modified Dubinin-Astakhov[122] model in order to predict the uptake of adsorbed H_2 within MOF-5 over the temperature range of 77-295 K and the pressure range of 0-100 bar. The MOF-5 properties reported here should facilitate predictions of system-level properties such as hydrogen discharge pressures, refueling dynamics, and capacity, while enabling other MOF applications beyond hydrogen storage.

3.2 Experimental Procedure

3.2.1 Materials Preparation

A summary of the conventional and electrochemical-based processes for industrial MOF synthesis is given in Ref [106]. The conventional synthesis process for MOFs involves combining metal salts (e.g., metal nitrates, sulfates, or acetates) with multi-topic organic linkers, the latter most commonly consisting of mono-, di-, tri- or tetracarboxylic acids. These constituents are dissolved together and stirred in a polar organic solvent such as an amine [e.g. triethylamine (TEA)] or amide [e.g. *N*,*N*-diethylformamide (DEF), *N*,*N*-dimethylformamide (DMF)]. MOF crystallites then form via self-assembly and subsequently precipitate from the solution within minutes to hours. Typical synthesis temperatures range from ambient up to approximately 200 ℃. After filtration, washing, and drying, the crystalline product is obtained in the form of a powder. Depending on the desired application, the powder can be further processed into compacts (e.g., pellets, strands, *etc.*)[106, 123, 124].

Laboratory-scale MOF synthesis procedures have recently been scaled from multi-kg to tons of product per batch, which will facilitate commercial applications of these materials[63, 64]. Moreover, sustainability is a big concern and was achieved by replacing solvent-based by water-based procedures[64]. Example space-time-yields (STY) for the synthesis of MOF (and other framework) materials observed in laboratory and industrial settings are given in Table 3.1. Up to three orders of magnitude improvement in STY is observed in transitioning from laboratory to commercial settings.

In the present study, MOF-5 powders were synthesized by BASF at room temperature using a procedure described by Yaghi and coworkers starting from 1,4-benzene dicarboxylic acid (H_2BDC, $C_8H_6O_4$, Merck), zinc acetate dihydrate ($Zn(CH_3COO)_2 \cdot 2H_2O$, Merck), and *N,N*-dimethylformamide (DMF, BASF AG) [125]. In a glass reactor equipped with a teflon-lined stirrer, 130 g of $Zn(CH_3COO)_2 \cdot 2H_2O$ was dissolved in 1200 ml DMF. Within 2 hours, a solution of 37.5 g of H_2BDC in 950 ml DMF was added under rigorous stirring. The precipitate was filtered off, washed three times with 1 L of dry acetone and dried under a stream of flowing nitrogen. Given the low vapor pressure of conventional MOF synthesis solvents (e.g. DMF has a vapor pressure of approximately 4 torr at 25 ℃), solvent exchange to a more volatile solvent (e.g. acetone has a vapor pressure of approximately 270 torr at 25 ℃) has been shown to be an effective method for solvent removal. Prior to characterization, MOF-5 was heated and evacuated at 130 ℃ and 50 mtorr for 1-3 hrs, yielding the desolvated or so-called 'activated' form of the material. An alternative route to desolvation of MOFs involves a liquid or super-critical CO2 solvent removal process [126]. The wet chemical analysis of the obtained solid yielded 34 wt% Zn, equivalent to 92% molar yield of MOF-5 calculated as Zn4O(BDC)3. The concentration from residual nitrate amounted to be less than 0.05 wt% N. Cubic shaped crystals with a size of < 1μm were observed by scanning electron microscopy (see Section 3.3.1.3 below). Powder x-ray diffraction was also performed to characterize the crystallites (See Figure 12 in Sec. 3.3.4.)

Table 3.1. Comparison of space-time-yields (STY) for synthesis of various framework materials in both laboratory and commercial settings. MeIM=2-Methylimidazolate, BTC=benzene-1,3,5-tricarboxylate , BDC=1,4-benzene dicarboxylate

Composition	**Literature Name**	**Laboratory STY ($kg/m^3/d$)**	**Ref.**	**Commercial Name**	**Industry STY ($kg/m^3/d$)**	**Ref.**
$Zn_4O(BDC)_3$	MOF-5 IRMOF-1	0.21	[116]	Basolite Z100H	299	-
$Cu_3(BTC)_2$	HKUST-1	8.6	[116]	Basolite C300	225	[106]
$Zn(MeIM)_2$	ZIF-8	1.3	[116]	Basolite Z1200	160	[106]
Aluminum-fumarate	Aluminum-fumarate MOF	~30	[116]	Basolite A520	up to > 3600	[64]

3.2.2 Materials Characterization

An extensive set of techniques was used to characterize several properties of the MOF-5 powders obtained, including: crystallinity, surface area, pore volume, particle size distribution, density, heat capacity, thermal conductivity, robustness with respect to humidity, and hydrogen storage properties.

3.2.2.1 Powder x-ray diffraction (PXRD)

MOF-5 powders were loaded into a flat sample holder under a dry nitrogen atmosphere and covered with a plastic foil to minimize degradation due to air moisture during analysis. The samples were measured at room temperature in reflection mode with a powder x-ray diffractometer (Rigaku Miniflex II) between 2° and 70° (2-Theta) with a step width of 0.02° and a measurement time of 3.6s per step. The powder X-ray diffraction (XRD) pattern was obtained using a scanning rate of 0.33°/min with 2θ from 2° to 70°.

3.2.2.2 Surface area and pore volume

Surface area was measured at 77 K using nitrogen sorption in an Autosorb AS6B-KR (Quantachrome Instruments). Prior to the measurement, the MOF-5 sample (31.6 mg) was placed in the sample cell and activated at 10^{-4} mbar for 2 hours at 130 ^{o}C. Surface area values were calculated using the Brunauer-Emmet-Teller (BET) equation [127] according to DIN 66131 (Determination of specific surface area of solids by means of gas adsorption after BET). The pore volume and area distribution were calculated applying the Barrett-Joyner-Halenda (BJH) equation [128] on the isotherm data according to DIN 66134 (Mesopore Analysis by Nitrogen Sorption using the Method of BJH). (See Section 3.1.1 below for results).

3.2.2.3 Particle size

Scanning electron microscopy (SEM) images were taken with a JEOL JSM 6400F Field Emission SEM with an acceleration voltage of 5 kV. Prior to SEM imaging, the MOF crystals were sputtered with a thin Au/Pd layer to make their surface electrically conducting. ImageJ software was used for image analysis [129]. Crystal size statistics were determined based on three unique SEM images comprising a total of 182 measured MOF-5 crystallites. The crystals generally possessed a cubic morphology; diameter measurements were taken along the diagonal of the cube face. (See Section 3.3.1.2 below for results).

3.2.2.4 Density

The volumetric density of stored hydrogen is an important performance metric for mobile fuel cell applications. The densities of high-surface-area materials can be quite low, ranging from 0.1 to 0.4 g/cm [105, 123, 124]. Consequently densification into pellets or custom-molded monoliths has been explored for such materials as MOF-177[130, 131], MOF-5[124] and activated carbons[132], resulting in higher densities of 0.5–0.8 g/cm^3.

Three varieties of density are of relevance for MOF powders: bulk density, framework density, and single crystal density. Bulk powder density includes all interparticle voids, along with all open and closed pore intraparticle volumes, as part of the total sample volume. In contrast, the framework density (i.e., skeletal density) includes only closed pore volumes and the volume occupied by the covalently-bonded framework atoms. Single crystal density includes both open and closed pore volumes.

Measurements of bulk density can result in a range of values due to differences in the number of taps (if any), size of the container, packing force, and particle size (the latter quantity can itself be affected by the processing procedure, e.g., milling). In gas storage applications it is desirable to completely fill the storage vessel with MOF powder in a manner that minimizes the presence of large voids. Repeated tapping and/or vibration of the powder and vessel can accomplish this. A standardized value for the packing or tap density can be measured using DIN ISO 787 Part II, ISO 3953, or ASTM B 527-93 using a jolting volumeter. The bulk density (ρ_{bulk}) of MOF-5 was determined by completely filling a stainless steel cylindrical vessel of known mass and volume (0.75 mL) with MOF powder. The filling process involved the incremental addition of small amounts of material to the vessel followed by light tapping. Measurements were repeated three times; the measured values deviate from one another by less than 5%. Additional measurements were performed using different numbers of taps and container volumes to evaluate the effects on tap density. In addition, a tap density measurement was taken using the standardized jolting volumeter.

The single crystal density (ρ_{sx} = 0.605 g/cm^3) was obtained from Ref. [117]. The framework density (ρ_{fm}), or skeletal density, was determined by helium density measurements using an AccuPyc 1330 Pycnometer (Micrometritics). For this measurement 8.0 mL of MOF-5 was placed in the standard sample holder at ambient temperature. Research grade helium was used. The measurements were repeated until the reproducibility was within +/- 0.005 g/mL.

3.2.2.5 Heat capacity

The heat capacity (c_p) was measured by a dynamic heat flow difference calorimeter (Mettler TA 3000). The MOF-5 sample (5.5 mg) was placed in an open alumina crucible under inert nitrogen and heated at a rate of 5 ℃/min from approximately 220 to 370 K with a metering range of 10 mW. The difference in the amount of heat required to increase the temperature of the sample compared to that of the reference material (sapphire with c_p = 30.9 mg) is measured as a function of oven temperature according to DIN 51007 (General principles of differential thermal analysis).

3.2.2.6 Thermal conductivity

The thermal conductivity of MOF-5 was calculated based on the product of its heat capacity, thermal diffusivity, and density. Thermal diffusivity measurements were performed with a commercial xenon flash thermal diffusivity instrument (Anter Flashline, FL3000S2) operating at 700 W, using 12.7 mm diameter pellets with an average thickness of 2 mm and densities of 0.35, 0.52, and 0.69 g/cm^3. The pellets were kept under a N_2 atmosphere during measurements to limit the effects of humidity. A thin layer of silver paint was applied to the top surfaces of the pellets to prevent them from fracturing during measurement. The lower surfaces (i.e., the side incident to the light) of the pellets were coated with graphite to improve adsorption of light. A 5 K/min ramp rate was used[133].

3.2.2.7 Hydrogen storage isotherms

Hydrogen adsorption measurements were performed using an automated Sievert's-type apparatus (Setaram, PCT-Pro 2000) with an oil-free scroll vacuum pump (Anest Iwata, model ISP90). The mass of MOF-5 loaded for adsorption measurements was 436 mg. Prior to measurements, the MOF-5 powder was activated for at least 6 hours under continuous vacuum (3 hrs. at room temperature followed by 3 hrs. at 130 ℃). The void volume of the sample, vessel, and gas lines was determined based on the expansion of low-pressure (< 5 bar) helium gas while maintaining isothermal conditions at approximately 28 ℃. This assumes that helium does not appreciably interact (adsorb) with the MOF sample under these conditions.

Adsorption isotherms were measured at six sample temperatures: 77, 103, 118, 138, 200 and 295 K. The 77 K isotherm was measured by immersing the sample holder in a liquid nitrogen bath; the 200 K isotherm was measured by covering the sample holder in solid CO_2 powder; the 295 K isotherm was measured at ambient temperature. For intermediate temperatures (103 K, 118 K, 138 K), the sample was cooled to the target temperature using a continuous flow liquid nitrogen cryostat (CryoPro-2009, Setaram). The sample temperature was monitored with an internal platinum resistance thermometer in direct contact with the powder. The temperature of the sample vessel was regulated by a temperature controller that operates heaters located on the exterior of the sample vessel and bottom of the Dewar surrounding the sample vessel. The sample vessel was allowed to equilibrate at the target temperature for approximately one hour.

Hydrogen adsorption isotherms were measured by the volumetric method[134]. To correct errors caused by the temperature gradient between the reservoir sub-volume (maintained at 27.6 ℃), sample sub-volume (set at cryogenic target temperature), and tubing sub-volume ($^1/_8$" tubing to minimize the volume), a separate hydrogen density was calculated for each sub-volume. A calibration test was performed using non-porous Al_2O_3 powder for each sample temperature, using conditions (e.g. reservoir and sample volumes, etc.) identical to that for the sample. Maximum error during calibration tests was typically 0.3 mmol of H_2 (at 77 K), in comparison to the 10 mmol of H_2 that was adsorbed at 77 K. The equilibrium gas phase density (ρ_g) was calculated from the equation of state for normal hydrogen by Leachman et al[135] employed in the NIST Standard Reference Database[136]. All experiments used ultra-high purity grade (99.999%) hydrogen and helium.

3.2.2.8 Robustness with respect to air exposure

Previous studies have shown that MOF-5 will decompose in air under humid environments [137, 138]. Consequently, robustness to humid air is an important property since it can impact the manufacturing and assembly of the material in a hydrogen storage system, as well as its long-term stability upon cycling. The impact of exposing MOF-5 to air was assessed using hydrogen uptake measurements (PCT-Pro 2000, Setaram) and time resolved x-ray diffraction. For PCT measurements, two grams of MOF-5 powders were removed from the glovebox and placed on the lab bench in contact with the ambient atmosphere for exposure times up to 8 hours. For diffraction studies approximately 0.02-0.05 g were exposed for up to 250 hours. As these experiments were meant to mimic an unintentional exposure event, the laboratory environment was not strictly controlled: exposure conditions were approximately 45% relative humidity and 22℃. To assess whether changes to MOF-5 performance due to exposure were reversible by activation, PCT measurements were performed for samples with (activated) and without activation (non-activated), where the activation conditions are the same as previously described (minimum of 6h total under continuous vacuum, with 3h at room temperature followed by at least 3h at 130 ℃).

3.3 Results and Discussion

Our discussion of MOF-5 properties is divided into three sections: structural properties, thermal properties, and hydrogen storage properties. These properties will strongly impact the design and performance of MOF-based hydrogen storage systems, and are essential input for the parameterization and validation of storage system models. A summary of the measured property data is given in Table 3.2.

Table 3.2. Summary of structural, thermal, and hydrogen isotherm materials properties for MOF-5. Unless otherwise indicated, all measurements performed on loose powder form of MOF-5

	Units	**Value**	**Conditions**
Structure Properties			
Bulk Density (ρ_{bulk})	gcm^{-3}	0.13^{a}	^{a}Limited manual taps
		0.22^{b}	^{b}Tapping w/ jolting
Framework Density (ρ_{fm})	gcm^{-3}	2.03	volumeter
BET Specific Surface Area	m^2g^{-1}	2763	
(S_A)	cm^3g^{-1}	1.27	N_2 isotherm 77K
Micropore Volume (V_{micro})	μm	0.36	Ar isotherm 87 K
Mean Particle Diameter			
Thermal Properties			
Thermal Conductivity (k)	$W m^{-1}K^{-1}$	0.091	300 K, ρ=0.35 gcm^{-3}
Heat Capacity (c_p)	$J g^{-1}K^{-1}$	0.72	300 K
Hydrogen Isotherm			Based on fitting to 77,
Parameters	$J mol^{-1}$	2239	138, 200 and 295 K
α	J	19.5	isotherms from 0 to 100
β	$mol^{-1}K^{-1}$	125.4	bar
n_{max}	mol/kg	1692	
P_o	MPa	2.01	
V_a	$ml g^{-1}$		

3.3.1 Structural Properties

We take the structural properties of an adsorbent to include its surface area, pore volume, density, and crystal size. These attributes strongly influence the gravimetric and volumetric densities of adsorbed species such as hydrogen. For example, the gravimetric excess hydrogen capacity of porous materials generally scales with surface area[139-141]. On the other hand, density, pore volume, and particle size control volumetric capacity. To some extent, bulk physical properties can be optimized through processing techniques. For example, compacting the material can increase density, and ensuring full removal of synthesis solvent from the MOF surfaces/pores can maximize surface area. Regarding compaction, a detailed study of the benefits associated with densification of MOF-5 powder into shaped bodies (tablets, strands, bars, etc.) [142] was previously reported by the authors [124]. Typically, a compromise exists between maximizing surface area and pore volume (or density) since materials with high surface area generally exhibit large pore volumes[143]. Thus, the gravimetric and volumetric capacities of an adsorbed species cannot be tuned independently. Lastly, we note that the crystalline pore structure of the MOF-5 powder obtained by the zinc acetate dihydrate synthesis [described in Section 3.2.1] is remarkably robust against both mechanical compaction [124] and degradation from moisture (For XRD plots, see Section 3.3.4).

3.3.1.1 Surface area and pore volume

The specific surface area is a key factor that determines the hydrogen capacity of a given MOF. The amount of adsorbed hydrogen (often expressed as *excess capacity*), can be estimated by assuming monolayer hydrogen coverage on the sorbent surface with a density equal to that of liquid hydrogen[144]. Under this approximation, the excess hydrogen capacity per unit mass (i.e. excess gravimetric capacity) is proportional to the sorbent's specific surface area where the proportionality constant is: 2.28×10^{-3} wt% H_2 m^{-2}. That is, a MOF possessing a specific surface area (S_A) of 500 m^2/g should store approximately 1 wt% (excess) hydrogen (at 77 K)[141]. The agreement of this surface area versus excess uptake relationship has been demonstrated for a wide range of sorbents[140, 145, 146]. Differences in uptake for a given material have been observed largely stemming from differences in sorbent preparation and desolvation methods which lead to variation in surface area and hydrogen uptake measurements for a given material. For example, MOF-5 isolated and desolvated in air with conventional solvents has a BET surface area of ~3100 m^2/g (comparable to the value reported in this study), whereas identically prepared MOF-5 isolated and desolvated in a nitrogen atmosphere with anhydrous solvents has a BET surface area of 3800 m^2/g[147].

Significant effort has been devoted to improving excess gravimetric hydrogen capacity by increasing specific surface area. However, as described above, increasing surface area results in a decrease to volumetric capacity. Typically, improvements to surface area occur via creation of larger micro pores, thereby decreasing the crystal and bulk densities. . demonstrates this tradeoff by plotting the BET specific surface area (S_A) as a function of micropore volume (V_{micro}) for several MOFs in the literature. (Data in . is taken from references[112, 148, 149] and references therein). It is clear that there is a direct relationship between BET surface area and micropore volume with a correlation factor of 2160 m^2 BET surface area per cm^3 of pore volume which is consistent with previous literature for carbon aerogels [Literature value 2559 m^2/cm^3][150]. Thus, it is important to identify approaches that enhance both gravimetric and volumetric density simultaneously. As is evident in . , MOF-5 represents a good compromise between gravimetric and volumetric hydrogen capacity.

We calculated the S_A and V_{micro} for MOF-5 based on nitrogen and argon adsorption isotherms collected at 77 and 87 K respectively. Experimental details for sample pretreatment and data collection can be found in Section 3.2.2.2 above. Based on these data, the S_A, V_{micro}, and mean pore width for MOF-5 are 2763 m^2g^{-1}, 1.27 cm^3g^{-1}, and 0.99 nm respectively. These S_A and V_{micro} data correlate well with literature values[133]. Additionally, the mean pore width value is close to that expected based on the fixed pore diameters measured from crystal structure data (1.1 and 1.5 nm).

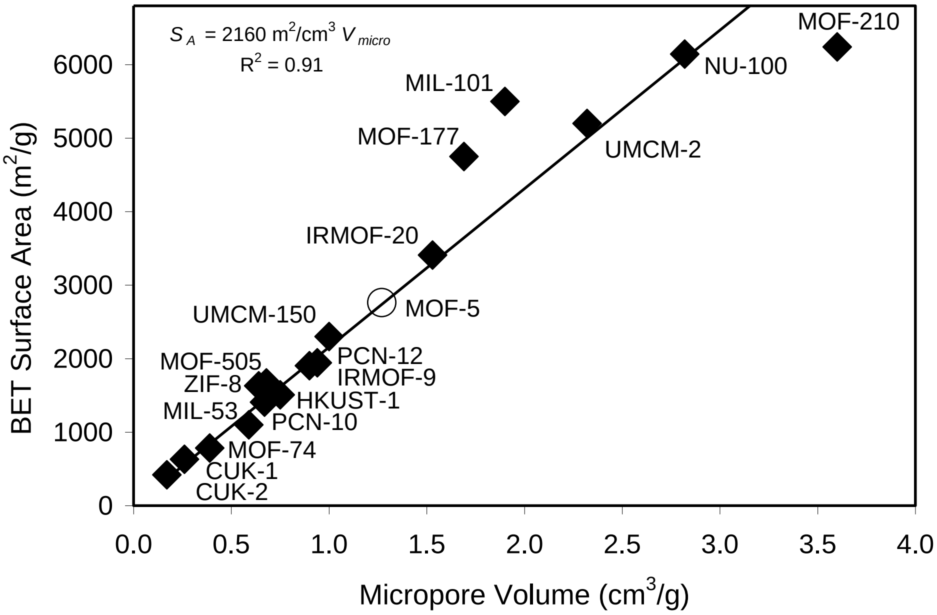

Figure 3.1. Comparison of space-time-yields (STY) for synthesis of various framework materials in both laboratory and commercial settings.

3.3.1.2 Crystallite and Particle size

Particle and crystallite size can have implications for packing density in a packed bed hydrogen storage system. (Here we use “crystallite” to refer to a single crystal of MOF-5, and “particle” to refer to an agglomerate of crystallites.) Particle sizes of less than 100 μm have been associated with increased interparticle friction; contributions from short-range electrostatic forces can also lead to agglomeration and inhibit packing[151]. Small particle size can also lead to an increased contribution of external surface area and intraparticle porosity, as well as decreased permeability and particle strength.

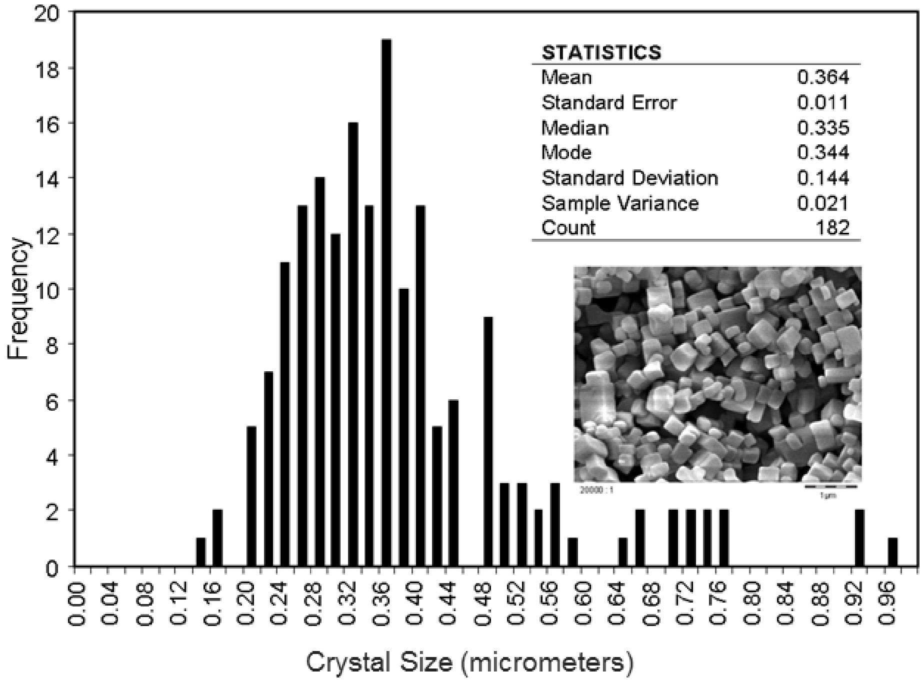

Figure 3.2. Crystal size histogram and statistics for MOF-5 powder. The distribution has a mean diameter of 0.36 μm and standard deviation of 0.144 μm.

Scanning electron microscopy (SEM) was used to characterize the crystallite size for as-synthesized MOF-5 powder. A representative SEM image is shown in Figure 3.2 (inset), where a cubic morphology is observed. The crystallite size histogram comprising data from three separate SEM images is also shown in Figure 3.2. Based on a total of 182 crystallites, the mean crystallite size is 0.36 ± 0.011 μm. As described below, this small crystal size of MOF-5 results in a relatively small bulk density (21% of the single crystalline value) as compared to other MOFs possessing larger crystal sizes

In addition to measuring the crystallite size, the dimensions of agglomerated particles were also measured. The distribution of particle sizes and the cumulative percentage of their volume fraction is shown in Figure 3.3. The mean of the particle size was found to be 0.22 mm, and 99% of the particles were found to have a diameter less than 0.86 mm. Comparison of the crystallite and particle size distributions indicates that due to inter-particle cohesion, essentially all sub-micron sized MOF-5 crystallites aggregate into particles having diameters larger than ~ 3 micron.

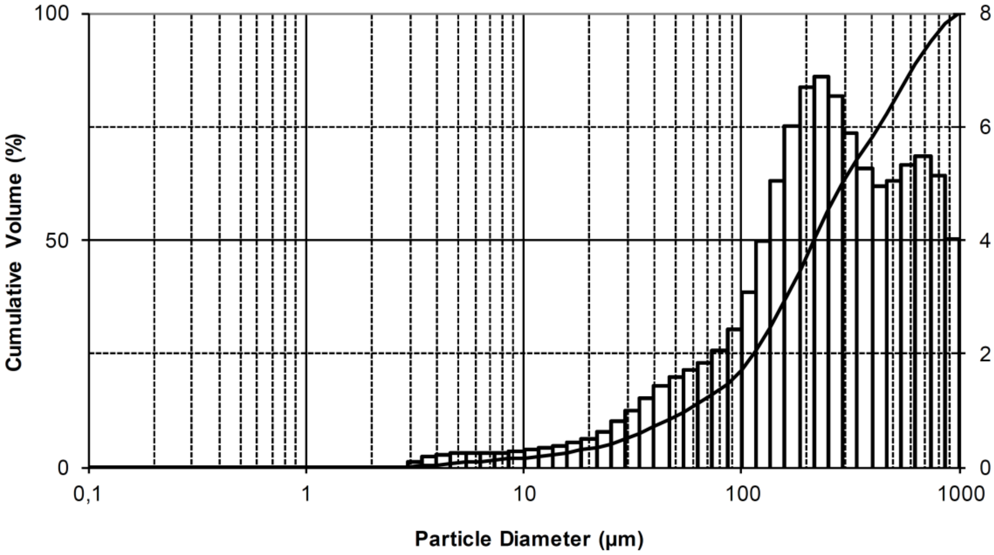

Figure 3.3. Particle size distribution and cumulative volume percentage for a representative MOF-5 powder. The distribution has a mean diameter of 215 μm; 99% of the particles have a diameter less than 857 μm.

3.3.1.3 Bulk Density

The bulk density of MOF-5 powder was initially measured using a small container (.75 ml) which was filled with MOF-5 and then tapped for approximately 5 seconds. This procedure resulted in a low density of 0.13 g/cm^3. To assess the effect of tapping upon bulk density, we loaded a known mass of MOF-5 powder into a larger graduated cylinder (25 cm^3), and manually tapped the cylinder on the floor of the glovebox; the cylinder elevation for each tap was 2-3 cm. The tapping process was repeated for an increasing number of taps, and the volume and mass of MOF-5 powder in the cylinder was recorded afterwards.

Figure 3.4 shows the bulk density as a function of the number of manual taps. It is clear that the powder density increases with the number of taps, starting from a value of 0.18 g/cm^3 at 200 manual taps and increasing to 0.21 g/cm^3 after 2000 taps. The MOF-5 tap density was also measured using a standardized jolting volumeter. In this case a series of 2000 taps were used, and the resulting density of 0.22 g/cm^3 was found to be in very good agreement with the manually-tapped sample. Additional testing demonstrated that the tap density can depend on the volume of the graduated cylinder employed and on the particle size. These tests resulted in a range of MOF-5 powder densities spanning 0.13 to 0.22 g/cm^3.

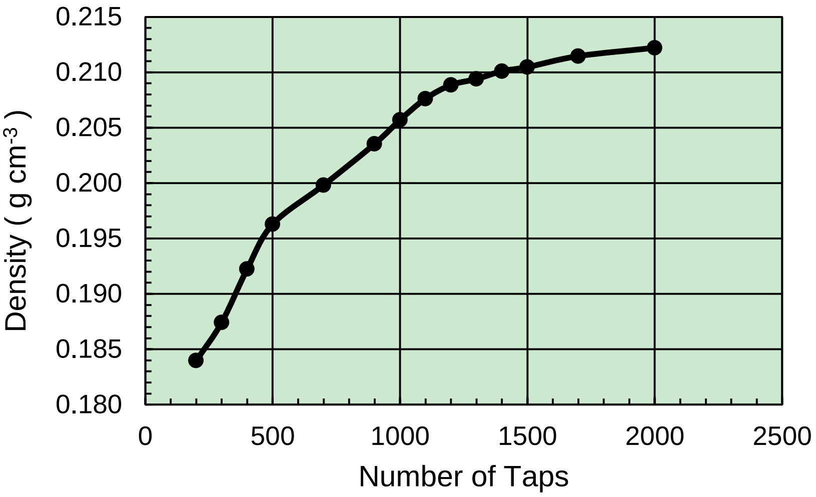

Figure 3.4. Tap density of MOF-5 as a function of the number of taps.

3.3.2 Thermal Properties

Although significant attention has been focused on improving the gas storage capacity of MOFs, relatively little effort has been devoted to assessing their thermal properties[152]. The thermal conductivity and heat capacity of MOFs (and other adsorbents) are significant because they will impact the design, performance, and cost of MOF-based storage systems[153-155]. For example, hydrogen uptake and release reactions involve the liberation (adsorption) or consumption (desorption) of heat; therefore efficient dissipation and delivery of heat is critical. Typically, adsorbent systems incorporate a heat exchanger for managing the temperature during fueling and delivery. The thermal conductivity properties of the storage media will have a direct influence on the heat exchanger design. If the thermal conductivity is low, the heat exchanger design requires additional complexity, which may add weight and cost. As a counter-measure, material enhancements (e.g. graphite additions) can be added to the material to increase the thermal conductivity. These additions displace some fraction of the storage material, resulting in a decrease in storage capacity and an increase in the system weight. Therefore, it is important to accurately evaluate thermal conductivity to minimize the amount of the enhancement materials. Moreover, the creation of accurate system models relies on the determination of thermal properties for materials of interest.

3.3.2.1 Heat capacity

The specific heat capacity (c_p) describes to the ability of a material to store thermal energy, and indicates the amount of energy needed to heat the material to a specified temperature. It is an important property for systems whose operation involves a temperature swing, such as in the thermal desorption of stored gasses. The heat capacity of powder MOF-5 in the temperature range of 220 – 370 K was determined using the procedure described in section 3.2.2.5, and is plotted in Figure 3.5. At 300 K, c_p for MOF-5 was measured to be 0.72 $Jg^{-1}K^{-1}$, which is comparable to that of alumina (0.77 $Jg^{-1}K^{-1}$) and graphite (0.71 $Jg^{-1}K^{-1}$). c_p increases approximately 33% over the measured temperature range, from approximately 0.6 $Jg^{-1}K^{-1}$ at 220 K to 0.8 $Jg^{-1}K^{-1}$ at 340 K.

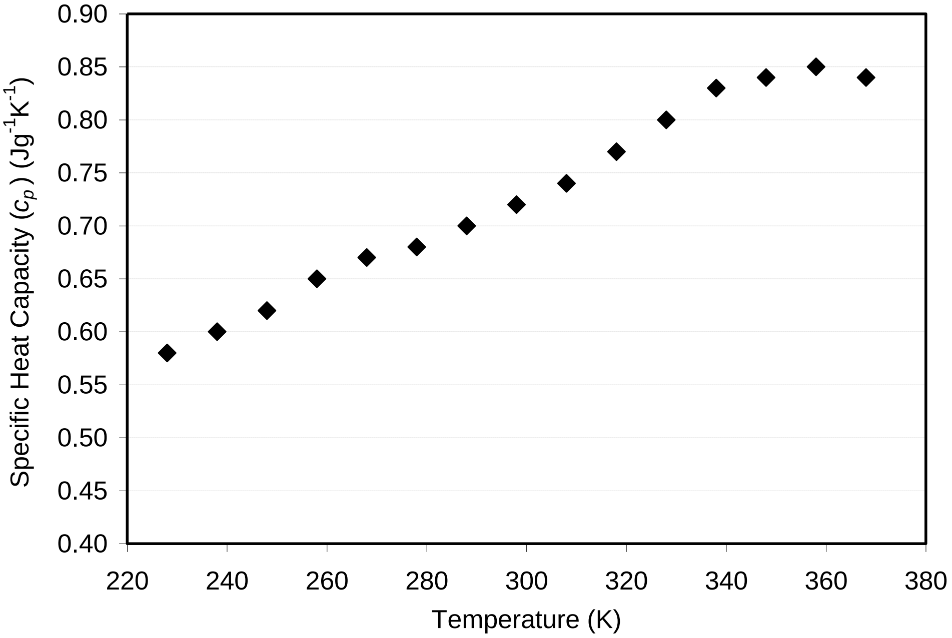

Figure 3.5. Specific heat capacity (c_p) ($Jg^{-1}K^{-1}$) for powder MOF-5 as a function of temperature (K).

3.3.2.2 Thermal conductivity

The thermal conductivity of most microporous materials (e.g. zeolites and MOFs) is low, stemming from their large pore size (>20 Å in diameter) and high free volume (>90% free volume). McCaughey *et al* have pointed out that the atomic number density for MOFs is even lower than that for zeolites (2.46×10^{28} atoms/m^3 for MOF-5 verses 5.13×10^{28} atoms/m^3 for sodalite), suggesting that MOFs will have an even lower thermal conductivity than other highly porous compounds[156]. Single crystal thermal conductivity measurements have been previously measured on 1-2 mm crystals of MOF-5 over a temperature range of 6-300 K in ref.[157]. This data, obtained using a longitudinal steady-state heat flow method, shows a peak thermal conductivity at 20 K of ~0.37 W/m·K and a minimum at 100 K of ~0.22 W/m·K. From 100 to 300 K, the thermal conductivity increases by 30%, attaining a value at 300 K of ~0.32 W/m·K. This value is much lower than that for other microporous single crystals such as zeolites (3.53 and 2.07 W/m·K for sodalite and faujasite, respectively)[152].

The intrinsic thermal conductivity for MOF-5 single-crystals represents an upper limit for the pure material. Data from powder samples includes the effects of interparticle porosity which will reduce the thermal conductivity below the single crystal value. We have measured the thermal conductivity for compacted MOF-5 powder at temperatures from 300 to 335 K and at three densities: 0.35, 0.52, and 0.69 g/cm^3. The thermal conductivity (k) was calculated as the product of heat capacity (c_p) [see Section 3.3.2.1], thermal diffusivity (α), and bulk density (ρ). See Sections 3.2.2.4 to 3.2.2.6 for experimental details. Measured thermal conductivity data is plotted in Figure 3.6. The thermal conductivity for MOF-5 remains relatively constant over the measured temperature range for all three densities. Values at 300 K for each density are as follows: 0.091 Wm^{-1}K^{-1} (ρ = 0.35 gcm^{-3}), 0.11 Wm^{-1}K^{-1} (ρ = 0.52 gcm^{-3}), and 0.16

$Wm^{-1}K^{-1}$ (ρ = 0.69 gcm^{-3}). (As the highest density pellets exceed the single-crystal density we presume some plastic deformation such as pore collapse has occurred in these samples during the compression process.) Based on these data, a modest improvement in *k* can be achieved via compression of the neat powder (e.g. ~20% improvement in *k* in going from ρ = 0.35 to 0.52 gcm^{-3}). The thermal conductivity for the 0.52 gcm^{-3} compact at 300 K is only 35% of the value of that for the single crystal (ρ = 0.61 gcm^{-3}) and is comparable to that of other hydrogen storage materials such as sodium alanate (~0.5 $Wm^{-1}K^{-1}$)[158]. Since higher thermal conductivities are desirable, the addition of conductive additives such as graphite or aluminum (e.g. graphite has a thermal conductivity of 1390 $Wm^{-1}K^{-1}$ at 400 K)[159] will likely be required to improve heat transfer. The impact of expanded natural graphite additives (ENG) on thermal conductivity of MOF-5/ENG compacts has been studied recently[150].

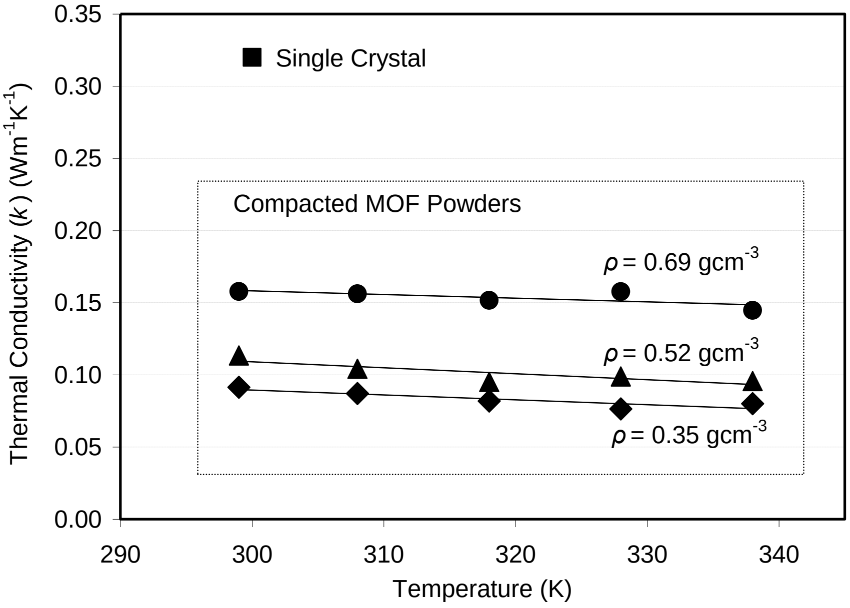

Figure 3.6. Thermal conductivity data for MOF-5 powders as a function of temperature and bulk density: 0.35 g cm^{-3} (diamonds), 0.52 g cm^{-3} (triangles) and 0.69

g cm^{-3} (circles). The thermal conductivity for a single crystal of MOF-5 at 300 K (square) is provided for reference[157].

3.3.3 Hydrogen Adsorption Isotherms

Hydrogen isotherm data is essential for constructing system models for capacity and dormancy under various operating scenarios. Toward this end, materials-level models that can describe empirical hydrogen adsorption isotherm data are needed. Until recently, efforts aimed at identifying such models have been scarce due to the complexities of performing measurements at multiple sub-ambient temperatures. For example, most measurements on sorbents have been limited to a small number of temperatures that are accessible using cryogenic baths (e.g. liquid nitrogen, liquid argon, solid CO_2). In this work, a continuous flow controlled cryostat is employed for collection of adsorption data at several intermediate temperatures: 103, 118, and 138 K. Cryogenic baths are used for 77 K and 200 K, while measurements at 295 K are performed without active temperature control. The resulting data is then used to determine model parameters that in turn provide an analytic expression for the adsorption properties in MOF-5 at arbitrary temperatures.

3.3.3.1 Modeling approach

Hydrogen adsorption data can be expressed in various forms, for example excess, absolute, or total adsorbed amounts[134]. The excess amount adsorbed (n_{ex}) is defined as the amount of adsorbate (e.g., hydrogen) stored in the porous volume of an adsorbent (e.g., MOF) at a given temperature and pressure above and beyond what would be present in the same volume in the absence of adsorbate-adsorbent interactions. The absolute amount adsorbed (n_a) is defined as the quantity of adsorbate molecules in the adsorption volume (V_a), including specifically adsorbed molecules as well as gas phase molecules. Finally, the total amount ($n_{tot.}$) represents the total amount of hydrogen stored in the hydrogen storage system and includes contributions of n_a and homogeneous bulk hydrogen gas (n_g) which can occupy interparticle and intraparticle voids. While excess isotherms are typically determined experimentally, absolute adsorption data is often an estimated value. Excess and absolute adsorption data are related by equation (3.1)[160].

$$n_{ex} = n_a - \rho_g V_a \quad (3.1)$$

where ρ_g denotes the density of bulk gas, and the volume occupied by the adsorbed phase, V_a, is assumed to be a constant. During adsorption the adsorbed gas occupies the space V_a spanned by the adsorption field generated by the adsorbent, and the average adsorbate density gradually increases up to an asymptotic value[134]. From equation (3.1), we can also infer that near ambient conditions (e.g., low pressure and/or above cryogenic temperatures), ρ_g will be significantly lower than the density of the adsorbed phase (ρ_a). Under such conditions, the approximation $n_{ex} \cong n_a$ holds. However, at higher pressures and/or cryogenic temperatures the density of the gas phase (ρ_g) increases at a faster rate than the density of the absorbed phase (ρ_a), and thus n_a will continue to increase as n_{ex} reaches a maximum (plateau).

The Dubinin-Astakhov (D-A) model[122] is a pore filling model for adsorption of subcritical gases in microporous adsorbents, i.e., those whose pore diameter is less than 2 nm. This model has been adapted to describe supercritical H_2 adsorption for a variety of microporous materials (e.g. carbons and MOFs). For these compounds the adsorption enthalpy is influenced by the superposition of attractive forces from neighboring walls of the adsorbent. In such microporous materials, the adsorption process is often interpreted as a volume of liquid adsorbate filling the pores. The D-A model can be readily applied to most MOFs given that their pore diameters (0.5 to 1.5 nm) fall within the applicable range. (The diameters of the two pores in MOF-5 are 1.5 and 1.1 nm.) Herein, we employ a modification of the D-A model[161] where excess adsorption is defined as:

$$n_{ex} = n_{max} \exp[-[\frac{RT}{\alpha + \beta T}]^m \ln^2(\frac{P_0}{P})] - \rho_g V_a \quad (3.2)$$

where α and β are enthalpic and entropic contributions to the characteristic free energy of adsorption, m is the heterogeneity parameter, and P_0, is the pressure corresponding to the limiting adsorption. One feature of equation (2) is the temperature-dependent expression of the characteristic free energy of adsorption (ε), where $\varepsilon = \alpha + \beta T$. Other approaches, including modifications of the D-A model and monolayer-based models (Unilan and Toth), have recently been used to fit MOF-5 hydrogen adsorption isotherms[123, 162].

3.3.3.2 Experimental and modeling results for excess capacity

The excess hydrogen adsorption (n_{ex}) by MOF-5 as a function of temperature (77 to 295 K) and pressure (0 to 100 bar) is shown in Figure 3.7. The storage capacities are expressed as excess gravimetric capacity (expressed as wt.%) and excess volumetric capacity (g H_2/L MOF-5). The experimental data are represented by symbols and the modeled fits by the solid lines. The measured excess adsorption at 77 K shows a maximum value of 6.0 wt. % (29.9 mol/kg) at 48 bar. (In the present study wt. % is defined as (g H_2/g MOF-5) x 100.) This value is comparable to previous measurements for MOF-5 powder, which vary between 4.7 wt. % and 7.1 wt. %[104]. As is expected, the adsorption decreases with increasing temperature. For example, at a temperature of 200 K and 80 bar, the maximum gravimetric capacity is only 1.3 wt. % (6.4 mol/kg).

The excess volumetric adsorption at its maximum value, based on the density for loosely-packed powder MOF-5 (ρ_{pwd}=0.13gcm^{-3}), is approximately 8 g H_2/L MOF-5 (near-right ordinate, Figure 3.7) as compared to 36 g H_2/L (rightmost ordinate, Figure 3.7) assuming a single crystal density (ρ_{sx}=0.605 gcm^{-3}). The powder and single-crystal morphologies represent the extremes of volumetric capacity in MOF-5. In principle, intermediate capacities may be achieved via materials engineering. For example, in a prior study we examined the extent to which volumetric density could be improved in MOF-5 via densification[123, 124].

Parametric description of the excess hydrogen stored in MOF-5 as a function of temperature and pressure was achieved by fitting the modified D-A model [eq. (3.2)] with m = 2. Values for the five parameters, n_{max}, α, β, P_0, and V_a, were obtained by nonlinear regression on the measured isotherms at 77, 138, 200 and 295 K. The resulting values for the model parameters are listed in Table 3.2, and the fits are represented as solid lines in Figure 3.7. Here, the value for the adsorbed volume (V_a) is 2.01 cm^3g^{-1}. The remaining parameter values, n_{max}=125.4 mol/kg, α=2239 $Jmol^{-1}$, β=19.5 $Jmol^{-1}K^{-1}$, and P_0=1692 MPa, are of comparable magnitude to those previously established[161] for AX-21.

As can be seen in Figure 3.7, the D-A model parameters for MOF-5 reproduce the empirical data across the measured temperature-pressure conditions (e.g. 77-298 K and 0-100 bar). Nevertheless the original intent of the various adsorption models was to impart physical insight into the adsorption process (e.g., α represents the enthalpic contribution to the free energy of adsorption). Given the empirical nature of the model, its various modifications, and its applicability to the MOF materials class, the clear physical meaning of the parameters becomes more ambiguous. In particular, we find the estimated adsorption volume (V_a=2.01 ml/g) is larger than the intra-crystalline pore volume, given by $1/\rho_{\mathrm{sx}} - 1/\rho_{\mathrm{fm}}$ = 1.16 ml/g, as well as the experimentally determined micropore volume (V_{micro}) of 1.2 ml/g [as reported in Section 3.3.1.1]. Likewise, the parameters (n_{max} in particular) obtained here by fits to data between 77 K and 295 K over-predict the expected excess adsorption at 30 K by at least 20%[163]. We also note that the modeled excess adsorption at 295 K is negative below a pressure of approximately 20 bar. Thus caution should be exercised in applying these parameterizations to operating conditions outside of the ones used here. Other models, including the Unilan model, have been found to better describe H_2 adsorption by MOF-5 over a wide range of temperature[123].

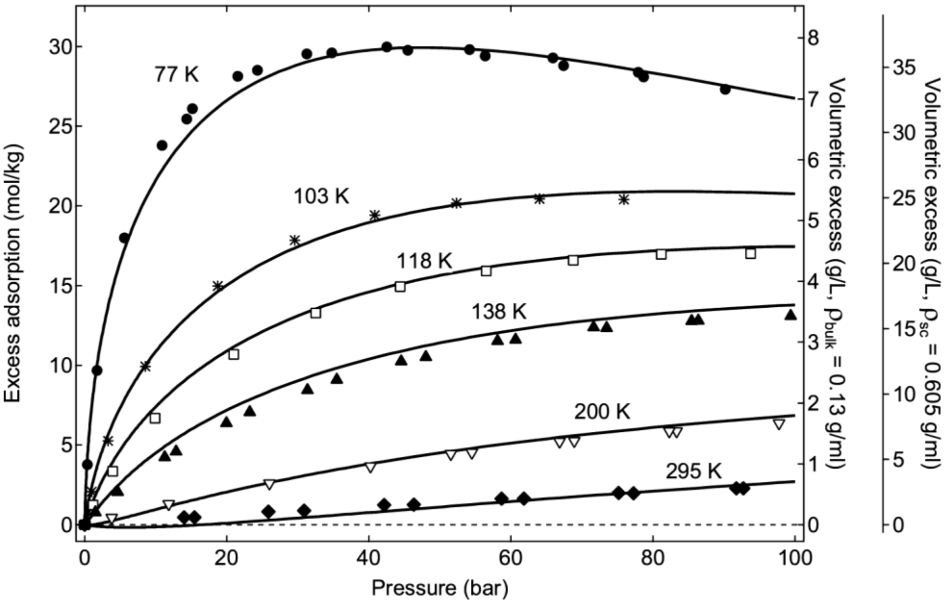

Figure 3.7. Excess hydrogen adsorption isotherms for powder MOF-5 at five temperatures (77, 103, 118, 138, 200 and 295 K). Measured data corresponds to symbol points, and solid lines are fits using the modified D-A equation (2). (Left axis) Gravimetric excess capacity in mol/kg. **(**Right axes**)** Volumetric excess adsorption (g/L), where the near-right ordinate is based on the MOF-5 loose-packed powder density (ρ_{bulk}=0.13 gcm^{-3}) and the rightmost ordinate assumes a density equal to the MOF-5 crystal density (ρ_{sx}=0.605 gcm^{-3}).

3.3.3.3 Modeled absolute and total capacity

MOF-5 absolute hydrogen isotherms based on the modified D-A model are shown in Figure 3.8. The absolute capacity includes excess adsorption as well as gas that is contained within the adsorption volume, V_a, according to equation (3.1) above. At low temperatures and high pressures, the amount of additional gas in the adsorption volume is appreciable. Consequently, the absolute adsorption amount can be nearly double that of the excess gravimetric capacity. For example, at 77 K and 75 bar, n_{ex} and n_a for

MOF-5 are 5.8 and 10.7 wt% respectively. Absolute H_2 uptake on a volumetric basis for bulk MOF-5 powder is provided on the right ordinate in Figure 3.8.

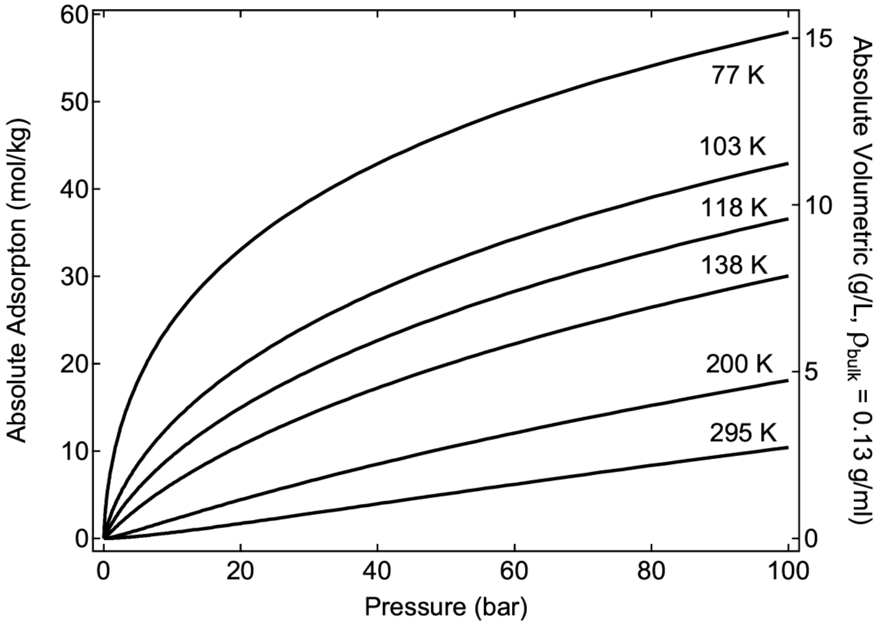

Figure 3.8. Absolute hydrogen adsorption isotherms for powder MOF-5 at six temperatures (77, 103, 118, 138, 200, and 295 K) based on D-A parameters in Section 3.3.2. On the left ordinate, absolute adsorption is listed in gravimetric units of mol/kg. The right ordinate lists absolute adsorption in volumetric units of g/L, assuming the bulk density of loosely-packed MOF-5 powder (ρ_{bulk}=0.13 gcm^{-3}).

For practical applications the *total* amount of stored hydrogen, n_{tot}, where $n_{tot} = n_{ex}+\rho_g V_v$ and $V_v = 1/\rho_{bulk}$ $_-1/\rho_{sk}$ is of the most importance. The total capacity MOF-5 depends on the temperature and pressure of operation (which affect ρ_g) and on the bulk adsorbent density (which affects the void volume, V_v). The total volumetric storage, estimated by multiplying the gravimetric total storage, n_{tot}, by the bulk density, ρ_{bulk}, is shown Figure 3.9. The MOF-5 powder density (0.13 g/cm^3, loose- packed) is used as the bulk density. Total volumetric capacities are compared with that of compressed H_2 at 77 K, which is illustrated as a dashed line in Figure 3.9. It can be seen that MOF-5 powder, even in a loosely-packed form, increases the H_2 storage capacity for temperatures below 200 K. This enhancement in volumetric storage capacity is considerably larger if one considers a MOF-5 single crystal (assuming the gravimetric capacity is the same for both MOF-5 powder and monoliths). The "breakeven" pressure is the point at which the total storage of compressed H_2 exceeds that of the sorbent, at which point the sorbent provides no net benefit. At 77 K, the breakeven point (~386 bar) that is estimated from the D-A parameters in Table 3.2 occurs outside of the experimental 0-100 bar pressure range.

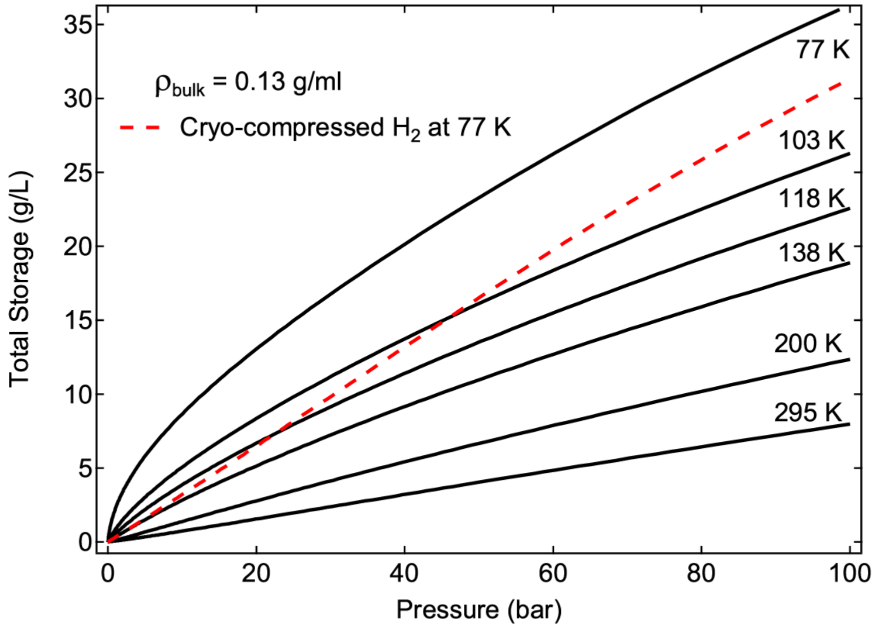

Figure 3.9. Total hydrogen storage within the gross volume occupied by the powder MOF-5, assuming a bulk powder density of ρ_{bulk} = 0.13 g/cm^3. The dashed red line indicates the density of bulk H_2 gas at 77 K.

3.3.3.4 Adsorption Enthalpy

The differential enthalpy of adsorption (ΔH_{ads}) for sorbents such as MOF-5 is an important parameter that, together with thermal attributes discussed above, affects the overall design and performance of on-board and/or forecourt thermal management systems. The amount of heat to be liberated from the storage bed during adsorption is related to the ΔH_{ads}. Here, we have calculated ΔH_{ads} as a function of excess hydrogen adsorption in MOF-5 by applying the Clausius-Clapeyron equation to excess adsorption isotherms. An estimate of ΔH_{ads} from experimental isotherms is plotted versus fractional excess adsorption (i.e., n_{ex} divided by $n_{\max}$ from Table 3.2) in Figure 3.10. The magnitude of the enthalpy decreases from about -5 kJ/mol at zero coverage to -4.3 kJ/mol at a fractional excess uptake of about 0.1, consistent with results previously published for powder MOF-5[123].

The differential enthalpy of adsorption can also be calculated analytically for the modified D-A model as a function of absolute adsorption: [161]

$$\Delta H_{abs} = -\alpha\sqrt{-\ln(n_a / n_{\max})} \quad (3.3)$$

Equation (3.3) is plotted in Figure 3.10 using the D-A parameters listed in Table 3.2. At low pressures, the excess and absolute adsorption amounts are similar, and thus the experimental and modeled ΔH_{ads} can be directly compared. Agreement between the experimental and modeled enthalpy is very good. These results confirm that adsorption models such (as the D-A model) are effective in describing the equilibrium PCT diagrams of H_2/MOF-5, and in modeling the thermodynamic properties of cryo-adsorption-based hydrogen storage. Further, these D-A parameter values can be used in the governing equations for heat and mass conservation in a hydrogen storage model for MOF-5.

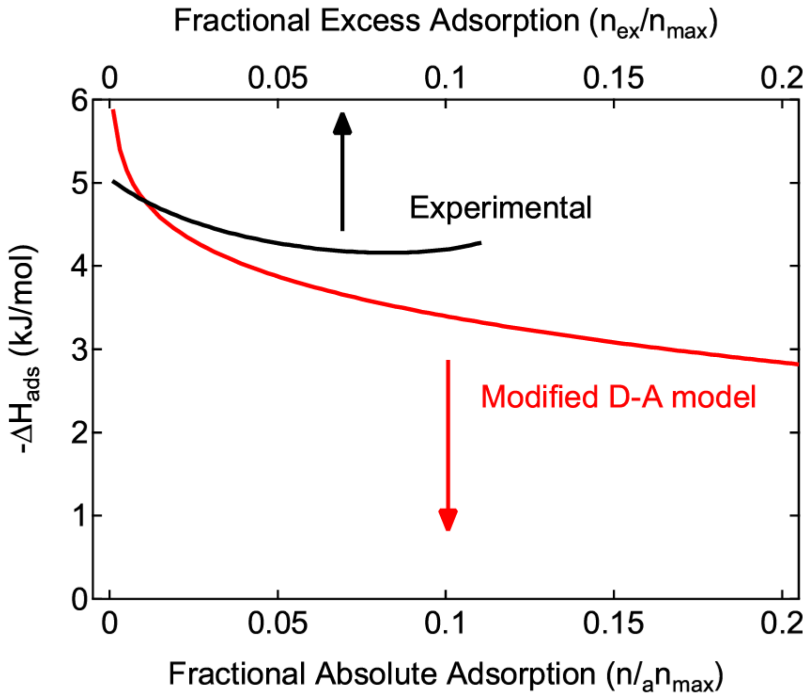

Figure 3.10. Differential H_2 adsorption enthalpy ($-\Delta H_{ads}$) of powder MOF-5. Experimental estimates of $-\Delta H_{ads}$ are plotted on the top axis versus the fractional excess adsorption. The modeled $-\Delta H_{ads}$ [eq (3.3)] is plotted on the bottom axis versus fractional absolute adsorption.

3.3.4 Robustness to Air Exposure

The robustness of MOFs with respect to air and/or water has attracted considerable attention during the past few years[147, 164-168], with many authors observing some degree of degradation following exposure. Given that stability is a desirable property – for example, assembly of a MOF-based gas storage system would be less costly if it could be performed in open air – here we examine the robustness of the pilot-scale version of MOF-5. Changes to the hydrogen adsorption properties and crystal structure of MOF-5 powders as a function of exposure time to humid air (45% relative humidity at 22^{0}C) are summarized in Figure 3.11 and Figure 3.12, respectively. Overall, the data suggests only a minor degradation of properties for exposure times up to 8 hours.

Regarding the impact on hydrogen uptake, Figure 3.11 compares the effects of exposure time and sample activation on excess H_2 adsorption. (A magnification of the maximum uptake region is shown as an inset.) For the shortest exposure time of 12 minutes a 1.2% to 1.5% decrease in maximum uptake from the baseline, (i.e., non-exposed) sample is observed for the activated and non-activated samples, respectively. At 1.5 hours of exposure the reduction in uptake increases only slightly (3.5% to 3.7%, activated vs. non-activated). Finally, for the longest exposure time of 8 hours the reduction in excess H_2 adsorption is 7.3%. Since it is unlikely that activation could reverse ligand displacement or loss of crystallinity, the similarity in uptake for the activated vs. non-activated samples suggests that the degree of irreversible structure change occurring in MOF-5 under these conditions is relatively small.

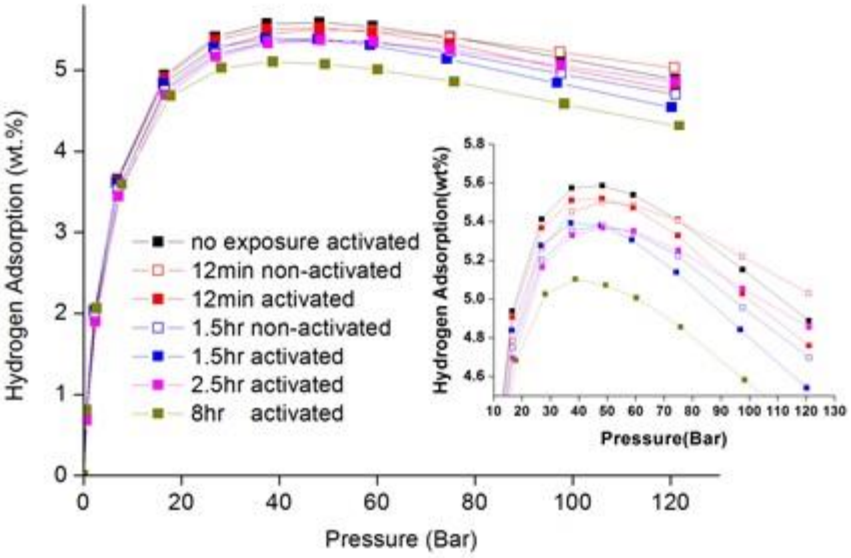

Figure 3.11. MOF-5 hydrogen uptake isotherms following exposure to humid air (45% relative humidity at 22^{0}C) for various times. “Activated” samples were heated to 130ºC and evacuated for at least 6 hours; “non-activated” samples were evacuated without heating for only 15 minutes. The inset shows a magnification of the maximum uptake region of the isotherms.

To confirm the H_2 uptake measurements, Figure 3.12 plots *in situ* x-ray diffraction patterns for samples continuously exposed to humid, laboratory air for times up to 250 hours. With increasing exposure time we observe a reduction in intensity for the diffraction peak at 7 degrees. A new peak at 9 degrees appears only after the sample is exposed for more than 100 hours. The emergence of this peak is similar to what has been observed in previous work [147] after 10 minutes exposure time. Unfortunately, the humidity conditions used in Ref. [147] were not reported; therefore a direct comparison is not straightforward. Nevertheless, such a difference could be traced to one or more factors, such as differences in MOF composition, initial structure, sample mass, and/or exposure conditions (humidity levels, exposure time, temperature, static/flowing exposure, etc.) For example, we observe some initial differences in the low-angle diffraction peaks in our samples compared to other literature reports [116, 147, 164, 168, 169], which could indicate the presence of retained salt or solvent.

We conclude that the robustness of the MOF-5 powder suggested by our PCT data is consistent with the XRD patterns. Taken together, these data suggest that brief exposure of MOF-5 (for example, during the few minutes needed to load/assemble a pressure vessel) should not result in significant reductions in performance. Additional studies are planned to more quantitatively assess the impact of factors such as higher humidity levels and compaction [123, 124].

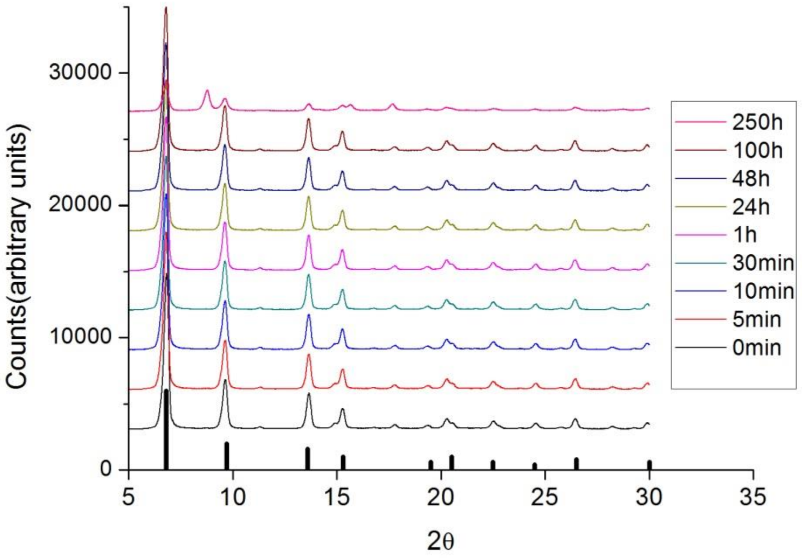

Figure 3.12. *In situ* X-ray diffraction pattern for MOF-5 powder as a function of exposure time to laboratory air (relative humidity around 45% at 22^{0}C). Vertical lines show the peak positions and relative intensities for the reference desolvated MOF-5 structure[125].

3.4 Conclustion

We have performed a comprehensive assessment of the primary thermo-physical properties of MOF-5 powders. Characterized properties include: packing density, surface area, pore volume, particle size distribution, thermal conductivity, heat capacity, stability against hydrolysis, differential enthalpy of H_2 adsorption, and Dubinin-Astakhov isotherm parameters. Although some of the characterized properties have been previously reported for laboratory-scale (i.e., small) quantities of MOF-5, variation arising from differences in MOF synthesis and activation pose challenges to achieving a consistent description of these properties. The present study aims to minimize these inconsistencies by analyzing an industrial, pilot-scale version of MOF-5. Consequently, the data should provide a reasonable approximation to the properties expected in industrial applications. Although here we emphasize properties relevant for hydrogen storage, the data can serve as a starting point for MOF-based systems in other applications such as catalysis, gas separations, *etc.*

The pilot-scale synthesis method described here using zinc acetate dihydrate yields a robust MOF-5 powder with good resistance to humidity degradation: Exposure to air (45% relative humidity, 22°C) for 1.5 hours resulted in only a ~3.5% reduction in excess H_2 uptake. The mean crystal diameter of the resulting finely-powdered MOF-5 was measured at 0.36 μm. The packing density of the powder is sensitive to the degree of tapping, and can vary from 0.13 to 0.22 g cm^{-3}. The powder can be easily shaped into pellets by uniaxial compaction, without the need for binder. Porous texture measurements indicate a BET specific surface area of 2763 m^2g^{-1} and a micropore volume of 1.27 cm^3g^{-1}. The thermal conductivity of 0.35 g cm^{-3} MOF-5 pellets was measured to be 0.091 $Wm^{-1}K^{-1}$ at 300 K. The heat capacity, c_p, of powder MOF-5 in the temperature range of 220 – 370 K was determined; at 300 K, $c_p = 0.72$ $Jg^{-1}K^{-1}$. We determined parameters for the modified Dubinin-Astakhov isotherm model, which accurately describes the concentration of adsorbed H_2 within MOF-5 over the temperature range 77-295 K and the pressure range 0-100 bar.

Chapter 4

Anisotropic Thermal Transport in MOF-5 Composites

4.1 Introduction

In chapter 3 we learned that the high surface area, building-block-like synthesis procedure, and permanent porosity of MOFs make them attractive candidates for applications such as gas storage, gas separations, and catalysis [170-172]. They have also demonstrated record-setting storage capacities for alternative transportation fuels such as hydrogen [173] and natural gas [174], and are also being explored for carbon capture applications [175].

While MOF attributes such as surface area and pore volume play an important role in determining their gas storage capacity, thermal transport properties should also be considered. For example, in gas storage applications requiring rapid uptake (e.g., refueling of a vehicle), the exothermic heat of adsorption [176, 177] should be expelled in an efficient fashion in order to maximize performance. As higher temperatures reduce storage capacity, the inclusion of a heat-exchanging manifold within the storage vessel has been explored to enhance heat removal [178]. For adsorbents having low thermal conductivities the demands placed upon heat exchanger increase, typically at the expense of reduced volumetric and gravimetric storage density (due to additional mass and volume associated with the heat-exchanging manifold), and potentially highercost. An alternative to an elaborate heat exchanger is to increase the thermal conductivity of the adsorbent medium itself.

Unfortunately, the thermal transport behavior of MOFs has received relatively little attention [124, 133, 157, 177, 179, 180]. Huang *et al.* predicted the thermal conductivity of single crystal MOF-5 to be 0.31 W/m K at 300K using molecular dynamics simulations [179]. Experimental measurements on single crystals of the same MOF were also reported over a temperature range of 6 to 300 K, with a value 0.32 W/m·K measured at 300 K [157]. In addition to these single crystal studies, Liu *et al.* [133] reported that the thermal conductivity of MOF-5 powders could be increased via compression/pelletization and through combination with high-conductivity additives such as expanded natural graphite (ENG), which has a thermal conductivity of ~150 W/m·K [181]. For example, in pellets densified to 0.5 g/cm^3 the addition of 10 wt.% ENG resulted in a factor of five improvement in thermal conductivity (0.56 W/m·K at 298 K) relative to neat MOF-5 pellets at the same density (0.10 W/m·K). Compaction alone also improves thermal conductivity, but to a smaller extent: neat MOF-5 pellets densified from 0.3 to 0.7 g/cm^3 exhibit a doubling of conductivity from 0.07 to 0.14 W/m·K.

These and other studies have shown that variations in processing and composition can significantly alter materials properties [182, 183]. For example, uni-axial compression has been linked to the formation of microstructural anisotropy in compacted ENG [184]. Similarly, the addition of high-aspect-ratio particles to a matrix phase can lead to anisotropic behavior [185] [186]. These observations suggest that MOF/ENG pellets could also exhibit anisotropic thermal transport arising from a combination of uni-axial compression and worm-like ENG additions.

The existence of anisotropic thermal transport could impact the design and operation of an adsorbent-based gas storage vessel. For example, consider a storage system that employs a stack of densified MOF “pucks.” The heat-exchanging manifold for this design could consist of circular plates sandwiched between puck faces. In this case it is desirable to maximize transfer along the axial direction of the pucks to/from the heat exchanging plates. Alternatively, for a cylindrical shell heat exchanger in contact with the rims of the pucks, facile transport along the radial direction of the pucks is desirable. These scenarios demonstrate that quantifying (and controlling) the degree of thermal anisotropy is an important consideration when processing the storage media. Nevertheless, one should recognize that densification and ENG additions generally reduce the gravimetric capacity of the storage medium [124, 133, 177, 180]. Therefore the tradeoff between improved thermal transport and lower capacity should be carefully considered.

In this chapter we examines the possibility for anisotropic thermal transport in uni-axially compressed MOF/ENG composites using thermal conductivity measurements and microstructural characterization on the prototype compound, MOF-5. Due to its high gas storage capacity and simple crystal structure, MOF-5 is perhaps the most widely studied MOF. It is comprised of 1,4-benzenedicarboxylate (BDC) organic linkers and Zn_4O tetrahedral clusters, the latter serving as secondary building units. MOF-5 can adsorb a large amount of hydrogen, up to 7.1 excess wt.% at 77 K and 40 bar [147]; recent studies have also suggested promising performance for natural gas storage [187]. In addition to its high gravimetric capacity, recent analysis by Goldsmith, *et al.* indicated that MOF-5 is one of a small number of MOFs that also exhibits high volumetric gas storage densities [188].

In the present chapter we demonstrate that the high-aspect ratio morphology of second-phase ENG additions, combined with uni-axial compression, results in anisotropic microstructural and thermal transport properties in composite MOF-5/ENG particles. Microscopy of pellet cross-sections confirms the presence of a textured microstructure having MOF particle boundaries and ENG orientations perpendicular to the pressing direction. Thermal conductivity data spanning from cryogenic to ambient temperatures reveal that the values perpendicular to the pressing direction are 2 to 4 times higher than in the pressing direction. We furthermore demonstrate that this anisotropy can be exploited using two straightforward processing techniques. First, a custom die/compression geometry allows for reorientation of the preferred heat flow path. Secondly, fabrication of a layered microstructure with alternating MOF-5 and ENG layers results in an order of magnitude increase in thermal conductivity, at the expense of only minor ENG additions (5 wt.%). These data suggest that the magnitude and preferred direction for thermal transport in MOF compacts may be tuned by altering the processing conditions and nature of the second-phase additions.

4.2 Experimental Procedure

4.2.1 Materials Preparation

MOF-5 powder was provided by BASF, and was synthesized using a process described previously [180]. Expanded natural graphite, ENG, was provided by SGL Group. Synthesis of ENG proceeds by soaking natural graphite flakes in sulfuric acid, followed by heating at 700^{0}C for 12-15 minutes to remove acid residues [184, 189]. MOF-5 and ENG powders are shown in Figure 4.1. MOF-5 powders are white in color, and are composed of small, cubic particles with diameters ranging from 0.1 to 1.5 mm [180]. In turn, each MOF particle is comprised of individual crystallites with diameters in the range of 0.2 to 3 μm [Figure 4.1b]. The diameter of the interparticle voids is typically several microns. Images of ENG powder are shown in the lower panel of Figure 4.1c, d. ENG consists of relatively large black vermicular particles ranging in length from approximately 0.5 to 4 mm. The density of ENG (~0.1 g/cm^3) is approximately 20 times smaller than normal graphite (2.25 g/cm^3) [189]. The worm-like structure of the ENG arises from the expansion of natural graphite's lamellar structure. ENG particles exhibit a high aspect ratio (length/diameter), ranging from 18 to 25 [190].

Figure 4.1. Images of MOF-5 (upper panel) and ENG powders (lower panel).

4.2.1.1 Pellets with Homogeneous ENG Distribution

Pellets formed in the laboratory and at a pilot-plant (BASF) were synthesized and characterized. (See section a in Appendices A for details regarding pellets formed using the pilot-plant approach.) Lab-scale pellets were formed using MOF-5 powder and a fractional mass of ENG (weighed on a digital scale) needed to achieve a desired ENG weight percent (0%, 5% and 10%). A SPEX 8000M Mixer/Mill was filled with the two powders and shaken in the milling machine for 20 seconds without milling balls. The MOF-5/ENG blends were subsequently loaded into punches and dies with different bore diameters and shapes. Specimens were compressed using a manual pellet press (Reflex Analytical), which was housed inside an Ar-filled glovebox. Cylindrical and rectangular shaped pellets were formed and characterized (Figure 4.2a,c). Cylindrical samples were used for microstructure characterization and room temperature thermal diffusivity measurements; rectangular samples were primarily used for steady-state heat flow thermal conductivity measurements, where a rectangular geometry best accommodates the size of the stainless-steel contacts of the instrument. To examine the impact of compression direction, two different types of die were designed for each sample shape. In the case of the cylindrical geometry, this allowed for pellets to be processed using uniaxial compression along either the radial or axial directions (Figure 4.5). Likewise, for the rectangular geometries, compression was performed parallel, or perpendicular to, the long axis of the pellet (Figure 4.7; also see section d in Appendices A).

4.2.1.2 Pellets with Layered ENG Distribution

As an alternative to mixing MOF-5 powder with ENG before compression, pellets with a layered MOF-5/ENG microstructure were also fabricated. In this case cylindrical pellets were made using radial pressing (Figure 4.5c). Before compression, known masses of pure MOF-5 and ENG were separated according to the desired ENG composition fraction, and then divided into several parts. These parts were then added into the die alternatively and pressed into pellet form. A pellet containing four ENG layers is shown in Figure 4.2b.

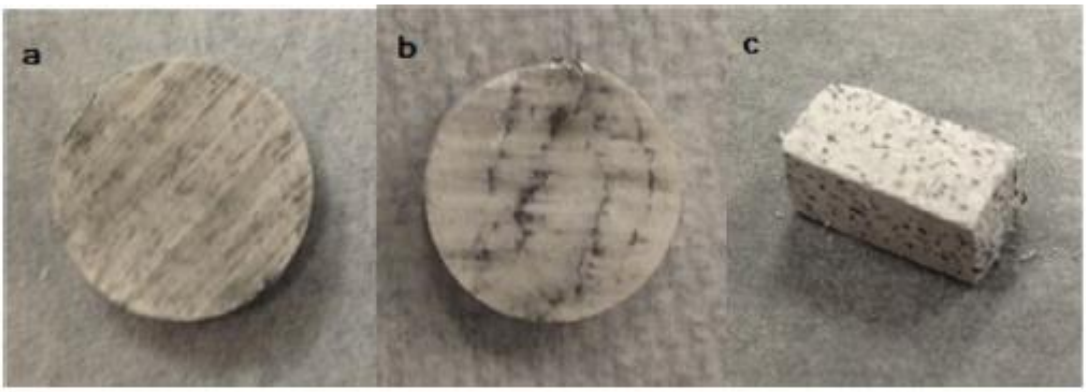

Figure 4.2. Cylindrical and rectangular MOF-5/ENG composite pellets. (a, b) Cylindrical pellet used for room temperature measurements and microstructure characterization. Pellet diameter = 1.28 cm, thickness = 3 mm, density = 0.4g/cm^3. The pellet in (a) has a homogeneous ENG distribution, while the pellet in (b) has a layered ENG distribution. (c) Rectangular sample used for low-temperature measurements (80 – 300 K). The sample dimensions are 10 × 5 × 5 mm. Sample density = 0.35 g/cm^3.

4.2.2 Materials Characterization

4.2.2.1 Microscopy

Optical [Olympus SZX12 model 2.2.0 (x90) & Nikon microphot-FXA (x1000)] and scanning electron microscopy (JEOL 6610, FEI Quanta 3D SEM/FIB, and Phillips XL30FEG) were used to investigate the microstructure of MOF-5 compacts. Pellets were cross-sectioned to observe the inter-particle boundaries and the orientation and distribution of ENG. Images were collected using Image-PRO Plus software and analyzed using ImageJ software. Scanning electron microscopy was used to conduct energy dispersive spectroscopy of the sample (Appendices A, Figure A.3). In order to reduce surface charging, the beam current was reduced, low vacuum mode was used, and/or the sample was coated with either silver (Ag) or gold (Au). Images and composition maps from the SEM were collected using either the AZTEC EDS system or the EDAX Genesis system. ImageJ [191] was used to quantify the orientation relationship of the ENG particles with respect to the pressing direction in order to characterize the impact of pressing direction on ENG alignment.

4.2.2.2 Room temperature thermal conductivity

The room temperature thermal conductivity κ was determined using a transient method for measuring the thermal diffusivity, combined with the following equation:

$$\kappa = \alpha \cdot C_p \cdot \rho. \quad (4.1)$$

Equation (4.1) [192] is a standard expression derived from the transient heat transport equation: $\frac{\partial T}{\partial t} = a \nabla^2 T$. Here α is the thermal diffusivity, which is a function of the thermal conductivity, κ, sample density, ρ, and specific heat capacity c_p: $\alpha = \kappa/(\rho\ c_p)$. The parameters κ, ρ, c_p (and therefore α) are temperature dependent, and were determined over the temperature range of interest, 25 – 65° C. ρ is determined using the pellet's external dimensions and mass. C_p measurements were performed on 6.35 mm pellets with a differential scanning calorimeter (DSC) (SENSYS DSC, Setaram), which was calibrated with a sapphire standard. Pellets were placed inside an alumina crucible while being handled inside an Ar-filled glovebox, and then transferred to the DSC (external to the glovebox). Data were collected using a heating rate of 5 ℃/min and a He carrier gas flow of 20 ml/s.

Thermal diffusivity measurements at room temperature and above were performed using a xenon thermal flash diffusivity instrument (Anter Flashline, FL3000S2) with N_2

as a protective gas, and with pellets having a 12.8 mm diameter and 3mm average thickness (Figure 4.2a). In this method the temperature of the rear surface of the sample is measured as a function of time after a laser pulse with known power is shined on the sample’s opposite surface. The method of Clark and Taylor [193], which accounts for heat loss of the sample during the measurement, was used to estimate the thermal diffusivity. The instrument was calibrated using an iron standard. A thin copper sheet was applied to the top surfaces to prevent the pellets from fracturing during measurement due to the temperature probes, and silver paint was used to adhere the copper to the sample surface. Graphite was coated on the lower surface of the pellet to improve light absorption. Before measurement, the pellets were evacuated at room temperature for at least 3 hours. Two measurements were taken for each pellet at the following temperatures: 25 ℃, 35 ℃, 45 ℃, 55 ℃, and 65 ℃. Notice that for this measurement technique the heat flow is along the axial direction of the pellet. It is therefore possible to characterize anisotropies in thermal conductivity by performing measurements on pellets pressed in distinct (i.e., axial or radial) directions. For pellets pressed axially (as described further below), the thermal flash sample geometry results in a heat flux which is largely perpendicular to the average ENG orientation (Figure 4.5a,b), Conversely, pellets pressed radially exhibit ENG orientations more closely aligned with the heat flow direction (Figure 4.5c).

The transient method compliments the steady-state method (described below) in that it provides reliable thermal conductivity data at room temperature and above. At these temperatures losses due to thermal radiation can be significant, leading to complications in the use of the steady-state technique.

4.2.2.3 Low-temperature thermal conductivity

The low-temperature thermal conductivity was measured in the temperature range of 80 to 300 K using a steady-state comparative method that is well-suited for materials having low thermal conductivity [69]. In contrast to the transient method, which requires measurement of both the thermal diffusivity and specific heat capacity, the steady state method directly measures the thermal conductivity using the dimensional Fourier law. This approach is more convenient at cryogenic temperatures. A rectangular-shaped sample with a cross section of 5 mm × 5 mm and length of 3 mm was sandwiched between two stainless-steel contacts (SS304) with the same cross section and thickness of 10 mm (initial attempts employed a longer sample with typical length of 10 mm. However, the radiation losses associated with a sample of this size led to poor estimates of the thermal conductivity. The temperature-dependent thermal conductivity of the stainless-steel contacts have been previously measured [70]. Stycast epoxy was used to mount the sample to the steel contact as well as reduce the contact resistance, and did not permeate the samples. A strain gauge heater was mounted on top of one steel contact, while the other contact (placed under the sample) was connected to the heat sink, thereby generating a heat flux from the top of the pellet to the bottom [71, 72].

Measurements were conducted in vacuum to prevent parasitic convection and adsorption within the MOF pores. Two copper cylinders were mounted outside the cold finger as radiation shields. The temperature of the sample holder was controlled by a Lakeshore 340 temperature controller. Six thermocouples (TC1–TC6) were inserted into small-bore holes in the top (TC1, TC2) and bottom (TC5, TC6) steel plates and affixed to the top and bottom of the sample (TC3, TC4) [see Appendices A, section e]. These probes were used to determine the heat fluxes through the steel contacts (TC5, TC6, TC1, and TC2) and the temperature drop across the sample (TC3, TC4) upon heating, from which the sample's thermal conductivity was derived. The sample’s thermal conductivity κ was determined using the 1D Fourier law:

$$\kappa = \frac{Q \cdot t_s}{A_s \left(T_3 - T_4 \right)}, (4.2)$$

where t_s and A_s are the sample thickness and cross-sectional area, and Q is the power through the sample. Q was estimated using the power A_b k_b $(T_5\text{-}T_6)/t_b$ transferred through the bottom steel plate, where k_b is the thermal conductivity of the steel contact and t_b is the distance between TC5 and TC6. T_3, T_4, T_5, T_6 are the temperatures measured using the thermocouples TC3, TC4, TC5 and TC6, respectively. A_b and t_b are the thickness and cross-sectional area of the bottom steel contact, respectively. Three major sources of error are associated with Q: uncertainty due to parasitic black-body radiation losses from the sample, uncertainty due to parasitic conduction losses through the thermocouples, and uncertainty in t_b due to the nonzero thermocouple diameter. Uncertainty in t_s due to surface roughness, uncertainties in temperature and voltage measurements, and the interfacial temperature drops at each end of the sample also contribute to the error. Accounting for the above sources of uncertainty, we estimate the maximum error in the thermal conductivity to be 18%. Since the same bottom steel contact was used for all measurements (fixing t_b), the relative uncertainty in thermal conductivity for the two samples is less than 9%.

4.3 Results and Discussion

4.3.1 Pellets with Homogeneous ENG Distribution

4.3.1.1 Microstructure

Figure 4.3a shows an optical microscopy image for a representative MOF-5 particle after milling with 5 wt.% ENG. Here the MOF-5 appears as a large white particle, and the ENG as black, rod-shaped particles adhered to the MOF surface. As the initial particle size of ENG is typically much larger than that of MOF-5, yet the particles depicted in Figure 4.3 suggest that ENG is smaller, we infer that some fracture of the ENG worms occurs during milling. An SEM image of the interface between an ENG particle and a MOF-5 particle in a MOF-5/ENG pellet is shown in Figure 4.3b. The compacted MOF-5 powder retains its cubic morphology with crystallite diameters less than 1 μm. The interface contains regions exhibiting good contact between the MOF and ENG, interspersed between gaps or pores. The ENG particle itself retains a layered or parallel sheet structure as previously identified [194]. The preservation of the ENG's lamellar graphite structure suggests that the high thermal conductivity of the original

ENG is maintained within the ENG particles.

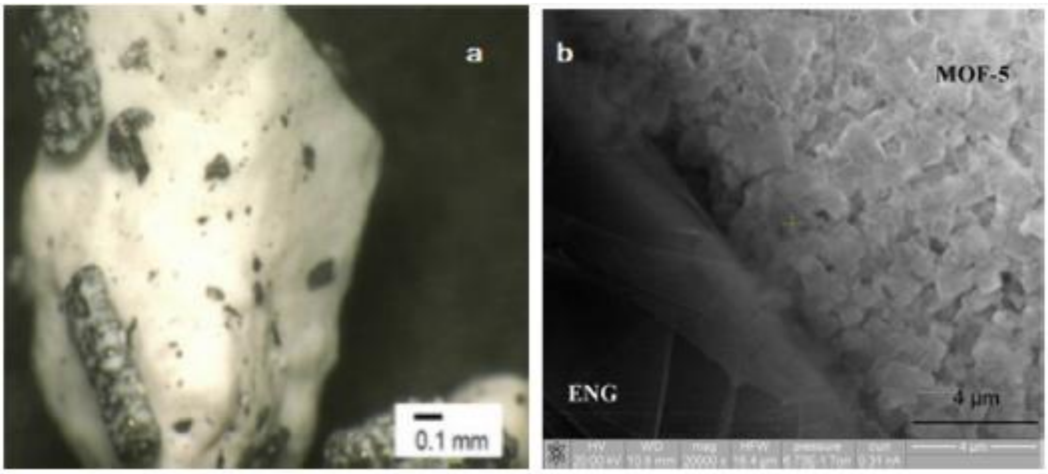

Figure 4.3. (a) Optical microscopy image of MOF-5 particles (white) coated with ENG (black) after milling. (b) SEM of the interface between MOF-5 and ENG within a densified pellet containing 5 wt.% ENG and with a pellet density = 0.50 g/cm^3.

The distribution of ENG within the MOF-5/ENG pellets was quantified by analyzing optical micrographs of pellet cross sections. Inspection of the cross-sectioned pellets revealed the presence of dark lines connecting ENG deposits. At higher magnifications these lines were shown to contain ENG particles, which appear to collect in the spaces between the MOF-5 conglomerates during compression Figure 4.4a, b. Pellets comprised of neat MOF-5 did not show features similar to those of Figure 4.4.

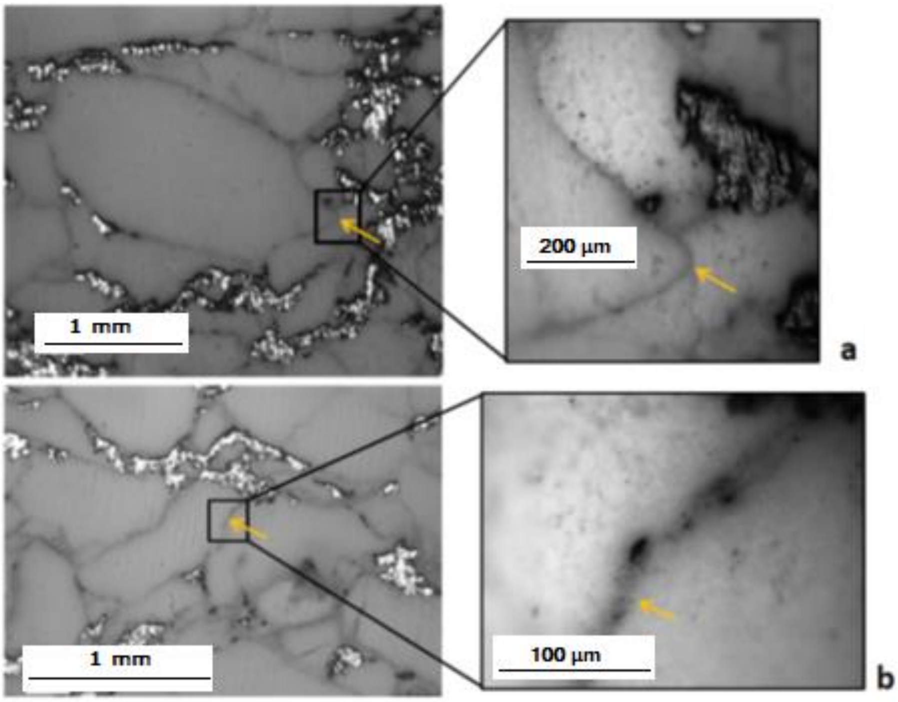

Figure 4.4. Cross sections of MOF-5 pellets containing 5 wt.% ENG and with density of 0.38 g/cc imaged using optical microscopy. The images depict boundary lines consisting of ENG deposits at (a) magnifications of x50 and x200 as well as at (b) x50 and x400.

Figure 4.5 shows micrographs of cross sections for three pellets formed using different pressing directions and amounts of ENG. The pressing direction in Figure 4.5a and b is along the axial direction of the pellet, while the pellet in Figure 4.5c was pressed radially. The images at the top of Figure 4.5 are of cross-sections obtained from cutting the pellet along the rectangular plain shown in the lower sketch. Arrows overlaid on the microscopy images indicate the compression direction.

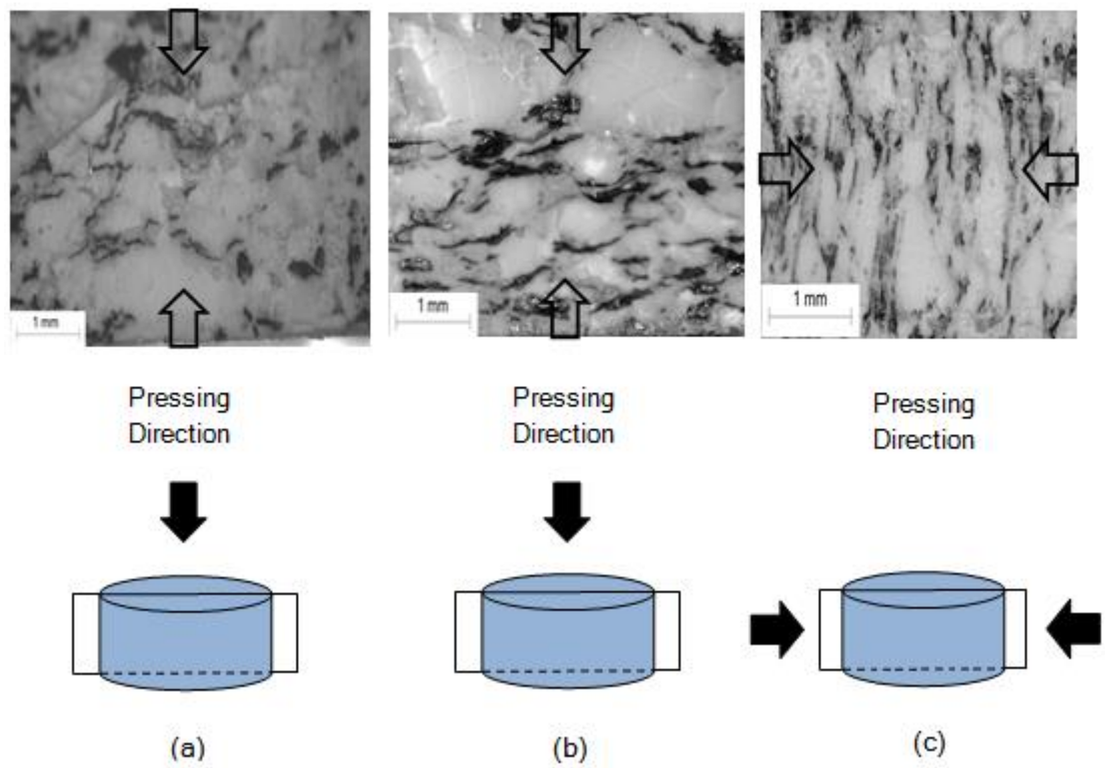

Figure 4.5. Cross section of a MOF-5/ENG pellet from optical microscopy. Arrows indicate the pressing direction. The sketch below each image shows the relationship of the cross-section plane to the pressing direction. (a) MOF-5 mixed with 5% ENG, pressed axially; (b) MOF-5 mixed with 10% ENG, pressed axially; and (c) MOF-5 mixed with 5% ENG, pressed radially.

The relationship between ENG orientation and the pressing direction was calculated using ImageJ image processing software. Table 4.1. Average orientation and standard deviation of ENG particles in MOF-5/ENG composites with respect to the pressing direction for the three pellets described in Fig. 5: (a) MOF-5 mixed with 5 wt.% ENG, pressed axially; (b) MOF-5 mixed with 10 wt.% ENG, pressed axially; and (c) MOF-5 mixed with 5 wt.% ENG, pressed radially. The solid black segment represents the average orientation of ENG in the pellet. Black arrows and the dashed line represent the pressing direction. The standard deviation refers to the distribution of ENG orientations observed in cross-sectioned pellets. Table 4.1shows the average angle of ENG particles with respect to the compression direction. The average angle of the ENG in all three cases depicted in Figure 4.5 is approximately 70 degrees, confirming that the ENG within the pellets has a tendency to align perpendicular to the pressing direction. Such behavior should encourage the formation of a percolating network in directions perpendicular to the pressing direction, resulting in higher thermal conductivity in the same directions (as described below). A similar relationship between the orientation of the ENG particles and pressing direction was observed across all of the pellets examined (14 in total, data not shown).

As shown in Figure 4.3, ENG particles tend to adhere to the surface of MOF-5 particles. Upon densification into pellets this surface adhesion results in the ENG populating the boundaries between MOF-5 particles. Consequently, the color differences between MOF-5 (white) and ENG (black), combined with this “interface decoration” effect, can be used to demark the boundaries between MOF-5 particles. As shown in Figure 4.5 (top) the boundaries also display an anisotropic texture as a result of uni-axial compression.

Table 4.1. Average orientation and standard deviation of ENG particles in MOF-5/ENG composites with respect to the pressing direction for the three pellets described in Fig. 5: (a) MOF-5 mixed with 5 wt.% ENG, pressed axially; (b) MOF-5 mixed with 10 wt.% ENG, pressed axially; and (c) MOF-5 mixed with 5 wt.% ENG, pressed radially. The solid black segment represents the average orientation of ENG in the pellet. Black arrows and the dashed line represent the pressing direction. The standard deviation refers to the distribution of ENG orientations observed in cross-sectioned pellets.

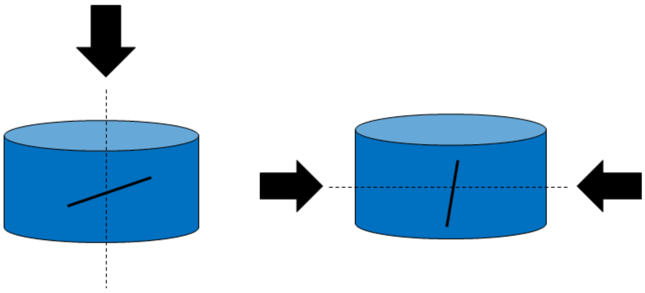

(a), (b) (c)

	Sample # from Figure 4.5		
	(a)	(b)	(c)
Average angle of ENG with respect to pressing direction	66.3^0	69.9^0	70.8^0
Standard deviation	18.6^0	17.7^0	18.8^0

4.3.1.2 Thermal conductivity

To assess the possibility for anisotropic transport, thermal conductivity measurements were performed on pellets synthesized using different compression directions, as previously described. Figure 4.6 shows near-ambient temperature thermal conductivity data for MOF-5/ENG pellets having different mass fractions of ENG and orientations of the pressing direction with respect to the direction of heat flow. The error bars in Figure 4.6 refer to the range of measured values, and not to the standard deviation. This range may be traced to variations in sample preparation (e.g., related to the distribution of ENG within a given pellet). The data show that the thermal conductivity of the pellet increases in proportion to the ENG weight percent, consistent with our prior findings [133]. For example, at 30 ℃ the thermal conductivities of pellets containing 0%, 5% and 10% ENG are 0.08, 0.38, and 0.99 W/m·K, respectively, for pellets in which the ENG is aligned parallel to the heat flow direction. A similar trend holds for the other ENG orientation and at other temperatures. As expected, the highest conductivity (0.99 W/m·K) is found for pellets containing the highest concentration of ENG (10 wt.%), in which the ENG is oriented parallel to the heat flow direction. Conversely, neat MOF-5 pellets have the lowest overall conductivity of less than 0.10 W/m·K, and this conductivity is largely independent of the compression direction.

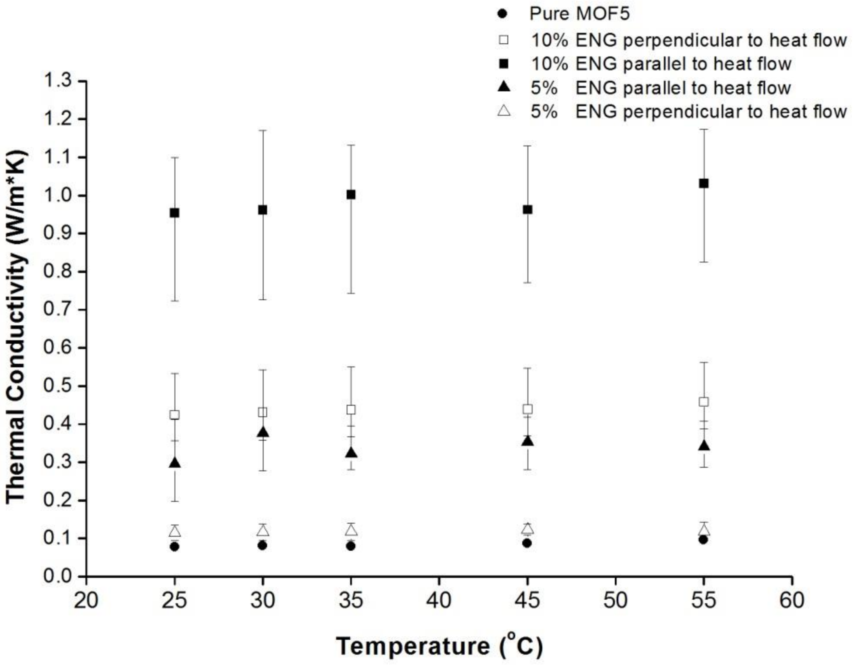

Figure 4.6. Near-ambient temperature thermal conductivity for MOF-5/ENG pellets (0.4g/cm^3) as a function of temperature, ENG content, and pressing direction. Error bars correspond to the range of measured values.

Figure 4.6 also illustrates that pellets having the same ENG composition, but different ENG orientations, exhibit differing thermal conductivities. Pellets with ENG orientations parallel to the heat flow (filled symbols) exhibit conductivities that are 2 to 4 times higher than in pellets where the orientation is perpendicular (open symbols). For the ENG concentrations considered here, this anisotropy appears to be independent of the amount of ENG added. Our observation of anisotropic transport in MOF-5/ENG composites is consistent with previous reports involving pellets synthesized from pure ENG [184]. In that case, thermal conductivities of 1.40 and 3.13 W/m·K were measured in the axial and radial directions, respectively, consistent with the alignment of vermicular graphite perpendicular to the pressing direction.

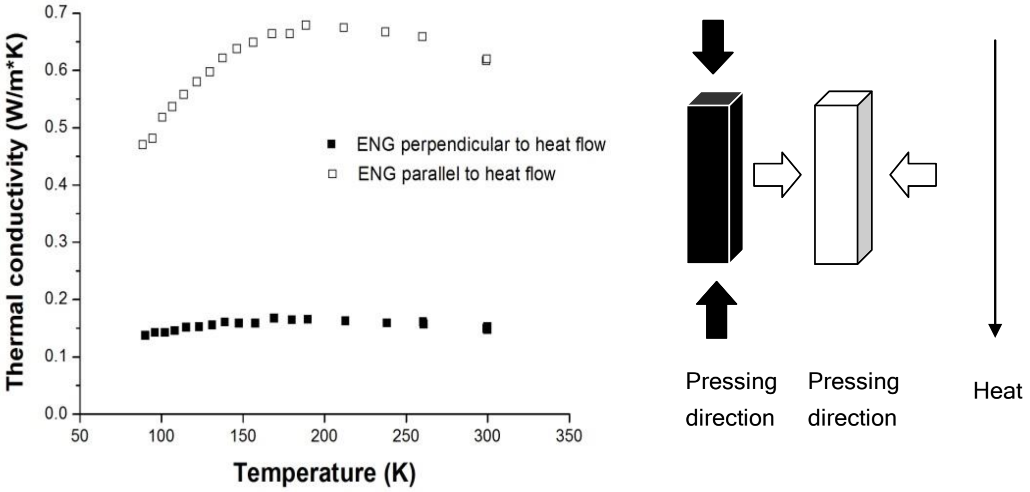

Figure 4.7. Thermal conductivity of 0.35 g/cm^3 pellets containing 5% ENG formed using two orthogonal pressing directions over the temperature range of 80 - 300K.

Figure 4.7 shows the thermal conductivity measured from cryogenic to room temperature (80 K to 300 K). The increasing thermal conductivity at low temperatures (80 - 200 K) arises from phonon excitations, while the moderate decrease above 200K is due to a reduction in the average phonon mean free path. The sample having ENG aligned parallel to the heat flow direction (white sample) exhibits the highest value of thermal conductivity 0.68 W/m·K. A much lower maximum conductivity is observed 0.17 W/m·K in the case of perpendicular ENG alignment. This factor of four improvement in thermal conductivity is consistent with the range we observed for room temperature measurements. These data further signify the presence of significant transport anisotropies arising from ENG orientation and/or MOF-5 boundary effects caused by anisotropic compression.

The differences in room temperature thermal conductivities obtained with the transient and steady-state heat flow method (SSHFM) (0.38 W/m·K for the transient method vs. 0.62 W/m·K for SSHFM) can be explained by the different sample fabrication and measurement techniques. For example, in the stead-steady state method Black-body radiation losses are expected to have a larger impact at elevated temperatures, leading to some loss in accuracy. These losses are described by the Stefan–Boltzmann law,

$$j = \sigma T^4, \qquad (4.3)$$

where j is the total power radiated per unit area, T is the absolute temperature and σ = 5.67×10^{-8} $\mathrm{Wm^{-2}K^{-4}}$ is the Stefan–Boltzmann constant. Equation (4.3) indicates that radiation at 300 K is 198 times larger than that at 80 K. Therefore the assumption that heat transfer occurs solely via conduction [Eq. (4.2)] becomes less valid as temperature increases. To minimize the radiation loss across the sample, the length of the sample in Figure 4.2c was reduced (by cutting) in order to decrease the heat path length between the two steel contacts. However, the cutting process increases the surface roughness of the pellet, thus introducing uncertainty in t_s in eq. (4.2). The Stycast epoxy accumulated in the hollow part of the sample will also contribute to the error of the calculated thermal conductivity. On the other hand, the transient method employs a sample with a very flat surface, as well as Clark and Taylor corrections for radiative losses near room temperature [195], leading us to conclude that the latter method is more reliable at higher temperatures.

4.3.2 Pellets with Layered ENG Distribution

4.3.2.1 Microstructure

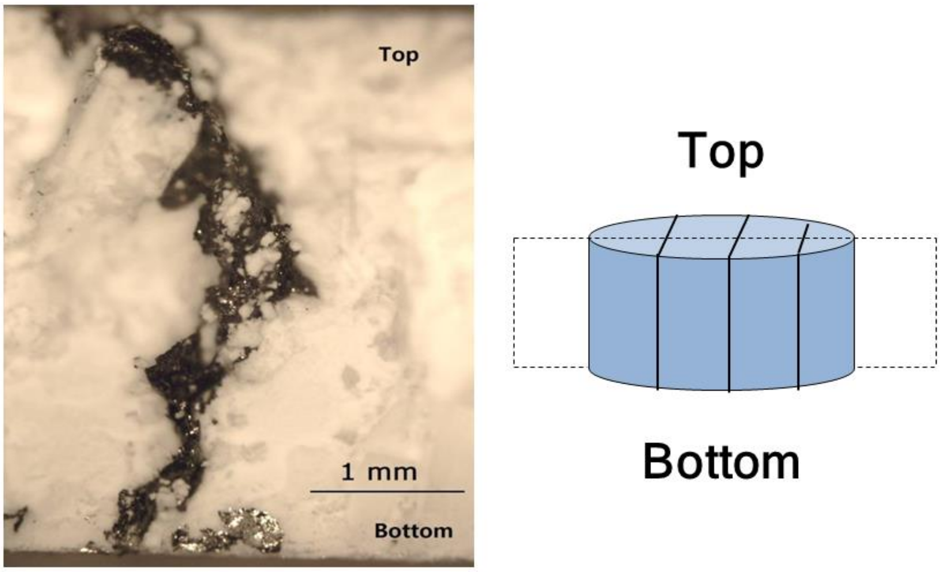

Figure 4.8. (Left) Optical microscopy image of a cross-section of a MOF-5 pellet containing ~5 wt.% ENG in a layered distribution. The graph shows the cross section of pellet after being cut perpendicular to the ENG layers; the top and bottom surfaces of pellet are labeled. MOF-5 layers are white, while the ENG layers are black. (Right) Schematics showing the orientation of the ENG layers. The dashed rectangle shows the cross-sectional plane.

We also explored direct manipulation of the ENG distribution as a means to improve the thermal conductivity in a specified direction. In this case we fabricated

MOF-5/ENG composite pellets having a microstructure consisting of alternating layers of MOF-5 and ENG. This approach serves as an alternative to the previous approach of tuning the ENG particle orientations via altering the pressing direction. Figure 4.8 illustrates the alternating regions of pure MOF-5 (white) and ENG (black) within such a pellet. The pellet contains approximately 5 wt.% ENG distributed amongst 3 separate layers. (The field of view in Figure 4.8 contains only one ENG layer.) Each ENG layer traverses the entire thickness of the pellets, connecting the top and bottom surfaces, potentially resulting in a “shorted” heat conduction pathway in the axial direction.

4.3.2.2 Thermal conductivity

The thermal conductivity of the layered pellet was measured at near-ambient temperatures using the transient method, as shown in Figure 4.9 (filled rectangles). The measured value at 35 ℃ is 4.35 W/m·K. In comparison, Figure 4.9 also presents the data taken from comparable pellets (filled triangles in Figure 4.6) containing 5 wt.% ENG aligned parallel to the (axial) heat flow direction. In the latter case (corresponding to homogeneously distributed ENG), the thermal conductivity was 0.30 W/m·K at 35 ℃. Therefore, the layered pellet exhibits more than an order of magnitude (~20x) increase in thermal conductivity compared to a pellet having a homogeneous ENG distribution. As previously mentioned, this impressive jump in thermal conductivity can be attributed to the layered microstructure of the pellet. This microstructure provides a very efficient, high thermal conductivity pathway, and does so without requiring an increase in the mass fraction of ENG.

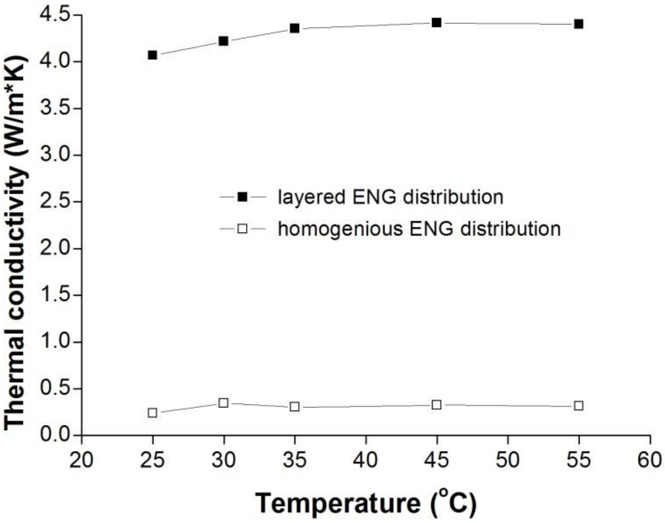

Figure 4.9. Thermal conductivity of pellets with two different ENG distributions (layered and homogeneous) at near-ambient temperatures. Both pellets contain approximately 5 wt. % ENG. Layered pellets contain ENG layers which are parallel to the heat flow direction. Data for the homogeneous pellets are reproduced from Figure 4.5, and refer to the samples identified as “5% ENG parallel to heat flow.”

4.4 Conclusion

Metal organic frameworks exhibit several properties that make them promising candidates for applications in gas capture, gas storage, and catalysis. Nevertheless, the high porosity of MOFs, and their resulting low intrinsic thermal conductivity, can potentially offset these advantages in cases where efficient heat transport is required. In this chapter we establish that the high-aspect ratio morphology of second-phase ENG additions, combined with uni-axial compression, results in anisotropic microstructural and thermal transport properties in composite MOF-5/ENG particles. The presence of a textured microstructure having particle boundaries and ENG orientations perpendicular to the pressing direction were confirmed via microscopy of pellet cross-sections.

Thermal conductivity measurements ranging from cryogenic to ambient temperatures indicated that heat transport perpendicular to the pressing direction is 2 to 4 times higher than in the pressing direction. Furthermore, we demonstrated that this anisotropy could be exploited using two straightforward processing techniques: First, the preferred heat flow path can be reoriented by use of a custom die/compression geometry. Second, fabrication of a layered microstructure with alternating MOF-5 and ENG layers results in a 20x increase in thermal conductivity, at the expense of only minor ENG additions (5 wt.%). These data suggest that the magnitude and preferred direction for thermal transport in MOF compacts may be tuned by altering the processing conditions and nature of the second-phase additions. We speculate that these techniques could also be effective in tailoring mass transport (permeation) within MOF composites.

Chapter 5

Kinetic Stability of MOF-5 in Humid Environments: Impact of Powder Densification, Humidity Level, and Exposure Time

5.1 Introduction

From Chapter 3 we learned that the high surface area and tunable properties of MOFs make them attractive candidates for applications such as gas storage, gas separations, and catalysis [170-172]. Among the many MOF compounds, MOF-5 has received considerable attention due to its ability to store gaseous fuels such as hydrogen at low pressures with high gravimetric and volumetric densities [5-9]. In addition, the techniques discussed in Chapter 4 for enhancing the thermal transport properties of MOF-5 composites will aid in the design of efficient heat exchanging strategies for MOF-based systems.

Despite these promising features, the limited stability of some MOFs with respect to reactive species such as water remains a point of concern [196-200]. These concerns extend to MOF-5, as its degradation has been observed via x-ray diffraction and correlated with decreasing hydrogen adsorption after exposure to humid conditions [59, 147, 201-205]. For example, Schrock and co-workers observed irreversible decomposition of MOF-5 after uptake of 8 wt.% water [206]. Other studies have suggested that the stability of MOFs is related to the composition of the metal site and the structure of the metal cluster [207]. Molecular dynamics and first-principles calculations have also been used characterize the degradation process in MOF-5. These models suggest that adsorbed water interacts more strongly with (Zn) metal sites than with the carboxylate linker, and have proposed reaction mechanisms associated with MOF hydrolysis [138, 164, 208, 209]. Other models have suggested that MOF-5 is relatively stable at low water loadings, indicating that degradation only occurs when a significant concentration of water is adsorbed on the metal cluster[210]. This implies that the humidity level will impact the rate of degradation.

While stability considerations are paramount for applications such as CO2 capture from flue gas (which may contain large quantities of water) [211-215], even “clean” applications such as the storage of high-purity hydrogen for fuel-cell vehicles may present challenges for MOFs. For example, exposure to humid air during system assembly or during in-service events such as re-fueling, etc., could contaminate the MOF media, thereby reducing capacity and cycle life. In these instances it is important to know not only that degradation can occur, but to also quantify the degree of degradation and its dependence on operating conditions. This information is essential for establishing a material’s “stability window,” which indicates the conditions under which suitable performance can be maintained.

Toward this goal, the present study quantifies the impact of humid air exposure on the properties of MOF-5 as a function of exposure time, humidity level, and morphology (i.e., powders vs. pellets). Properties examined include hydrogen storage capacity, surface area, and crystallinity. Water adsorption/desorption isotherms are measured using a gravimetric technique and exhibit a large hysteresis; the first uptake cycle resembles a type V isotherm with a sudden increase in water uptake at ~50% relative humidity. For humidity levels below this threshold, only minor degradation is observed for exposure times of 2 hours for powders, and 24 hours in pellets. On the other hand, irreversible degradation can occur in a matter of minutes at higher humidity. FTIR spectroscopy suggests that molecular and/or dissociated water is inserted into the skeletal framework after long exposure times. Densification into pellets can slow the degradation of MOF-5 significantly, and may therfore present a partial "engineering solution" for the limited stability of some MOFs.

5.2 Experimental Details

5.2.1 Materials Preparation

MOF-5 powder was provided by BASF, and was synthesized using a process described previously [180]. In some cases expanded natural graphite, ENG (SGL Group), was added at moderate levels to MOF-5 as a means to improve thermal conductivity [133, 216]. All storage and handling of the materials was performed in an Ar glovebox. Pelletized versions of MOF-5 were also examined, with and without ENG additions. Composite MOF-5/ENG pellets were synthesized by adding ENG to MOF-5 to achieve pellets having a mass fraction of 5 wt.% ENG. A SPEX 8000M Mixer/Mill was filled with the MOF-5/ENG mixture and shaken in the milling machine for 20 seconds without milling balls. The powders were loaded into a cylindrical die with diameter equal to 6.35mm, and pressed to a height of 5mm; the resulting pellets had a density of approximately 0.36 g/cm^3. The pelletizing process was performed inside the glovebox. Figure 5.1 shows the MOF-5 powders and pellets used during the experiment.

Figure 5.1. MOF-5 morphologies examined. Left: powder; right: pellets.

Stability testing under humid conditions was performed at 22 ℃ using tworelative humidity (RH) levels: 45% and 61%. These conditions were maintained using a gas flow system that mixed dry air with water vapor. The flow apparatus employs a Bronkhorst W303A Liquid flow controller with a Controlled Evaporator Mixer (CEM). The flow rate for dry air was set to 20 L/minute, and the water vapor flow rate was 10.7 g/h for 45% RH, and 16.9 g/h for 61% RH. These two streams were mixed and connected to a large Erlenmeyer flask, which served as a controlled humidity chamber. Samples were transferred to the humidity chamber after first being loaded into a bottle within the glovebox. The bottle was placed inside the flask and opened. The bottle opening was positioned so as to block the impingement of the humid airflow directly onto the sample; this geometry was intended to minimize convection effects, and mimic water adsorption from a quasi-static atmosphere. A given sample was exposed for a specified time, with exposure times of 30 min., 2 h, 24 h, 48 h and 66 h for powders, and 30 min, 2 h, 24 h, 66 h for pellets. The mass of the sample used for each measurement was approximately 0.37 g. For powders, fresh samples were used for each exposure experiment; for pellets, samples underwent a cumulative exposure process in which (for example) a pellet exposed for 2 h was removed from the humidity chamber, characterized, and then returned to the chamber for another 22 h, to achieve a total exposure of 24 h.

5.2.2 Characterization

The surface area of MOF-5 powders was measured at 77 K using nitrogen sorption on a Micromeritics ASAP 2420. A minimum of 0.5 grams of sample was used during each test. Prior to measurement, the sample was evacuated for 8 hours at 200°C. Twenty-five sample points were taken; the surface area was calculated using the Brunauer–Emmet–Teller (BET) equation [127] according to DIN 66131 (“Determination of specific surface area of solids by means of gas adsorption using the method of BET”) using data points within the range $0.05 < p/p_0 < 0.2$.

The impact of exposure to humid conditions on hydrogen uptake was assessed using a

Sieverts' apparatus (PCT-Pro 2000, Setaram). As a first step, samples were activated to remove any weakly-bound (i.e., physisorbed) water in the material: samples were evacuated at room temperature for at least 6 hours, then evacuated and heated to 130°C over night. Less aggressive activation conditions (evacuation for 4 h at 85°C) proved sufficient for samples exposed to the lower humidity condition (45% RH) for brief intervals (e.g., 30 minutes). These activation conditions represent what could be possible for "in service" activation of a commercial MOF-based system after accidental exposure or brief (intentional) exposure during system manufacture or assembly.

Water adsorption isotherms were measured using a gravimetric technique (VTI-SA+ Vapor Sorption Analyzer). Samples were first dried by heating for 6 hours at 120°C. Isotherms were taken at 25°C using relative humidity increments/decrements equal to 10%, with a range spanning from 5% to 85%. Equilibrium was assumed to be established when the change in sample mass was less than 0.01% in a 2 minute interval. A cycle consisted of a single adsorption followed by desorption. Three cycles were completed, and the activation process was applied before each cycle.

X-ray diffraction (XRD, Rigaku Miniflex II diffractometer using Cu Kα radiation (λ = 1.5418 Å)) was used to assess changes in crystallinity resulting from exposure to humid air. Samples were transferred to the diffractometer in sealed vials. Each vial was opened, and the MOF-5 powder was chopped and pressed onto an off axis silicon crystal sample substrate. The time between opening the vial and the beginning of the scan was less than 30 seconds. Diffraction data was collected over a range of 5-40^{o} 2θ at a scan rate of

5^o/min, resulting in a total experiment time of 7 minutes. The sample was then immediately scanned a second time in order to observe the degree of structural change that had occurred during the initial scan. No change was observed in any of the samples.

Fourier transform infrared spectrometry (FTIR) was used to assess changes in bonding resulting from exposure to humidity. Measurements were made using a Thermo Scientific Nicolet FTIR spectrometer. Samples were scanned from 4000 to 600 cm^{-1} with a resolution of 0.24 cm^{-1}. Averaging was performed over 128 scans; the time to conduct all scans was 5 minutes. Powder samples were loaded and scanned in air. Since the scan time was short compared to the exposure time in the humidity chamber, we expect that any changes to FTIR peaks primarily reflect effects from humidity exposure before the scan.

5.3 Results and Discussion

5.3.1 MOF-5 powder

We first discuss the stability of powder-based samples. Hydrogen uptake isotherms for samples exposed to humidity (RH = 45% and 61% at 22°C) for various exposure times are shown in Figure 5.2. The x-axis specifies the equilibrium hydrogen pressure, and y-axis is the excess adsorbed hydrogen in weight percent (wt. %): $[m(H_2)/m(\text{MOF-5})] \times 100$. Experimental data (symbols) are fit (lines) using the Unilan isotherm model [217].

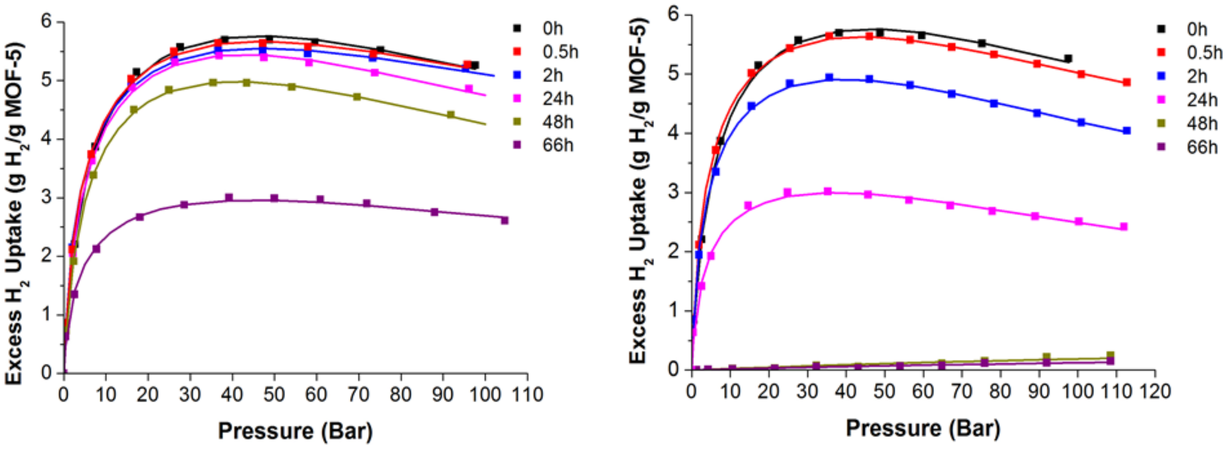

(a) Relative humidity = 45%   (b) Relative humidity = 61%

Figure 5.2. Excess gravimetric hydrogen uptake in MOF-5 powders as a function of relative humidity and exposure time. Top: relative humidity = 45%, T = 22°C; Bottom: relative humidity = 61%, T = 22°C. Isotherms are plotted before exposure to humid air (0 h), and after 5 increasingly longer exposure times: 0.5 h, 1.5 h, 24 h, 48 h and 66 h. Solid symbols represent experimental data; these data are fit using the Unilan isotherm model (solid lines).

Figure 5.2(a) shows data for the lower humidity level, RH = 45%. For samples exposed for the two shortest time periods, 0.5 h and 2 h, the decrease in maximum hydrogen uptake is less than 3% compared to the baseline (unexposed) material. This indicates that the MOF-5 powders do not undergo “sudden death” when exposed to moderately humid conditions for short times. For a 24-hour exposure, the peak in the adsorption isotherm also decreases by only slightly (~5%), from 5.7 to 5.4 wt.%. However, more significant changes are observed for longer exposures; for example, uptake drops to half of that for the pristine material after 66 hours exposure. In contrast, at the higher RH value (61%), Fig. 3(b), significant decreases in hydrogen storage capacity appear after 2 hours of exposure. After 24 h uptake decreases by approximately 50%, which is an order of magnitude larger than the losses seen at RH = 45%. After 48 hours the powder has lost essentially all of its gas storage capability (uptake below 0.5 wt. %).

Figure 5.2 shows that exposure to humid environments for periods longer than approximately ~2 h negatively impacts the adsorption of H_2 in MOF-5 powders. Two possible explanations for this behavior are: (*i.*) water molecules preferentially adsorb in MOF-5, and thereby block sites for H_2 uptake, or (*ii.*) water molecules react irreversibly with MOF-5, for example, by decomposing/insertion into its crystal structure[147, 209]. The first scenario is unlikely given that each sample exposed to humid conditions is evacuated and heated over night to remove any adsorbed water before hydrogen isotherm measurements are performed. Therefore, we hypothesize that the most likely explanation for the observed decrease in H_2 uptake is an irreversible structure change wherein MOF-5 transforms into a new composition/structure that is less amenable to gas storage, presumably due to loss of porosity, surface area, *etc.*

To test this hypothesis, the BET surface areas of MOF-5 powders with different exposure times to the two relative humidity levels were measured, as shown in figure 5.2. In general, the changes to surface area *vs.* exposure time & RH follow closely the trends seen for hydrogen uptake in fig. 5.2. Prior to exposure, the measured surface area was 2355 m^2/g. For the RH = 45% samples, relatively small changes in SA are observed for exposure times up to 48 h. At 66 hours the surface area then drops more precipitously to a value which is half (1217 m^2/g) its initial maximum, which is again consistent with the changes observed to the isotherms in fig. 5.2(a). [It is also evident that the pellets (discussed in more detail below) exhibit enhanced robustness to humidity; the pellets maintain higher BET surface areas compared to those of powders for the same exposure conditions. The surface area of the unexposed pellets (corresponding to t = 0 in fig. 5.3) is slightly above that of the unexposed powders due that media being sourced from a different batch of MOF-5 material.] In contrast, for the RH = 61% samples the BET surface area decreases more rapidly, achieving a value of nearly zero (34 m^2/g) after 66 hours. The declining surface area for both RH values indicates that the porosity of the MOF-5 powders is continuously reduced upon exposure to humid conditions.

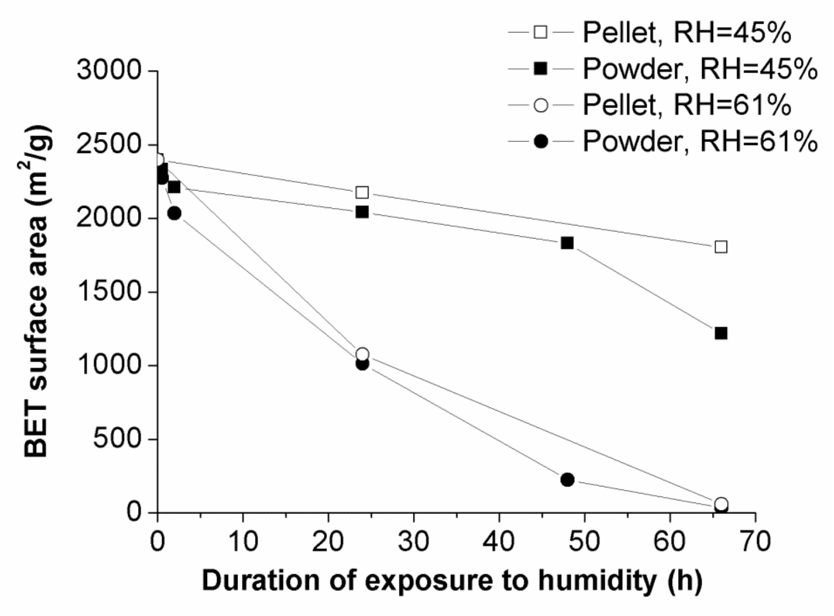

Figure 5.3. BET surface area of MOF-5 powders (filled data points) and pellets (open symbols) as a function of exposure time to humid air with relative humidities (RH) of 45% (square symbols) and 61% (circular symbols). T = 22°C in all cases. Data points at t = 0 correspond to samples which were not exposed to humidity.

X-ray diffraction (XRD) was used to assess changes to the crystallinity of MOF-5 associated with exposure to humidity. Figure 5.4 shows diffraction patterns for MOF-5 powders as a function of exposure time for the RH = 45% and RH = 61% cases. For RH

= 45%, Fig. 5.4(a), during exposures up to 48 hours the only change in the XRD pattern (relative to the unexposed material) is a very small shift of some peaks to smaller 2-theta values, indicating a slight expansion of the crystal[209]. After 66 hours, a new peak appears at $2\theta=9^0$, consistent with the formation of a new phase. The position of the new peak is in agreement with prior studies [147], and resembles the pattern for ZnBDC•xH_2O. (We note that the full crystal structure of the emergent phase has not been completely determined [218].) In contrast, for the RH = 61% case the same peak appears much sooner, after only 24 hours of exposure, fig. 5.4(b). Additional changes to the diffraction pattern are evident at longer exposure times. Comparing the XRD patterns for both RH conditions it is clear that the extent of the change in crystallinity/structure with respect to exposure time closely follows the trends observed in both the H_2 uptake isotherms and the surface area.

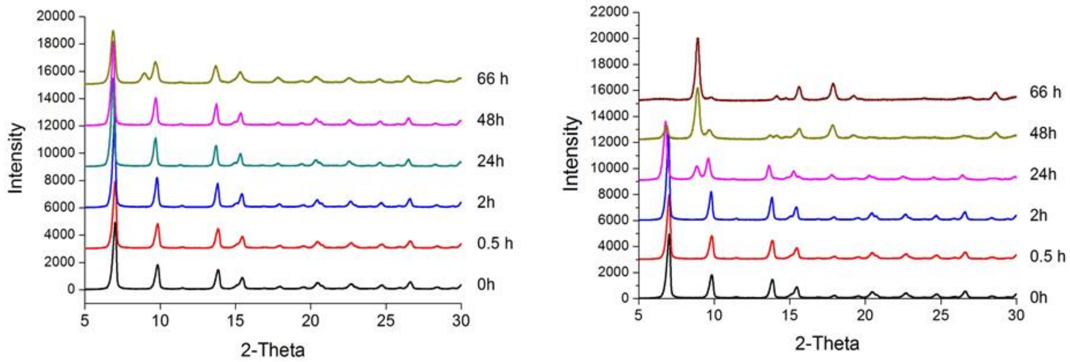

(a) Relative humidity = 45%

(b) Relative humidity = 61%

Figure 5.4. XRD spectra for MOF-5 powders as a function of exposure time to humid air with relative humidities of 45% (top) and 61% (bottom). In both cases T = 22°C.

To quantify the amount of water vapor adsorbed by MOF-5, water adsorption and desorption isotherms were measured at 25˚C using a gravimetric apparatus, Figure 6.

Here the x-axis represents RH, and the y-axis represents the weight percent ([m(water)/m(MOF-5)] x 100) of adsorbed water. Three adsorption/desorption cycles were performed using the same powder sample. During the first uptake cycle less than 1 wt.% of water is adsorbed for RH up to 45%. The water uptake then jumps dramatically to more than 12 wt.% at RH values between 45 – 55 %. For higher RH the uptake saturates at capacities of 12-14 wt.%. This adsorption behavior is consistent with a type V isotherm, which is expected for systems exhibiting relatively strong adsorbate-adsorbate interactions in comparison to (weaker) adsorbate-adsorbent interactions.

The sudden increase in water uptake in MOF-5 evident in the isotherm over the relatively narrow region of RH spanning 45 – 55% explains the dramatic differences in H_2 uptake, surface area, *etc*. observed for the two humidity levels (RH = 45 and 61%) in the exposure experiments. These two levels fall, respectively, just below and just above the transition region in Fig. 6, indicating that these measurements can be rationalized by the sudden increase in the adsorbed water content of the MOF as RH increases from 45 to 61%.

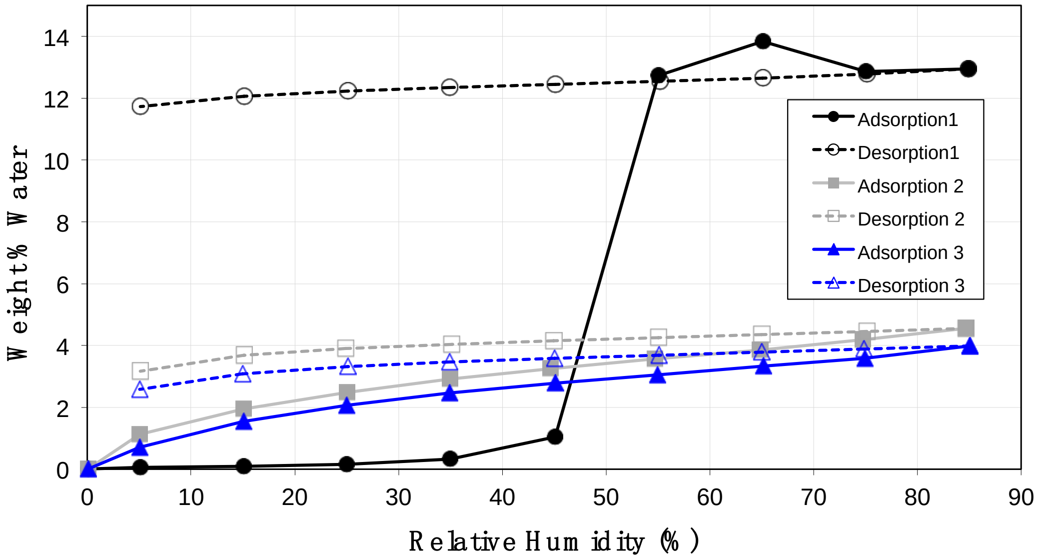

Figure 5.5. Water adsorption in MOF-5 powder at 25°C vs. relative humidity for three adsorption/desorption cycles.

Figure 5.5 also shows that the isotherm for the first adsorption-desorption cycle exhibits a large hysteresis; this is because the amount of adsorbed water decreases only slightly during the desorption cycle, ~1 wt.%, suggesting a strong chemisorption-like binding of H_2O to the MOF-5 framework. In the subsequent 2nd and 3rd cycles relatively little water adsorption occurs; the sample has lost approximately 2/3 of its water uptake ability. As previously described, these latter cycles were performed following separate sample activation steps. Therefore, the low uptake observed for these cycles likely reflects the failure of the activation procedure to remove strongly bound H_2O from the first uptake cycle, in concert with a structure change as suggested by XRD.

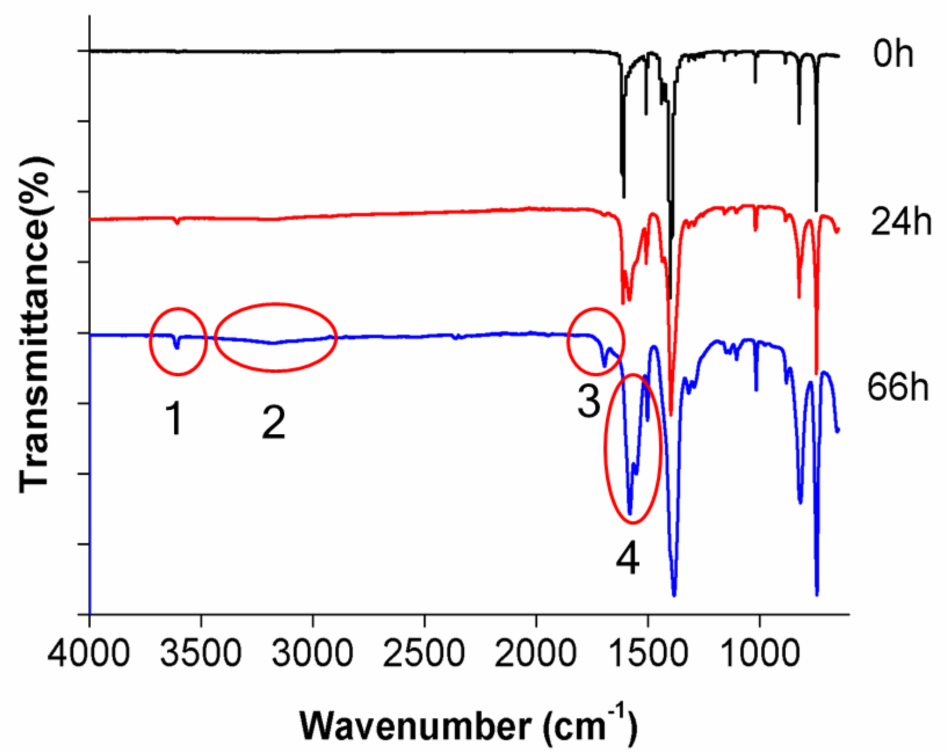

Figure 5.6. FTIR spectra for MOF-5 powders exposed to air with RH = 61% for 0 h, 24 h, and 66 h at 22 ℃.

FTIR spectroscopy was used to examine changes to bonding in MOF-5 resulting from humidity exposure. Figure 5.6 shows the FTIR spectrum for MOF-5 powders exposed to air with RH = 61% for 0, 24, and 66 h at 22 ℃. Prior to FTIR analysis, all samples underwent overnight activation (evacuation and heating at 130°C) to remove physisorbed water. Therefore, changes to the FTIR spectrum resulting from exposure should be attributable to irreversible insertion and/or chemisorption of water within the MOF-5 crystal structure. Four new/shifted peaks emerge in the spectrum upon exposure for 66 h, and are labeled with numbers 1 through 4. These peaks suggest a pathway for the reaction of water with MOF-5, and can be assigned to specific bonds illustrated in Figure 5.7. At low water loadings, water molecules are expected to be physically adsorbed near the Zn cluster, Figure 5.7(b) [210]. Irreversible insertion of water into the framework is expected to occur at higher loadings, and is consistent with the emergence of peaks 1 and 2, in which molecular water bonds to Zn, displacing oxygen from the linker, Figure 5.7(c). More specifically, peak 1 at 3600 cm^{-1} can be assigned to O-H stretching in a water molecule that is adsorbed at a Zn site. Similarly, the broad peak from 3400 to 3000 cm^{-1} (labeled ‘2’) can be traced to an O-H stretch, but in which the hydrogen also participates in a H-bond, presumably with the displaced oxygen attached to the linker. The peak at position 3 arises from C=O stretching in a carbonyl group, while peak 4 is also due to C=O stretching, but where the oxygen additionally participates in a hydrogen bond, presumably with a hydrogen from molecular water.

Figure 5.7(d)-(e) depict additional reactions that involve the dissociation of water, and which based on the FTIR spectrum, we speculate may co-exist. As an initial step, hydrogen from dissociated H_2O bonds with oxygen from the BDC linker to form carboxylic acid, while the remaining hydroxyl group bonds with Zn, Figure 5.7(d). In addition, if several carboxylic acids are formed, then two of these groups from separate linkers may join to form a dimer structure, Figure 5.7(e); this structure would provide another source for peak 4, Figure 5.6. In this case the two participating BDC linker fragments are totally disconnected from their respective metal clusters due to water insertion reactions.

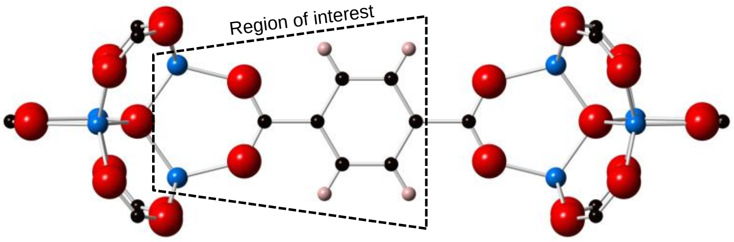

(a) Portion of MOF-5 crystal structure

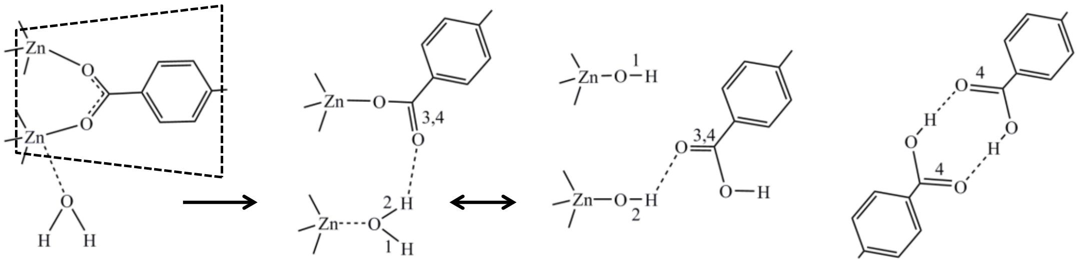

(b) Physisorbed water (c) Water insertion (d) Water dissociation (e) Dimer structure

Figure 5.7. (a) Magnification of a portion of the MOF-5 crystal structure. Red represents O, blue: Zn, black: C, pink, H. The trapezoid represents the region of interest for water interactions with MOF-5, as shown in the lower four panels. (b) Physisorption of water near the Zn cluster. (c) Insertion of molecular water into the MOF-5 framework via bonding to Zn and displacement of the BDC linker. (d) Water insertion and dissociation, resulting in a hydroxyl group bonding to Zn and carboxylic acid at the terminus of the linker. (e) An example of a carboxylic acid dimer that may contribute to peak 4 in the FTIR spectra. Numbers 1 – 4 refer to bonds associated with peaks in the FTIR spectrum in Figure 5.6.

The previous discussion suggests that MOF-5 is unstable in the presence of water. This is to be expected based on earlier studies which involved exposure to liquid water or more extreme humidity conditions [59, 147]. However, for the moderate humidity levels examined here, powders exposed for periods ranging from ~30 minutes to 2 hours do not experience a significant degradation in surface area or H_2 storage capacity. This suggests that kinetics play a role in the degradation process. We next examine how the morphology of the material – i.e., powders *vs.* pellets – impacts the rate of MOF-5 degradation in humid environments.

5.3.2 MOF-5 Pellets

Our prior studies have found that controlled densification can significantly improve the effective volumetric density of gases stored in MOFs, with only minor losses to excess gravimetric density [124, 177]. From the standpoint of packaging and system assembly, the use of densified morphologies such as pellets or pucks would also present advantages compared to the use of powders. In addition, a densified structure may present fewer or less facile pathways for the infiltration of water vapor into the MOF, potentially reducing the degradation observed for powders. In this section we characterize the stability of MOF-5 pellets with respect to humidity, and compare their performance to that of powders.

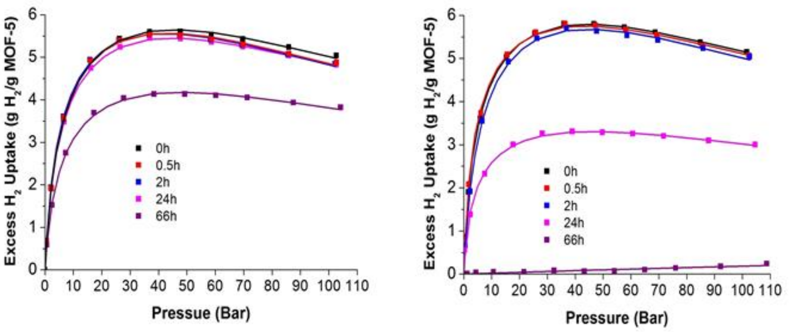

(a) Neat MOF-5, RH=45%

(b) Neat MOF-5, RH=61%

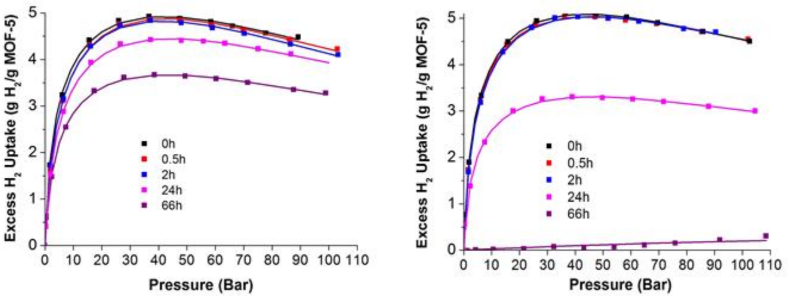

(c) MOF-5/5% ENG, RH=45%

(d) MOF-5/5% ENG, RH=61%

Figure 5.8. Excess gravimetric H_2 adsorption amount for MOF-5 pellets (density ~0.37 g/cm^3) exposed to a humid environment for 0.5h, 2h, 24h and 66h, respectively. (a) Pure MOF-5 pellet, RH=45%; (b) Pure MOF-5 pellet, RH=61%; (c) MOF-5/5%ENG pellet, RH=45%; (d) MOF-5/5%ENG pellet, RH=61%. Symbols represent experimental data, lines are fits to the data using the Unilan isotherm model.

Figure 5.8(a)-(b) shows the excess gravimetric H_2 adsorption in MOF-5 pellets (density~0.36 g/cm^3) following exposure to the same two humidity conditions used previously for powders (RH = 45% and 61% at 22°C). Exposure times were 0.5 h, 2 h, 24 h and 66 h. Similar to the powder results, increasing the relative humidity from 45 to 61% has a large effect on the MOF's hydrogen capacity. For example, H_2 uptake in pellets is not significantly reduced after 24 h exposure to RH=45%, Figure 5.8(a). However, after an identical exposure time at RH=61%, H_2 capacity drops by ~50% relative to uptake in the unexposed system, Figure 5.8 (b). Because gravimetric uptake is related to geometric properties of MOFs such as specific surface area and micropore volume [219], a loss in hydrogen capacity can also presumably be related to a comparable loss in these quantities, as previously discussed.

Another observation relates to the “kinetic stability” of the densified MOF. Here kinetic stability refers to the rate of degradation/decomposition of the MOF at a given RH, temperature, and exposure time. We first recall that in powders, Figure 5.2(a), the exposure time at which a significant decrease in excess hydrogen uptake was observed at RH = 45% was 2 h. In contrast, for pellets a much longer exposure time of ~24 hours is required to achieve a comparable loss in H_2 capacity. Similar trends hold for longer exposure times: powders exposed to RH = 45% for 66 hours exhibit a H_2 capacity of 3 wt.%, whereas for pellets the uptake is significantly higher, 4.1 wt.%, Figure 5.8 (a). This behavior also carries over to samples exposed to the higher humidity RH = 61% environment: after 2 h exposure, powder MOF-5 has an H_2 capacity of 4.9 wt.%, while for pellets the capacity is essentially unchanged from that of the unexposed material, 5.6 wt.%, as shown in Figure 5.2 (b) and Figure 5.8 (b), respectively

We speculate that the improved resistance of the pellets to water-induced degradation results from reduced water permeation into the pellets. Permeation is proportional to both the concentration and the diffusivity of water, and in principle the higher density of the pellets may impact both of these quantities. Nevertheless, given a high enough RH combined with a long exposure time, pellets will ultimately degrade to the point where all of their gas storage capacity is lost. The behavior is shown in Figure

5.8 (b), where a pellet exposed for 66 h to RH = 61% loses essentially all of its adsorption ability. This data indicates that densification can slow – but not stop – the degradation of MOF-5 upon exposure humid environments.

As a final comparison we briefly consider the impact of Expanded Natural Graphite (ENG) additions on the stability of MOF-5 pellets. As previously described, small additions (5 wt.% or less) of expanded natural graphite (ENG) have been shown to improve the thermal conductivity of MOF-5-based pellets, without significant penalty to their hydrogen capacity [124, 133, 216]. Given the low intrinsic conductivity of MOFs [157], it is conceivable that use of second phase additions such as ENG will be a common strategy in applications where heat transfer through a MOF-based medium is needed. Our earlier studies have shown that ENG tends to accumulate at the interfaces between MOF-5 particles during pelletization [216]. As these interfaces may present facile diffusion pathways for water molecules into MOF pellets, we hypothesize that interfacial ENG may impede water transport, and thereby slow degradation resulting from water entry into the pellet. To test this hypothesis, humidity exposure tests were also performed on ENG-containing pellets. Pellets synthesized from a physical mixture of MOF-5 and 5 wt.% ENG were exposed to RH of 45% and 61%, and then subjected to H_2 uptake testing, Figure 5.8 (c) and (d). The maximum excess gravimetric hydrogen uptake for the composite MOF-5/ENG system is lower than that of pure MOF-5 due to the fact that ENG has a lower hydrogen capacity compared to MOF-5. Accounting for this effect, we observe that the MOF-5/ENG pellet shows similar robustness to that of the pure MOF-5 pellets, Figure 5.8 (a) and (b).

5.4 Conclusion

An important obstacle limiting the commercialization of MOFs is the limited robustness of some MOF compositions to reactive species, including water. To accelerate the transition of MOFs from lab bench to applications, an understanding of the operating conditions under which reasonable performance can be expected – i.e., a “stability window” – would be of great value. Toward this goal, in the present chapter we have quantified the impact of humid air exposure on the properties of the well-known MOF-5 compound as a function of exposure time, humidity level, and morphology (powders vs. pellets). Properties examined include hydrogen storage capacity, surface area, and crystallinity. Water adsorption/desorption isotherms were measured using a gravimetric technique; the isotherms exhibit a large hysteresis indicative of chemisorption-like binding of H2O to the MOF-5 framework. The first uptake is consistent with a type V isotherm having a sudden increase in uptake at ~50% relative humidity. Stability assessments were performed slightly below and above this threshold. Below the threshold only minor degradation is observed for exposure times up to several hours, indicating that MOF-5 is more stable than commonly thought under moderately humid conditions. In contrast, irreversible degradation can occur in a matter of minutes at higher humidity. FTIR spectroscopy suggests that molecular and/or dissociated water is inserted into the skeletal framework after long exposure times.

Densification into pellets was observed to slow the degradation of MOF-5 significantly, and may present an opportunity to extend the stability window of some MOFs.

Chapter 6

Water Adsorption and Insertion in MOF-5

6.1 Introduction

In Chapter 5 discussed the limited stability of MOFs to humidity [196-200], which would, of course, restrict their use in applications such as CO_2 capture from flue gas, or in contexts where exposure to humid air is likely. Perhaps the best-known example of this stability issue is the prototype compound, MOF-5, which has attracted considerable attention as a gas storage material due to its high storage densities [124, 133, 180, 188, 216]. The degradation of MOF-5 has been reported in several studies following exposure to humid air [59, 147, 201-205]. For example, Long and co-workers reported on the hydrolysis of MOF-5 by measuring the XRD spectrum and hydrogen uptake isotherm of a sample before and after exposure to air [147]. Schrock and co-workers identified the water loading threshold for degradation of MOF-5; irreversible decomposition was observed after uptake of 8 wt.% water [206]. Cychosz *et al.* analyzed the structure of several MOFs following exposure to DMF (2 mL) solutions containing 50 to 2000 μL water; they concluded that MOF stability was related to the composition and geometry of the MOF's metal cluster [207].

Experiments conducted by the present authors observed a sudden increase in water uptake (type V isotherm) in MOF-5 – coinciding with a rapid, irreversible structure change – upon exposure to air with relative humidity of 50% or higher [220]. Below this threshold water uptake was limited, and little structure change was observed for exposure times lasting up to several hours. The faster rates of decomposition observed at higher humidity levels suggests that the (local) water coverage within the MOF may influence the energetics associated with its irreversible hydrolysis.

Although the limited stability of MOF-5 with respect to water is now well established [17-26], the reaction mechanism associated with water-induced degradation has been more difficult to uncover. In this regard a small number of studies have employed (classical) molecular dynamics (MD) and first-principles calculations to characterize the atomic-scale features of this process. Greathouse and Allendorf performed one of the earliest MD studies of the water/MOF-5 system. Using a semi-empirical force field, they revealed that adsorbed water interacts more strongly with Zn sites than with the carboxylate linker, and that water molecules can insert into MOF-5 upon breaking of Zn-O bonds in the metal cluster [138]. Han and co-workers subsequently extended this approach by using the ReaxFF force field. This study proposed a reaction mechanism associated with MOF hydrolysis in which adsorbed water dissociates into an hydroxyl group and hydrogen. Subsequently, the –OH group bonds to Zn by breaking the Zn-O bond between the metal cluster and the linker. The remaining hydrogen then joins with the organic linker to form carboxylic acid[221].

In principle, density functional theory (DFT)-based calculations should provide a highly-accurate description of the bond-breaking processes present during MOF hydrolysis. However, these calculations remain a challenge due to the large number of atoms in the computational cell (106 atoms in the MOF-5 primitive cell; 424 in the conventional cell). For this reason, cluster approximations *[164]* or structure simplifications [166, 208, 210] are commonly adopted to make the calculations tractable. For example, Low and co-workers used cluster models of several MOFs to examine hydrothermal stability[164]. More recently, De Toni *et al*. modeled the effect of water loading on the hydration process in the simplified MOF-5 analogue, IRMOF-0h, in which the benzene ring in the linker was replaced by a linear arrangement of two C atoms[210]. Similarly, Bellarosa *et al.* studied the formation of water clusters during the degradation process of MOF-5 using a simplified primitive cell containing higher-symmetry linker orientations [208].

Building on these earlier investigations, the present study revisits the reaction mechanism for MOF-5 hydrolysis using DFT calculations. The primary goal is to elucidate the connection between water uptake in MOF-5 and its hydrolysis. This is accomplished by calculating the energetics of water insertion as a function of water coverage. Distinguishing features of our approach are the use of a van der Waals-aware density functional and full treatment of the MOF crystal structure (i.e., without structure simplifications or cluster model approximations). As a first step we calculate the thermodynamics of water adsorption at various sites in MOF-5. Subsequently, the energetics for hydrolysis are evaluated as a function of the local coverage of water near the Zn-O insertion point. Water insertion is found to be exothermic only after a critical number of H_2O molecules are adsorbed in close proximity on a given Zn-O cluster. This finding corroborates experimental observations of an induction period – presumably associated with nucleation of small, adsorbed water clusters – preceding hydrolysis [220, 222]. Finally, the reaction pathway for water insertion into the framework was evaluated in the presence of explicit, adsorbed water molecules. For coverages where insertion is thermodynamically favorable, the barrier for insertion is predicted to be low, only 0.17 eV. Such a small barrier indicates the likelihood for rapid hydrolysis at moderate humidity levels, in agreement with prior experiments [220].

6.2 Computational Method

Water adsorption and insertion calculations were performed using Density Functional Theory [78] (VASP [223, 224] code). Calculations were performed using conventional gradient-corrected functionals (PBE-GGA) [82] and with the vdW-DF2 [96] van der Waals-augmented functional. The MOF-5 crystal structure was adopted from diffraction experiments [225]. The full 3D-periodic crystal structure, based on the 106-atom MOF-5 primitive cell, was used without cluster approximations or other structural simplifications [164, 166, 208, 210]. All calculations were performed with a plane-wave energy cut-off energy of 500 eV; the Brillouin zone was sampled at the Γ-point. Interactions between core and valence electrons were described using the projector-augmented-wave (PAW) method [224] with valence electron configurations: Zn: $3d^{10}4s^2$; O: $2s^22p^4$; C: $2s^22p^2$. The climbing image nudged elastic band method (CI-NEB) [226, 227] was used to calculate the activation energy barrier for water insertion into MOF-5. Seven NEB images were used to plot the energy profile for the reaction pathway.

The MOF-5 structure was optimized separately using the PBE-GGA and vdW-DF2 functionals in the absence of water by minimizing the atomic forces and stresses on the cell with respect to the cell shape, volume, and atom positions. The lattice parameters obtained following these relaxations, 26.12 Å (PBE-GGA) and 26.35 Å (vdW-DF2), are in reasonable agreement with experimental values (25.67-25.89 Å) [228].

To identify favorable locations for water adsorption, a single water molecule was placed at several candidate adsorption sites; for each configuration all atomic degrees of freedom were relaxed while keeping the cell shape and volume fixed at the value obtained from relaxation of the water-free structure using the same functional (GGA or vdW-DF2). The adsorption energy was calculated according to the equation:

$$\mathrm{E_{ad}} = \mathrm{E_{MOF-5,water}} - \mathrm{E_{MOF-5}} - n\,\mathrm{E_{water}} \quad (6.1)$$

Here, $\mathrm{E_{MOF-5,water}}$ refers to the energy for MOF-5 with *n* adsorbed water molecules, $\mathrm{E_{MOF-5}}$ is energy of the empty MOF-5 cell, and $\mathrm{E_{water}}$ is the energy of an isolated water molecule calculated using a orthorhombic simulation cell with dimensions of 10×11×12 Å.

6.3 Results and discussion

6.3.1 Adsorption of Isolated Water Molecules

Figure 6.1 (a) shows the conventional unit cell of MOF-5. The crystal structure consists of BDC linkers and Zn_4O metal-oxygen clusters. Five distinct sites were explored for water adsorption. These sites are illustrated as large purple spheres in Figure 6.1 (b) and labeled with the greek letters α, β, γ, δ, and ε. The positions of the sites are consistent with those from prior experiments [229] and simulations [230]. The three sites α, β, and γ refer to sites on the Zn-O cluster, while δ and ε refer to sites on the benzene ring in the linker. Site α is the closest site to the central oxygen in the Zn cluster; this site is also equidistant to 3 of the Zn atoms bonded to the central oxygen. Site β is closest to one of the four Zn atoms in the cluster, and is equidistant to three of the four oxygens bonded to Zn. Site γ is proximate to two oxygens bonded to Zn. On the linker, site δ is centered above the face of the benzene ring. Site ε is positioned at the edge of the benzene with equal distances to two hydrogen atoms. Table 6.1 lists the number of each type of site on a single metal cluster or linker. In total, there are 20 adsorption sites on the metal cluster and 12 sites on the linker.

Table 6.1. Number and location of each type of adsorption site depicted in Figure 6.1.

Location	**Site Name**	**Number of Sites**
	α	4
Zn-O cluster	β	4
	γ	12
Linker	δ	6
	ε	6

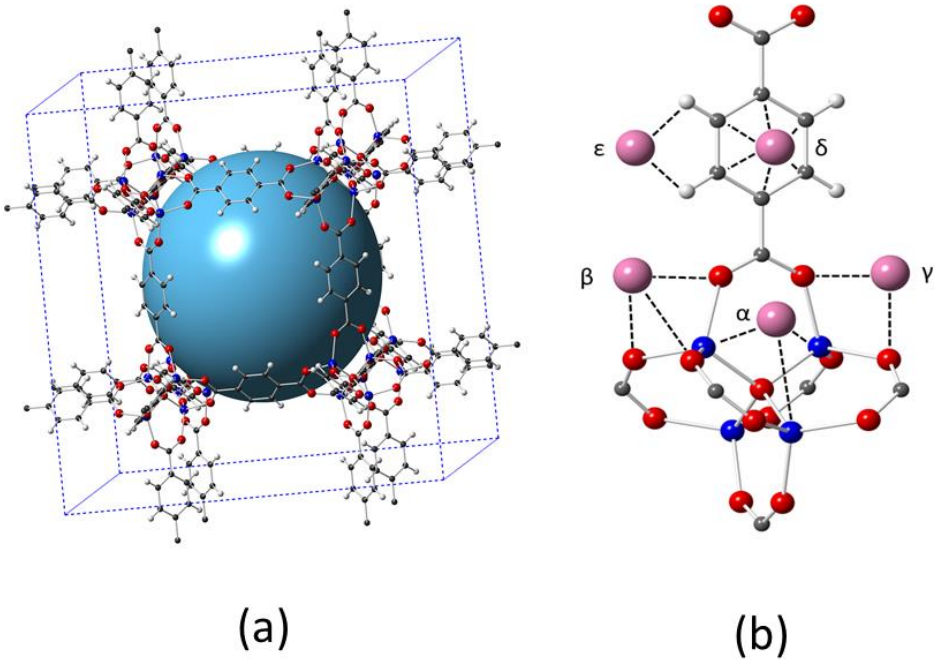

Figure 6.1. (a) Conventional unit cell of MOF-5. Red spheres represent Oxygen, blue: Zn, grey: C, white: H. (b) Magnification of the metal cluster and organic linker from panel (a). The purple spheres represent 5 distinct sites for water adsorption, and are labeled with Greek symbols.

Figure 6.2 (a) plots the adsorption energy, E_{ad}, for a single water molecule for each adsorption site as a function of the exchange-correlation functional employed (PBE-GGA and vdW-DF2). The vdW-DF2 functional predicts more exothermic binding energies than does the GGA across all of the binding sites. This difference is particularly large for the α site, where the binding predicted by the GGA is approximately 0.2 eV weaker. The weaker binding observed for the GGA is consistent with earlier calculations involving CO_2 and CH_4 adsorption in MOFs [187, 231, 232], and can be attributed to the lack of van der Waals interactions in this functional. More generally, the range of binding energies predicted by the vdW-DF2 across all sites (~ -0.23 eV) is significantly wider than for the GGA; in the latter case the adsorption energies are clustered around -0.15 eV. This trend has also been observed for the adsorption of small molecules in other MOFs [187, 231, 232]. A final difference between the functionals pertains to the site preference for H_2O adsorption. The α site is predicted to be the most stable site for adsorption by the vdW-DF2 functional, whereas the GGA predicts the β site to have the largest binding energy. The present calculations predict an adsorption energy at the β site of -0.19 eV for the GGA functional; this value is in good agreement with the energy (-0.21 eV) predicted by a previous computational study [208].

Figure 6.2 (b-d) tabulates bond distances between the proximal oxygen atom in an adsorbed water molecule and various atoms in the MOF. This is done for adsorption sites located on the metal cluster (sites α, β, γ) and as a function of the exchange-correlation functional. In all cases the bond lengths are greater than 3Å, consistent with a weak, physisorption interaction. Distances predicted by the vdW-DF2 functional are systematically shorter than those from the GGA; this is expected given the larger adsorption energies reported in Figure 6.2 (a).

Another recent computational study of water adsorption in a simplified model of MOF-5 (IRMOF-0h) found a much shorter O(water)-Zn distance of 2.0 Å [210]. The shorter distances found in that study are likely an artifact of the structure simplification employed there; in IRMOF-0h every benzene in the linker is replaced by two carbon atoms. By removing the bulky benzene rings it is conceivable that water molecules can gain closer access to the metal cluster. This assertion was verified by performing adsorption calculations on IRMOF-0h. Indeed, water was observed to adsorb in this structure with much shorter bond distances of 2.57 Å. Additional comparisons with the

IRMOF-0h structure used in Ref. [210] are provided in Figure C.2 in appendix C.

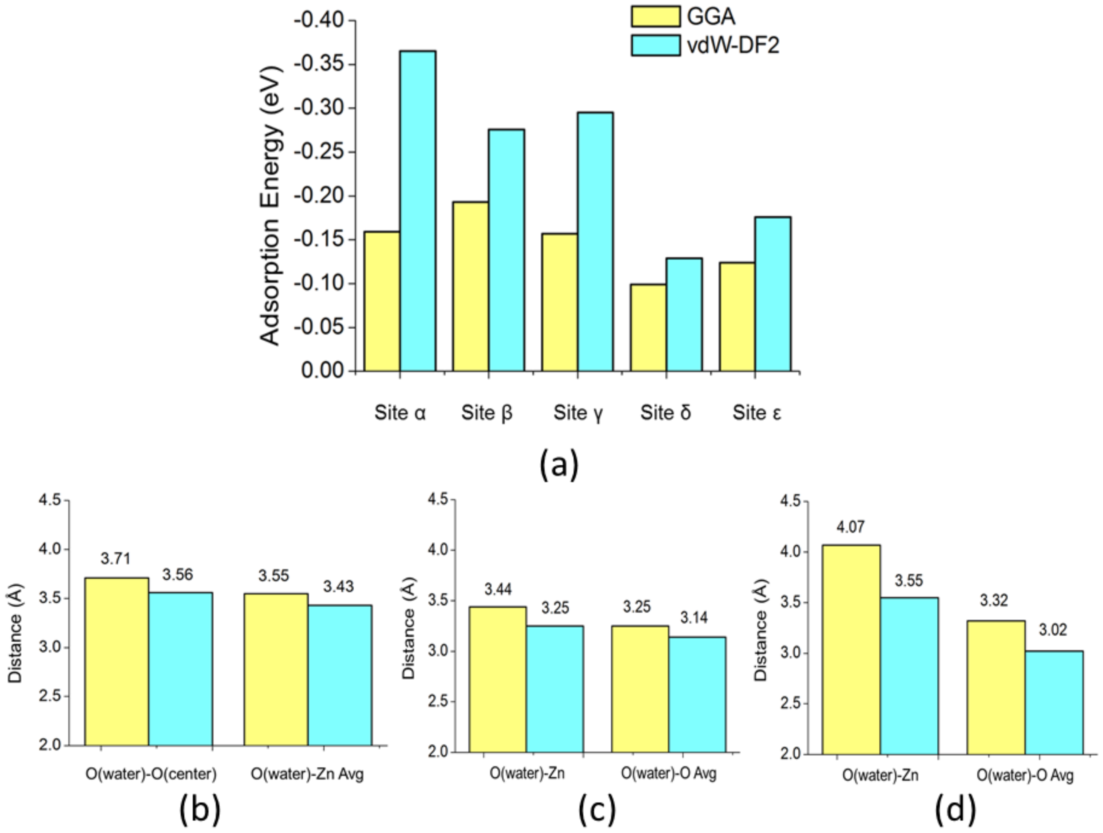

Figure 6.2. (a) Calculated adsorption energies for water as a function of exchange-correlation functional and adsorption site in MOF-5. (b-d) Calculated distance from proximal O in an adsorbed water molecule to various atoms in MOF-5 for adsorption sites located on the metal cluster (sites α, β, and γ).

6.3.2 Adsorption of Multiple Water Molecules

In reality, multiple water molecules can be adsorbed simultaneously on MOF-5 upon exposure to humid air. According to our previous study [220], the saturation water loading in MOF-5 is ~13 wt.% when exposed to air with relative humidity exceeding 50%. Assuming all water molecules preferentially fill the most energetically favorable adsorption sites (α, β, γ sites residing on the Zn-O cluster), this loading corresponds to the adsorption of approximately 5 water molecules per metal cluster. We aim to determine the dependence of water adsorption energies on the Zn-O cluster as a function of coverage and adsorption geometry. To accomplish this, multiple water molecules were placed at α, β, and γ sites on the same Zn-O cluster. Coverages of 1 to 4 molecules were examined. We adopt a naming scheme where the number and identity of filled sites specifies the coverage and adsorbed configuration. For example, the configuration identified as "αα" contains two water molecules adsorbed on α sites. Similarly, "αβγ" corresponds to a configuration where three water molecules are adsorbed in α, β, and γ sites simultaneously. Given the large number (~1,300) of possible configurations for even a small number of adsorbed molecules (4) on a single Zn-O cluster, a systematic enumeration of all configurations was not attempted. Rather, a subset of configurations in which the adsorbed molecules were clustered (i.e., adsorbed at predominantly adjacent sites) was explored. Our preference for these configurations is based on the expectation that water-water interactions are energetically favorable at higher coverages [208].

From Figure 6.1(a) we observe that site α has the lowest adsorption energy for a single water molecule. If water molecules interact weakly, then we expect that only α sites will be filled. Figure 6.3 compares the total adsorption energies for the lowest energy adsorbed configurations identified by our search to configurations in which only α sites are filled. For the highest loading considered, 4 water molecules, the total adsorption energy assuming only α sites are occupied is -1.14 eV. For this configuration the distance between adjacent H_2O molecules is large, 5.74 Å, signaling that H_2O-H_2O interactions are likely weak. In contrast, a configuration in which H_2O is adsorbed with the configuration ααβγ yields a lower (i.e., more exothermic) adsorption energy of -1.40 eV. In this case the water cluster adopts a more compact arrangement, with H_2O-H_2O distances given by: 2.86 Å (α-β); 4.83 Å (α-γ); 2.97 Å (β-γ). A similar trend holds for loadings of 2 and 3 molecules: adsorption is preferred in configurations that involve nearby αγ and γγγ sites (on average, the γ-γ distance is 2.9 Å). As anticipated, these data suggest that water-water interactions play an important role during the adsorption process: incoming water molecules preferentially adsorb at adjacent sites rather than filling only α sites, which are more widely separated. This tendency is consistent with the type V isotherm measured in our previous study of water uptake in MOF-5 [220]; such an isotherm indicates the presence of sizeable water-water interactions.

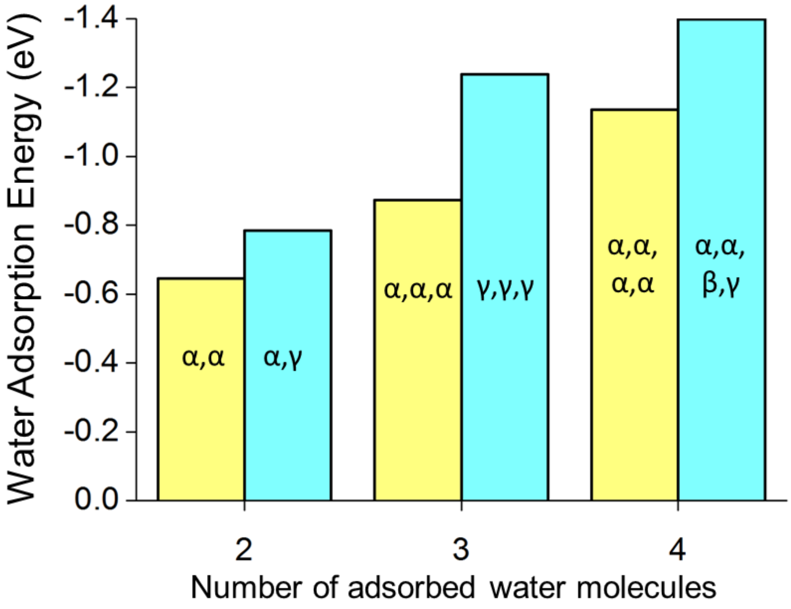

Figure 6.3. Calculated total adsorption energy for water molecules as a function of water coverage and adsorption configuration. For each coverage the yellow bar on the left represents the adsorption energy in the case where only α sites are filled. Blue bars on the right represent the adsorption energy for the most energetically favorable water distribution. Adsorption geometries are labeled inside each bar.

6.3.3 Water insertion

Having determined the geometries and adsorption energies for small water clusters in MOF-5, we now examine the energetics of water insertion into the framework as a function of water coverage. Prior experiments indicate that hydrolysis of MOF-5 occurs more rapidly at higher water loadings, and is preceeded by an induction period, presumably owing to the nucleation of small water clusters [208, 220, 222]. The exothermicity for water insertion was assessed by evaluating the insertion energy:

$$\Delta \mathrm{E} = \mathrm{E}_{\mathrm{final}} - \mathrm{E}_{\mathrm{initial}}.(6.2)$$

In this expression $\mathrm{E}_{\mathrm{initial}}$ corresponds to a low-energy configuration of *n* adsorbed water molecules on a given metal cluster, as previously described. $\mathrm{E}_{\mathrm{finial}}$ represents the energy of a related structure in which one of the adsorbed molecules is inserted as a molecular unit into the MOF by breaking a Zn-O bond. Water insertion will be favorable if $\Delta \mathrm{E} < 0$. Several candidate final (inserted) configurations were considered, including various displacements and twists of the linker following Zn-O bond scission. $\Delta \mathrm{E}$ was calculated for coverages ranging from 1 to 4 water molecules.

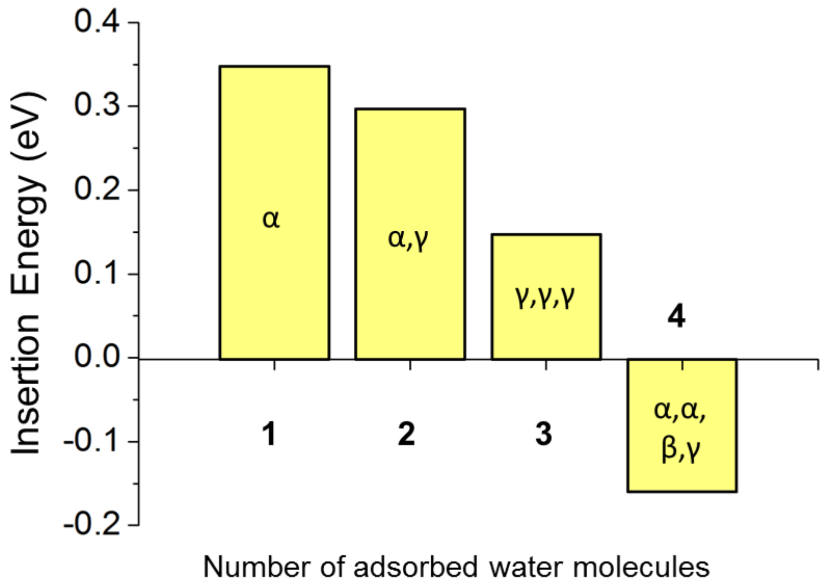

Figure 6.4. Water insertion energy in MOF-5 as a function of coverage on a Zn-O cluster. The labels within in each bar indicate the configuration of adsorbed H_2O before insertion.

The insertion energy for water into MOF-5 as a function of coverage is shown in Figure 6.4. With only one molecule adsorbed water insertion is endothermic: $\Delta E = 0.35$ eV. Insertion becomes increasingly less endothermic as the size of the water cluster grows to 2 or 3 molecules. Finally, insertion becomes exothermic when the cluster size reaches 4 molecules, with $\Delta E = -0.16$ eV. The observation that water insertion is exothermic only at higher coverages is roughly consistent with experimental observations of rapid degradation in MOF-5 upon exposure to air containing relatively high concentrations of water (50% relative humidity or higher) [220]. As previously described, the water loading determined in those isotherm experiments, equal to 13 wt.% or approximately 5 water molecules per metal cluster, is close to the loading identified here (4 molecules) and in an earlier GGA-based study[208]. Although experiments suggest that degradation is most rapid at a loading equivalent to 5 molecules per cluster, entropic effects could shift some molecules to sites on the linker. Such an effect would bring the predicted computational loading into even better agreement with experiments.

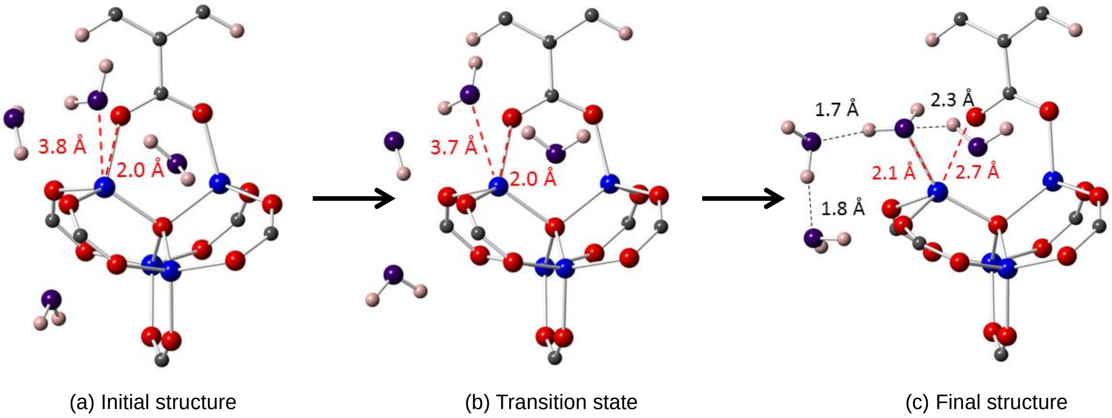

(a) Initial structure (b) Transition state (c) Final structure

Figure 6.5. Water insertion process in MOF-5. (a) Magnification of MOF-5 structure with 4 water molecules physically adsorbed near the Zn-O cluster. (b) Transition state. (c) Final MOF-5 structure containing a Zn-O bond broken via the insertion of a single water molecule. The color scheme for MOF atoms is the same as in Figure 6.1(b); O atoms in the water molecules are purple to distinguish them from oxygen in the MOF (blue). Black dashed lines/text indicate hydrogen bond lengths between H and O in adjacent water molecules._Red lines/text illustrate Zn-O bond distances.

The reaction pathway for water insertion is illustrated in Figure 6.5; the energy profile for this pathway is plotted in Figure 6.6. The initial state for the reaction is shown in Figure 6.5(a), where four water molecules are physically adsorbed at α, α, β, γ sites, which is the same low-energy configuration reported in Figure 6.3. (This configuration is also depicted as the first image in Figure 6.6, where its energy is assigned a value of zero.) Upon approaching the transition state, shown in Figure 6.5(b) (image 4 in Figure 6.6), the water molecule occupying the β site migrates towards the Zn atom. Finally, Figure 6.5(c) represents the final state where the water has been inserted into the framework by breaking a Zn-O bond. The inserted molecule forms a new bond of length 2.1 Å between Zn and O(water). The original (now broken) Zn-O(MOF) bond lengthens to 2.7 Å from its initial value of 2.0 Å. The O(MOF) stranded by water insertion subsequently forms a double bond with its neighboring C, forming carbonyl group. Meanwhile the 3 adsorbed water molecules remain in close proximity to the inserted molecule, forming a "water chain" with inter-molecular H-O distances of 1.7 to 2.3 Å. These distances are consistent with inter-molecular H-O bond lengths typical of hydrogen bonding in water, ~2.0 Å. The formation of such a water chain has also been discussed in prior studies [208, 210]and is expected to stabilize the transition and/or hydrolyzed states.

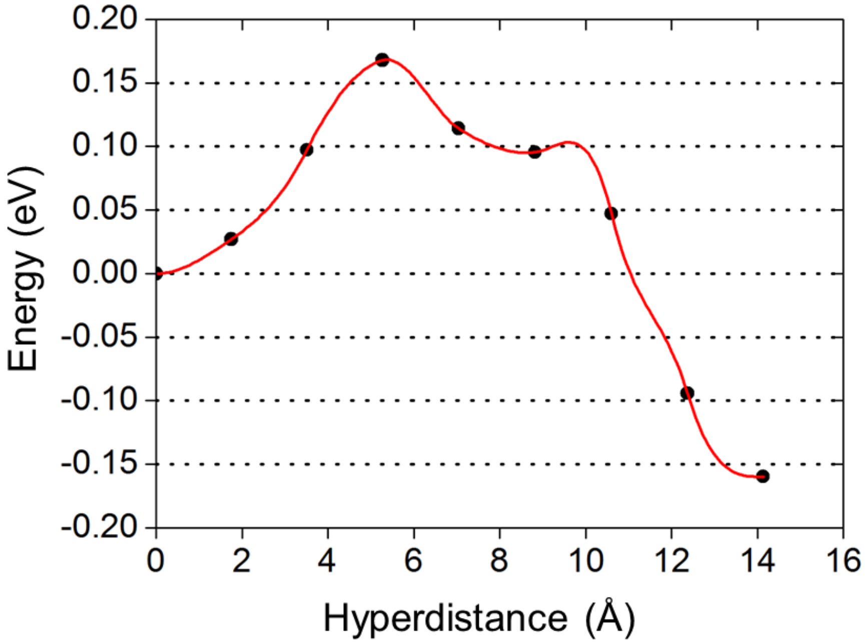

Figure 6.6. Calculated energy barrier for the insertion of a water molecule into MOF-5. The insertion process breaks a Zn-O bond, and occurs in the presence of 3 additional adsorbed water molecules adsorbed on the metal cluster.

Returning to the energy profile for water insertion (Figure 6.6), we note that the activation barrier for this process is small, only 0.17 eV. Our barrier is in qualitative agreement with the 0.08 eV barrier reported in Ref. [210]. The slightly smaller barrier reported in Ref. [210] may be an artifact of the hypothetical IRMOF-0h compound used in that study. A comparison of water adsorption distances in MOF-5 and IRMOF-oh is provided in the Appendix C.

The calculated activation energy for water insertion is used in conjunction with classical rate theory to estimate the time required for hydrolysis of MOF-5 upon exposure to humid air under conditions similar to those used in our recent experimental study[220]. In that study, MOF-5 powders exhibited negligible surface area and hydrogen uptake capacity after 48 hours of exposure to humid air with 61% relative humidity (RH).

The number of water molecules inserted into one gram of MOF-5 in time t can be written as

$$N = pAZt \cdot \exp(-E_a/kT) \quad (6.3)$$

Here A is the specific surface area of MOF-5 (3,800 m^2/g [233]), Z represents the number of collisions/adsorption attempts between gas phase water molecules and the pore surface of MOF per unit area-second, p is the probability that adsorbed water occupies sites with a loading and configuration amenable to insertion (such as the low-energy ααβγ configuration described above), and E_a is the activation energy for insertion from that configuration. Additional details regarding this calculation are provided in the Appendix C.

The rate theory calculation indicates that for a loading of 4 water molecules per cluster, on average approximately 290 hours of exposure time is needed for water insertion to occur. This estimate is in reasonable agreement with the exposure time (~48 hours) needed to significantly degrade the surface area and hydrogen uptake properties of MOF-5 powders [220] at a slightly higher loading of 13 wt.% H_2O (equivalent to about 5 H_2O molecules per cluster) which is the saturation coverage resulting from exposure to air with RH = 61% [220]. Moreover, our estimate is likely an upper bound to the time needed for hydrolysis, as it relates only to a specific local loading and adsorption geometry (ααβγ); it is likely that other configurations and higher loadings also lead to water insertion. For example, the GGA-based calculations of Bellarosa et al. [208] revealed that water insertion was barrierless for local coverages of 5 H_2O molecules.

The mechanisms considered above all relate to the insertion of water in molecular form. In addition, calculations were preformed to examine the energetics for dissociative water insertion. For this scenario, a relaxed structure was generated in which the original Zn-O bond present in MOF-5 was broken and replaced by Zn-OH(water) and O–H(water) bonds. However, the energy of this hypothetical structure was found to be much higher (~1 eV) compared with that of the initial structure, indicating water dissociation is not energetically favored in this configuration. This is consistent with the findings of Ref. [208], who reported that dissociative insertion was moderately endothermic (0.8 eV) relative to a meta-stable physisorbed state.

6.4 Conclusion

Enhancing the robustness of metal-organic frameworks to water and other reactive species remains an unmet challenge in translating these materials from the lab bench to practical applications. Understanding the processes responsible for MOF hydrolysis is a prerequisite for the rational design of new compounds with improved stability. Toward this goal, the present study has examined the energetics associated with water adsorption and insertion into the prototype compound, MOF-5 as a function of coverage. A distinguishing feature of our study is the inclusion of dispersion interactions – which are expected to play an important role in molecular adsorption – and modeling of the full periodic unit cell of MOF-5.

A comparison of a van der Waals-aware functional (vdW-DF2) and a conventional gradient-corrected functional (PBE-GGA) revealed important qualitative and quantitative differences regarding the energetics and site preference for water adsorption. The vdW-DF2 functional favors water adsorption on the SBU, rather than on the linker. This differs from the trend predicted by the PBE-GGA, which exhibits a more uniform distribution of adsorption energies on both the linker, and SBU.

A key finding of our study is that the thermodynamics of water insertion into MOF-5 is coverage dependent: Insertion becomes thermodynamically favorable only when a critical number of water molecules (4 or more) are co-adsorbed as relatively compact clusters on the same structural building unit of the MOF. This obervation is in good agreement with experimental measurements, which show that hydrolysis is slow at low water coverages and is preceded by an incubation period; we speculate that the latter process owes to the nucleation and growth of water clusters of sufficient size on a given SBU. Once a sufficient coverage has been achieved, the insertion of molecular water into Zn-O bonds proceeds with a low activation barrier, consistent with a rapid hydrolysis reaction.

Our calculations lend further support to the notion that the rate of MOF degradation depends strongly on the operating environment. While it is now clear that some MOFs are unstable to hydrolysis in an absolute sense, under low-to-moderate humidity conditions the rate of hydrolysis can be slow enough to allow exposure for several days without significant degradation. Efforts to expand this “stability window” to higher temperatures and humidity levels will benefit from the mechanistic understanding provided by this study.

Chapter 7

Stability of MOF-5 in a Hydrogen Gas Environment with Expected Fueling Station Impurities

7.1 Introduction

In Chapters 5 and 6 we learned that as a zinc-based MOF containing carboxylate linkers, MOF-5 is susceptible to chemical degradation in humid conditions. This is a consequence of the relatively weak metal-ligand bond between Zn and O [138, 147, 164, 202, 203, 208-210]. In addition to humidity-induced degradation, some MOFs exhibit stability issues with respect to common impurities in hydrogen fuel streams. Studies have identified MOFs that are unstable in the presence of high concentrations of hydrogen sulfide[234-236], ammonia[237-239], and other impurities in industrial gas streams [240, 241]. In most cases, MOF degradation is manifested as a decrease in storage capacity due to a reduction in the surface area and pore volume, change in long-range crystal structure or local chemical bonding[138, 147, 164, 220]

While most studies have focused on scenarios in which MOFs are exposed to high concentrations of harmful impurities, these environments are far more severe than what would be typically encountered in an on-board hydrogen storage system. As is the case for semiconductor and Li-ion battery production, strict environmental controls can be implemented at the production and packaging phases. Once installed in a vehicle hydrogen storage materials would be subjected only to impurities in the hydrogen fuel stream itself.

Table 7.1. Impurity test gas mixtures used in this MOF-5 study.

Gas Mixture	Impurity	Test Gas Concentration	J2719 Threhold Limit	Cycle Test	Storage Test
		ppm	*ppm*		
1	NH_3	7	0.1	Y	N
2	H_2S	1	0.004[a]	Y	Y
3	HCl	9	0.05[b]	Y	N
4	H_2O	8	5	Y	Y
5	CO	2	0.2	Y	N
	CO_2	5.7	2		
	CH_4	8.3	2[c]		
	O_2	9.6	5		
	N_2	119	100		
	He	505	300		
Not Tested	HCHO	-	0.01	-	-
Not Tested	HCOOH	-	0.2	-	-

[a] Total sulfur category in J2719 includes hydrogen sulfide (H_2S), carbonyl sulfide (COS), carbon disulfide (CS_2) and mercaptans

[b] Total halogenates category in J2719 includes hydrogen bromide (HBr), hydrogen chloride (HCl), chlorine (Cl_2) and organic halides (R-X)

[c] Total hydrocarbons category in J2719 includes ethylene, propylene, benzene, phenol (paraffins, olefins, armoatic compounds, alcohols, aldehydes).

Hydrogen gas from the fueling station is required in the US to be is compliant to fuel quality standards outlined in SAE J2719[242]. (The international standard ISO 14687-2 provides identical purity standards.) Impurity limits set by J2719 are driven primarily by the need to protect the catalyst and polymer electrolyte components in the fuel cell stack. As a result, threshold limits for ammonia (0.1 ppm), carbon monoxide (0.2 ppm), sulfur species (0.004 ppm), and halogenates (0.05 ppm) are exceptionally stringent. Complete threshold limits are summarized in Table 7.1. Although SAE J2719 does recognize impurities that are known to poison and/or deactivate conventional metal hydride-based storage materials (e.g., CO and O_2), the impact of impurities on adsorbent materials such as MOFs are currently not accounted for.

The identity and concentration of impurities in the hydrogen fuel stream depends on the hydrogen production method. For example, hydrocarbons, carbon monoxide, and sulfur species are more likely to be present in hydrogen produced by steam methane reformation, the predominant method. Field data from existing hydrogen stations confirms that the J2719 impurity limits are achievable although some station samples still exceed the requirements[243]. Nitrogen, oxygen, and water are contaminants likely to leak in from the atmosphere during refueling process itself.

To our knowledge, no systematic studies exist regarding the chemical stability of MOFs after exposure to hydrogen streams containing impurities identified in J2719. The use pattern of the hydrogen storage system will strongly influence the mechanism by which degradation can occur. For example, if a MOF-based system is cycled frequently at cryogenic temperatures (i.e. *cycling*), it may accumulate the more strongly-bound impurity species by selective adsorption, potentially reducing the available storage capacity for hydrogen molecules. However, chemical degradation side-reactions involving the adsorbed impurities will proceed slowly at cryogenic temperatures. For MOFs stored at higher temperatures for extended periods (i.e. *storage*), chemical side-reactions will proceed faster, but the accumulation of impurities will be considerably smaller.

In this study we examine the degradation potential of 10 impurities listed in SAE J2719. These impurities were mixed with nominally pure hydrogen gas at a concentration of up to several ppm, and include: NH_3, H_2S, HCl, H_2O, CO, CO_2, CH_4, O_2, N_2, and He. We subject MOF-5 powder samples to these gas mixtures for pressure cycle testing at 77 K, and ambient temperature static exposure testing for 1 week. The hydrogen storage capacity of the MOF-5 is tested at regular intervals during the pressure cycling, and is tested at the start and end of each static exposure test. Powder XRD and FTIR spectra of the MOF-5 are collected on the post-test samples to check for changes in the crystal structure, and confirm the absence of new phases. The results indicate that common hydrogen fuel impurities at low levels do not lead to significant degradation of MOF-5 powder in either the pressure cycling or ambient static exposure tests.

7.2 Experiment detail

7.2.1 Materials preparation

MOF-5 powders were synthesized by BASF at room temperature using a procedure described by Yaghi and coworkers starting from 1,4-benzene dicarboxylic acid (H2BDC, C8H6O4, Merck), zinc acetate dihydrate (Zn(CH3COO)2 ·2H2O, Merck), and N-dimethylformamide (DMF, BASF AG)[125]. In a glass reactor equipped with a Teflon-lined stirrer, 130 g of Zn(CH3-COO)2 ·2H2O was dissolved in 1200 mL DMF. Within 2 h, a solution of 37.5 g of H2BDC in 950 mL DMF was added under vigorous stirring.

The precipitate was filtered off, washed three times with 1 L of dry acetone and dried under a stream of flowing nitrogen. Given the low vapor pressure of DMF (approximately 4 torr at 25 ^{o}C), solvent exchange to an acetone (vapor pressure of approximately 270 torr at 25 ^{o}C) has been shown to be an effective method for solvent removal. Prior to testing and characterization, MOF-5 was heated and evacuated at 130 ^{o}C overnight, yielding the desolvated (‘activated’) form of the material. Following the initial removal of solvent, all handling and storage of MOF-5 was restricted to an active recirculation glovebox with a high-purity Argon atmosphere.

7.2.2 Impurity test gases

The SAE J2719 requirements for fueling stations are summarized in Table 7.2. This standard is based on the potential constituents from hydrogen

Table 7.2. Estimated maximum impurity accumulation by MOF-5 based on SAE J2719 PPM levels

SAE J2719 Constituents	**Specification PPM level**	**Maximum Accumulation (wt. %)**		**Potential degradation mechanisms**
		After 300 cycles	**After 1500 cycles**	
Water	5	0.03720	0.186	Pore structure degradation
Hydrocarbons	2	0.01488	0.074	Surface area blocking
Oxygen	5	0.03720	0.186	No accumulation effect
Helium	300	2.23200	11.160	No accumulation effect
Nitrogen, Argon	100	0.74400	3.720	No accumulation effect
Carbon dioxide	2	0.01488	0.074	Surface area blocking
Carbon monoxide	0.2	0.00149	0.007	Surface area blocking
Total sulfur	0.004	0.00003	0.0001	Structure damage possible Not significant at accumulation level
Formaldehyde	0.01	0.00007	0.0004	No accumulation effect
Formic acid	0.2	0.00149	0.007	Not detectable at accumulation level
Ammonia	0.1	0.00074	0.004	Structure damage possible Not significant at accumulation level
Total halogenates	0.05	0.00037	0.002	Structure damage possible Not significant at accumulation level

production. It is improbable that a single production method would result in a mixture with all twelve of the contaminants listed in the standard. In addition, preparation of a single gas mixture containing all J2719 contaminants is impractical due to the interactions of the impurities with each other. For example, hydrogen chloride and hydrogen sulfide will react together and with water. Therefore, five separate hydrogen impurity gas mixtures were prepared according to the J2719 levels that could be formulated and qualified by the specialty gas company (Airgas). The separate mixtures allowed for independent analysis of the effect of each impurity. Formulation and qualification of the impurity test gas mixtures at the trace levels in SAE J2719 also proved a challenge, necessitating the use of higher impurity levels. Consequently, the following 5 gas mixtures were examined (in all cases the balance of gas is H_2):

Mixture 1: Ammonia (NH_3), at 5 to 10 ppm

Mixture 2: Hydrogen sulfide (H_2S), at 1 ppm

Mixture 3: Hydrogen chloride (HCl), at 5 to 10 ppm

Mixture 4: Water (H_2O), at 5 to 10 ppm.

Mixture 5: Carbon monoxide (CO), at 2 ppm; Carbon dioxide (CO_2) at 5 ppm; Methane (CH_4) at 2 ppm; Oxygen (O_2) at 5 ppm; Nitrogen (N_2) at 100 ppm; Helium (He) at 500 ppm. We note that the 6 impurities present in this mixture are presumed to not react with each other.

The delivered impurity test gas levels are shown in Table 7.1. Since the majority of these levels exceed the impurity limits defined in J2719, the test gas mixtures used in this study provide a more stringent test of MOF-5 robustness.

7.2.3 Cycle test procedures

Pressure cycling protocols utilized in this study borrow from methods previously used to study conventional hydride materials [244]. Previous work has established numerous cycle test methods. These include intrinsic cycling, where the same hydrogen gas is re-used each cycle, and extrinsic cycling, where a fresh aliquot of hydrogen is introduced in each cycle. Many of the existing cycle test methods were developed to study aging mechanisms unique to metal hydrides, including alloy disproportionation and particle breakup. The present study employs only extrinsic pressure cycling, as this method best simulates the MOF-5 degradation mechanisms expected in on-board hydrogen storage systems.

Pressure cycle testing at 77 K was performed using an automated manometric sorption instrument, following a programmed routine. Each cycle starts with a 5 min adsorption period, where a 168 ml reservoir is filled with a fresh dose of 100–105 bar impurity gas mixture, which is then expanded into an evacuated sample cell containing MOF-5. The empty sample cell has a free space of approximately 15 ml, with the MOF-5 sample displacing a volume of approximately 200 μl. At the end of the 5 min adsorption period, the sample cell is closed off. The equilibrium pressure at this point is in the 75–85 bar range, which corresponds to 5.5–5.8 wt.% excess hydrogen at 77 K. This is followed by a 5 min desorption period in which the hydrogen in the sample cell is expanded into an evacuated 1174 ml reservoir. Following the desorption period, the hydrogen pressure in the entire instrument is slowly ramped down to 1 bar, and then opened to continuous vacuum for 5 min. During the active vacuum period nearly all of the adsorbed hydrogen should be removed. This cycle pattern is repeated 300 times in total for each test gas. Cycling is interrupted approximately every 60 cycles to measure the hydrogen adsorption capacity of the sample.

Pressure cycle tests were conducted for all five test gas mixtures listed in Table 7.1. Throughout each period of continuous cycling the sample cell is immersed in a liquid nitrogen (LN2) bath, and is allowed to warm up only for the capacity test. To prevent MOF-5 powder from being blown out of the sample cell during the repeated desorption steps, which involve a large pressure differential, a 2 micron sintered metal filter gasket was placed immediately above the sample cell. The filter has a 0.125 inch hole drilled in it to allow an internal PRT sensor to extend into the sample cell. Fresh samples of MOF-5 powder were utilized for each cycle test.

An example of the pressure cycling procedure is provided in Figure 7.1. To accurately track the adsorbed hydrogen amounts during this particular cycling experiment, smaller volumes were employed for both the adsorption (V_r =12.31 ml) and desorption (V_r = 167.63 ml) phases. During the 5 min adsorption phase (labeled A in Figure 7.1), the pressure drops to about 26 bar and the adsorbed amount reaches 5.8 wt. % on average. During the 5 min desorption period (labeled as D in Figure 7.1), the average equilibrium pressure is 3.8 bar, which corresponds to an excess hydrogen concentration of 3.2 wt.%. During the 5 minute vacuum period (labeled as V in Figure 7.1), it is assumed that the hydrogen concentration drops to approximately 0 wt.% (although the value was not directly measured). This confirms that the MOF-5 sample adsorbs around 5.8 wt% (excess basis) of hydrogen gas each cycle. Further, the hydrogen uptake between the first five and last five cycling periods in this particular experiment appears to be unchanged.

7.2.4 Storage test procedure

Long-term impurity storage tests were performed for impurity mixtures using a manometric sorption instrument. The sample cell containing powder MOF-5 sample was charged with the test gas mixture up to an equilibrium pressure of approximately 40 bar, with the sample cell initially immersed in liquid nitrogen. The sample cell was then valved off and allowed to warm to room temperature. It was left under pressure at room temperature for 1 week. Storage tests were performed for the H_2O and H_2S test gas mixtures.

7.2.5 Capacity Test Procedure

Capacity tests consist of measuring a single hydrogen adsorption isotherm at 77 K, up to a maximum pressure of approximately 90 bar. Hydrogen adsorption measurements were performed using a manometric sorption instrument (PCT-Pro 2000, Setaram) with an oil-free scroll vacuum pump (Anest Iwata model ISP90). Free space measurements were performed using helium at room temperature for each sample. The sample cell was immersed in a liquid nitrogen bath, with the LN_2 level filled to a specific height. Excess adsorption amounts were calculated by the standard method[245]. Further details on the isotherm measurement methods can be found in Ref [177].

Initial capacity tests were collected prior to starting the pressure cycling and storage procedures. Before being loaded in the sample cell, MOF-5 powder samples were degassed to remove any weakly-bound water. Samples were evacuated at room temperature for at least 6 hours, then evacuated and heated to 130 ℃ overnight.

Final capacity tests were collected at the end of both pressure cycling and storage. For pressure cycling, capacity tests were measured approximately every 60 cycles until the end of the 300 cycle tests. With the exception of the initial capacity tests, the MOF-5 samples were degassed only by pulling vacuum on the sample at room temperature (no heating) before capacity tests. (For the initial capacity tests the freshly loaded MOF-5 sample was degassed at 130 ℃, as described in the previous paragraph.)

Settings, dose increments and step times were identical for all capacity test measurements. Due to the difficulty in switching test gas bottles in the middle of storage and pressure cycle testing, capacity tests were performed using the same impurity gas mixtures utilized in the corresponding cycle and storage procedures. Throughout this document, the unit of weight percent (wt. %) refers to the mass of adsorbed hydrogen per 100 g of adsorbent. The mass of adsorbed hydrogen is not included in the denominator.

7.2.6 XRD and FTIR Characterization

Powder X-ray diffraction (XRD, Rigaku Miniflex II diffractometer using Cu Kα radiation ($\lambda = 1.5418$ Å)) was used to assess changes in crystallinity resulting from exposure to testing gas containing impurities. Samples were transferred to the diffractometer in sealed vials. Each vial was opened, and the MOF-5 powder was chopped and pressed onto an off-axis silicon crystal sample substrate. The time between opening the vial and the beginning of the scan was less than 30 seconds. Diffraction data was collected over a range of 5-40 ° (2θ) at a scan rate of 5 °/min, resulting in a total experiment time of 7 minutes. The sample was then immediately scanned a second time in order to observe the degree of structural change that had occurred during the initial scan. No change was observed in any of the samples.

Fourier transform infrared spectrometry (FTIR) was used to assess changes in bonding resulting from exposure to impurities. Measurements were made using a Thermo Scientific Nicolet FTIR spectrometer. A scan range of 4000 to 600 cm^{-1} was used, with a scan time of 5 minutes. Powder samples were loaded and scanned in air. As demonstrated previously [180], the MOF-5 powders used in this study do not show structure change when exposed to air for less than 5 minutes. We expect that any changes to FTIR peaks primarily reflect effects from exposure to impurities in the testing gas.

7.3 Result and discussion

7.3.1 Maximum Impurity Accumulation

We first estimate the maximum impurity accumulation that could occur in the MOF-5 adsorbent bed on a worst-case basis during repeated refueling and operation (see Table 7.2). In this scenario, we assume that the impurity concentrations in the fuel stream are at the maximum allowable levels in J2719. Furthermore, MOF-5 is assumed to retain 100% of the impurity species dosed into the storage tank at each cycle. The tank is filled to 100 bar at 80 K from empty each cycle, and at the end of each cycle the temperature is 140 K and the pressure is 0 bar. The results are summarized in Table 7.2.

For this calculation, the storage vessel is assumed to be filled with loosely packed MOF-5 powder at a packing density of 0.13 g/cm^3. Based on previous results [177], the hydrogen storage density of powder MOF-5 (with 0.13 g/cm^3 packing density) at 100 bar and 80 K is known to be 33 g/L. Since the temperature of the MOF-5 media is assumed to rise to 140 K by the end of each fuel cycle, in a real system the less strongly bound gaseous impurities (He, N_2, O_2) will be removed along with the hydrogen each cycle (i.e., no accumulation). However the more strongly bound gas species have the potential to accumulate as cycling progresses. (For the purposes of illustrating a worst-case scenario,

Table 7.2 assumes all species are retained regardless of their strength of interaction with MOF-5.)

Worst-case estimates of impurity accumulation amounts are listed in

Table 7.2. After 300 cycles the maximum H_2O concentration in the MOF-5 pores is less than 0.04 wt% (relative to the MOF-5 mass). Previous results have suggested that due to the hydrophobic nature of the MOF-5, as manifested in the "S-shaped" Type 5 isotherm, low concentrations of water are unlikely to have a measurable impact on MOF-5 degradation [220].

Hydrocarbons, carbon dioxide and carbon monoxide are expected to affect MOF-5 primarily by occupying active hydrogen sorption sites. They are not expected to initiate chemical side-reactions that degrade the crystalline pore structure. After 300 cycles, however, their maximum attainable concentrations do not appear high enough to have a significant effect on the hydrogen storage capacity. Given the lack of test data, a cycling experiment using an impurity mixture of He, O_2, CH_4, N_2, CO, and CO_2 was performed in order to test our analysis.

The trace impurities with the lowest concentrations (sulfur, halogenates, ammonia, formic acid, formaldehyde) accumulate only to levels of 0.0003–0.002 wt.% after 300 cycles. It is unclear whether such low amounts are detectable, or capable of impacting MOF-5 hydrogen storage attributes. Rather than individually test all of these ultra-low concentration fuel impurities, we omitted formic acid and formaldyde from the test sequence on the assumption that any possible degradation mechanisms would be equal to or less than that of the other impurities.

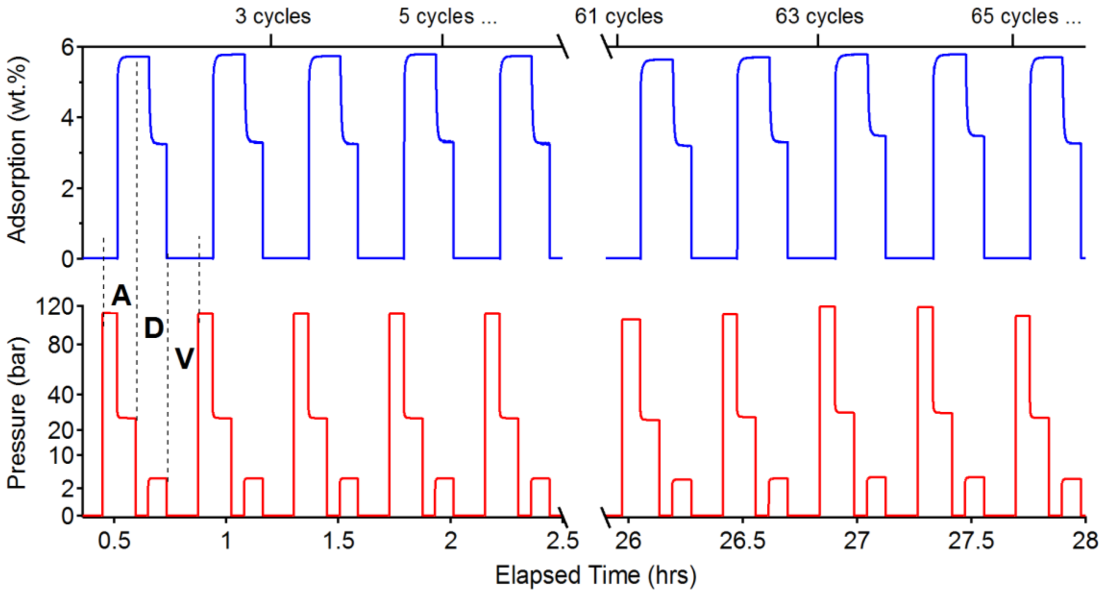

Figure 7.1. An example of the pressure cycling procedure shown as excess adsorption and pressure versus test time. The lower graph displays the reservoir pressure, plotted on a square root scale. The upper axis displays the calculated adsorption amount of the MOF-5 sample. Both are plotted versus total elapsed time. For cycle number two. the adsorption phase (labelled **A**), desorption phase (labelled **D**) and vacuum phase (**V**) are annotated in the graph. The split *x*-axis shows the first 5 and last 5 cycles from this experiment.

7.3.2 Impurity cycle test

7.3.2.1 Ammonia

The ammonia impurity mixture contains a concentration of 7 ppm, roughly 70 times larger than the 0.1 ppm threshold in J2719. Hydrogen capacity tests measured on the MOF-5 sample during pressure cycling with the ammonia test gas are summarized in Figure 7.2(a). The adsorption isotherms after 63, 125, 183, 247, 309 cycles overlap exactly (within measurement error), indicating no hydrogen uptake capacity loss after pressure cycle testing.

The powder XRD spectra shown in Figure 7.2 (b), measured before and after cycle testing, fails to detect any significant change to the long-range crystal structure due to the cycling. Two small changes are present in the FTIR spectra shown in Figure 7.2 (c). The broad and weak peak around 3300 cm^{-1} can be attributed to O-H bond stretching in carboxylic acid, and the peak near 1600 cm^{-1} arises from the C=O bond in carboxylic acid. A possible reaction signaled by the emergence of these peaks is that the Zn-O bond between the metal cluster and organic linker breaks, with an H from NH_3 combining with COO^- to form carboxylic acid. Since this kind of reaction may only affect a small fraction of Zn-O bonds, a corresponding change in the long-range crystal structure is not apparent from the powder XRD spectrum.

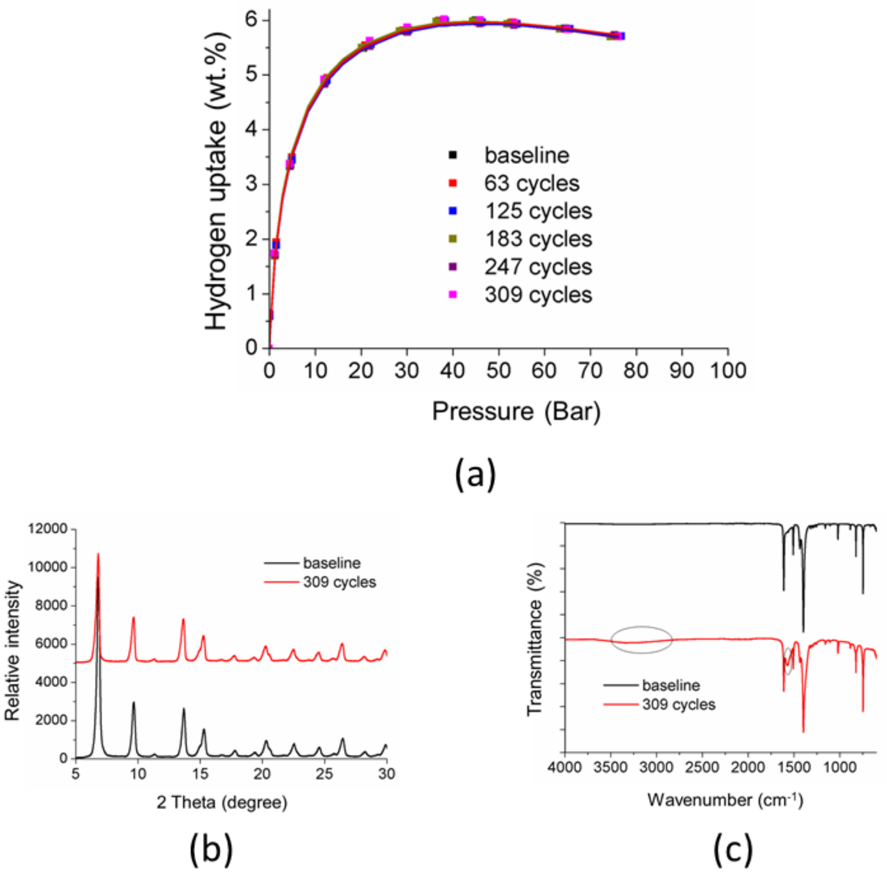

(a)

(b)

(c)

Figure 7.2. (a) Adsorption isotherm of MOF-5 powders with test gas mixture 1 including NH_3 as the impurity. Capacity measurement are taken every 60 cycles (b) XRD spectra for MOF-5 powders before and after cycle test (c) FTIR spectra for MOF-5 powders before and after cycle test.

7.3.2.2 Hydrogen Chloride (Halogenates)

The characterization results of MOF-5 powder before and after pressure cycling with hydrogen chloride are shown in Figure 7.3. As noted in Sec. 7.2, the 9 ppm impurity concentration of hydrogen chloride in this hydrogen test gas is 180 times larger than the 0.05 ppm threshold limit in J2719. The hydrogen adsorption isotherms in Figure 7.3 (a) indicates a small apparent decrease in hydrogen uptake after 307 cycles. The maximum excess H_2 adsorption amount at 77 K decreases from 6.0 wt.% to 5.85 wt.% after 307 cycles.

Further characterization confirms that this capacity loss can be traced to MOF-5 structure decomposition. The powder XRD pattern of the post-cycling sample has a new peak emerging at $2\theta=9^o$, as shown in Figure 7.3(b) as circled on the graph. This peak is known to appear in the powder XRD spectrum for MOF-5 following water-induced structure degradation [220]. The emergence of the 9 ℃ peak indicates MOF-5 crystal structure degradation. The FTIR spectrum in Figure 7.3(c) shows the same impurity-induced peaks at 3300 cm^{-1} and 1600 cm^{-1} that are present in Figure 7.2 (c). This suggests a common reaction pathway leading to the structure decomposition for ammonia, hydrogen chloride, and water impurities.

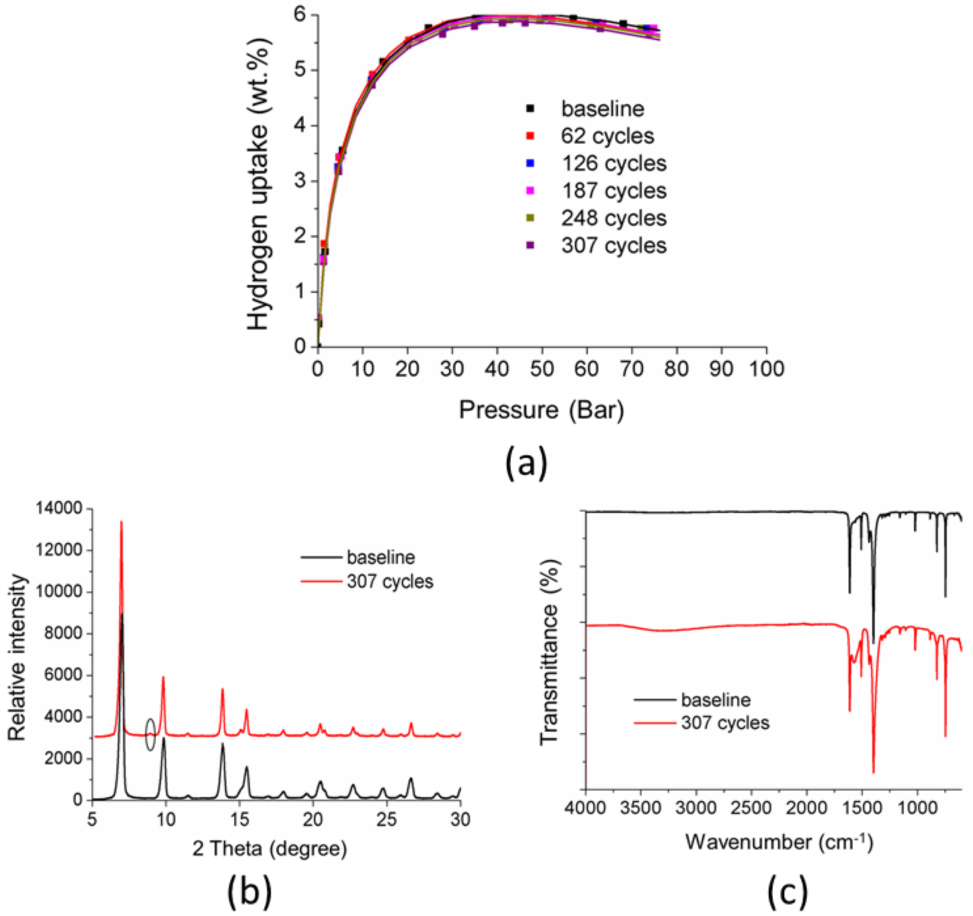

Figure 7.3. (a) Adsorption isotherm of MOF-5 powders with test gas mixture 3 including HCl as the impurity. Capacity measurement are taken every 60 cycles (b) XRD spectra for MOF-5 powders before and after cycle test (c) FTIR spectra for MOF-5 powders before and after cycle test.

7.3.2.3 Water, Hydrogen Sulfide (Sulfur), and Inerts Mixture

Results for the remaining three mixtures (mixtures 2, 4 and 5 in Table 7.1) are summarized in Appendices D, in Figure D.1, D.2 and D.3, respectively. Mixture 2 contains hydrogen sulfide, while mixture 4 contains water. Mixture 5, which includes a set of mostly inert impurity species, is denoted "inerts" for identification. For all three of these impurity gas mixtures, there was no measurable change in the hydrogen adsorption capacity tests measured during the course of pressure cycling. This confirms that there is no hydrogen capacity loss due to pressure cycling with these impurity mixtures.

For all three impurity mixtures, the MOF-5 structure appears unchanged following 300 pressure cycles. The powder XRD patterns (Figure D.1(b), D.2(b) and D.3(b)) and FTIR spectra (Figure D.1(c), D.2(c) and D.3(c)) collected on the pre-cycling and post-cycling MOF-5 samples do not show any significant changes. Since the impurity concentrations in Mixtures 2, 4 and 5 significantly exceed the threshold levels specified in J2719, we conclude that these contaminants will not impact the adsorption capacity of MOF-5 powders within 300 cycles.

7.3.2.4 Summary of pressure cycling tests

Figure 7.4 provides a summary of the hydrogen capacity measured during pressure cycling tests for all five impurity gas mixtures. It is recalled that each hydrogen adsorption capacity test consisted of measuring an excess adsorption isotherm at 77 K, using the same impurity gas employed in the ongoing cycling sequence. The capacity is therefore defined in terms of the maximum excess adsorption at 77 K. The hydrogen capacities plotted on the y-axis in Figure 7.4 are expressed as a percentage of the initial capacity measured at the beginning of the cycle testing (i.e., capacity at cycle 0). For all five of the impurity gases tested, the capacity retention was above 97% after 300 cycles.

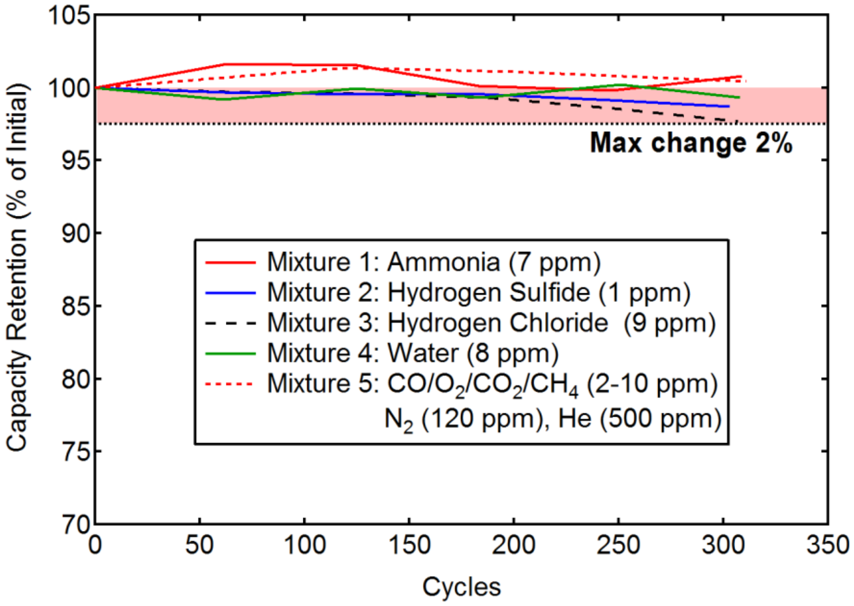

Figure 7.4. Summary of MOF-5 hydrogen storage capacity at 77 K during pressure cycling with impurity gas mixtures. The y-axis indicates the maximum excess adsorption amount measured during the capacity test each point during the pressure cycling test, expressed as a percentage of the maximum excess adsorption measured before the start of the cycle test.

7.3.3 Static exposure tests

7.3.3.1 Water

A one week static exposure test was performed at room temperature using the water impurity mixture (mixture 4), and was carried out according to the procedure described in section 7.2. Figure 7.5 summarizes the pre- and post-storage characterization results for this MOF-5 sample. The hydrogen uptake curves shown in Figure 7.5(a) indicate that there was no adsorption capacity change following the one week exposure. The XRD and FTIR profiles also indicate a stable bonding and crystal structure of MOF-5 samples following the exposure test. When combined with the earlier pressure cycling test results, the static exposure test results confirm that H_2O concentrations up to 8 ppm in the hydrogen fuel do not affect hydrogen storage performance of MOF-5 within 300 cycles and 1 week exposure. According to J2719 standard, the content of H_2O should be less than 5 ppm, which is even safer for MOF-5 as hydrogen storage material.

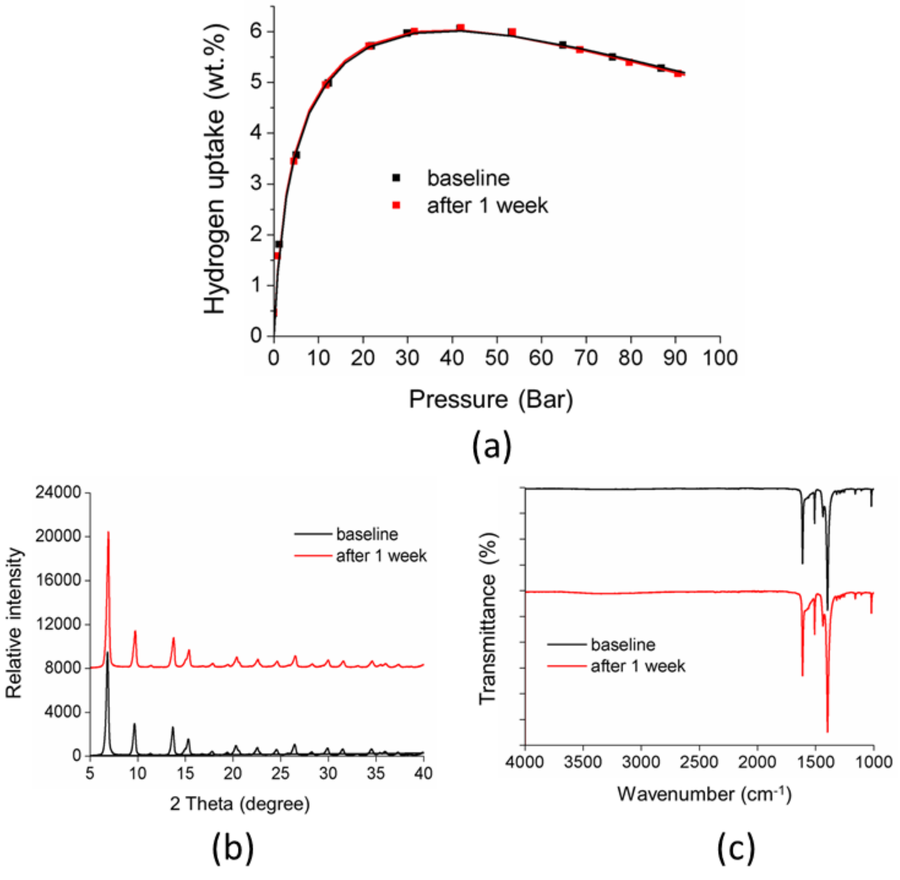

Figure 7.5. (a) Adsorption isotherm of MOF-5 powders with test gas mixture 4 including H_2O as the impurity. Capacity measurement are taken before and after 1 week static exposure (b) XRD spectra for MOF-5 powders before and after static exposure (c) FTIR spectra for MOF-5 powders before and after static exposure.

7.3.3.2 Hydrogen Sulfide (Sulfur)

MOF-5 was subjected to a one week static exposure test at room temperature using the hydrogen sulfide impurity mixture (mixture 2). Figure 7.6 summarizes the characterization results of the MOF-5 powder before and after the 1 week storage. The hydrogen uptake isotherms in Figure 7.6 (a) indicate no decrease in adsorption capacity. The unchanged peaks in XRD and FTIR in Figure 7.6 (b) (c) also shows the very well maintained bond and crystal structure of MOF-5 samples during the exposure test. Combining the result of cycle test and static exposure with hydrogen including H_2S, we can conclude that 0.9 ppm H_2S in hydrogen doesn’t have effect on the hydrogen storage performance of MOF-5 within 300 cycles and 1 week’s exposure. According to J2719 standard, the content of H_2S should be less than 0.004 ppm, which is much safer for MOF-5 as hydrogen storage material.

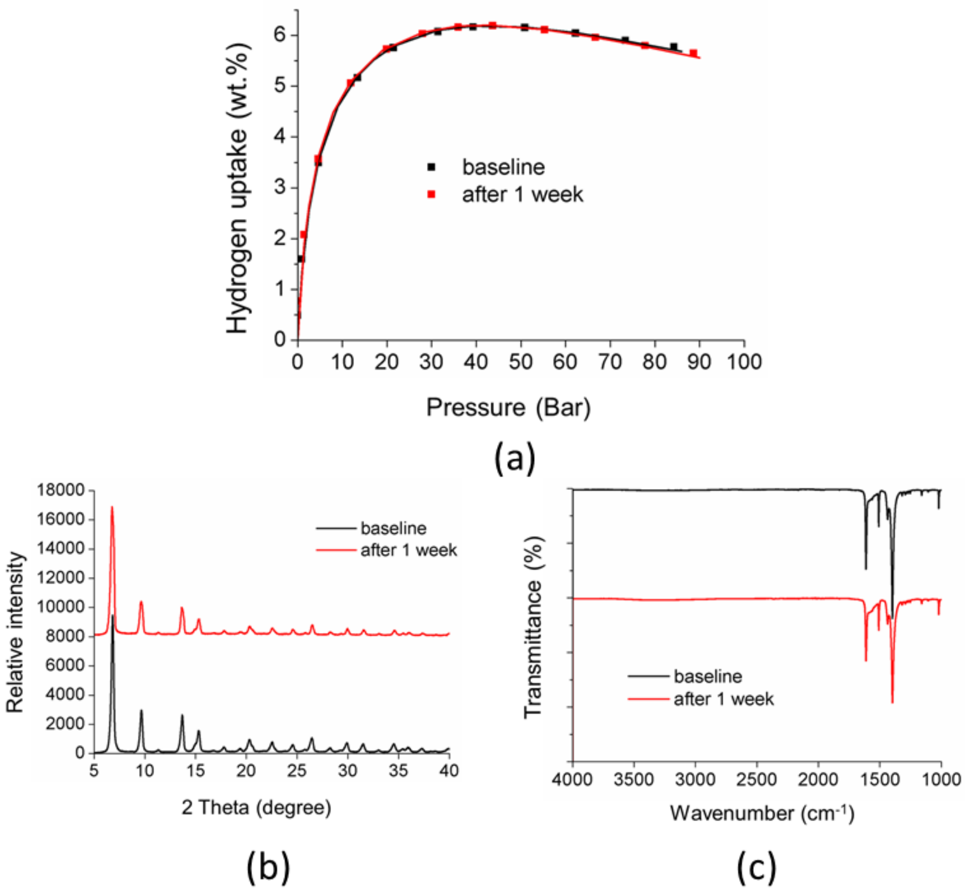

Figure 7.6. (a) Adsorption isotherm of MOF-5 powders with test gas mixture 2 including H_2S as the impurity. Capacity measurement are taken before and after 1 week static exposure (b) XRD spectra for MOF-5 powders before and after static exposure (c) FTIR spectra for MOF-5 powders before and after static exposure.

7.4 Conclusion

Hydrogen gas conforming to purity standards outlined in SAE J2719 can contain contaminants in the fuel stream. We studied the effect of these impurities on both the hydrogen storage capacity and structural stability of the metal-organic framework MOF-5. Four impurity hydrogen mixtures were prepared by introducing ammonia, hydrogen sulfide, hydrogen chloride, water, respectively. The remaining six (mostly inert) impurities were combined into the fifth hydrogen mixture. Only the hydrogen chloride mixture yielded a measurable decrease in hydrogen storage capacity (from 6 wt.% to 5.8 wt.%.) during the course of pressure cycle testing at 77 K. No measurable decrease was noted for the other hydrogen impurity mixtures during pressure cycling. Cycling with hydrogen chloride amounts also induced small changes to the MOF-5 crystal structure and local chemical structure. Changes to the chemical bonding structure were observed for samples cycled with trace ammonia amounts, but corresponding changes to the long-range crystal structure or hydrogen storage capacity could not be detected. Static exposure of MOF-5 to the water and hydrogen sulfide impurities had no measurable effect on the sample. The impurity levels used in this study actually exceed the J2719 threshold standard by at least of a factor of 10 for each contaminant. These results demonstrate that hydrogen from a fueling station compliant with J2719 should not impact the performance of MOF-5 in hydrogen storage system within 300 cycles and 1 week's static exposure, thereby providing a robust performance for real application.

Chapter 8

Imaging the Microstructure and Hydrogen Permeation in MOF-5 Pellets

8.1 Introduction

The discussions in previous chapters and in the literature suggest that there is a rapidly-growing body of information regarding the fundamental, "materials properties" of MOF-5. However, much less is known regarding the properties of MOF-5 compacts, such as pellets, pucks, or monoliths. These densified forms – which are typically formed via the compression of powders – are likely to be the preferred morphology for MOF media in a real system as they would allow for ease of handling and increase volumetric performance.

Ideally, the densification of MOF powders should not degrade other aspects of performance. For example, densification should not significantly slow the transport or permeation of hydrogen within the pellet. Additionally, the microstructure of the pellet should be relatively homogeneous, and not contain large variations in density or in the distribution of 2nd phase additions intended to enhance thermal conductivity (such as ENG).

An example illustrating the first scenario is the so-called MATI ("modular adsorption tank insert”) hydrogen storage system[246]. The MATI system uses several large diameter MOF-5 pucks as the storage media. During refilling, it is desirable to fill the tank with hydrogen (approximately 5 kg) very quickly, typically in less than 5 minutes. The large quantity of hydrogen to be stored, combined with the desire to store it rapidly, raises concerns that use of densified media may slow the uptake process (compared to a system using powder-based media). In this case it is desirable to characterize the hydrogen penetration pathway during adsorption and desorption. *In situ* imaging of hydrogen permeation in MOF-5 pucks could provide such information.

To cite another example, in a large scale MOF-5/ENG pellet it is desirable to have a uniform distribution of ENG within the pellet to maximize the enhancement to thermal transport. More generally, maintaining a highly uniform density throughout the MOF compact will lead to optimal performance.

In this Chapter several imaging analysis techniques are used to characterize densified forms of MOF-5, such as pucks and pellets. Neutron imaging radiography is used to measure the transient hydrogen distribution during adsorption and desorption. Neutron tomography reveals the three-dimensional distribution of ENG (expanded natural graphite) particles in MOF-5/ENG pellets. Finally, the density of MOF-5 pellets are analyzed using x-ray tomography. The application of these imaging techniques provides new insights into the properties and performance of densified MOF media.

8.2 Method

8.2.1 Material preparation

Table 8.1. Sizes and compositions of pellets used in neutron imaging and microCT experiments.

	Diameter (mm)	Height (mm)	Composition
Radiography 1	6.35	5	Pure MOF-5
Radiography 2 & tomography	26.8	10	MOF-5+10% ENG
MicroCT	31	10	Pure MOF-5

MOF-5 powder was provided by BASF, and was synthesized using a process described previously [180]. In some cases expanded natural graphite, ENG (SGL Group), was added at moderate levels to MOF-5 as a means to improve thermal conductivity [133, 216]. Pelletized versions of MOF-5 were examined, with and without ENG additions. Composite MOF-5/ENG pellets were synthesized by adding ENG to MOF-5 to achieve pellets having a mass fraction of 5 wt.% ENG. A SPEX 8000M Mixer/Mill was filled with the MOF-5/ENG mixture and shaken in the milling machine for 20 seconds without milling balls. The powders were loaded into a cylindrical die and pressed. Three types of pellets were used during neutron imaging and microCT experiments; the diameter and composition of pellets summarized shown in Table 8.1. For pellet density characterization experiments, three varieties of pellets were formed from MOF-5 powders that were pre-filtered using meshes with hole diameters of 2mm, 1.18mm, and

0.841mm, respectively.

8.2.2 Neutron imaging

8.2.2.1 Facility and sample holder

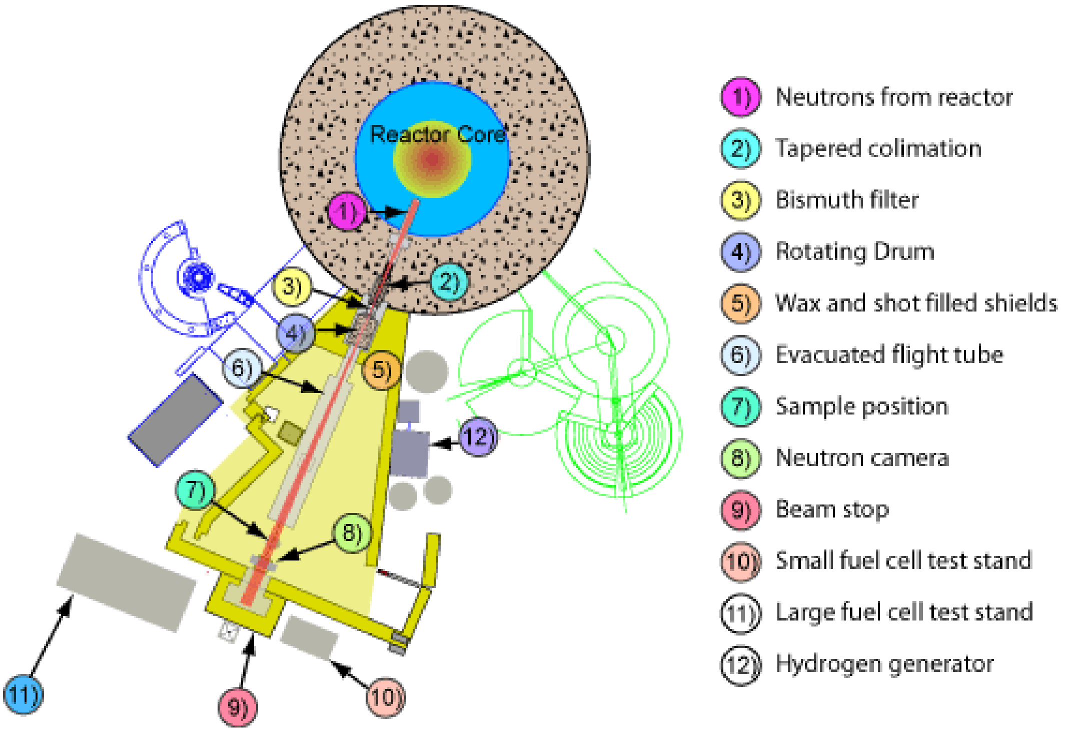

Figure 8.1. Plan view of the neutron imaging facility at the NIST Center for Neutron Research[247].

The plan view of the NIST neutron imaging facility used in our experiment is shown in Figure 8.1. This facility is located at Beam Tube 2 (BT-2) at the NIST Center for Neutron Research. The CNR provides a source of thermal neutrons that is collimated using a tapered plug (1 and 2 in Figure 8.1). This conically shaped beam will be nearly uniform in intensity across the diameter of the beam at the image plane downstream. This type of optical arrangement is generally referred to as pinhole optics.

Although the CNR produces mostly thermal neutrons there are still a significant amount of high energy neutrons and gamma rays as a byproduct. These high energy neutrons and gamma rays represent a background that can be dangerous to electronic equipment and to personnel operating the beam line. Therefore, a high energy neutron and gamma ray filter is placed directly downstream of the tapered collimator. This filter consists of 10 cm of bismuth single crystal cooled to liquid nitrogen (LN) temperatures (77 K) (3 in Figure 8.1). Cooling the bismuth dramatically reduces the vibrational phonon modes in the crystal, which strongly scatter thermal neutrons. When cooled, the crystal becomes nearly transparent (60 % transmission) to thermal neutrons and remains nearly opaque to high energy neutrons and gamma rays.

The filtered beam can then be collimated with a simple thermal neutron pinhole located directly downstream of the LN cooled bismuth filter. After the pinhole is a rotating drum with four positions (4 in Figure 8.1). Three of the positions have holes for additional collimation or filters if needed. These collimators are currently 1 cm, 2 cm, and open collimation. The fourth position is used to block the beam when the facility is not in use.

Neutrons and gamma rays scattered out of the beam must be stopped to prevent them from becoming a hazard to personnel or to other scientific neutron data collection experiments in the CNR. The shielding used to do this is a steel encased mixture of wax and steel shot. The high-energy neutrons are turned into thermal neutrons in the wax and stopped be the material and the gammas are absorbed by the steel shot (see 5 in Figure 8.1).

The beam that is now collimated passes out of the drum and into a sealed, evacuated aluminum flight tube (6 in Figure 8.1). The flight tube ends right before the sample position (7 in Figure 8.1), which is open to air. At the sample position an object to be radiographed sits on a rotating and translating stage. Behind the object is the neutron camera that is used to digitize the 2-dimensional neutron distribution (8 in Figure 8.1).

Finally the beam is stopped in an appropriately named "beam stop" (9 in Figure 8.1). The beam stop is necessary since the sample and camera do not stop all of the neutrons; in addition high energy neutrons and gammas are still present in the beam. Therefore, in the interest of safety the beam stop is designed to stop the unattenuated beam (beam without obstructions like the sample and camera).

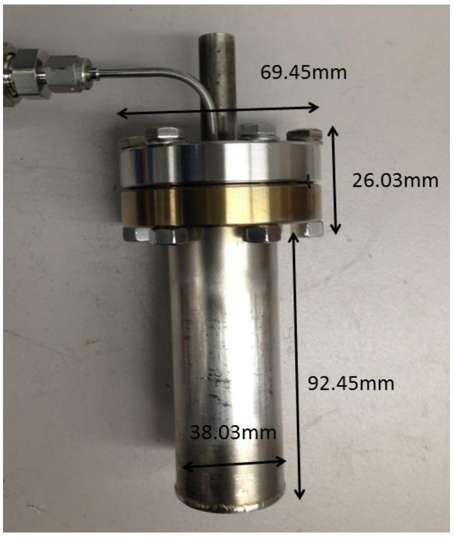

Figure 8.2. Picture of vessel used in NIST neutron imaging experiment. Dimensions are shown in the graph.

In our experiment, the vessel, sample holder and sample ring are all made of stainless steel. The structure and size of the vessel are shown in Figure 8.2.

8.2.2.2 Neutron radiography

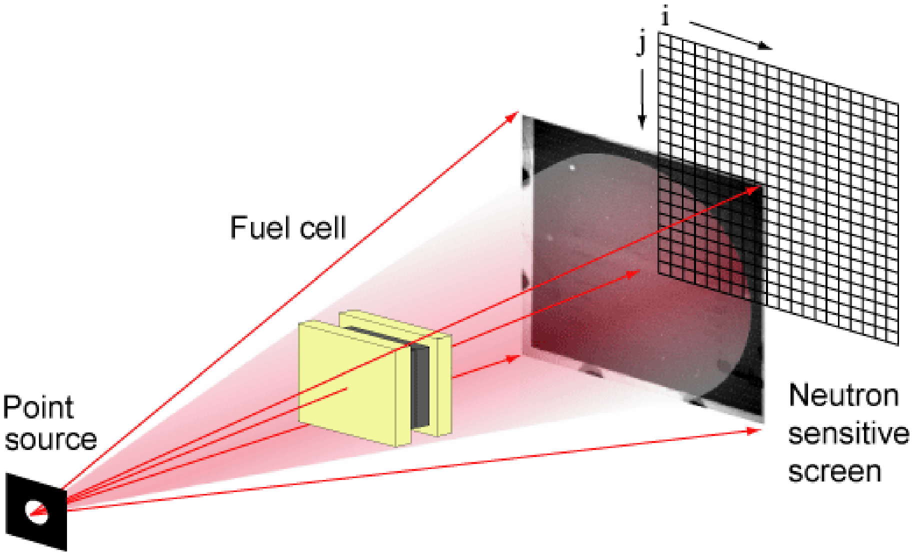

Figure 8.3. Schematic representation of neutron imaging radiography[247].

Figure 8.3 shows a schematic of the neutron radiography technique. Neutron radiographs are the neutron shadows of objects placed in the beam. Using a 2 dimensional neutron camera the image captured is actually a gray level image where the gray level of each pixel is proportional to the number of neutrons that made it through the object. The number of measured neutrons is then correlated to the amount of neutron scattering and absorbing material in the beam and can be determined from the attenuation law known as Beer's Law:

$$I(i,j) = I_0(i,j) \cdot \exp(-\mu t) \quad . \qquad (8.1)$$

In this equation, μ is known as the attenuation coefficient of the material, I_0 is the initial intensity and t represents the thickness of the material. In this experiment, the value of μt is plotted as the intensity of a data point in the neutron radiography images. The attenuation coefficient μ is also equal to $N\sigma$, where N is the atom density, and σ is the total neutron cross section. Generally, when the sample holder is filled with hydrogen, σ includes effects from both MOF-5 and hydrogen gas. We can remove the effect from MOF-5 by dividing the filled-sample radiograph by an empty-sample or “background” radiograph. The attenuation coefficient of hydrogen at a certain pressure can be calculated if attenuated neutron intensity and sample thickness are known. The attenuation coefficient of each point on the sample can then be plotted in a graph with different colors. The density of adsorbed hydrogen, N, can also be determined from $\mu = N\sigma$.

8.2.2.3 Neutron tomography

By rotating an object 180 degrees, and taking neutron radiographs at defined angular positions, a complete 3-dimensional image of the object’s composition can be made. For a 2-D slice of a sample shown in Figure 8.4, if the sample is rotated by θ, the measured attenuation profile can then be written as $R_\theta(x')$, where x’ is the offset distance from the center beam. We can write the following relation:

$$R_\theta(x') = \int_{-\infty}^{\infty}\int_{-\infty}^{\infty} f(x,y)\delta(xcos\theta + ysin\theta - x')dxdy, \qquad (8.2)$$

where f(x,y) is the attenuation coefficient at the position (x,y). After the sample is rotated by 180 degrees, we can get the complete attenuation profile from detector. Then we can use the inverse Radon transform to get the spatial attenuation coefficient f(x,y) of the sample[248].

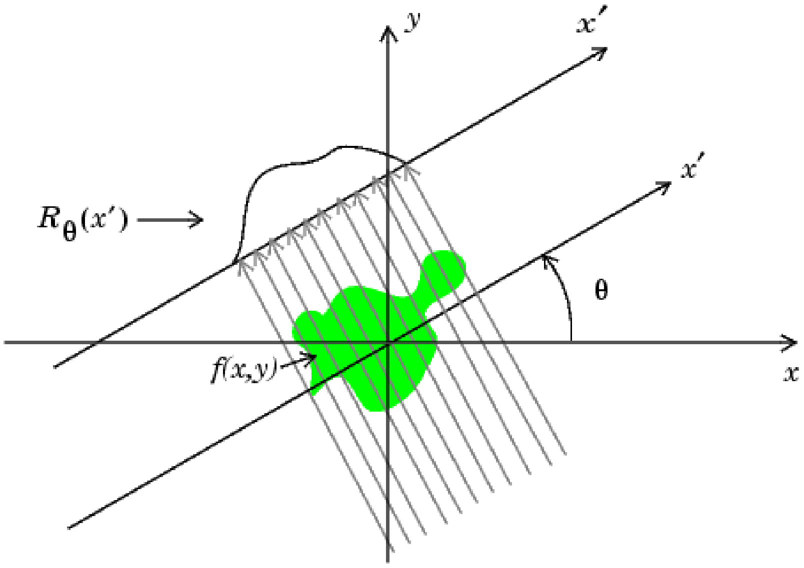

Figure 8.4. Cartoon illustrating the technique of tomography. The sample is colored green. The sample is rotated from its previous orientation by a degree of θ. The parallel arrays represent the neutron beam[249].

8.2.3 MicroCT

Specimens were placed in a 34 mm diameter tube and scanned using a microCT (μCT100 Scanco Medical, Bassersdorf, Switzerland). Scan settings were: voxel size 11.4 μm, 70 kVp, 57 μA, 0.5 mm AL filter, 1250 projections / 180 degrees and integration time 500 ms.

8.3 Results and discussion

8.3.1 Transient hydrogen distribution

During the adsorption of hydrogen in a MOF-5-based storage system, hydrogen will permeate MOF-5. Neutron imaging radiography was used during the adsorption/desorption processes to measure the transient distribution of hydrogen in real time.

In the present experiment a small hydrogen storage vessel was used to represent the tank. The vessel was filled with small, randomly-oriented pellets of nominally pure MOF-5, and hydrogen adsorption/desorption cycling was performed at a temperature 77 K. The inlet/exit for hydrogen was at the top of the vessel.

Figure 8.5 shows the transient hydrogen density distribution during adsorption and desorption using a color-code scheme (black = low/no hydrogen density; red = high hydrogen density). The first panel, Figure 8.5(a) and numbered as frame 77 in a time-ordered sequence is dark. This indicates the presence of little/no hydrogen present in the vessel. As the adsorption progresses in the following frames a color change is observed in the radiography image, indicating that hydrogen is accumulating inside the sample holder.

A closer look at Figure 8.5 (a) reveals a non-uniform distribution of hydrogen in the vessel. For example, the data shows a higher concentration of hydrogen at the top of the vessel, where hydrogen enters. Also, there is a higher concentration near the center of the vessel (along the central vertical axis) than along the edges. This distribution suggests that as hydrogen enters the vessel it is first adsorbed by the pellets near the top entrance. It then spreads more slowly from the top to the bottom.

Figure 8.5 (b) shows the transient hydrogen density distribution during desorption. In a small region close to the bottom of the vessel a higher hydrogen density appears to be present. This is likely an artifact of small movements of the vessel during the imaging process.

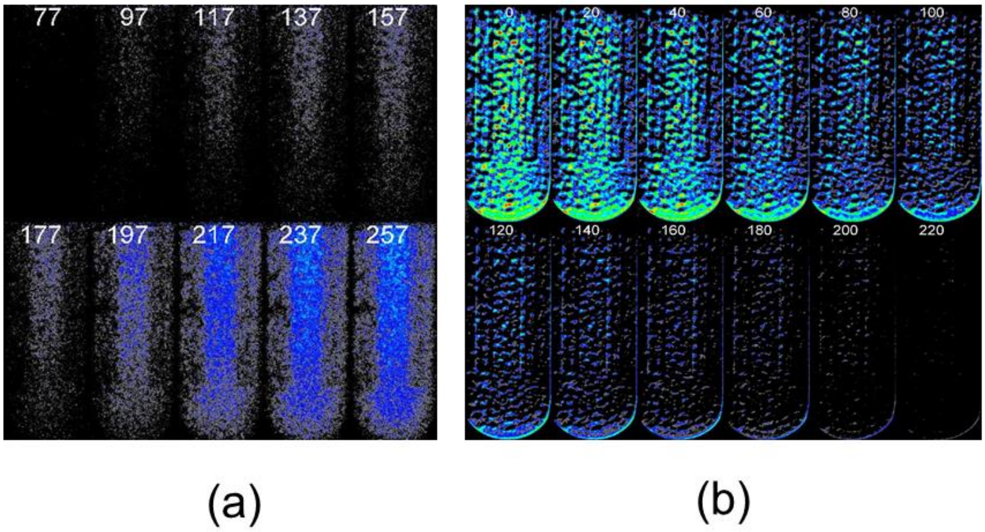

Figure 8.5. (a) Temproal evolution of the hydrogen density distribution in a vessel containing MOF-5 pellets during adsorption. (b) Hydrogen density distribution during desorption. Red represents high hydrogen density, while black represents low hydrogen density.

The transient distribution of hydrogen in a larger MOF-5 puck was also imaged. Neutron radiography images for hydrogen uptake in such a puck are shown in Figure 8.6. Similar to Figure 8.5, black represents low hydrogen density, and red represents high density. At low pressure (0.2-0.3 bar) Fig. 8.5 shows that only a small amount of hydrogen is adsorbed. When the pressure was increased to 3 bar, the color intensity of the radiography image has increased to light blue, indicating increasing adsorbed hydrogen density. As the pressure reaches 9.2 bar, the hydrogen density increases further. In all frames of Figure 8.6, the hydrogen density appears to be uniform across the puck, indicating fast diffusion within the solid.

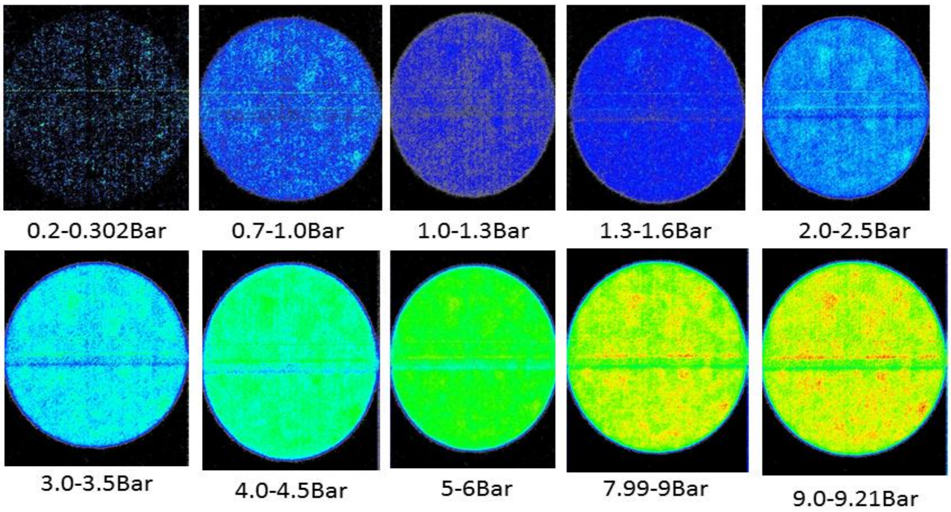

0.2-0.302Bar 0.7-1.0Bar 1.0-1.3Bar 1.3-1.6Bar 2.0-2.5Bar

3.0-3.5Bar 4.0-4.5Bar 5-6Bar 7.99-9Bar 9.0-9.21Bar

Figure 8.6. Transient hydrogen density distribution of a MOF-5 puck. Red stands for higher density, and black stands for lower density.

To quantify the permeation process in more detail, Figure 8.7 shows the hydrogen density as a function of pressure and distance to the center of the pellet. In this calculation the pellet is divided into several rings, each with a width of 1mm, inside of which the average adsorbed hydrogen density is calculated using the method mentioned in section 8.2.2.2. The x-axis represents the distance from pellet center, and the y-axis is the calculated adsorbed hydrogen density averaged over a given ring. Data from images collected at different pressures are included in the graph. It is clear that the average hydrogen density increases as the hydrogen pressure in the sample holder increases. At any given pressure the hydrogen density curve is almost flat across the pellet from center to rim, indicating uniform adsorption within the pellet. This behavior is consistent with the uniformly-colored pellet images shown in Figure 8.6.

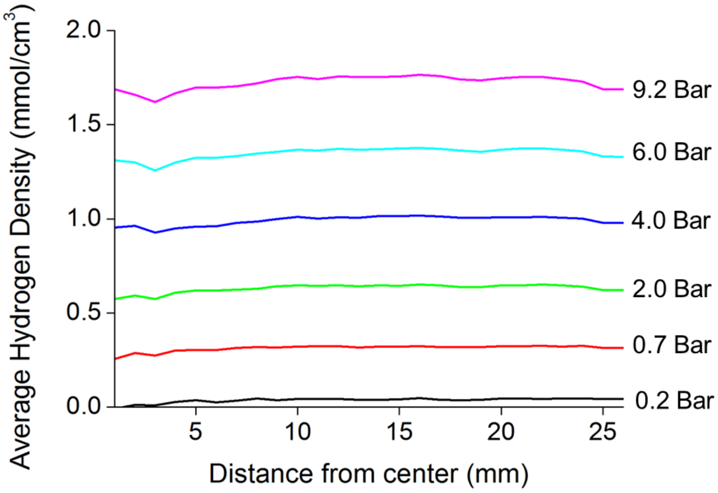

Figure 8.7. Average adsorbed hydrogen density as a function of hydrogen gas pressure and radial distance from pellet center.

8.3.2 Neutron imaging tomography

In this experiment, we use a as sample. Figure 8.8 shows a cross sectional image for a MOF-5 pellet including 10% ENG obtained from neutron imaging tomography. The color bar below the image shows the correspondence between color and attenuation coefficient. The attenuation coefficient can be calculated according to $\mu = \rho \cdot N_A \cdot \sigma / M$, where ρ is the density of the material, N_A is avogadro's number, σ is the neutron scattering cross section, and M is the atomic mass of the material. According to the calculation, ENG particle has an attenuation coefficient of 0.612 cm^{-1}, which is represented by blue in the image. It can be seen that ENG particles are distributed across the pellet cross section, forming network inside the pellet. This network can improve the pellet's thermal conductivity, as demonstrated by previous studies[133, 216].

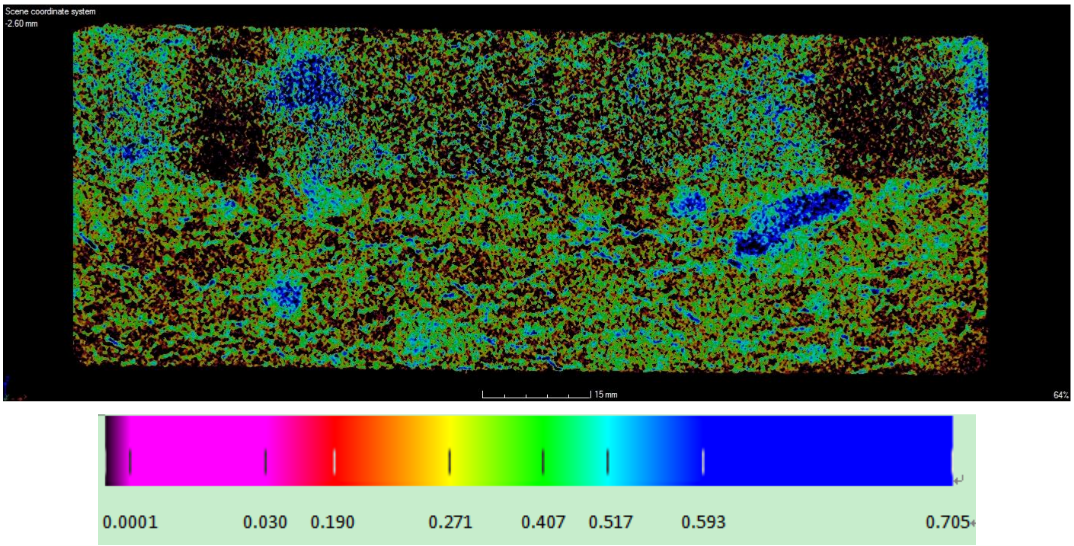

Figure 8.8. Tomography of MOF-5/ENG pellet using neutron imaging technique. The color bar shows the attenuation coefficient.

8.3.3 Density variation

The hydrogen storage media in the MATI system consists of densified "pucks" of MOF-5. These pucks have been compacted to a nominal density of 0.4 g/cc, which is 2 to 3 times the density of tapped powder. We expect that the best performance for these systems will be achieved when the density variation within the pucks is small. The spatial density distribution can be measured using x-ray computed tomography (microCT).

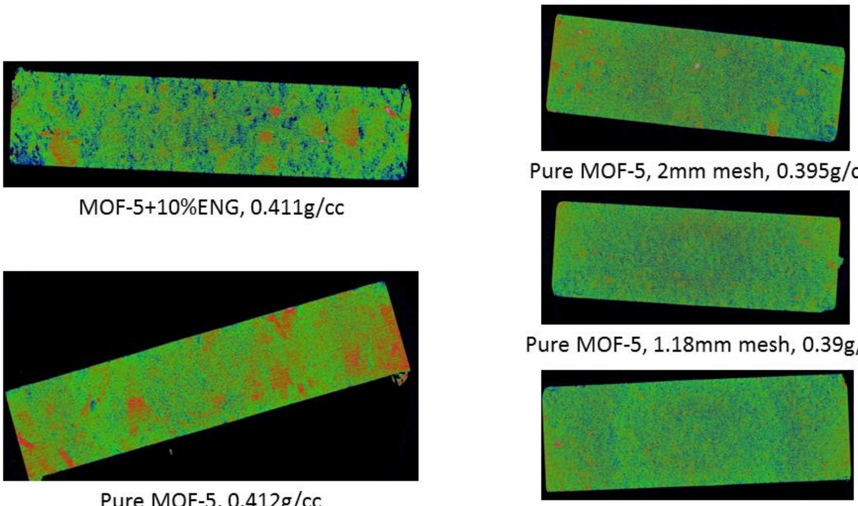

MOF-5+10%ENG, 0.411g/cc

Pure MOF-5, 0.412g/cc

Pure MOF-5, 2mm mesh, 0.395g/cc

Pure MOF-5, 1.18mm mesh, 0.39g/cc

Pure MOF-5, 0.841mm mesh, 0.39g/cc

Figure 8.9. MicroCT tomography images for a MOF-5/ENG pellet, and for several pure MOF-5 pellets fabricated using powders filtered with different mesh sizes. Blue represents regions of low density, while red represents high density.

Figure 8.9 shows several microCT tomography cross-sectional images of MOF-5 pellets having different compositions and pre-treatment conditions. The upper left image corresponds to a MOF-5 pellet containing 10 wt.% ENG. Based on the imaging analysis, this pellet has a relatively large density variation, as evidenced by the presence of regions with either high (red) or low (blue) density. The lower left image of a pellet made from pure MOF-5 also shows large density variation.

To minimize these density variations, a pre-treatment process in which the powders are filtered using meshes of different pore diameter was explored. The resulting tomography images for the pellets made from filtered powders are shown on the right of Figure 8.9. MOF-5 powders for these pellets were filtered with meshes having diameters of 2mm, 1.18mm and 0.841mm (top to bottom in Fig. 8.8). No obvious extreme density regions are obeserved in the filtered systems. Table 8.2 summarizes the standard deviations of the densities of MOF-5 pellets synthesized with and without powder filtering. The standard deviation of the pellet synthesized from the smallest aperture mesh (0.841mm) is almost 1/3 of the pellet for which no pre-meshing was performed.

Table 8.2. Standard deviation in the density of pellets with different filtering pre-treatment. The sizes listed in the left column refer to the aperature size of the mesh used to filter MOF-5 powders before pressing into pellets.

Pellet	Std (g/cc)
No mesh	0.0271
2mm	0.0246
1.18mm	0.0114
0.841mm	0.0107

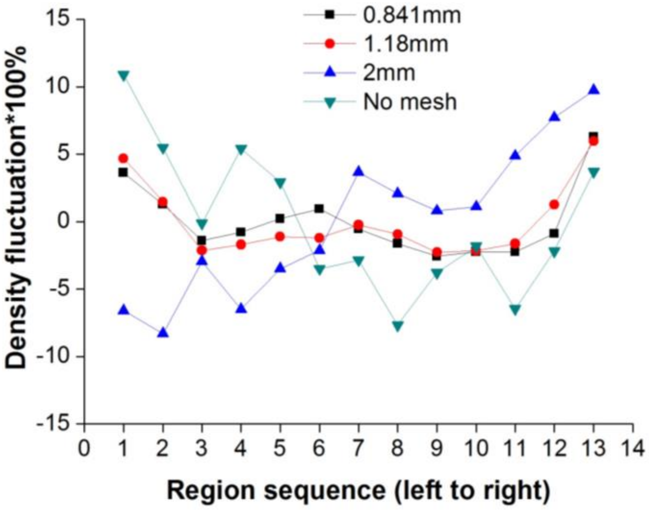

Figure 8.10, Density fluctuation percentage across the cross sections of MOF-5 pellets using different pre-meshing treatments.

The density variation across the cross section of MOF-5 pellets is plotted in Figure 8.10. Here the rectangular sample cross section was divided into 13 samller regions from left to right, and the average density of each region, defined as ρ_n, was calculated. This density was then compared to the average density of the entire cross section, ρ_a. Density fluctuations, F, are plotted along the y-axis, and were calculated using $F = \frac{\rho_n - \rho_a}{\rho_a} \times 100\%$. If the pellet is very uniform, then ρ_n in each region should be very close to ρ_a, which in turn gives F values very close to 0. Density fluctuations in the pellet with 0.841mm and 1.18mm pre-treatment meshing are small, within 2%, except for the two regions at the rim. This indicates that making pellet with meshed MOF-5 powders can improve the density uniformity.

8.4 Conclusion

Metal-organic frameworks (MOFs) are promising materials for use in on-board hydrogen storage systems. In this study we introduce several imaging analysis method to characterize densified versions of MOF-5, such as pucks and pellets. Neutron imaging radiography is used to characterize the transient hydrogen distribution during adsorption and desorption. In these experiments two types of MOF-5 samples were examined: small MOF-5 pellets, and larger MOF-5 pucks. The adsorbed hydrogen density can be monitored both qualitatively and quantitatively. Neutron tomography was used to characterize the ENG network pellets containing 2nd phase additions. Finally, microCT was used to analyze density variations within MOF-5 pellets synthezied using different compositions and pre-treatment conditions. Pellet made from filtered powders exhibited the lowest density variations. The successful application of those imaging analysis methods points out potential ways to improve the performance of systems based on densified MOF media.

Chapter 9

Conclusion

Greenhouse gas emissions, air pollution, and fossil fuel exhaustion are driving the search for environmentally benign fuels. Among the many possible candidates, Hydrogen continues to attract attention as an alternative energy carrier due to its abundance and “clean” combustion products (i.e., water). However, storing hydrogen efficiently at high densities remains a challenge; traditional hydrogen storage methods such as high pressure compression and liquefaction suffer from safety concerns, low efficiencies, and high cost. Storing hydrogen in an adsorbent, is a promising solution to the hydrogen storage problem.

Metal Organic Frameworks (MOFs) are popular candidates for hydrogen storage. MOFs hold the record for specific surface area, and their structure and composition can be varied extensively, resulting in many thousands of known and hypothetical MOFs with a wide range of properties. Among these many possibilities, this study has adopted MOF-5 as a prototype material since it is the most widely studied MOF and can store hydrogen with high gravimetric and volumetric densities. In this thesis we have focused on characterizing and improving mass and heat transport in MOF-5 composites.

9.1 Heat transport in MOF-5

At the first step we measured the basic thermal properties such as thermal conductivity and heat capacity of MOF-5 powders. We learned that the high porosity of MOF-5, and its resulting low intrinsic thermal conductivity, can potentially offset its high H_2 uptake property in cases where efficient heat transport is required. We then established that the high-aspect ratio of second-phase ENG additions, combined with uni-axial compression, results in anisotropic microstructural and thermal transport in composite MOF-5/ENG pellets. Thermal conductivity measurements ranging from cryogenic to ambient temperatures indicated that heat transport perpendicular to the pressing direction is 2 to 4 times higher than in the pressing direction. Furthermore, we demonstrated that this anisotropy could be exploited using two straightforward processing techniques: First, the preferred heat flow path can be reoriented by use of a custom die/compression geometry. Second, fabrication of a layered microstructure with alternating MOF-5 and ENG layers results in a 20x increase in thermal conductivity, at the expense of only minor ENG additions (5 wt.%). These data suggest that the magnitude and preferred direction for thermal transport in MOF compacts may be tuned by altering the processing conditions and nature of the second-phase additions. We speculate that these techniques could also be effective in tailoring mass transport (permeation) within MOF composites.

9.2 Robustness of MOF-5

Regarding the robustness of MOF-5, we explored the effects of humidity and hydrogen fuel station impurities on the degradation of MOF-5.

We have quantified the impact of humid air exposure on the properties of the well-known MOF-5 compound as a function of exposure time, humidity level, and morphology (powders vs. pellets). Properties examined include hydrogen storage capacity, surface area, and crystallinity. Isotherms were measured using a gravimetric technique; we find that the water adsorption/desorption isotherms exhibit a large hysteresis indicative of chemisorption-like binding of H_2O to the MOF-5 framework. The first uptake is consistent with a type V isotherm having a sudden increase in uptake at ~50% relative humidity. We then performed stability assessments slightly below and above this threshold. Below the threshold only minor degradation is observed for exposure times up to several hours, indicating that MOF-5 is more stable than commonly thought under moderately humid conditions. In contrast, irreversible degradation can occur in a matter of minutes at higher humidity. FTIR spectroscopy suggests that molecular and/or dissociated water is inserted into the skeletal framework after long exposure times. Densification into pellets was observed to slow the degradation of MOF-5 significantly, and may present an opportunity to extend the stability window of some MOFs.

Density functional calculations were used to understand the detailed degradation mechanism in MOF-5. Distinguishing features of our calculations are the application of a van der Waals-aware density functional and use of the full MOF-5 primitive cell without any structure simplifications or approximations. Five distince water adsorption sites were investigated. Based on these sites, we then studied different configurations containing multiple adsorbed water molecules. Water molecules preferentially adsorb at adjacent sites rather than filling only low-energy, but dispersed α sites, indicating the importance of water-water interactions during the adsorption process. We examined the energetics of water insertion involving 1 to 4 adsorbed water molecules, and find out that the insertion process is energetically favorable, with an energy barrier of 0.17 eV, when there are 4 water molecules adsorbed on a metal cluster. This study contributes to real application by providing important information about water insertion threshold, which could be taken into account in real life application.

In addition to examining the impact of humidity, we also studied the effect of other impurities on both the hydrogen storage capacity and structural stability of MOF-5. Four impurity hydrogen mixtures were prepared by introducing ammonia, hydrogen sulfide, hydrogen chloride, and water. The impurity levels used in this study exceed the J2719 standard by at least of a factor of 10 for each contaminant. Our measurements show that only the hydrogen chloride-containing mixture yielded a measurable decrease in hydrogen storage capacity (from 6 wt.% to 5.8 wt.%.) during the course of pressure cycle testing at 77 K. No measurable decrease was noted for the other hydrogen impurity mixtures during pressure cycling. Cycling with hydrogen chloride impurities also induced small changes to the MOF-5 crystal structure and local chemical structure. Changes to the chemical bonding structure were also observed for samples cycled with trace ammonia amounts, but changes to the long-range crystal structure or hydrogen storage capacity could not be detected. Static exposure of MOF-5 to water and hydrogen sulfide containing gasses found that both impurities have no measurable effect. These results demonstrate that hydrogen from a fueling station compliant with J2719 standard should not impact the performance of MOF-5 in a hydrogen storage system within 300 cycles and 1 week's static exposure.

9.3 Outlook and Future work

After more than a decade of active research, the discovery of new MOFs continues today at a rapid pace. Although the translation of MOFs from the laboratory to use in a viable hydrogen storage system still faces many challenges, the ability of MOFs to store hydrogen at high densities at low pressure will drive interest in these compounds for years to come. As discussed in this thesis, understanding the transport and robustness properties of these compounds is essential, as these phenomena will strongly impact the cost, efficiency, and manufacturability of systems based on MOF media.

Looking to the future, there are several ways to expand on the present study. Regarding thermal properties, more research is needed to develop additional improvements to the thermal conductivity. In the present study MOF pellets with ENG layers aligned along the axial direction of the pellet were synthesized. The addition of horizontal ENG layers to the pellet would be desirable, as it would create a connected, 3D conducting network. Accomplishing this structuring without degrading the hydrogen capacity (i.e., at low ENG loading) could pose a challenge. Synthesizing a large quantity of these pellets could also be challenging from a cost perspective; reduced cohesion between MOF and ENG particles may lead to less robust pellets which are subject to crumbling. An alternative strategy would be to use higher-conductivity materials in place of ENG. This could be done in the presence or absence of the orientation/layering strategies demonstrated previously for ENG. Finally, MOFs with smaller pore sizes may be intrinsically more thermally conductive than the prototype MOF-5 compound studied here. Little is currently known regarding the thermal transport properties of other MOFs. Atomic scale modeling of how differences in structure across different MOFs correlate with transport could also be pursued.

Regarding the robustness of MOFs, our work has focused on irreversible degradation due to chemical attack by reactive species such as water and ammonia. A related, but much less studied question pertains to robustness to the activation process. Many MOFs are known to retain solvent or salt during synthesis; removing these species is the aim of the "activation" step, which typically involves heating and evacuation of the MOF. However, in many cases it is very difficult to remove these retained species, or even worse, the MOF can undergo pore collapse during activation. An important question is then: why can some MOFs be activated to a pristine state, while for others activation is incomplete, or results in pore collapse? Understanding the factors that control whether a MOF can be synthesized in pristine form would be a major step in the rational design of MOFs for specific applications.

Appendices

A. Supporting information for Anisotropic Thermal Transport in MOF-5 Composites

a) Description of pilot-plant pelletizing process

The pilot-plant pelletizing process involved mixing the MOF-5 powder and ENG worms in a drum blender. The drum was rotated until a homogenous mixture was achieved. Then the powder mixture was compacted into 6 mm tall, 6 mm diameter cylindrical pellets using a mechanical punch. Example pellet morphologies are shown in Figure A.1. In some cases the outer surface of the pellets had a gradient of ENG from the top to bottom due to smearing of ENG within the mold during pellet extraction. The images in the paper show that the ENG gradient on the outer surface is not present within the pellet.

Some breaking of the ENG worms does occur during mixing. It was observed that more ENG is broken during the pilot plant mixing process than in the lab mixing process. The pilot plant mixture shows ENG coating large conglomerates of MOF-5 as shown in Figure A.2. The ENG in both the lab and pilot-plant pellets is distributed evenly within the pellets. The ENG gradient shown in Figure A.1 (right) was shown to be a superficial effect caused by smearing of ENG on the surface of the pilot-plant press.

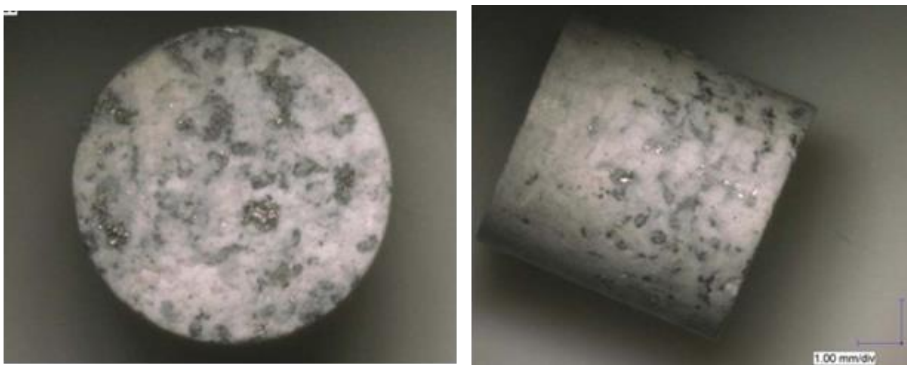

Figure A.1. Pilot-plant pellets 6x6 mm, 5% ENG, density of.391 g/cc with standard deviation of 0.013 g/cm^3. Both top view (left) and side view (right) are shown here.

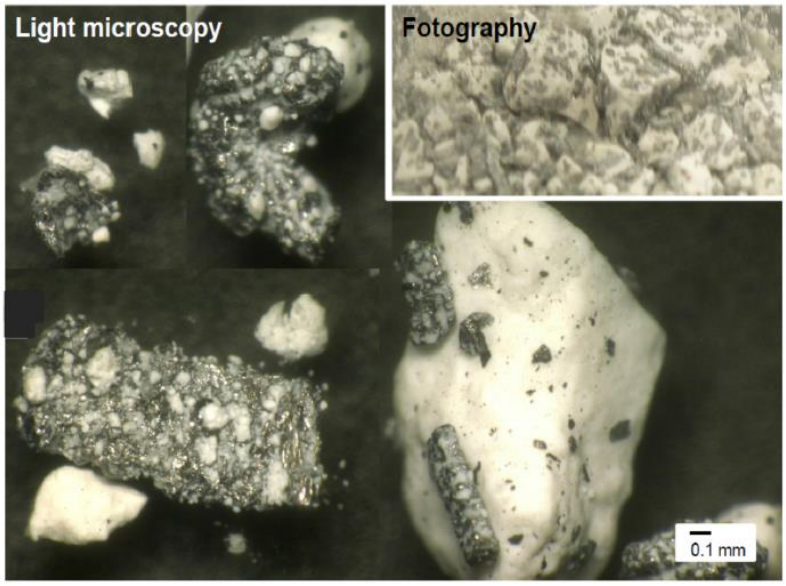

Figure A.2. MOF-5 conglomerates surrounded by ENG particles prior to the compaction of pellets.

b) Sample preparation and imaging details

The pellets were cross sectioned in order to observe the orientation and distribution of ENG using microscopy. The pellets were firmly stabilized, cut with a very thin, sharp blade using evenly applied pressure. Due to the brittle nature of the pellets the sample would occasionally partially crumble while being cut instead of allowing for a clean slice. To prevent this effect, cross sections were also made by embedding pellets in

Epofix or Specifix Resin then slicing with a diamond saw.

Challenges with obtaining SEM images were due to excessive edge charging, area charging and line by line charging. Charging of a sample occurs when there is excessive building up of electrons on a sample surface due to a poor electrical ground connection between the sample and the SEM sample stage. The presence of charging implies that the pellets are poor electrical conductors. To reduce charging the beam current was reduced, low vacuum mode was used and/or the sample was coated with either silver (Ag) or gold (Au). In order to create a better ground connection silver (Ag) or carbon (C) conductive paint was used in addition to conductive tape. Coating the sample was not necessary when using the low vacuum mode with the Quanta SEM. Pellets exposed to air or the SEM chamber environment for an hour or more during the imaging process exhibited large fractures and crumbling of the surface. To delay the degradation of the sample, each cross section was placed in separate Argon filled vials; sample preparation and imaging time was kept to less than one hour.

c) Pellet characterization: Energy Dispersive X-ray Spectroscopy

Dark areas were observed in the micrographs within both the lab and pilot-plant compact pellets. These areas were predicted to be ENG while the white or gray portion was predicted to be MOF-5 based on the images of the individual powders. To confirm the elemental content of the compact pellets Energy Dispersive X-ray Spectroscopy (EDS) was used. Elemental maps of the pellet surface were obtained for C, Zn and O. The individual maps were overlaid and compared to the original image as seen in Figure A.3(a) and 3(b). It was observed that the dark areas, previously assumed to be ENG deposits, correspond to the very carbon dense areas on the map.

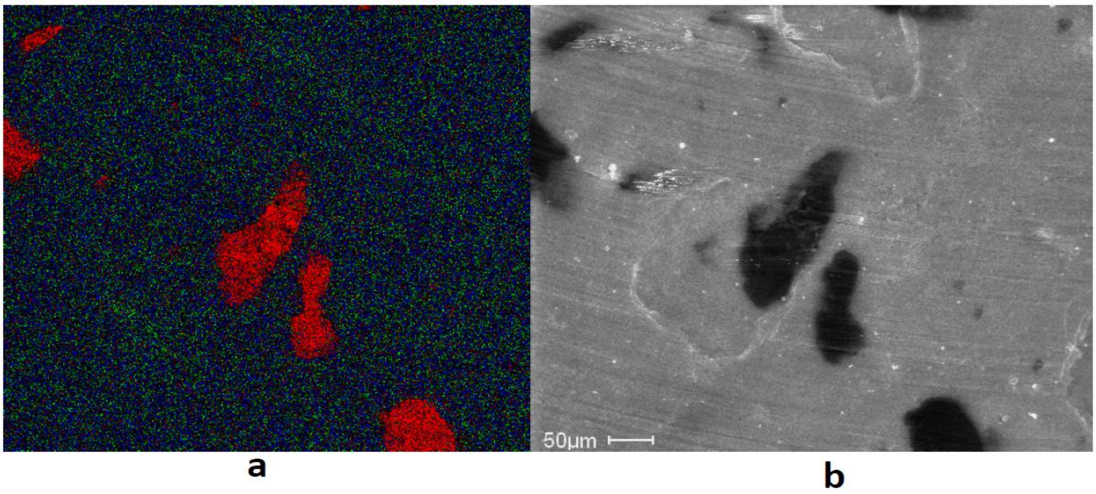

Figure A.3. Quanta SEM used to obtain images with red = Carbon, green = Zinc, blue = Oxygen (a) Elemental map of lab made MOF-5 + 5wt.% ENG pellet with density of 0.5019 g/cc (b) SEM image of area mapped for lab pellet.

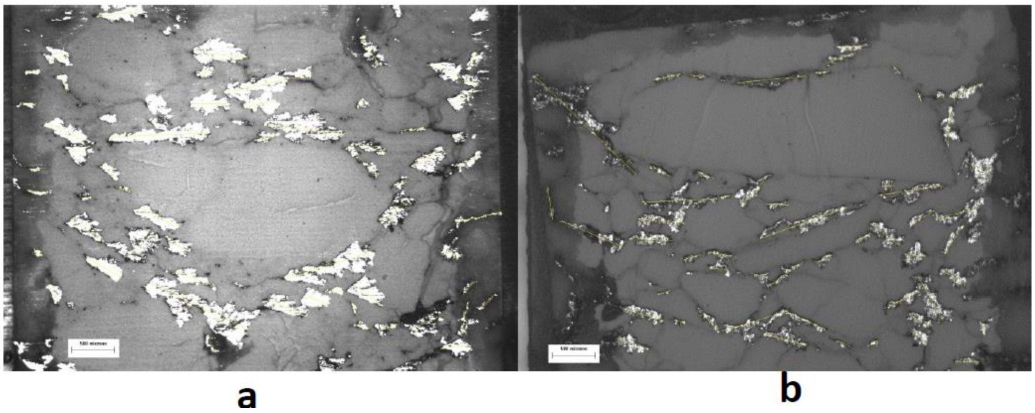

Figure A.4. (a) a lab prepared pellet containing MOF-5 with 5wt% ENG and a density of 0.378g/cc embedded in resin and (b) a pilot plant pellet containing MOF-5 with 5wt% ENG and a density of 0.378g/cm^3 embedded in resin.

Figure A.4 (a) and (b) shows a lab pellet and a pilot plant pellet cross section analyzed using ImageJ software to confirm the anisotropic orientation of the ENG. The angle of ENG relative to the radial orientation is measured then averaged. Eleven pilot plant pellets were analyzed and found to have ENG deposits with an average angle of 27.22 °and a standard deviation of 2.8 °. Comparatively seven lab prepared pellets were analyzed and found to have ENG deposits with an average angle of 23.45 ° and a standard deviation of 2.6 °. The lab and pilot plant were also similar in length of ENG deposits with an average length of 0.32mm (STDEV = 0.04) and 0.39mm (STDEV = 0.08) respectively.

d) Schematic of pressing geometry for cylindrical pellets

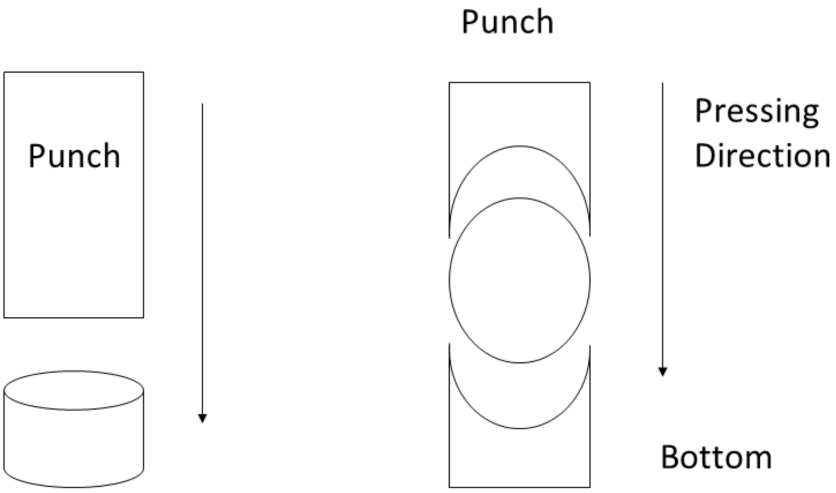

Figure A.5. (Left) Pressing cylindrical pellet along the axial direction. (Right) Pressing cylindrical pellet along the radial direction

e) Thermal couple positions for the steady state heat flow method

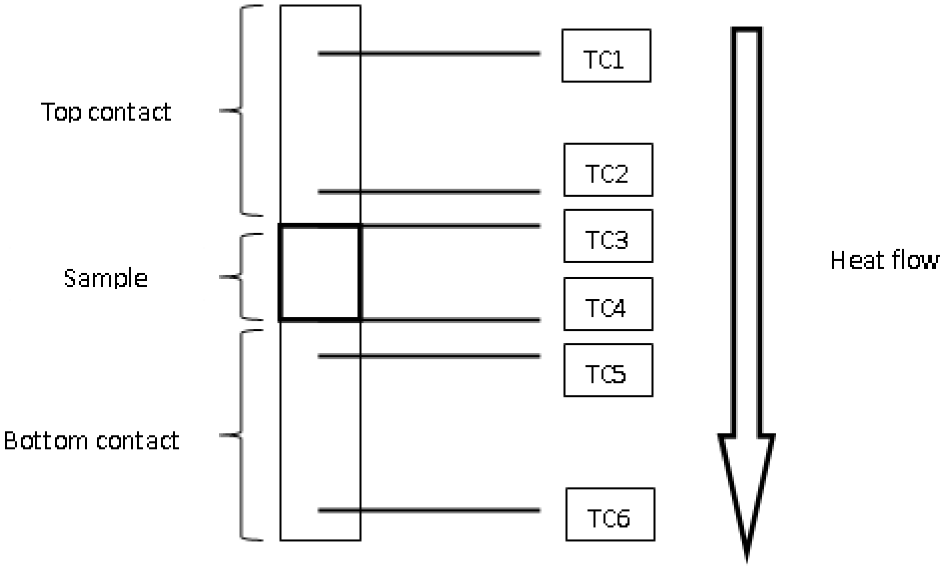

Figure A.6. Thermal couple positions for the steady state heat flow method

B. Supporting information for Kinetic Stability of MOF-5 in Humid Environments: Impact of Powder Densification, Humidity Level, and Exposure Time

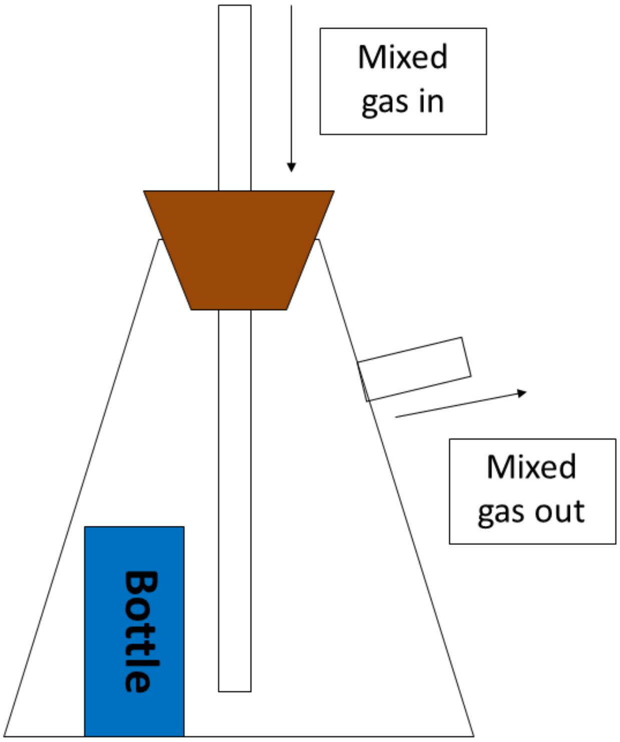

Figure B.1. Geometry of humidity chamber for sample exposure.

C. Supporting information for Water adsorption on, and Insertion into MOF-5

a) Bond Lengths for Water adsorption in IRMOF-0h

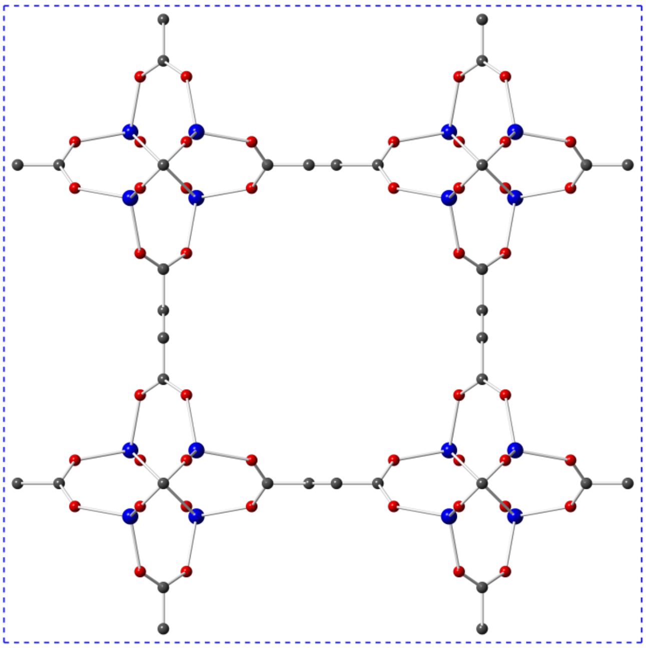

Figure C.1. Crystal structure for the hypothetical MOF, IRMOF-0h, which was used to approximate MOF-5 in Ref. [210]. This structure is a simplification of the MOF-5 structure, wherein the benzene ring present in the MOF-5 linker is replaced with two C atoms. Carbon atoms are grey, oxygen is red, and Zn atoms are shown in blue.

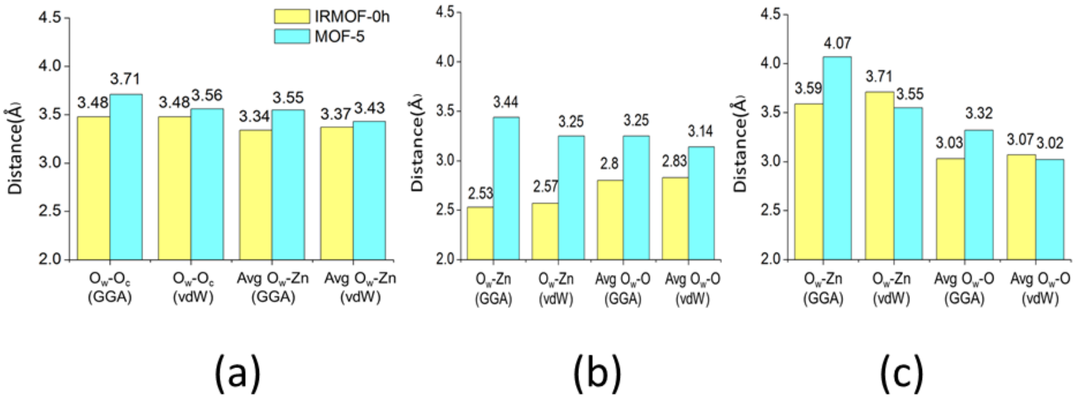

Figure C.2. Calculated distance between certain atom in water and that in MOF-5 metal cluster. Results from GGA and vdW functionals are compared. Panel (a) (b) (c) correspond to site α, β and γ.

b) Estimate of Time Required for Water Insertion into MOF-5

The hydrolysis rate for MOF-5 can be expressed as a product of two probabilities:

$$Rate = P1 \times P2 = Z \cdot A \cdot P * \exp\left(-\frac{E_a}{kT}\right) \qquad \text{(C.1)}$$

Here P1 represents the probability for water vapor to be adsorbed in a configuration amenable to MOF hydrolysis. This term can be expressed as a product of three quantities, *Z, A*, and *P*, which are described in further detail below. P2 is he probability of insertion into the framework from a given adsorbed configuration, and is related to a Boltzmann factor involving the activation energy, exp(-E_a/kT).

The parameter Z represents the rate at which water vapor molecules (assumed to be an ideal gas) collide with a unit area of MOF-5, and is described by the Hertz-Knudsen equation [250]: $Z = \frac{P_{water}}{\sqrt{2\pi mkT}}$. Here P_{water} is the partial pressure of water vapor (taken to be 0.025 mBar), *m* is the molecular mass of water, *k* is the Boltzmann constant, and T is the absolute temperature. Substituting these values yields Z = 9.1×10^{25} s^{-1} m^{-2}. The parameter *A* represents the surface area of 1 g of MOF-5.

Based on experimental measurements [233], a value of 3,800 m^2 is adopted. The product $Z \cdot A$ then gives the number of collisions between water and 1 g MOF-5 per second.

Next we determine the parameter P, which represents the probability that adsorbed water exhibits a local loading and configuration favorable for insertion. Our DFT calculations indicate that a thermodynamic driving force for insertion exists when a minimum of 4 water molecules are simultaneously adsorbed on a Zn-O cluster in close proximity, such as in an ααβγ configuration. Here a cluster is defined as the sum of a Zn-O structural building unit (SBU) and the 6 linkers connected to that SBU. (As each linker is shared with an adjacent SBU, only the half of the linker closest to a given SBU is included in that SBU's cluster.) Each cluster therefore contains 4 Zn, 13 O, 12 H and 24 C atoms. Using tabulated atomic masses, there are 7.8×10^{20} clusters per gram of MOF-5.

The number of molecules of gas-phase air present in the pores of 1 g of MOF-5 can be determined using the density of air (1.2041 kg/m^3 at 1 bar), its average molecular mass (29 amu), and the specific pore volume of MOF-5 (1.27 cm^3/g[180]). According to the ideal gas law, the ratio of the number of water molecules to air molecules is equal to the ratio of partial pressures: $n_{water}:n_{air} = P_{water}:P_{air}$. Together, these data allow us to estimate the number of water molecules in the pore: 7.9×10^{17}.

The foregoing analysis indicates that the number of MOF-5 clusters is 1000 times larger than the number of gas phase water molecules under the stated conditions. Assuming that diffusion is fast enough such that any water molecule can access/adsorb on any cluster, then the probability that four molecules adsorb on the same cluster is 10^{-9}. Furthermore, the probability that these 4 water molecules fill ααβγ sites is given by: $\frac{C_{4\cdot}^{2}C_{4\cdot}^{1}C_{12\cdot}^{1}}{C_{32\cdot}^{4}} = 0.008$, assuming that adsorption can occur on these sites with equal probability. Here, the terms C_n^k refer to the number of combinations associated with filling *k* sites out of the *n* available on a given cluster. In the numerator the subscripts *n* reflect the fact that each cluster contains 4 α sites, 4 β sites, and 12 γ sites. (The subscript '32' in the denominator counts the total number of adsorption sites, including δ and ε sites on the linker.) Finally, the total probability for four water vapor molecules to be adsorbed at ααβγ sites is: $P = 10^{-9} \cdot \frac{C_{4\cdot}^{2}C_{4\cdot}^{1}C_{12\cdot}^{1}}{C_{32\cdot}^{4}} = 8*10^{-12}$. With this, we now have enough information to evaluate equation (C.1).

According to our previous experiments [220], water uptake of MOF-5 saturates at 12 wt.%. This water does not desorb when the relative humidity is subsequently lowered, indicating that the uptake is irreversible. Water uptake coincides with the emergence of new peaks in the MOF-5 x-ray diffraction pattern and FT-IR spectra; it is therefore highly likely that this water has been inserted into the MOF-5 crystal structure via hydrolysis. For 1 g of MOF-5, the expected saturated water loading is 0.0072 mols, or $N = 4.04*10^{21}$ molecules. Dividing this loading by the rate (equation (C.1), yields an estimate for the average insertion time, t = N/rate = 286 hours.

D. Stability of MOF-5 in a hydrogen gas environment with expected fueling station impurities

a) Hydrogen uptake isotherm at 77K for 300 cycles, XRD and FTIR spectra of H_2S as impurity

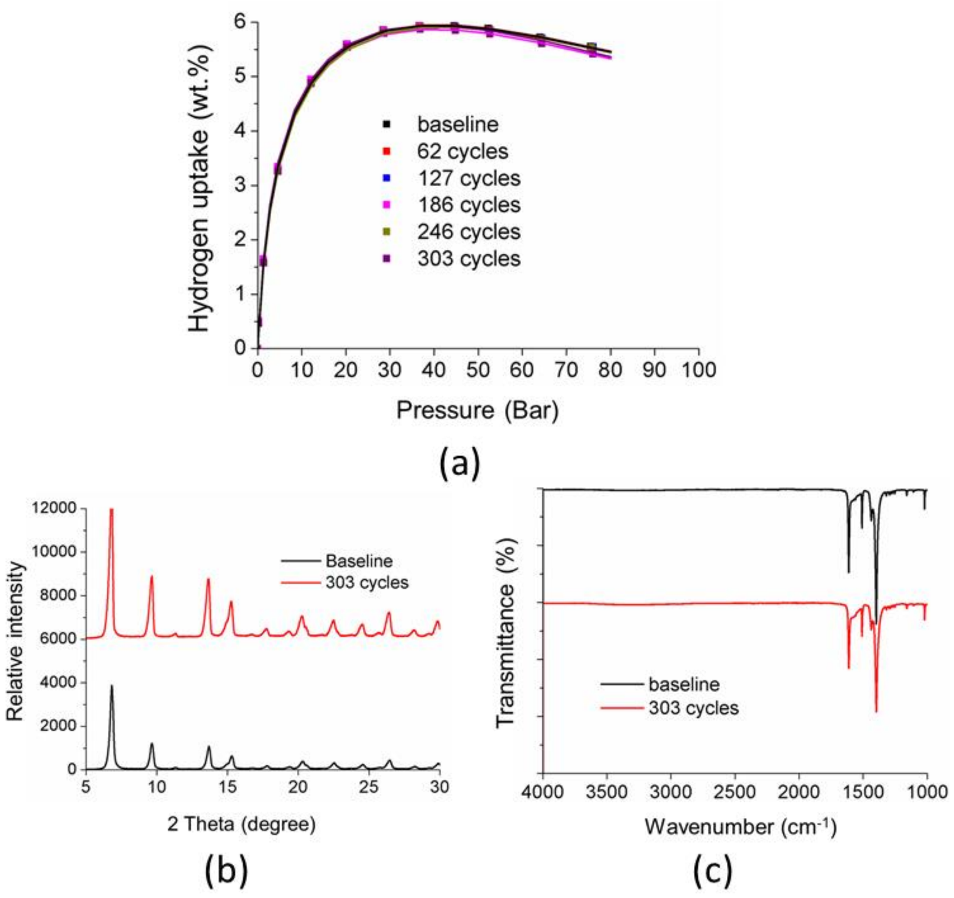

Figure D.1. (a) Adsorption isotherm of MOF-5 powders with test gas mixture 2 including H_2S as the impurity. Capacity measurement are taken every 60 cycles (b) XRD spectra for MOF-5 powders before and after cycle test (c) FTIR spectra for MOF-5 powders before and after cycle test.

b) Hydrogen uptake isotherm at 77K for 300 cycles, XRD and FTIR spectra of H_2O as impurity

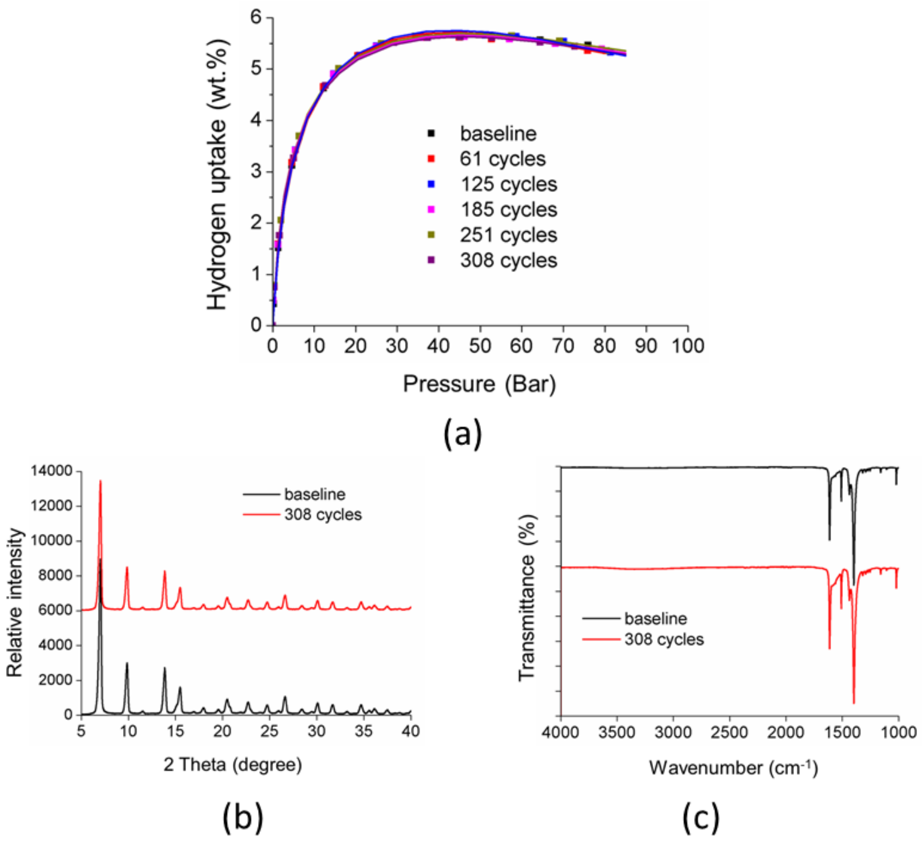

Figure D.2. (a) Adsorption isotherm of MOF-5 powders on with testing gas mixture 4 including H2O as the impurity. Capacity measurement are taken every 60 cycles (b) XRD spectra for MOF-5 powders before and after cycle test (c) FTIR spectra for MOF-5 powders before and after cycle test.

c) Hydrogen uptake isotherm at 77K for 300 cycles, XRD and FTIR spectra of gas mixture 5

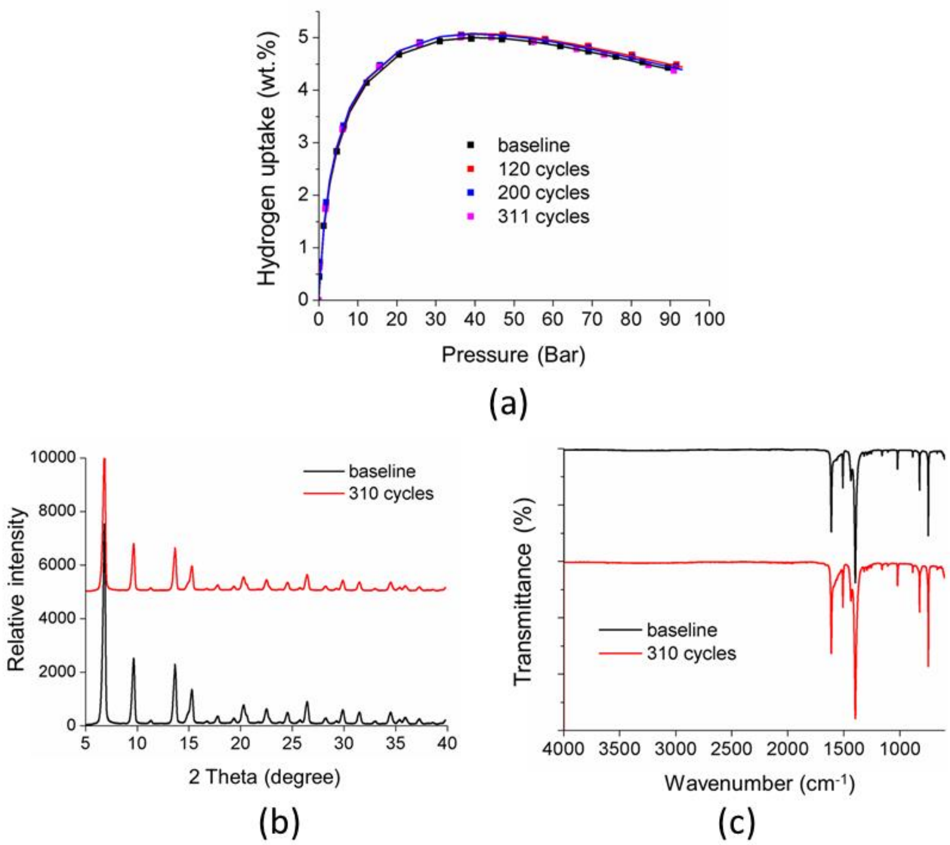

(a)

(b)

(c)

Figure D.3. (a) Adsorption isotherm of MOF-5 powders on with testing gas mixture 5 including CO, CO2, CH4, O2, N2, and He as the impuritiesy. Capacity measurement are taken every 60 cycles (b) XRD spectra for MOF-5 powders before and after cycle test (c) FTIR spectra for MOF-5 powders before and after cycle test.

Bibliography

[1] http://instituteforenergyresearch.org/topics/encyclopedia/fossil-fuels/.

[2] I.P.o.C. Change, Climate Change 2013: The Physical Sicience Basic, in, New York, USA, 2013.

[3] "Enhanced greenhouse effect — Glossary", Australian Academy of Scihuman impact on the environment, (2006).

[4] "Enhanced Greenhouse Effect", Ace.mmu.ac.uk, (Retrieved 2010-10-15).

[5] A.C.D.M.L. NOAA.

[6] P.K.R.E.G.M.D. Tans, (http://www.esrl.noaa.gov/gmd/ccgg/trends/ (accessed at May 27, 2015)).

[7] C.e.a. Le Quéré, The global carbon budget 1959-2011, (2013).

[8] http://en.wikipedia.org/wiki/Air_pollution.

[9] E.E.A. (EEA), National emissions reported to the Convention on Long-range Transboundary Air Pollution, (2011).

[10] U.S.E.P. AGENCY, National Summary of Sulfur Dioxide Emissions, (2011).

[11] M.T. Halbouty, Giant Oil and Gas Fields of the Decade, 1990-1999, (2003).

[12] "Reserves to Production Ratio", Investopedia, (2009).

[13] BP Statistical Review of World Energy, bp.com/statisticalreview, (2014).

[14] Wikipedia, Hydrogen fuel, http://en.wikipedia.org/wiki/Hydrogen_fuel.

[15] F.S.E.C. (n.d.). Hydrogen Basics., http://www.fsec.ucf.edu/en/consumer/hydrogen/basics/index.htm.

[16] “Module 1, Hydrogen Properties”, Hydrogen Properties.

[17] I. Energy, List of common conversion factors (Engineering conversion factors), (Retrieved 2008-10-05).

[18] Compressed Hydrogen Storage.

[19] U.E. Bossel, Baldur Energy and the Hydrogen Economy.

[20] J. Yang, A. Sudik, C. Wolverton, D.J. Siegel, High capacity hydrogen storage materials: attributes for automotive applications and techniques for materials discovery, Chemical Society Reviews, 39(2) (2010) 656-675.

[21] B.C. Kamel Bennaceur, Franklin M. Orr, Jr, T. S. Ramakrishnan, Claude Roulet, Ellen Stout, Hydrogen: A Future Energy Carrier, Oilfield Review, (2005).

[22] P.p.a.S.I.f.H.D. Workshop, Hydrogen Delivery, Liquefaction and Compression, http://www1.eere.energy.gov/hydrogenandfuelcells/pdfs/liquefaction_comp_pres_praxair.pdf, (May 7, 2003).

[23] B. Bogdanović, M. Schwickardi, Ti-doped alkali metal aluminium hydrides as potential novel reversible hydrogen storage materials1, Journal of Alloys and Compounds, 253–254(0) (1997) 1-9.

[24] J. Graetz, Metastable Metal Hydrides for Hydrogen Storage, ISRN Materials Science, 2012 (2012) 18.

[25] L. Schlapbach, A. Zuttel, Hydrogen-storage materials for mobile applications, Nature, 414(6861) (2001) 353-358.

[26] B. Sakintuna, F. Lamari-Darkrim, M. Hirscher, Metal hydride materials for solid hydrogen storage: A review, International Journal of Hydrogen Energy, 32(9) (2007) 1121-1140.

[27] A. Züttel, P. Wenger, S. Rentsch, P. Sudan, P. Mauron, C. Emmenegger, LiBH4 a new hydrogen storage material, Journal of Power Sources, 118(1–2) (2003) 1-7.

[28] P. Chen, Z. Xiong, J. Luo, J. Lin, K.L. Tan, Interaction of hydrogen with metal nitrides and imides, Nature, 420(6913) (2002) 302-304.

[29] S.-i. Orimo, Y. Nakamori, J.R. Eliseo, A. Zuettel, C.M. Jensen, Complex hydrides for hydrogen storage, Chemical Reviews, 107(10) (2007) 4111-4132.

[30] W. Grochala, P.P. Edwards, Thermal decomposition of the non-interstitial hydrides for the storage and production of hydrogen, Chemical Reviews, 104(3) (2004) 1283-1315.

[31] E. Poirier, R. Chahine, P. Benard, L. Lafi, G. Dorval-Douville, P.A. Chandonia, Hydrogen adsorption measurements and modeling on metal-organic frameworks and single-walled carbon nanotubes, Langmuir, 22(21) (2006) 8784-8789.

[32] R. Stroebel, J. Garche, P.T. Moseley, L. Joerissen, G. Wolf, Hydrogen storage by carbon materials, Journal Of Power Sources, 159(2) (2006) 781-801.

[33] Y.F. Zhao, Y.H. Kim, A.C. Dillon, M.J. Heben, S.B. Zhang, Hydrogen storage in novel organometallic buckyballs, Physical Review Letters, 94(15) (2005).

[34] A.C. Dillon, M.J. Heben, Hydrogen storage using carbon adsorbents: past, present and future, Applied Physics a-Materials Science & Processing, 72(2) (2001) 133-142.

[35] R. Chahine, T.K. Bose, LOW-PRESSURE ADSORPTION STORAGE OF HYDROGEN, International Journal Of Hydrogen Energy, 19(2) (1994) 161-164.

[36] H. Li, M. Eddaoudi, M. O'Keeffe, O.M. Yaghi, Design and synthesis of an exceptionally stable and highly porous metal-organic framework, Nature, 402(6759) (1999) 276-279.

[37] M. Eddaoudi, D.B. Moler, H.L. Li, B.L. Chen, T.M. Reineke, M. O'Keeffe, O.M. Yaghi, Modular chemistry: Secondary building units as a basis for the design of highly porous and robust metal-organic carboxylate frameworks, Accounts Of Chemical Research, 34(4) (2001) 319-330.

[38] F.H. Stephens, V. Pons, R.T. Baker, Ammonia - borane: the hydrogen source par excellence?, Dalton Transactions, (25) (2007) 2613-2626.

[39] Q. Zhang, G.M. Smith, Y. Wu, Catalytic hydrolysis of sodium borohydride in an integrated reactor for hydrogen generation, International Journal of Hydrogen Energy, 32(18) (2007) 4731-4735.

[40] C.W. Hamilton, R.T. Baker, A. Staubitz, I. Manners, B-N compounds for chemical hydrogen storage, Chemical Society Reviews, 38(1) (2009) 279-293.

[41] T.B. Marder, Will we soon be fueling our automobiles with ammonia-borane?,

Angewandte Chemie-International Edition, 46(43) (2007) 8116-8118.

[42] D.H. Everett, Pure Appl. Chem., 31(4) (1972) 577.

[43] G. Ferey, Hybrid porous solids: past, present, future, Chem. Soc. Rev., 37(1) (2008) 191-214.

[44] J.L.C. Rowsell, O.M. Yaghi, Metal–organic frameworks: a new class of porous materials, Microporous Mesoporous Mater., 73(1-2) (2004) 3-14.

[45] S.R. Batten, S.M. Neville, D.R. Turner, Coordination Polymers: Design, Synthesis, and Application, 2009.

[46] M.C. Hong, L. Chen, Design and Construction of Coordination Polymers, 2009.

[47] J.R. Long, O.M. Yaghi, The pervasive chemistry of metal-organic frameworks, Chem. Soc. Rev., 38(5) (2009) 1213-1214.

[48] O.K. Farha, I. Eryazici, N.C. Jeong, B.G. Hauser, C.E. Wilmer, A.A. Sarjeant, R.Q. Snurr, S.T. Nguyen, A.Ö. Yazaydın, J.T. Hupp, Metal–Organic Framework Materials with Ultrahigh Surface Areas: Is the Sky the Limit?, J. Am. Chem. Soc., 134(36) (2012) 15016-15021.

[49] O.K. Farha, A. Özgür Yazaydın, I. Eryazici, C.D. Malliakas, B.G. Hauser, M.G. Kanatzidis, S.T. Nguyen, R.Q. Snurr, J.T. Hupp, De novo synthesis of a metal–organic framework material featuring ultrahigh surface area and gas storage capacities, Nat Chem, 2(11) (2010) 944-948.

[50] K. Koh, A.G. Wong-Foy, A.J. Matzger, A Porous Coordination Copolymer with over 5000 m2/g BET Surface Area, J. Am. Chem. Soc., 131(12) (2009) 4184-4185.

[51] B. Panella, M. Hirscher, S. Roth, Hydrogen adsorption in different carbon nanostructures, Carbon, 43(10) (2005) 2209-2214.

[52] M. Hirscher, B. Panella, Hydrogen storage in metal-organic frameworks, Scripta Materialia, 56(10) (2007) 809-812.

[53] D.J. Collins, H.C. Zhou, Hydrogen storage in metal-organic frameworks, Journal Of Materials Chemistry, 17(30) (2007) 3154-3160.

[54] R.J. Kuppler, D.J. Timmons, Q.-R. Fang, J.-R. Li, T.A. Makal, M.D. Young, D. Yuan, D. Zhao, W. Zhuang, H.-C. Zhou, Potential applications of metal-organic frameworks, Coordination Chemistry Reviews, 253(23–24) (2009) 3042-3066.

[55] D.J. Tranchemontagne, J.L. Mendoza-Cortes, M. O'Keeffe, O.M. Yaghi, Secondary building units, nets and bonding in the chemistry of metal-organic frameworks, Chem. Soc. Rev., 38(5) (2009) 1257-1283.

[56] C.E. Wilmer, M. Leaf, C.Y. Lee, O.K. Farha, B.G. Hauser, J.T. Hupp, R.Q. Snurr, Large-scale screening of hypothetical metal–organic frameworks, Nat Chem, 4(2) (2012) 83-89.

[57] S. Ma, H.-C. Zhou, Gas storage in porous metal-organic frameworks for clean energy applications, Chem. Commun., 46(1) (2010) 44-53.

[58] T.-H. Park, K.A. Cychosz, A.G. Wong-Foy, A. Dailly, A.J. Matzger, Gas and liquid phase adsorption in isostructural Cu3[biaryltricarboxylate]2 microporous coordination polymers, Chem. Commun., 47(5) (2011) 1452-1454.

[59] L. Huang, H. Wang, J. Chen, Z. Wang, J. Sun, D. Zhao, Y. Yan, Synthesis,

morphology control, and properties of porous metal–organic coordination polymers, Microporous and Mesoporous Materials, 58(2) (2003) 105-114.

[60] J.L.C. Rowsell, A.R. Millward, K.S. Park, O.M. Yaghi, Hydrogen Sorption in Functionalized Metal−Organic Frameworks, Journal of the American Chemical Society, 126(18) (2004) 5666-5667.

[61] M. Eddaoudi, D.B. Moler, H. Li, B. Chen, T.M. Reineke, M. O'Keeffe, O.M. Yaghi, Modular Chemistry: Secondary Building Units as a Basis for the Design of Highly Porous and Robust Metal−Organic Carboxylate Frameworks, Accounts of Chemical Research, 34(4) (2001) 319-330.

[62] B. Panella, M. Hirscher, Hydrogen Physisorption in Metal–Organic Porous Crystals, Advanced Materials, 17(5) (2005) 538-541.

[63] M. Jacoby, HEADING TO MARKET WITH MOFS, Chemical & Engineering News Archive, 86(34) (2008) 13-16.

[64] M. Gaab, N. Trukhan, S. Maurer, R. Gummaraju, U. Müller, The progression of Al-based metal-organic frameworks – From academic research to industrial production and applications, Microporous and Mesoporous Materials, 157(0) (2012) 131-136.

[65] A.V. Neimark, P.I. Ravikovitch, Calibration of Pore Volume in Adsorption Experiments and Theoretical Models, Langmuir, 13(19) (1997) 5148-5160.

[66] S. Brunauer, The adsorption of gases and vapors, Princeton University Press, (1943).

[67] A.R. Miller, The Adsorption of Gases on Solids, Cambridge University Press, (1949).

[68] P.d.H. Griffiths, J.A., Fourier Transform Infrared Spectrometry (2nd ed.), Wiley-Blackwell, ISBN 0-471-19404-2 (18 May 2007).

[69] J. Hone, M. Whitney, C. Piskoti, A. Zettl, Thermal conductivity of single-walled carbon nanotubes, Physical Review B, 59(4) (1999) R2514-R2516.

[70] T. Ashworth, Smith, David R., Thermal Conductivity 18, in, 1985.

[71] H. Chi, C. Chen, J.D. Phillips, C. Uher, Transport properties of ZnTe:N thin films, Applied Physics Letters, 103(4) (2013) -.

[72] K.J. Zhang, A. Yadav, K.H. Kim, Y. Oh, M.F. Islam, C. Uher, K.P. Pipe, Thermal and Electrical Transport in Ultralow Density Single-Walled Carbon Nanotube Networks, Advanced Materials, 25(21) (2013) 2926-2931.

[73] W.J. Parker, R.J. Jenkins, C.P. Butler, G.L. Abbott, Flash Method of Determining Thermal Diffusivity, Heat Capacity, and Thermal Conductivity, Journal of Applied Physics, 32(9) (1961) 1679-1684.

[74] R.D. Cowan, Pulse Method of Measuring Thermal Diffusivity at High Temperatures, Journal of Applied Physics, 34(4) (1963) 926-927.

[75] J.A. Cape, G.W. Lehman, Temperature and Finite Pulse‐Time Effects in the Flash Method for Measuring Thermal Diffusivity, Journal of Applied Physics, 34(7) (1963) 1909-1913.

[76] J.O. Blumm, J. , Improvement of the mathematical modeling of flash measurements, High Temperatures - High Pressures, 34(5) (2002) 515 – 521.

[77] U.S. Patent 3, 484.

[78] P. Hohenberg, W. Kohn, Inhomogeneous Electron Gas, Physical Review, 136(3B) (1964) B864-B871.

[79] W. Kohn, L.J. Sham, Self-Consistent Equations Including Exchange and Correlation Effects, Physical Review, 140(4A) (1965) A1133-A1138.

[80] M. Born, R. Oppenheimer, Zur Quantentheorie der Molekeln, Annalen der Physik, 389(20) (1927) 457-484.

[81] D. CEPERLEY, B. ALDER, Quantum Monte Carlo, Science, 231(4738) (1986) 555-560.

[82] J.P. Perdew, K. Burke, M. Ernzerhof, Generalized Gradient Approximation Made Simple, Physical Review Letters, 77(18) (1996) 3865-3868.

[83] H. Wu, J.M. Simmons, G. Srinivas, W. Zhou, T. Yildirim, Adsorption Sites and Binding Nature of CO2 in Prototypical Metal−Organic Frameworks: A Combined Neutron Diffraction and First-Principles Study, J. Phys. Chem. Lett., 1(13) (2010) 1946-1951.

[84] Y.Y. Sun, Y.-H. Kim, K. Lee, S.B. Zhang, Accurate and efficient calculation of van der Waals interactions within density functional theory by local atomic potential approach, J. Chem. Phys., 129(15) (2008) 154102-154108.

[85] S.D. Chakarova-Käck, E. Schröder, B.I. Lundqvist, D.C. Langreth, Phys. Rev. Lett., 96 (2006) 146107.

[86] B. Jeziorski, R. Moszynski, K. Szalewicz, Chem. Rev., 94 (1994) 1887.

[87] A. Heelmann, G. Jansen, Phys. Chem. Chem. Phys., 5 (2003) 5010.

[88] A.J. Misquitta, B. Jeziorski, K. Szalewicz, Phys. Rev. Lett., 91 (2003) 033201-033201.

[89] V.P. Osinga, S.J.A. van Gisbergen, J.G. Snijders, E.J. Baerends, J. Chem. Phys., 106 (1997) 5091.

[90] A. Tkatchenko, R.A. DiStasio, R. Car, M. Scheffler, Phys. Rev. Lett., 108 (2012) 236402-236401.

[91] A. Tkatchenko, M. Schefer, Phys. Rev. Lett., 102 (2009) 073005.

[92] O. Bludský, M. Rubens, P. Soldán, P. Nachtigall, J. Chem. Phys., 128 (2008) 114102.

[93] S. Grimme, Accurate description of van der Waals complexes by density functional theory including empirical corrections, J. Comput. Chem., 25(12) (2004) 1463-1473.

[94] S. Grimme, Semiempirical GGA-type density functional constructed with a long-range dispersion correction, J. Comput. Chem., 27(15) (2006) 1787-1799.

[95] S. Grimme, J. Antony, S. Ehrlich, H. Krieg, J. Chem. Phys., 132 (2010) 154104-154101.

[96] M. Dion, H. Rydberg, E. Schröder, D.C. Langreth, B.I. Lundqvist, Van der Waals Density Functional for General Geometries, Physical Review Letters, 92(24) (2004) 246401.

[97] T. Bučko, J. Hafner, S. Lebègue, J.G. Ángyán, J. Phys. Chem. A, 114 (2010)

11814.

[98] N. Atodiresei, V. Caciuc, J.H. Franke, S. Blügel, Phys. Rev. B, 78 (2008) 045411.

[99] T. Kerber, M. Sierka, J. Sauer, J. Comput. Chem., 29 (2008) 2088.

[100] G. Román-Pérez, J.M. Soler, Phys. Rev. Lett., 103 (2009) 096102-096101.

[101] G.R. Jennes, O. Karalti, W.A. Al-Saiadi, K.D. Jordan, J. Phys. Chem. A, 115 (2011) 5955.

[102] D. Bohm, D. Pines, Phys. Rev., 92 (1953) 609.

[103] J.L.C. Rowsell, O.M. Yaghi, Metal–organic frameworks: a new class of porous materials, Microporous and Mesoporous Materials, 73(1–2) (2004) 3-14.

[104] M.P. Suh, H.J. Park, T.K. Prasad, D.W. Lim, Hydrogen storage in metal-organic frameworks, Chemical Reviews, 112(2) (2012) 782-835.

[105] S.T. Meek, J.A. Greathouse, M.D. Allendorf, Metal-organic frameworks: A rapidly growing class of versatile nanoporous materials, Advanced Materials, 23(2) (2011) 249-267.

[106] A.U. Czaja, N. Trukhan, U. Müller, Industrial applications of metal-organic frameworks, Chemical Society Reviews, 38(5) (2009) 1284-1293.

[107] C. Wang, D. Liu, W. Lin, Metal-organic frameworks as a tunable platform for designing functional molecular materials, Journal of the American Chemical Society, 135(36) (2013) 13222-13234.

[108] J.Y. Jung, F. Karadas, S. Zulfiqar, E. Deniz, S. Aparicio, M. Atilhan, C.T. Yavuz, S.M. Han, Limitations and high pressure behavior of MOF-5 for CO2 capture, Physical Chemistry Chemical Physics, 15(34) (2013) 14319-14327.

[109] Y. Yu, Y. Ren, W. Shen, H. Deng, Z. Gao, Applications of metal-organic frameworks as stationary phases in chromatography, TrAC - Trends in Analytical Chemistry, 50 (2013) 33-41.

[110] M. Sindoro, A.Y. Jee, S. Granick, Shape-selected colloidal MOF crystals for aqueous use, Chemical Communications, 49(83) (2013) 9576-9578.

[111] N.T.S. Phan, P.H.L. Vu, T.T. Nguyen, Expanding applications of copper-based metal-organic frameworks in catalysis: Oxidative C-O coupling by direct C-H activation of ethers over Cu2(BPDC)2(BPY) as an efficient heterogeneous catalyst, Journal of Catalysis, 306 (2013) 38-46.

[112] L.J. Murray, M. Dinc, J.R. Long, Hydrogen storage in metal-organic frameworks, Chemical Society Reviews, 38(5) (2009) 1294-1314.

[113] J.L.C. Rowsell, O.M. Yaghi, Strategies for hydrogen storage in metal-organic frameworks, Angewandte Chemie - International Edition, 44(30) (2005) 4670-4679.

[114] R.K. Ahluwalia, J.K. Peng, Automotive hydrogen storage system using cryo-adsorption on activated carbon, International Journal of Hydrogen Energy, 34(13) (2009) 5476-5487.

[115] M. Lamari, A. Aoufi, P. Malbrunot, Thermal effects in dynamic storage of hydrogen by adsorption, AIChE Journal, 46(3) (2000) 632-646.

[116] L. Huang, H. Wang, J. Chen, Z. Wang, J. Sun, D. Zhao, Y. Yan, Synthesis, morphology control, and properties of porous metal-organic coordination polymers,

Microporous and Mesoporous Materials, 58(2) (2003) 105-114.

[117] M. Eddaoudi, D.B. Moler, H. Li, B. Chen, T.M. Reineke, M. O'Keeffe, O.M. Yaghi, Modular chemistry: Secondary building units as a basis for the design of highly porous and robust metal-organic carboxylate frameworks, Accounts of Chemical Research, 34(4) (2001) 319-330.

[118] B. Panella, M. Hirscher, Hydrogen physisorption in metal-organic porous crystals, Advanced Materials, 17(5) (2005) 538-541.

[119] M. Jacoby, Heading to market with MOFS, Chemical and Engineering News, 86(34) (2008) 13-16.

[120] M. Gaab, N. Trukhan, S. Maurer, R. Gummaraju, U. Müller, The progression of Al-based metal-organic frameworks - From academic research to industrial production and applications, Microporous and Mesoporous Materials, 157 (2012) 131-136.

[121] H. Li, M. Eddaoudi, M. O'Keeffe, O.M. Yaghi, Design and synthesis of an exceptionally stable and highly porous metal- organic framework, Nature, 402(6759) (1999) 276-279.

[122] M.M. Dubinin, V.A. Astakhov, Description of Adsorption Equilibria of Vapors on Zeolites over Wide Ranges of Temperature and Pressure, in: Molecular Sieve Zeolites-II, AMERICAN CHEMICAL SOCIETY, 1971, pp. 69-85.

[123] J. Purewal, D. Liu, A. Sudik, M. Veenstra, J. Yang, S. Maurer, U. Müller, D.J. Siegel, Improved hydrogen storage and thermal conductivity in high-density MOF-5 composites, Journal of Physical Chemistry C, 116(38) (2012) 20199-20212.

[124] J.J. Purewal, D. Liu, J. Yang, A. Sudik, D.J. Siegel, S. Maurer, U. Müller, Increased volumetric hydrogen uptake of MOF-5 by powder densification, International Journal of Hydrogen Energy, 37(3) (2012) 2723-2727.

[125] D.J. Tranchemontagne, J.R. Hunt, O.M. Yaghi, Room temperature synthesis of metal-organic frameworks: MOF-5, MOF-74, MOF-177, MOF-199, and IRMOF-0, Tetrahedron, 64(36) (2008) 8553-8557.

[126] A.P. Nelson, O.K. Farha, K.L. Mulfort, J.T. Hupp, Supercritical processing as a route to high internal surface areas and permanent microporosity in metal#organic framework materials, Journal of the American Chemical Society, 131(2) (2009) 458-460.

[127] S. Brunauer, P.H. Emmett, E. Teller, Adsorption of Gases in Multimolecular Layers, Journal of the American Chemical Society, 60(2) (1938) 309-319.

[128] E.P. Barrett, L.G. Joyner, P.P. Halenda, The determination of pore volume and area distributions in porous substances. I. Computations from nitrogen isotherms, Journal of the American Chemical Society, 73(1) (1951) 373-380.

[129] W.S. Rasband, ImageJ, U.S. National Institutes of Health, Bethesda, Maryland, USA, http://rsb.info.nih.gov/ij/, (1997–2005).

[130] R. Zacharia, D. Cossement, L. Lafi, R. Chahine, Volumetric hydrogen sorption capacity of monoliths prepared by mechanical densification of MOF-177, Journal of Materials Chemistry, 20(11) (2010) 2145-2151.

[131] A. Dailly, E. Poirier, Evaluation of an industrial pilot scale densified MOF-177

adsorbent as an on-board hydrogen storage medium, Energy and Environmental Science, 4(9) (2011) 3527-3534.

[132] M. Jordá-Beneyto, D. Lozano-Castelló, F. Suárez-García, D. Cazorla-Amorós, A. Linares-Solano, Advanced activated carbon monoliths and activated carbons for hydrogen storage, Microporous and Mesoporous Materials, 112(1-3) (2008) 235-242.

[133] D. Liu, J.J. Purewal, J. Yang, A. Sudik, S. Maurer, U. Mueller, J. Ni, D.J. Siegel, MOF-5 composites exhibiting improved thermal conductivity, International Journal of Hydrogen Energy, 37(7) (2012) 6109-6117.

[134] K.J. Gross, K.R. Carrington, S. Barcelo, A. Karkamkar, J. Purewal, S. Ma, H. Zhou, P. Dantzer, K. Ott, T. Burrell, T. Semeslberger, Y. Pivak, B. Dam, D. Chandra, Recommended Best Practices for the Characterization of Storage Properties of Hydrogen Storage Materials, V3.34 (Feb 21, 2012), Available at: http://www1.eere.energy.gov/hydrogenandfuelcells/pdfs/best_practices_hydrogen_storage.pdf.

[135] J.W. Leachman, R.T. Jacobsen, S.G. Penoncello, E.W. Lemmon, Fundamental equations of state for parahydrogen, normal hydrogen, and orthohydrogen, Journal of Physical and Chemical Reference Data, 38(3) (2009) 721-748.

[136] M.L.H. E.W. Lemmon, M.O. McLinden, NIST Standard Reference Database 23: Reference Fluid Thermodynamic and Transport Properties—REPROP, Version 9.0, 2010.

[137] S. Hausdorf, J. Wagler, R. Mossig, F.O.R.L. Mertens, Proton and water activity-controlled structure formation in zinc carboxylate-based metal organic frameworks, Journal of Physical Chemistry A, 112(33) (2008) 7567-7576.

[138] J.A. Greathouse, M.D. Allendorf, The interaction of water with MOF-5 simulated by molecular dynamics, Journal of the American Chemical Society, 128(33) (2006) 10678-10679.

[139] B. Panella, M. Hirscher, S. Roth, Carbon, 43 (2005) 2009-2214.

[140] H. Kabbour, T.F. Baumann, J.H. Satcher Jr, A. Saulnier, C.C. Ahn, Toward new candidates for hydrogen storage: High-surface-area carbon aerogels, Chemistry of Materials, 18(26) (2006) 6085-6087.

[141] R. Chahine, T.K. Bose, Characterization and Optimization of Adsorbents for Hydrogen Storage, 11th WHEC, (1996).

[142] J.F. Le Page, Manufacture, Use of Solid Catalysts, (1987) 75–123.

[143] S. Ma, H.C. Zhou, Gas storage in porous metal-organic frameworks for clean energy applications, Chemical Communications, 46(1) (2010) 44-53.

[144] A. Züttel, P. Sudan, P. Mauron, P. Wenger, Model for the hydrogen adsorption on carbon nanostructures, Applied Physics A: Materials Science and Processing, 78(7) (2004) 941-946.

[145] B. Panella, M. Hirscher, H. Pütter, U. Müller, Hydrogen adsorption in metal-organic frameworks: Cu-MOFs and Zn-MOFs compared, Advanced Functional Materials, 16(4) (2006) 520-524.

[146] H. Frost, T. Düren, R.Q. Snurr, Effects of surface area, free volume, and heat of

adsorption on hydrogen uptake in metal-organic frameworks, Journal of Physical Chemistry B, 110(19) (2006) 9565-9570.

[147] S.S. Kaye, A. Dailly, O.M. Yaghi, J.R. Long, Impact of Preparation and Handling on the Hydrogen Storage Properties of Zn4O(1,4-benzenedicarboxylate)3 (MOF-5), Journal of the American Chemical Society, 129(46) (2007) 14176-14177.

[148] O.K. Farha, A.Ö. Yazaydin, I. Eryazici, C.D. Malliakas, B.G. Hauser, M.G. Kanatzidis, S.T. Nguyen, R.Q. Snurr, J.T. Hupp, De novo synthesis of a metal-organic framework material featuring ultrahigh surface area and gas storage capacities, Nature Chemistry, 2(11) (2010) 944-948.

[149] H. Furukawa, N. Ko, Y.B. Go, N. Aratani, S.B. Choi, E. Choi, A.O. Yazaydin, R.Q. Snurr, M. O'Keeffe, J. Kim, O.M. Yaghi, Ultrahigh porosity in metal-organic frameworks, Science, 329(5990) (2010) 424-428.

[150] C. Scherdel, G. Reichenauer, M. Wiener, Relationship between pore volumes and surface areas derived from the evaluation of N2-sorption data by DR-, BET- and t-plot, Microporous and Mesoporous Materials, 132(3) (2010) 572-575.

[151] R.M. German, Particle Packing Characteristics, Metal Powder Industries Federations, Princeton, NJ (1989).

[152] A.J.H. McGaughey, M. Kaviany, Thermal conductivity decomposition and analysis using molecular dynamics simulations: Part II. Complex silica structures, International Journal of Heat and Mass Transfer, 47(8–9) (2004) 1799-1816.

[153] S. Kumar, M. Raju, V. Senthil Kumar, System simulation models for on-board hydrogen storage systems, International Journal of Hydrogen Energy, 37(3) (2012) 2862-2873.

[154] J. Xiao, L. Tong, C. Deng, P. Bénard, R. Chahine, Simulation of heat and mass transfer in activated carbon tank for hydrogen storage, International Journal of Hydrogen Energy, 35(15) (2010) 8106-8116.

[155] M.A. André, D. Cossement, P.A. Chandonia, R. Chahine, D. Mori, K. Hirose, Energy Eng., 55 (2009) 2985–2996.

[156] R.W.G. Wyckoff, Crystal Structures (2nd ed.), John Wiley and Sons, Interscience, New York (1963).

[157] B.L. Huang, Z. Ni, A. Millward, A.J.H. McGaughey, C. Uher, M. Kaviany, O. Yaghi, Thermal conductivity of a metal-organic framework (MOF-5): Part II. Measurement, International Journal Of Heat And Mass Transfer, 50(3-4) (2007) 405-411.

[158] D.E. Dedrick, M.P. Kanouff, B.C. Replogle, K.J. Gross, Thermal properties characterization of sodium alanates, Journal of Alloys and Compounds, 389(1-2) (2005) 299-305.

[159] F.P. Incropera, D.P. DeWitt, Fundamentals of Heat and Mass Transfer, (1996).

[160] K. Murata, J. Miyawaki, K. Kaneko, A simple determination method of the absolute adsorbed amount for high pressure gas adsorption, Carbon, 40(3) (2002) 425-428.

[161] M.A. Richard, P. Bénard, R. Chahine, Gas adsorption process in activated carbon

over a wide temperature range above the critical point. Part 1: Modified Dubinin-Astakhov model, Adsorption, 15(1) (2009) 43-51.

[162] E. Poirier, A. Dailly, Investigation of the hydrogen state in IRMOF-1 from measurements and modeling of adsorption isotherms at high gas densities, Journal of Physical Chemistry C, 112(33) (2008) 13047-13052.

[163] W. Zhou, H. Wu, M.R. Hartman, T. Yildirim, Hydrogen and methane adsorption in metal-organic frameworks: A high-pressure volumetric study, Journal of Physical Chemistry C, 111(44) (2007) 16131-16137.

[164] J.J. Low, A.I. Benin, P. Jakubczak, J.F. Abrahamian, S.A. Faheem, R.R. Willis, Virtual High Throughput Screening Confirmed Experimentally: Porous Coordination Polymer Hydration, Journal of the American Chemical Society, 131(43) (2009) 15834-15842.

[165] M. Sabo, A. Henschel, H. Fröde, E. Klemm, S. Kaskel, Solution infiltration of palladium into MOF-5: Synthesis, physisorption and catalytic properties, Journal of Materials Chemistry, 17(36) (2007) 3827-3832.

[166] L. Bellarosa, S. Calero, N. López, Early stages in the degradation of metal-organic frameworks in liquid water from first-principles molecular dynamics, Physical Chemistry Chemical Physics, 14(20) (2012) 7240-7245.

[167] M. De, ChemPhysChem, 13 (2012) 3497–3503.

[168] K. Schröck, F. Schröder, M. Heyden, R.A. Fischer, M. Havenith, Characterization of interfacial water in MOF-5 (Zn4(O)(BDC) 3)-a combined spectroscopic and theoretical study, Physical Chemistry Chemical Physics, 10(32) (2008) 4732-4739.

[169] J. Hafizovic, M. Bjørgen, U. Olsbye, P.D.C. Dietzel, S. Bordiga, C. Prestipino, C. Lamberti, K.P. Lillerud, The inconsistency in adsorption properties and powder XRD data of MOF-5 is rationalized by framework interpenetration and the presence of organic and inorganic species in the nanocavities, Journal of the American Chemical Society, 129(12) (2007) 3612-3620.

[170] U. Mueller, M. Schubert, F. Teich, H. Puetter, K. Schierle-Arndt, J. Pastre, Metal-organic frameworks-prospective industrial applications, Journal of Materials Chemistry, 16(7) (2006) 626-636.

[171] K. Schlichte, T. Kratzke, S. Kaskel, Improved synthesis, thermal stability and catalytic properties of the metal-organic framework compound Cu3(BTC)2, Microporous and Mesoporous Materials, 73(1–2) (2004) 81-88.

[172] O.M. Yaghi, M. O'Keeffe, N.W. Ockwig, H.K. Chae, M. Eddaoudi, J. Kim, Reticular synthesis and the design of new materials, Nature, 423(6941) (2003) 705-714.

[173] L.J. Murray, M. Dinca, J.R. Long, Hydrogen storage in metal-organic frameworks, Chemical Society Reviews, 38(5) (2009) 1294-1314.

[174] T.A. Makal, J.-R. Li, W. Lu, H.-C. Zhou, Methane storage in advanced porous materials, Chemical Society Reviews, 41(23) (2012) 7761-7779.

[175] S. Keskin, T.M. van Heest, D.S. Sholl, Can Metal–Organic Framework Materials

Play a Useful Role in Large-Scale Carbon Dioxide Separations?, ChemSusChem, 3(8) (2010) 879-891.

[176] B. Schmitz, U. Müller, N. Trukhan, M. Schubert, G. Férey, M. Hirscher, Heat of Adsorption for Hydrogen in Microporous High-Surface-Area Materials, ChemPhysChem, 9(15) (2008) 2181-2184.

[177] J. Purewal, D. Liu, A. Sudik, M. Veenstra, J. Yang, S. Maurer, U. Müller, D.J. Siegel, Improved Hydrogen Storage and Thermal Conductivity in High-Density MOF-5 Composites, The Journal of Physical Chemistry C, 116(38) (2012) 20199-20212.

[178] http://www.hydrogen.energy.gov/pdfs/review11/st006_van_hassel_2011_o.pdf.

[179] B.L. Huang, A.J.H. McGaughey, M. Kaviany, Thermal conductivity of metal-organic framework 5 (MOF-5): Part I. Molecular dynamics simulations, International Journal Of Heat And Mass Transfer, 50(3-4) (2007) 393-404.

[180] Y. Ming, J. Purewal, D.a. Liu, A. Sudik, C. Xu, J. Yang, M. Veenstra, K. Rhodes, R. Soltis, J. Warner, M. Gaab, U. Müller, D.J. Siegel, Thermophysical properties of MOF-5 powders, Microporous and Mesoporous Materials, 185(0) (2014) 235-244.

[181] A. Rodríguez Sánchez, H.-P. Klein, M. Groll, Expanded graphite as heat transfer matrix in metal hydride beds, International Journal of Hydrogen Energy, 28(5) (2003) 515-527.

[182] L. Lian, F. Ma, H. Zheng, D. Yang, K. Xu, Effect of Uniaxial Strain on Heat Capacity and Thermal Conductivity of Graphene Nanoribbons Passivated by Hydrogen, Integrated Ferroelectrics, 144(1) (2013) 101-106.

[183] D.C. Venerus, D.N. Kolev, Anisotropic Thermal Conductivity in Cross-Linked Polybutadienes Subjected to Uniaxial Elongation, Macromolecules, 42(7) (2009) 2594-2598.

[184] L.W. Wang, Z. Tamainot-Telto, S.J. Metcalf, R.E. Critoph, R.Z. Wang, Anisotropic thermal conductivity and permeability of compacted expanded natural graphite, Applied Thermal Engineering, 30(13) (2010) 1805-1811.

[185] A.M. Marconnet, N. Yamamoto, M.A. Panzer, B.L. Wardle, K.E. Goodson, Thermal Conduction in Aligned Carbon Nanotube–Polymer Nanocomposites with High Packing Density, ACS Nano, 5(6) (2011) 4818-4825.

[186] V.V. Ganesh, N. Chawla, Effect of particle orientation anisotropy on the tensile behavior of metal matrix composites: experiments and microstructure-based simulation, Materials Science and Engineering: A, 391(1–2) (2005) 342-353.

[187] M.K. Rana, H.S. Koh, H. Zuberi, D.J. Siegel, Methane Storage in Metal-Substituted Metal–Organic Frameworks: Thermodynamics, Usable Capacity, and the Impact of Enhanced Binding Sites, The Journal of Physical Chemistry C, 118(6) (2014) 2929-2942.

[188] J. Goldsmith, A.G. Wong-Foy, M.J. Cafarella, D.J. Siegel, Theoretical Limits of Hydrogen Storage in Metal–Organic Frameworks: Opportunities and Trade-Offs, Chemistry of Materials, 25(16) (2013) 3373-3382.

[189]

http://www.sglgroup.com/cms/_common/downloads/products/product-groups/eg/construction-materials-ecophit/ECOPHIT_G_e.pdf.

[190] A. Celzard, J.F. Marêché, G. Furdin, Surface area of compressed expanded graphite, Carbon, 40(14) (2002) 2713-2718.

[191] Rasband, W.S., ImageJ, U. S. National Institutes of Health, Bethesda, Maryland, USA, http://imagej.nih.gov/ij/, 1997-2014.

[192] J.R. Cannon, The One–Dimensional Heat Equation, in: Encyclopedia of Mathematics and Its Applications 23 (1st ed.), Addison-Wesley Publishing Company/Cambridge University Press, 1984, pp. pp. XXV+483.

[193] L.M. Clark, R.E. Taylor, RADIATION LOSS IN FLASH METHOD FOR THERMAL-DIFFUSIVITY, Journal Of Applied Physics, 46(2) (1975) 714-719.

[194] Y.F. Zhao, M. Xiao, S.J. Wang, X.C. Ge, Y.Z. Meng, Preparation and properties of electrically conductive PPS/expanded graphite nanocomposites, Composites Science and Technology, 67(11–12) (2007) 2528-2534.

[195] L.M. Clark Iii, R.E. Taylor, Radiation loss in the flash method for thermal diffusivity, Journal of Applied Physics, 46(2) (1975) 714-719.

[196] F. Gul-E-Noor, B. Jee, A. Poppl, M. Hartmann, D. Himsl, M. Bertmer, Effects of varying water adsorption on a Cu3(BTC)2 metal-organic framework (MOF) as studied by 1H and 13C solid-state NMR spectroscopy, Physical Chemistry Chemical Physics, 13(17) (2011) 7783-7788.

[197] F. Gul-E-Noor, D. Michel, H. Krautscheid, J. Haase, M. Bertmer, Time dependent water uptake in Cu3(btc)2 MOF: Identification of different water adsorption states by 1H MAS NMR, Microporous and Mesoporous Materials, 180(0) (2013) 8-13.

[198] Z. Liang, M. Marshall, A.L. Chaffee, CO2 adsorption, selectivity and water tolerance of pillared-layer metal organic frameworks, Microporous and Mesoporous Materials, 132(3) (2010) 305-310.

[199] H. Jasuja, Y.-g. Huang, K.S. Walton, Adjusting the Stability of Metal–Organic Frameworks under Humid Conditions by Ligand Functionalization, Langmuir, 28(49) (2012) 16874-16880.

[200] J.B. DeCoste, G.W. Peterson, H. Jasuja, T.G. Glover, Y.-g. Huang, K.S. Walton, Stability and degradation mechanisms of metal-organic frameworks containing the Zr6O4(OH)4 secondary building unit, Journal of Materials Chemistry A, 1(18) (2013) 5642-5650.

[201] S. Hausdorf, J. Wagler, R. Moβig, F.O.R.L. Mertens, Proton and Water Activity-Controlled Structure Formation in Zinc Carboxylate-Based Metal Organic Frameworks, The Journal of Physical Chemistry A, 112(33) (2008) 7567-7576.

[202] S. Han, Y. Huang, T. Watanabe, S. Nair, K.S. Walton, D.S. Sholl, J. Carson Meredith, MOF stability and gas adsorption as a function of exposure to water, humid air, SO2, and NO2, Microporous and Mesoporous Materials, 173(0) (2013) 86-91.

[203] H. Jasuja, N.C. Burtch, Y.G. Huang, Y. Cai, K.S. Walton, Kinetic Water Stability of an Isostructural Family of Zinc-Based Pillared Metal-Organic Frameworks, Langmuir, 29(2) (2013) 633-642.

[204] Z.J. Liang, M. Marshall, A.L. Chaffee, CO2 adsorption, selectivity and water tolerance of pillared-layer metal organic frameworks, Microporous And Mesoporous Materials, 132(3) (2010) 305-310.

[205] S. Paranthaman, F.-X. Coudert, A.H. Fuchs, Water adsorption in hydrophobic MOF channels, Physical Chemistry Chemical Physics, 12(28) (2010) 8124-8130.

[206] K. Schrock, F. Schroder, M. Heyden, R.A. Fischer, M. Havenith, Characterization of interfacial water in MOF-5 (Zn4(O)(BDC)3)-a combined spectroscopic and theoretical study, Physical Chemistry Chemical Physics, 10(32) (2008) 4732-4739.

[207] K.A. Cychosz, A.J. Matzger, Water Stability of Microporous Coordination Polymers and the Adsorption of Pharmaceuticals from Water, Langmuir, 26(22) (2010) 17198-17202.

[208] L. Bellarosa, J.M. Castillo, T. Vlugt, S. Calero, N. López, On the Mechanism Behind the Instability of Isoreticular Metal–Organic Frameworks (IRMOFs) in Humid Environments, Chemistry – A European Journal, 18(39) (2012) 12260-12266.

[209] L. Bellarosa, S. Calero, N. Lopez, Early stages in the degradation of metal-organic frameworks in liquid water from first-principles molecular dynamics, Physical Chemistry Chemical Physics, 14(20) (2012) 7240-7245.

[210] M. De Toni, R. Jonchiere, P. Pullumbi, F.-X. Coudert, A.H. Fuchs, How Can a Hydrophobic MOF be Water-Unstable? Insight into the Hydration Mechanism of IRMOFs, ChemPhysChem, 13(15) (2012) 3497-3503.

[211] P. Li, J. Chen, J. Zhang, X. Wang, Water Stability and Competition Effects Toward CO2 Adsorption on Metal Organic Frameworks, Separation & Purification Reviews, 44(1) (2014) 19-27.

[212] Y. Li, Z. Ju, B. Wu, D. Yuan, A Water and Thermally Stable Metal–Organic Framework Featuring Selective CO2 Adsorption, Crystal Growth & Design, 13(9) (2013) 4125-4130.

[213] J. An, N.L. Rosi, Tuning MOF CO2 Adsorption Properties via Cation Exchange, Journal of the American Chemical Society, 132(16) (2010) 5578-5579.

[214] S.R. Caskey, A.G. Wong-Foy, A.J. Matzger, Dramatic Tuning of Carbon Dioxide Uptake via Metal Substitution in a Coordination Polymer with Cylindrical Pores, Journal of the American Chemical Society, 130(33) (2008) 10870-10871.

[215] A. Demessence, D.M. D’Alessandro, M.L. Foo, J.R. Long, Strong CO2 Binding in a Water-Stable, Triazolate-Bridged Metal−Organic Framework Functionalized with Ethylenediamine, Journal of the American Chemical Society, 131(25) (2009) 8784-8786.

[216] Y. Ming, H. Chi, R. Blaser, C. Xu, J. Yang, M. Veenstra, M. Gaab, U. Müller, C. Uher, D.J. Siegel, Anisotropic thermal transport in MOF-5 composites, International Journal of Heat and Mass Transfer, 82(0) (2015) 250-258.

[217] G. Halsey, H.S. Taylor, THE ADSORPTION OF HYDROGEN ON TUNGSTEN POWDERS, Journal Of Chemical Physics, 15(9) (1947) 624-630.

[218] A. Thirumurugan, C.N.R. Rao, 1,2-, 1,3- and 1,4-Benzenedicarboxylates of Cd

and Zn of different dimensionalities: Process of formation of the three-dimensional structure, Journal of Materials Chemistry, 15(35-36) (2005) 3852-3858.

[219] R. Chahine, T.K. Bose, Characterization and optimization of adsorbents for hydrogen storage, Hydrogen Energy Progress Xi, Vols 1-3, (1996) 1259-1263.

[220] Y. Ming, J. Purewal, J. Yang, C. Xu, R. Soltis, J. Warner, M. Veenstra, M. Gaab, U. Müller, D.J. Siegel, Kinetic Stability of MOF-5 in Humid Environments: Impact of Powder Densification, Humidity Level, and Exposure Time, Langmuir, (2015).

[221] S.S. Han, S.-H. Choi, A.C.T. van Duin, Molecular dynamics simulations of stability of metal-organic frameworks against H2O using the ReaxFF reactive force field, Chemical Communications, 46(31) (2010) 5713-5715.

[222] P. Guo, D. Dutta, A.G. Wong-Foy, D.W. Gidley, A.J. Matzger, Water Sensitivity in Zn4O-Based MOFs is Structure and History Dependent, Journal of the American Chemical Society, 137(7) (2015) 2651-2657.

[223] G. Kresse, J. Furthmuller, Efficient iterative schemes for ab initio total-energy calculations using a plane-wave basis set, Physical Review B, 54(16) (1996) 11169-11186.

[224] P.E. Blochl, PROJECTOR AUGMENTED-WAVE METHOD, Physical Review B, 50(24) (1994) 17953-17979.

[225] N.L. Rosi, J. Eckert, M. Eddaoudi, D.T. Vodak, J. Kim, M. O'Keeffe, O.M. Yaghi, Hydrogen Storage in Microporous Metal-Organic Frameworks, Science, 300(5622) (2003) 1127-1129.

[226] G. Henkelman, H. Jónsson, Improved tangent estimate in the nudged elastic band method for finding minimum energy paths and saddle points, The Journal of Chemical Physics, 113(22) (2000) 9978-9985.

[227] G. Henkelman, B.P. Uberuaga, H. Jónsson, A climbing image nudged elastic band method for finding saddle points and minimum energy paths, The Journal of Chemical Physics, 113(22) (2000) 9901-9904.

[228] M. Eddaoudi, J. Kim, N. Rosi, D. Vodak, J. Wachter, M. O'Keeffe, O.M. Yaghi, Systematic Design of Pore Size and Functionality in Isoreticular MOFs and Their Application in Methane Storage, Science, 295(5554) (2002) 469-472.

[229] J.L.C. Rowsell, E.C. Spencer, J. Eckert, J.A.K. Howard, O.M. Yaghi, Gas Adsorption Sites in a Large-Pore Metal-Organic Framework, Science, 309(5739) (2005) 1350-1354.

[230] T. Mueller, G. Ceder, A Density Functional Theory Study of Hydrogen Adsorption in MOF-5, The Journal of Physical Chemistry B, 109(38) (2005) 17974-17983.

[231] M.K. Rana, H.S. Koh, J. Hwang, D.J. Siegel, Comparing van der Waals Density Functionals for CO2 Adsorption in Metal Organic Frameworks, The Journal of Physical Chemistry C, 116(32) (2012) 16957-16968.

[232] H.S. Koh, M.K. Rana, J. Hwang, D.J. Siegel, Thermodynamic screening of metal-substituted MOFs for carbon capture, Physical Chemistry Chemical Physics, 15(13) (2013) 4573-4581.

[233] B. Panella, K. Hönes, U. Müller, N. Trukhan, M. Schubert, H. Pütter, M. Hirscher, Desorption Studies of Hydrogen in Metal–Organic Frameworks, Angewandte Chemie International Edition, 47(11) (2008) 2138-2142.

[234] C. Petit, B. Mendoza, T.J. Bandosz, Hydrogen Sulfide Adsorption on MOFs and MOF/Graphite Oxide Composites, ChemPhysChem, 11(17) (2010) 3678-3684.

[235] J.J. Gutierrez-Sevillano, A. Martin-Calvo, D. Dubbeldam, S. Calero, S. Hamad, Adsorption of hydrogen sulphide on Metal-Organic Frameworks, RSC Advances, 3(34) (2013) 14737-14749.

[236] L. Hamon, C. Serre, T. Devic, T. Loiseau, F. Millange, G. Férey, G.D. Weireld, Comparative Study of Hydrogen Sulfide Adsorption in the MIL-53(Al, Cr, Fe), MIL-47(V), MIL-100(Cr), and MIL-101(Cr) Metal−Organic Frameworks at Room Temperature, Journal of the American Chemical Society, 131(25) (2009) 8775-8777.

[237] D. Saha, S. Deng, Ammonia adsorption and its effects on framework stability of MOF-5 and MOF-177, Journal of Colloid and Interface Science, 348(2) (2010) 615-620.

[238] C. Petit, T.J. Bandosz, Enhanced Adsorption of Ammonia on Metal-Organic Framework/Graphite Oxide Composites: Analysis of Surface Interactions, Advanced Functional Materials, 20(1) (2010) 111-118.

[239] L. Huang, T. Bandosz, K.L. Joshi, A.C.T. van Duin, K.E. Gubbins, Reactive adsorption of ammonia and ammonia/water on CuBTC metal-organic framework: A ReaxFF molecular dynamics simulation, The Journal of Chemical Physics, 138(3) (2013) 034102.

[240] L. Ding, A.Ö. Yazaydin, How Well Do Metal–Organic Frameworks Tolerate Flue Gas Impurities?, The Journal of Physical Chemistry C, 116(43) (2012) 22987-22991.

[241] L. Valenzano, B. Civalleri, S. Chavan, G.T. Palomino, C.O. Areán, S. Bordiga, Computational and Experimental Studies on the Adsorption of CO, N2, and CO2 on Mg-MOF-74, The Journal of Physical Chemistry C, 114(25) (2010) 11185-11191.

[242] S. International, Hydrogen Fuel Quality for Fuel Cell Vehicles, (2011).

[243] http://www.nrel.gov/hydrogen/images/cdp_infr_25.jpg.

[244] D. Chandra, Chapter 12, Solid State Hydrogen Storage: Materials and Chemistry, CRC Press, LLC: Boca Raton, U.S.A, (2008).

[245] M.-A. Richard, D. Cossement, P.-A. Chandonia, R. Chahine, D. Mori, K. Hirose, Preliminary evaluation of the performance of an adsorption-based hydrogen storage system, AIChE Journal, 55(11) (2009) 2985-2996.

[246] http://www.hydrogen.energy.gov/pdfs/progress12/iv_d_9_drost_2012.pdf.

[247] NIST, http://physics.nist.gov/MajResFac/NIF/facility.html.

[248] A. Kak, M. Slaney, Principles of computerized tomography, New York, NY: IEEE Press, (1988).

[249] http://homepages.inf.ed.ac.uk/rbf/CVonline/LOCAL_COPIES/AV0405/HAYDEN/Slice_Reconstruction.html.

[250] J. Szekely, J.W. Evans, H.Y. Sohn, GAS-SOLID REACTIONS, (1976).